Complete Performance Model of Optic Filters for PV Applications

Georgia Frantzi

Delft University of Technology

TU Delft Delft University of Technology

Complete Performance Model of Optic Filters for PV Applications

By

Georgia Frantzi (4899172)

in partial fulfilment of the requirements for the degree of

Master of Science in Sustainable Energy Technology

at the Delft University of Technology

to be defended publicly on Thursday July 16, 2020 at 14:00 PM.

This thesis is confidential and cannot be made public until August 31, 2021.

Thesis committee:	Dr. Ir.O. Isabella,	Associate Professor - PVMD	*Supervisor*
	Prof. Dr. Ir. T. Klein,	Professor - Building Product Innovation	*External committee member*
	Dr. Ir. R. Santbergen,	Assistant Professor - PVMD	*Committee member*
	Ir. J. C. Ortiz	PhD candidate – PVMD	*Daily Supervisor*

Abstract

Building energy consumption is one of the highest of any sector. Building integrated Photovoltaics (BIPV) have the potential to eventually contribute to 50%-70% of the total energy demand. However, one of the main barriers that hinder the acceptance of solar energy systems as an integrated part in the buildings' envelope is the limited aesthetics. The common black and blue panels with visible cells usually cause incompatibility with the outer appearance of architectural structures. Consequently, the combination of BIPV technology with colored PV modules will provide solutions to architects and stakeholders who are often skeptical on embed PV systems in buildings attributable to their appearance.

To overcome this barrier, different techniques have been developed to provide color to photovoltaic modules. One of the most promising technologies are optical filters. These devices selectively reflect light via interference effects, thus providing the possibility of changing the color appearance of a module. Light reflection, however, reduces the current generated by the solar cells, but also, reduces thermalization losses that negatively impact the cell performance by increasing its operational temperature.

In this thesis, a spectrally resolved thermal model in MATLAB has been developed to fully assess what is the real impact of different optic filters under real operational conditions in terms of temperature, efficiency and energy yield. The model considers the angular dependence of optic filter's on PV modules on both appearance and performance for installations on a façade, roof and free mounted PV (BAPV). In addition, the optimum optic filter thicknesses for ten main colors has been determined based on maximum energy yield.

The model has been validated for three consecutive days and the simulated results for colored modules and module without optic filter were proved to be very close to the corresponding measured values; deviation of 1.5 degrees of simulation models have been obtained during the temperature peak of the modules. The simulation results show that the performance of the optic filters changes depending on the location, installation layout and the incident irradiance. More specifically, temperature drop of 9 degrees has been observed on roof installations from colored modules compared to the corresponding standard module. In addition, the implementation of air gap between the module and the roof has been verified to decrease up to 20 degrees the working temperature and significantly increase the overall energy yield for both colored and standard modules. Nevertheless, in terms of yearly energy yield (kWh/m^2), from the tested colors the relative decrease with respect to the standard module was found approximately 16% observed from the most lossy colors.

Preface

This thesis is made as a completion of my master's education in Sustainable Energy Technology program at Delft University of Technology. Several persons have been contributed academically, practically and with support to this master thesis.

First, my deepest gratitude goes to my family. Mum and Dad thank you so much for supporting my dreams with love and understanding. Nothing would have been possible without you. Besides, I would like to thank my lifelong companion *Kyriakos* who was always by my side and complete my life with love and happiness. I would like to dedicate this thesis to my adorable little nephews *Sotiri* and *Foti* who mean the word to me, Σας Λατρεύω!

I would like to thank the *PVMD group* for the excellent working environment. Besides I would like to thank Dr. Olindo Isabella for sharing his knowledge and support. My gratitude is also to my daily supervisor Juan Camilo Ortiz who besides the complications that he faced during this year he has been an excellent guidance and support not only as a supervisor but also as a friend.

I would like to thank my precious friend *Abdallah* for his valuable friendship and the unforgettable memories that we shared together. These two years would not have been the same without you! To my wonderful friends from Cyprus, I want to say that I am so grateful having you in my life and thank you so much for believing in me. In addition, I am grateful to my officemates, *Harsh*, *Annanta*, *Devika, Lyndon* and *Patricia*. To all my friends from Jaagpad, student housing thank you guys!

Coming to the end of this journey, I am so happy for my choice following this master's degree at TU Delft. During the past two years not only, I gained valuable knowledge but also, I have grown as a person and broaden my horizons.

Georgia Frantzi

Delft, July 16th 2020

Contents

1 Introduction

1.1 Background

Residential and commercial buildings consume approximately 40% of the total global energy demand [1]. The buildings either for housing or commercial purposes are a significant part of our daily lives and their main purpose is to shelter. Housing buildings connect families and give with their appearance and structure a nice charming atmosphere. On the other hand, commercial buildings for example schools, Universities, offices and public areas are meant to connect people, inspire and share motivation with nice designs and colors. Towards a sustainable future and since regulations are now becoming more ambitious the application of Photovoltaics (PV) becomes even more important part of the architecture concept[1]. According to the potential of solar energy on facades and roof can eventually contribute to 50-70% of the total electricity demand[2].

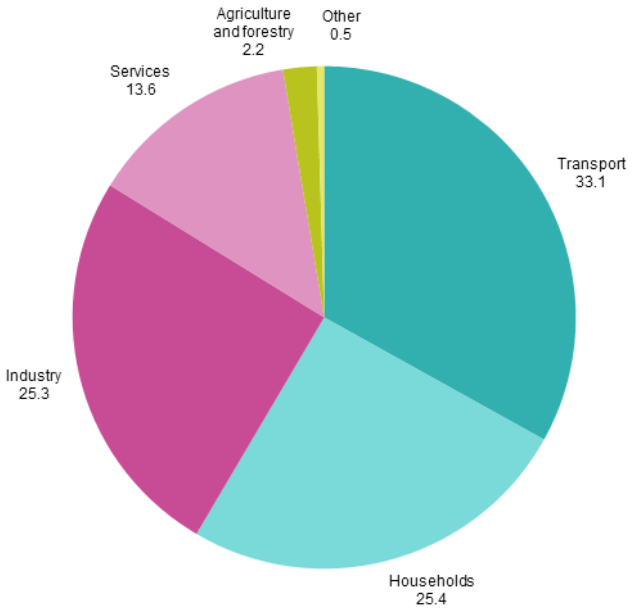

Figure 1.1 Final Energy Consumption EU-2018 [3]

It is very important to transform those buildings into zero energy buildings while at the same time keep their aesthetics and appearance unaffected. The building integrated photovoltaics (BIPV) market in Europe is currently on a transition[1]. Especially the technologies of modules with flat and flexible surfaces in terms of size, shape and appearance are easy to be integrated and suitable for buildings installations [4]. Although their price is much higher than a PV system on a roof (BAPV), the cost is compensated by the sophisticated aesthetics that BIPV provide compared to the standard installations. All in all, it is important to evolve in BIPV technology and create new approaches that will help the society re-imagine the solar buildings. Colored PV modules based on different technologies have now risen the interest of many architects and engineers who are looking for alternative and interesting approaches on installing PV modules on roof and facades and finally contribute them as an important part in the building industry.

Motivation

Renewable forms of energy present an opportunity to make life in cities more attractive

Thomas Herzog, 2001

According to a survey WernerWeiß [5] it was shown that around 85% of the architects believe that as long as aesthetics is concerned the colored PV installations will increase significantly and replace the standard black even if that means lower efficiency.

Nevertheless, there are still some issues which needed to overcome in order to finally include PV modules as a building component. Although many people are concern about PV modules in terms of affordability, according to *F. Frontini et.al* [4] it is more of a matter of affordability and performance since their price is now considered as cheap as other building materials. *F. Frontini et.al* [4] tackled also some other concerns such as technological and morphological integrability. Technological integrability, considers the constructive compatibility between new and traditional buildings, in terms of materials. Morphological integrability deals with the visual perception of the building. As far as aesthetics is concerned, stakeholders are willing to accept and compromise the economic factor as long as BIPV have nice installations [6].

1.2 Previous Work

Colored PV modules with optic filters based on interference effects can provide a wide range of possibilities for integration of solar modules into building environment. TU Delft's PVMD group has shown a lot of interest on that field. Previous years students have done an incredible work with interesting results. Since the current thesis continues the research of previous works, it is important first to give a summary of some outcomes of their results.

Juan Camilo Ortiz [7] studied the optimum design of optic filters which will reduce the fabrication cost of expensive metal back reflector and at the same time boost the aesthetics and flexibility of modules. Juan developed during his thesis a computational model to translate the color of an optic filter according to human perception of color. The model is based on the studies performed by the international committee of illumination (CIE). For optic filter materials, Juan suggested SiO_2 and Si_3N_4 as they are characterized for their non absorptive nature, availability for industrial scaling and their refractive index values which remain constant over the entire visible spectrum. Also, different thickness combinations of the optic filter have been studied and color matrices have been generated. It was found that when the optic filter is directly installed on texture surfaces it becomes difficult to observe bright colors since the surface has low reflectivity. More specifically, the reflectance for the same wavelength range was found to drop by 40% when compared to the same filter applied on flat glass.

Simona Villa [8] focused on the angular resilience of interference filters and how to fabricate them on mini modules. Also, an investigation of the optical behavior and electrical performance was performed. It was found that when the angle of incidence (AOI) increases, a blue shift phenomenon takes place where the reflection peak shifts towards lower wavelengths. This is mainly because the light optical path increases and therefore constructive and destructive interferences take place on different wavelengths. Mini modules where successfully manufactured for different colors and texturing designs. It was concluded

that the flat glass modules are strongly angular depended however randomly textured and grooved glass has the most angular resilient.

1.3 Aim of the current work

Until now, important information of the optical performance and angular resilience of colored PV modules has been investigated. Although, some aspects of optic filters regarding the real impact on performance and the consequences on energy yield are not yet known.

Therefore, the objectives of the current thesis are:

1. *To develop a spectrally resolved thermal model (MATLAB) that considers angular dependence on both appearance and performance of optic filter's implementation on PV modules.*
2. *Consideration of different installations; BAPV, and BIPV on façade and roof.*
3. *Temperature results to fully assess what is the real impact of optic filters compared to a module without optic filter under real operational conditions.*
4. *Determination of the working efficiency for different colors.*
5. *Validated MATLAB model that gives results for the thermal performance and energy yield for different locations and different optic filters.*
6. *User friendly model that give results for different modules layouts, installation types and colors.*

2 State of the art

2.1 Methods to produce color

2.1.1 Colored Solar Cells

During the manufacturing of solar cells, the deposition of *antireflection coatings (ARC$_s$)* at the front is a standard procedure [9]. The ARC$_s$ will color the solar cell and a normal transparent glass will be placed on top. The most commonly used ARC is a thin single layer of amorphous hydrogenated silicon nitride (a-SiN$_x$). The purpose of the coding is to improve the passivation and minimize the reflection. In addition, by varying the thickness of the ARC, different colors of solar cell are obtained [10].

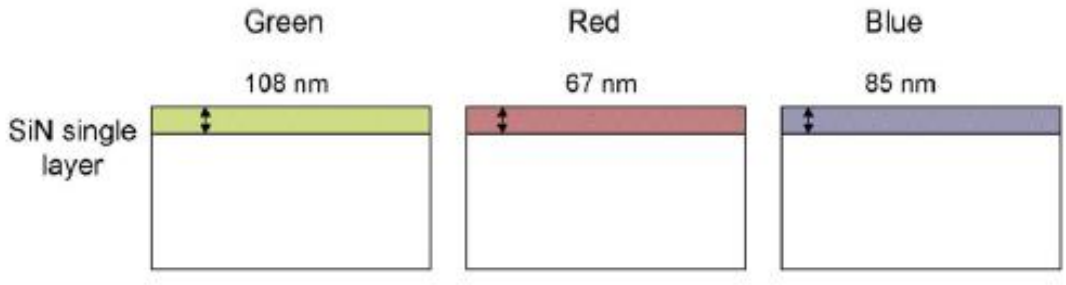

Figure 2.1 Observed color for different thicknesses of SiN ARC [9].

Minghua Li et.al [11], presented a method to use *double layer antireflection coating of SiO$_2$/SiN$_x$* on textured surfaces of multicrystaline silicon. It was concluded that the application of SiO$_2$ increases the range of colors and at the same time it decreases the optical losses. *Figure 2.2* illustrates that the short current density (J$_{sc}$) decreases significantly for different thicknesses of ARC. On the other hand, the SiO$_2$ on top of the standard SiN$_x$ limits the J$_{sc}$ losses as can be seen from *Figure 2.2 b)*. More specifically, the range of colors that can been obtained for different SiO$_2$ thicknesses are presented where the optimum thickness of SiN$_x$ is constant at 80nm.

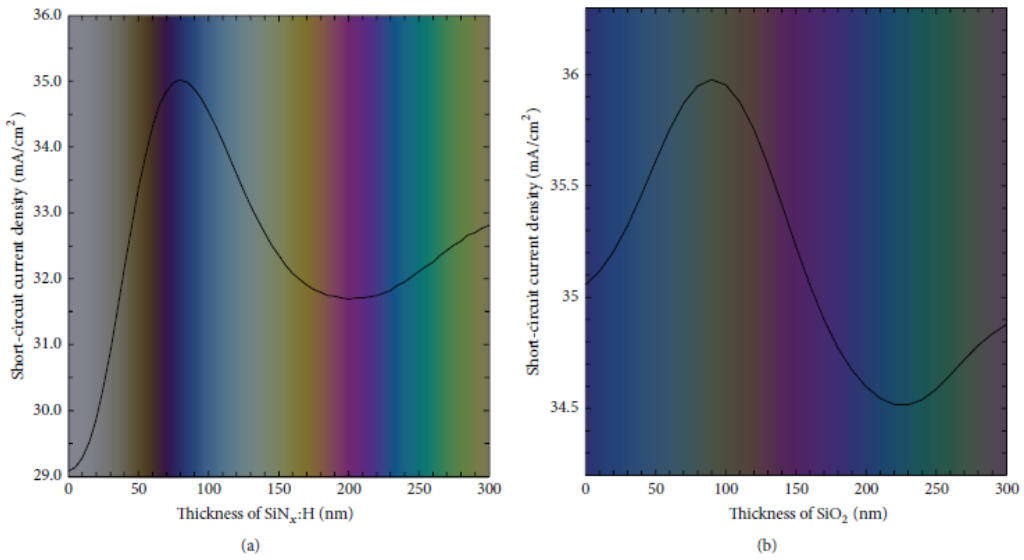

Figure 2.2 Perceived color and J_{sc} as a function of thickness; a) for a standard single layer SiN_x , b) for SiO_2 on top of a standard SiN_x (d=80nm) [11].

Another method to produce color on solar cells is by applying *plasmonic coloring*. Plasmonic effects of color can be achieved from sub-wavelength metallic structures which are surrounded by dielectric material. At the metal-dielectric interface collective free electron oscillations can be generated which are called surface plasmons [12].The sizes and the shapes of the nanoparticles are depended on the thickness of the deposited films and the surface roughness of the substrate solar cell. The resonance wavelength is determined by the dielectric characteristics of the applied materials and the size and shape of the structures. At the wavelength resonance, the absorption and scattering increases which causes optical losses but at the same time scattering improves light trapping [12].

To produce color the c-Si solar cells are coated with metallic nanoparticles that tuning their color. More specifically, *Peharz et al* [12] tune the color of the cells by applying a layer of metallic nanoparticles on top of the solar cells. An important parameter which controls the obtained color is the Ag deposition time. From Figure 2.3 first row, it can be seen that the 40seconds of Ag deposition time give a blue color whereas as the deposition time increases the color tends to be more brownish. On the other hand, it can been observed from *Figure 2.3* second row, that for the monocrystalline cells as the Ag deposition time increases the color changes from blue to a mixture of yellow and green colors.

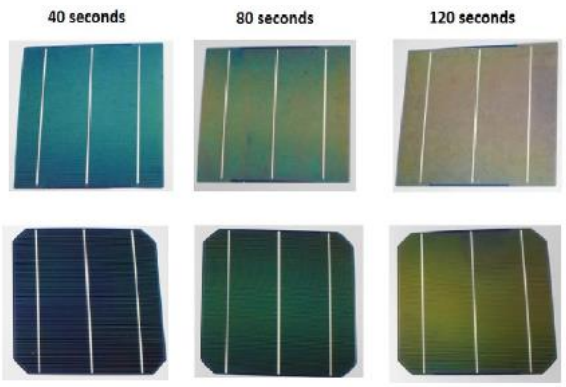

Figure 2.3 Industrial c-Si solar cells coated with different types of Ag nano-particles by annealing sputtered Ag films. The first row refers to polycrystalline cells and the second row to monocrystalline cells [12].

The resonance peak in the reflection spectrum is almost independent from the angle of incidence. On the other hand, the solar cell colors realized with dielectric thin films have a high angle of view dependence. This is a disadvantage since the angular dependency of colors is an issue for façade applications [12]. Another important disadvantage of that technology is that the color homogeneity is uniform. Also, it is almost impossible to observe bright colors without losing a lot of performance.

2.1.2 Color on module level

One method to obtain color on module level is by using a *ceramic ink pattern*. The Dutch company *Kameleon Solar* [13], uses digitally print ceramic ink on the front glass before its tempered. The printed ceramic inks are placed in a way that an empty space around it allow light to pass through the cells. The glass is afterwards tempered, and the inks are becoming strong as the glass while ensuring the lifetime of the color to last for a period of 50 years. By using this method, the company can print images, logos and more complex designs for façade applications.

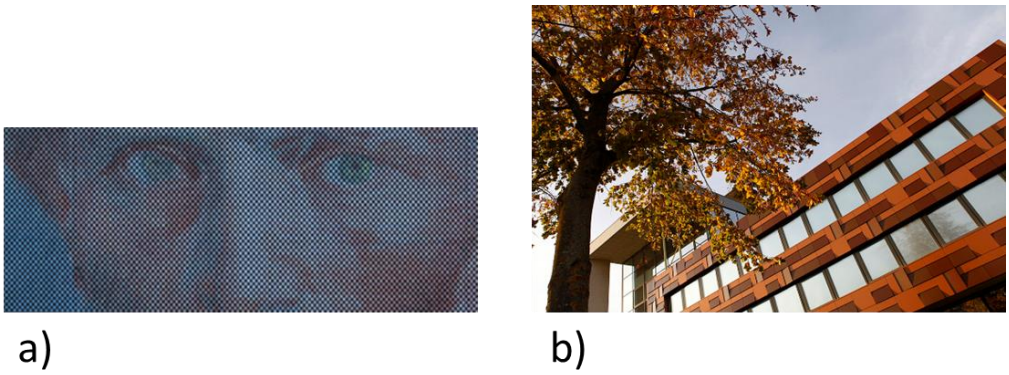

Figure 2.4 Example of colored PV modules using print ceramic ink. a) PV module with a printed image of Van Gogh b) PV modules with a solid color installed on a façade [13].

To obtain a solid color, the components behind the glass must be uniform in color; generally black. Also, the company counters the transformation of the ceramic ink color due to the background and therefore, before printing the ink the correct combination that is required is calculated to give the proper color.

The next method of coloring on module level is inspired by the *Morpho butterfly effect* which is a bionic concept based on 3D photonic structures[14]. The use of the Morpho butterfly effect overcomes the issues of inhomogeneous appearance based on the angle of incidence and allows color choices and saturated colors. In a microscopic analysis, the wings of Morpho butterflies consist a 3D structure of vertical ridges with horizontal lamellae. The Morpho effect follows the principle of thin film interference and structure effects interact in one three-dimensional photonic structure where multilayer interference, diffraction and scattering are taking place. Because of these complex interactions, the function of the layer for a high range of angle of incidence is perfectly uniform. The spectral reflectance peak is caused by a Bragg stack interference effect as shown in Figure 2.5 The Morpho effect: Interference from a finite Bragg stack *[14]*. Such structures that mimic the butterfly's wing are really challenging to manufacture.

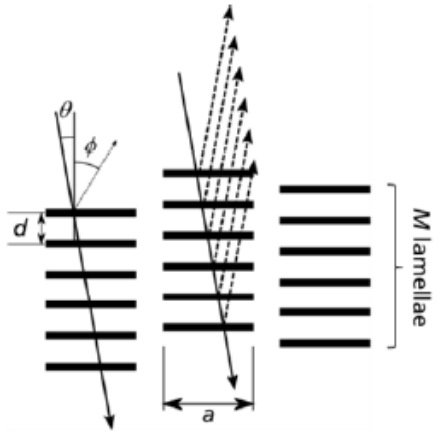

Figure 2.5 The Morpho effect: Interference from a finite Bragg stack [14].

Figure 2.6a) shows the angular stability of such structure which is measured on a glass for a green color. It can be observed that indeed the reflection is relatively stable until the angle of 50 degrees. From Figure 2.6 it is observed that the filter has a very good angular tolerance and nice bright colors.

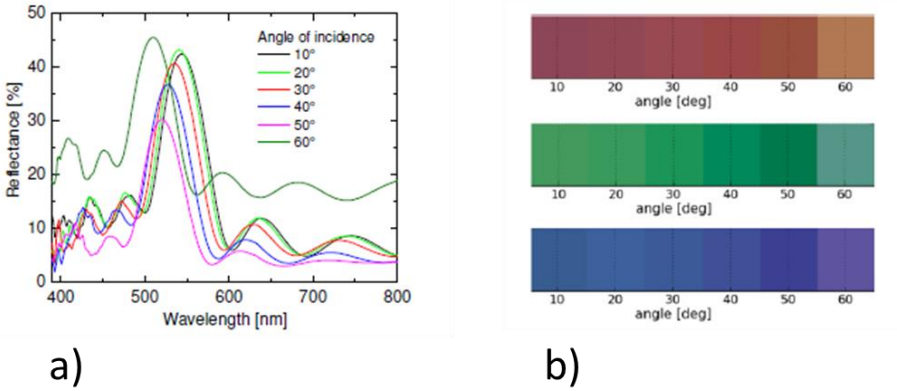

Figure 2.6 a) Angle dependent reflectance spectra measure from the glass b) measured reflectance in RGB space

K.Chung et.al [15], move beyond the limitations of actual butterfly wings and have developed a flexible angle independent structural color reflector inspired by *Morpho Butterfly Wings*. The flexible thin film is consisting of 8 pairs of TiO_2 and SiO_2 and it can reproduce the saturated color of Morpho Butterfly. Also,

it is concluded that it provides better color and brightness stability for different angles and directions. Another advantage of this thin film is that it can bent and fold freely [15].

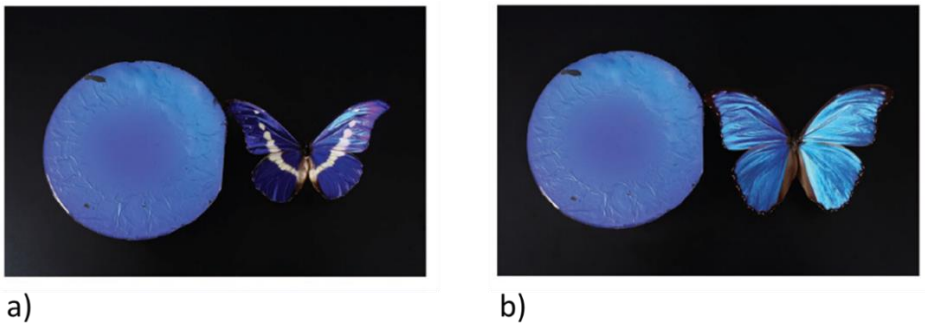

Figure 2.7 Comparison of the fabricated thin film with a) Morpho rhetenor and b) Morpho didius [15].

Figure 2.8 Illustrates the analysis of optical performance of *Morpho rhetenor* and *didius* butterflies and the corresponding analysis for the designed thin film. The results indicate that the film displays a saturated blue color with a peak reflectance of 55%. Also, the observed color is comparable to the Morpho butterfly. Moreover, it is observed that the change of the color and brightness with different angles is significantly smaller than the *Morpho butterflies*. More specifically, the color remains constant and the brightness changes approximately 40%. It can be seen from the Figure 2.8 j), that the color and the brightness are not changing as the film rotates from its normal axis. Therefore, the thin film is not only reproducing comparable colors with the Morpho butterflies but also outperforms and maintain color and brightness stability [15].

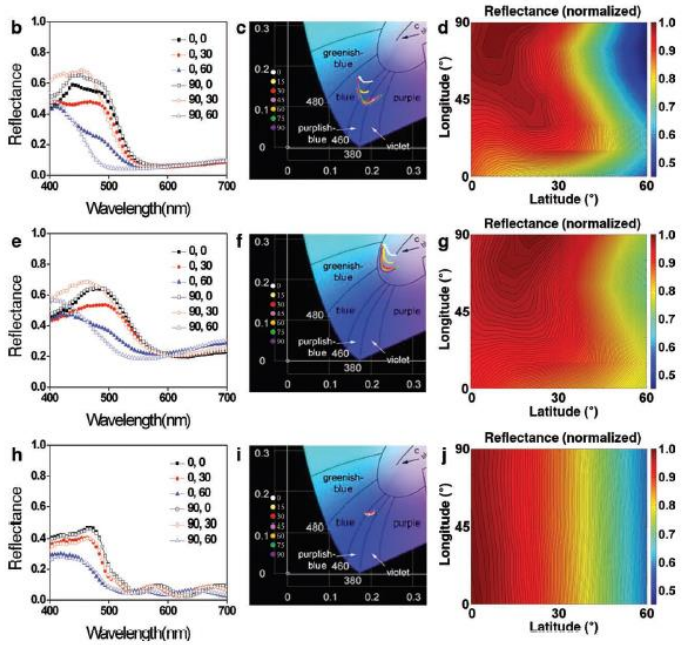

Figure 2.8 Analysis of optical performance: b) Spectral reflectance of Morpho rhetenor butterfly c) changes of its apparent color d) angle-dependence of overall brightness. e-g) corresponding data for Morpho didius butterfly. h-j) Data for the thin film [15].

To conclude, there are different technologies that can be used for coloring the PV modules. The colored layer is sometimes inhomogeneous or either homogeneous. Comparing ARC and plasmonic coloring

technologies it is important to address that in both technics the color is directly on solar cells and a normal glass is placed on the top, therefore, it is easy to distinguish the different cells and their interconnections. Coloring on the module level is proved to be a better approach. More specifically, comparing the technologies that have been addressed, the method of printed dots is a typical example of inhomogeneous layer [6]. To observe a strong color, the density of the dots needs to increase and therefore, the module efficiency decreases [6]. On the other hand, thin film stacks which mimic the *Morpho effect* seems to be the best technological approach for coloring the modules. This is because not only the color is homogeneous and stable, but also It can maintain a high efficiency for the modules. According to *Benedikt Blasi et. al [*6] this method has improved visual appearance and has the possibility to be industrialized mass production.

2.2 BIPV

Building integrated photovoltaic product installations is increasing every year. Many engineers and designers are searching for new and innovative technologies on installing and producing these products to meet the requirements of the market [16].The main idea behind BIPV is to allow the combination of renewable electricity generation and building materials [17]. According to A. K. Shukla et.al [17] BIPV products transform building from energy consumer to energy producer. Figure 2.9 illustrates the main applications of BIPV module products. The interest of BIPV has been increased due to the lack of ground space and the unused roof space. The roof is the most preferable place for installation due to solar irradiance. However, installing on a façade allows a big available surface area [17].

Figure 2.9 Classification of BIPVs Product [17]

Roofs are ideal field for BIPV since in most locations (central Europe) the optimum pitch angle for PV is around 30°. Common designs are for example the in-roof installation of PV modules by replacing the tiles and the full-roof covering of PV modules as more economical and alternative [18]. Examples of these installations are illustrated in Figure 2.10 a) In-roof installation of PV modules, b) full-roof covering of PV modules [18]*Figure 2.10*.

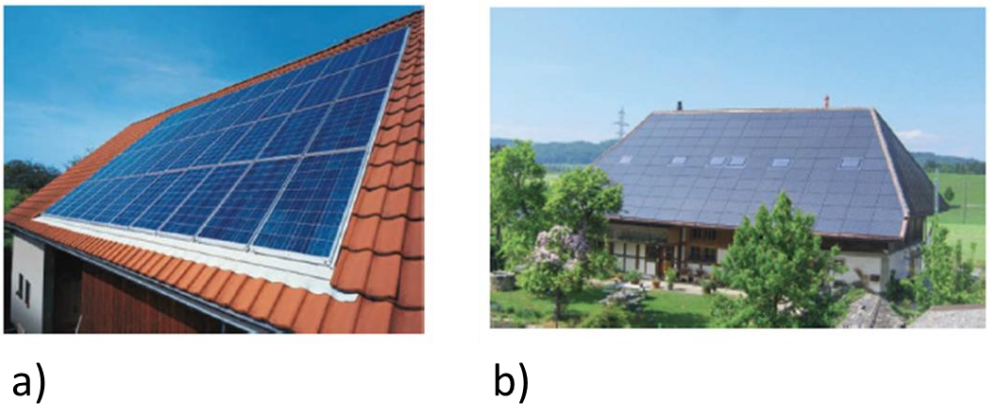

Figure 2.10 a) In-roof installation of PV modules, b) full-roof covering of PV modules [18]

The second major area for the installation of integrated PV modules on buildings is the façade as shown in *Figure 2.11* . The main disadvantage of those systems is that the vertical installation causes 20-40% energy yield. However, façade installation make possible to fulfil a lot of demand due to its high available area [18].

Figure 2.12 Integrated PV modules on a façade [18]

Building energy consumption is one of the highest of any sector [19]. Although solar energy is the prime energy source for zero energy buildings, the installations of PV modules on housing is very limited compared to its potential. The acceptance of solar energy systems as integrated part of the buildings envelope is primarily due to the limited aesthetics of the standard PV modules which are now in the market [19]. The common black and blue panels with visible cells, may cause incompatibility with respect to the outer appearance of architecture. Therefore, it is might not be accepted by the stakeholders and architects. Consequently, combining BIPV technology with colored PV modules will give solutions for a better integration of solar energy in building industries. According to N. Jolissaint [19], multilayered interference filters which transform the common glass into a color glass have become an attractive solution for building facades.

Kohlesilo project is a renovated building with BIPV with *Kromatix™ solar glass* installed on the roof and on the façade[20]. The *Kromatix™ solar glass* are developed from a Swiss company Swissino in partnership with the EPFL (Swiss Polytechnic Institute). The building is in Basel and is now offering space for offices, conferences and circus school. PV colors of black, green, blue, grey and gold are used to cover the area of the whole building. More specifically, the roof is consisting of mono c-Si framed standard size modules whereas the south façade area is covered by frameless glass-glass modules. The total surface of the modules is approximately 126m^2 and is estimated for an installed power of 15.7kW_p. The generated power is around 16,400 kwh which is almost 40% of the building's energy consumption.

Figure 2.13 Coal silo building in Basil covered with colored Kromatix™ solar glass [20]

Another fascinating project of *Swissinso* company is the *Copenhagen International School's (CIS).* This new building is covered by approximately 12,000 solar panels using *Kromatix™* blue-green solar glass with an installed capacity of 720kW_p. It is one of the largest building-integrated solar power plants in the world. The main idea was to connect the movement of the sea water with the turquoise/lagoon-green colored façade elements. Based on their coloring technology, the observed color changes with the angle of incidence. Therefore, the architect decided to install the panels with an angle of approximately 4^o with different orientations in order to create lively appearance and dynamic expression of the façade with respect to the surrounding ocean [19].

Figure 2.14 Copenhagen International School's (CIS) covered with Kromatix™ *blue-green solar glass* [19].

Colored PV modules will not only benefit in terms of aesthetics, but also the self-cooling will substantially extend the lifetime and the energy yield of these systems. According to *Xingshu Sun et.al* [21] comprehensive opto-electro-thermal simulations have shown that the working temperature is reduced up to 10^{o}C. In comparison with other technologies, the radiation cooling is much simpler since is only based on fundamental physics. According to *Xingshu Sun et.al* the commercial solar modules dissipating as heat the 80% of the incoming irradiance and potentially raisin their temperature 20^{o}C-30^{o}C above ambient temperature. This extra heating has an impact on the long-term efficiency and lifetime which eventually reduces dramatically the total energy output. More specifically, the efficiency of an average crystalline silicon (cSi) commercial module decreases 0.45% for every 1^{o}C increase of the temperature. For BIPV installations the ideal scenario is to install products that have expected lifetime as close as possible to the building. In that way, not only householders and architects will be more attractive on those systems but also the technology will become even more economical effective in the long term.

3 Optic Filters

Since the current thesis project is the development of a complete performance model for modules with optic filters, it is important to understand first the theories, definitions and concepts behind optical filters. The derivations of the final equations are beyond the scope of this work. More information can be found from the thesis of previous students Juan Camilo Ortiz [7] and Simona Villa [8]. All the theories and explanations are mainly based on the comprehensive textbook thin-film Optical Filters by Mcleod [10]. Firstly, an explanation will be given about the fundamentals of optics and the theory behind single and multilayers layers interference will be discussed. Finally, the main design rules of optic filters will be addressed.

3.1 Fundamentals

The refractive index of a medium *n* is a dimensionless quantity and is defined as the ratio of the light speed c on vacuum divided by the speed of light in a specific medium v_i. Also, the refractive index characterizes the material properties that eventually determine the propagation of a wave though it [22] .The ratio also represents the phase velocity as shown in equation 3.1. The refractive index is often denoted by *N* when it is a complex number, and it is composed to a real part n and an imaginary part k known as the extinction coefficient.

$$N = \frac{c}{v_i} = n - ik \tag{3.1}$$

The *k* coefficient indicates the attenuation of the wave when it propagates in a medium and it is related to the absorption coefficient as shown by equation 3.2.

$$a = \frac{4\pi k}{\lambda} \tag{3.2}$$

From equation 3.2, it can be observed that the absorption coefficient a is wavelength dependent and consequently the extinction coefficient k is also a function of λ. Therefore, the refractive index N is always a function of λ. This dependency is known as the chromatic dispersion phenomenon in which the phase velocity of a wave changes with the frequency. In optics, a consequence of dispersion is the diverse refraction angles between the colors of an incident light. Figure 3.1 shows the example of a prism where the white incident light is spatially separated to different colors. More specifically, the violet color travels slower through the prism compared to the lower frequency red light that has a smaller refractive index.

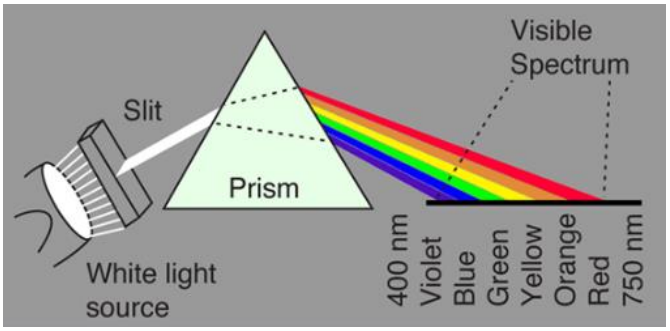

Figure 3.1 Chromatic dispersion phenomenon in a prism [23]

3.2 Law of Refection

The sketch in Figure 3.2 considers an absorption-free media; *k*=0. When a light ray incident on an interface of two non-absorptive media with refractive index n_o and n_1, the incident ray will partially split to a reflected ray and a refracted ray. The reflected ray will leave from the surface at an angle equal to the incident ray This law of reflection is derived from Fermat's principle.

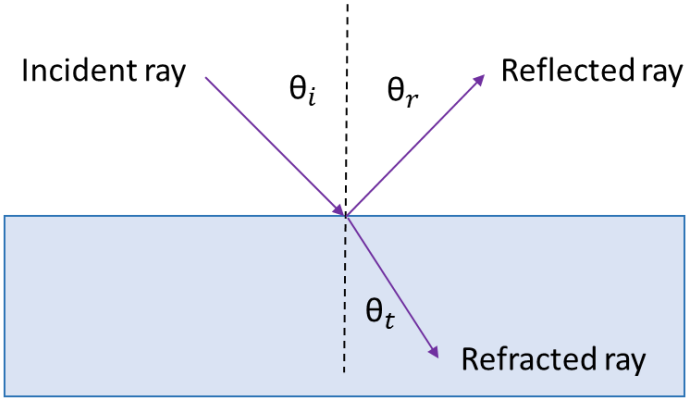

Figure 3.2 Example of an incident ray on an interface of two media

Considering that the incident ray reaches the surface with an angle θ_i, the Fermat's Principle states that *the light follows the path of least time*[24]. Equation 3.3 is also known as the Law of Refection shows that the reflected angle θ_r is equal to the incident angle θ_i

$$\theta_i = \theta_r \tag{3.3}$$

Regarding the refracted ray, the angle of propagation θ_t is different to θ_i. This is because the materials of the media have different refractive indices and therefore the propagation speed of the transmitted light changes. The angle in which the refracted ray is transmitted is described from Snell's Law. Snell's Law equation 3.4, states the relationship of the incident angle and the refraction angle of a ray which passes from a homogeneous medium with n_i into another homogeneous medium n_t [22]. The law states that the ratio of the sines of the angles of the incident and refracted ray is equal to the ratio of refractive indices of the two media. Simultaneously this is equal to the ratio of the velocities in the two media. Therefore, the angle in which the refracted ray will travel in a medium depends on the refractive index of the material. The higher the refractive index, the slower the light traverses the medium and the lower the angle of the refracted ray (towards the dotted line in Figure 3.2).

$$\frac{sin\theta_t}{sin\theta_i} = \frac{n_i}{n_t} = \frac{v_t}{v_i} \tag{3.4}$$

For an absorptive media, in equation 3.4 the n is therefore replaced by the complex refractive index *N.*

3.3 Interference on thin-film coatings

To describe the performance of thin-film optical devices, an additional layer between the media is considered as shown in Figure 3.3. First, to characterize a stack of layers as thin film, the thickness of the layers needs to be smaller than the coherence length of the incident light. As described before, when light is incident to a surface it splits into two components of reflection and transmission rays. Following, the transmission ray will eventually reach the bottom surface of the thin-film and split again into reflection and transmission rays. Consequently, the reflected waves of the first and the second interface; R_1 and R_2 will interfere with each other. This physical phenomenon is called light interference and it occurs on the interfaces of thin film layers.

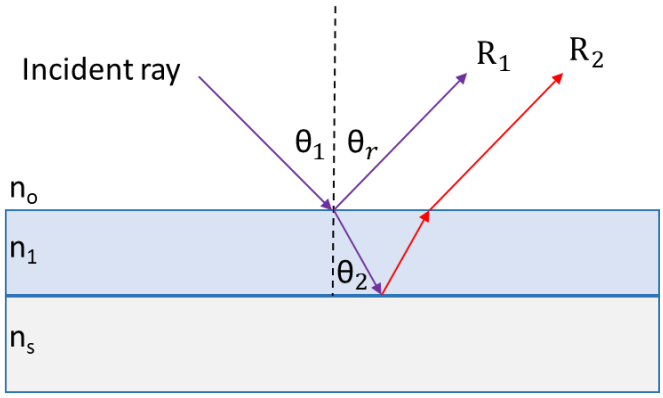

Figure 3.3 Thin film interference phenomenon between two interfaces

In addition, when a wave travels from a medium of a low reflective index media to another of high refractive index ($n_1<n_2$) then the reflected ray will experience a phase shift of 180°. On the contrary, if the wave travels from a high refractive index material to another with a lower refractive index ($n_1>n_2$), the reflected ray will not experience a phase shift.

Wave interference is when two waves come across to one another and interact. Consequently, their effects are adding together. Interference results between waves which are correlated or coherent which means either they are coming from the same source or they have the same frequency

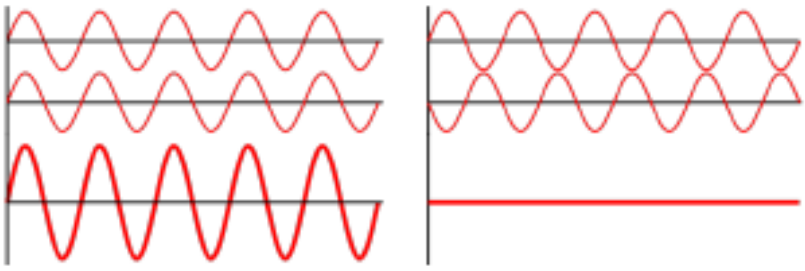

Figure 3.4 Constructive and destructive wave interference [8]

More specifically, *constructive interference* takes place when the two waves line perfectly, interact with each other and as a result a new wave is formed which has an amplitude bigger than the original waves.

That occurs when the phase difference is an even multiple of π. A representation of the phenomenon is shown in Figure 3.4 (left).

On the contrary, *destructive interference* occurs when the two waves that are not perfectly aligned interact with each other and as a result a wave is formed with an altitude smaller than the individual waves. In the case where the waves interact with each other and they have a phase difference of exactly half a wavelength, they cancel each other, and no wave is formed. Destructive interference happens when the phase difference is an odd multiple of π. Figure 3.4 (right), shows the phenomenon of destructive interference between two waves that ultimately cancel each other.

In addition, a combination of both constructive and destructive interference can happen when the phase difference of the waves is between the extremes of constructive and destructive interference as shown in Figure 3.5. As a result, the amplitude of the generated wave will have an amplitude between the minimum and the maximum values.

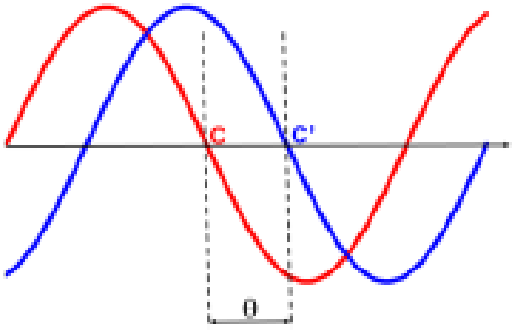

Figure 3.5 Combination of constructive and destructive interference [7]

Figure 3.6 illustrates a thin film layer with a thickness d and refractive index n_1 and considers $n_o<n_1<n_2$. The incident ray of a given wavelength, will hit the interface at point A, and eventually split with a reflected wave R_1. Since the n_o is smaller than n_1, the reflected wave will experience a phase shift 180°. The refracted light, will travel through the refractive index n_1 and eventually hit the interface$_2$ at point B. With the same phenomenon, the refracted light will split, and a second reflected light will occur with a phase shift of 180°. Finally, when the reflected light hits the surface at point C, no phase shift will occur since the light travels from a refractive index higher than n_o. Although, the transmitted ray R_2 will also not experience any additional phase shift since it not caused from transmission.

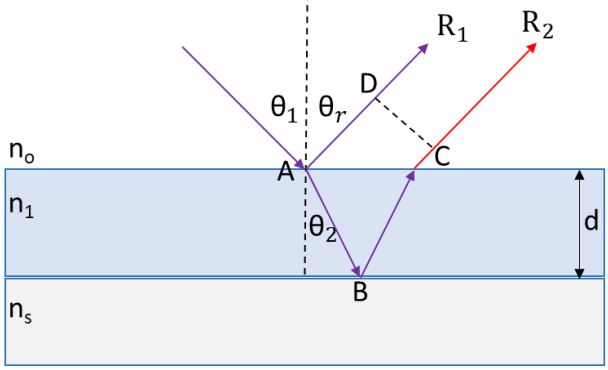

Figure 3.6 Optical path difference between a reflected wave at point A and a transmitted wave at point C

To characterize the condition of interference between the R_1 and R_2 two parameters need to be considered. First, is the phase difference between the two waves due to the reflection from the interfaces. As discussed before, the R_1 will experience one phase shift of 180° at point A, and the R_2 ray, will experience at point B a phase shift of 180^0. Secondly, the optical path difference (OPD) must be calculated. The OPD, expressed in equation 3.5, is defined as the product of the geometrical length of the path followed by a wavelength with the refractive index of the material which is propagates [28]

$$OP = n \times d \tag{3.5}$$

The interference between the two waves, will be constructive if the optical path difference between the two rays is equal to an integer of the light wavelength. Whereas it will be destructive, if the optical path difference is equal to a non-integer value of the light wavelength. The equations 3.6 and 3.7 show the conditions of constructive and destructive interference accordingly [25].

All in all, it can be concluded that the degree of interference depends on the phase difference of the waves. Where the phase difference, depends on the thickness of the layer, the angle of incidence and the refractive indexes of the materials.

$$m\lambda = 2dn_1\cos(\vartheta_t) \tag{3.6}$$

$$\left(m - \frac{1}{2}\right) = \lambda = 2dn_1\cos(\vartheta_t) \tag{3.7}$$

3.4 Quarter Wavelength Optical Thickness

If m=1 and the angle of incident is equal to 0 then the thickness which is required to maximize the transmission and reduce reflectance to a minimum for a given wavelength (λ) is:

$$d = \frac{\lambda}{4\, n_1} \tag{3.8}$$

A design layer with the thickness d is consider as a layer with Quarter Wavelength Optical Thickness (QWOT). That means that if a layer is designed for a specific wavelength; equal to 500nm then the reflectance is the minimum only for that specific wavelength. Therefore, this condition is highly dependent on the wavelength of the incident ray. [25]

In the current thesis, optic filters are used based on two materials with different refractive index. Figure 3.7 demonstrates an optic filter which is formed by high (H) and low (L) refractive index alternately, beginning with n_H. For two given thicknesses d_H and d_l such that destructive interference is achieved for a specific wavelength λ_o the reflectance of light at that specific wavelength will be bolstered as the number of layer pair increases.

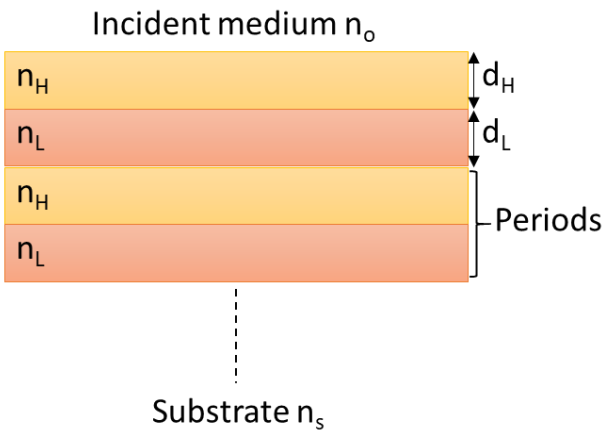

Figure 3.7 Optic filter formed by high and low refractive index

This effect is represented in Figure 3.8, where the reflectance is increasing at the design wavelength as the number of pairs are increasing.

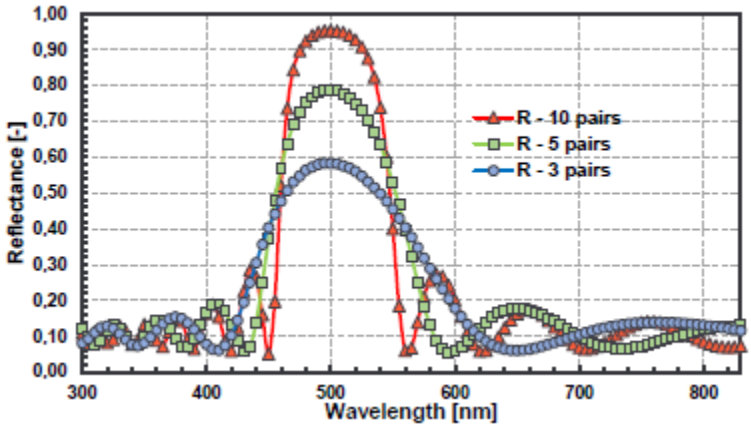

Figure 3.8 The effect of n_H/n_l pairs on the reflectance [7]

The width of reflectance is given by equation 3.9 [26]. Therefore, to maximize the width of reflection, the difference between the refractive index of the layers needs to be as high as possible.

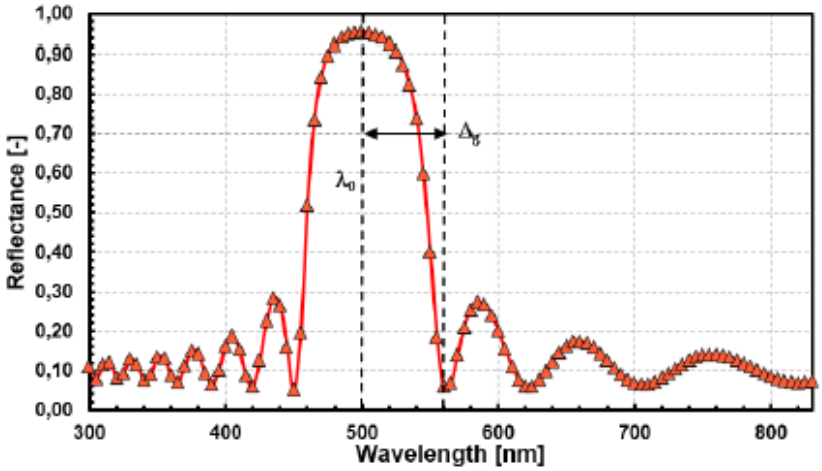

Figure 3.9 Characteristics of the design reflectance of an optic filter [7]

$$\Delta_g = \frac{2}{\pi} sin^{-1}\left(\frac{n_H - n_L}{n_H + n_L}\right) \quad 3.9$$

From Figure 3.9, it is observed that smaller reflection peaks are occurred before and after the design wavelength λ_o. This is called ripple effect and is happening for any wavelength for which the layers are an odd number of QWOT. The ripple effect corresponds to wavelengths equal to λ_o /3, λ_o /5, λ_o /7.

Finally, an important parameter which influences the reflected color of an optic filter is the oblique angle of incidence. The optimum reflection of an optic filter is designed for an angle of incidence equal to zero. Therefore, for a different angle of incidence, the reflection zone will shift accordingly. More specifically, the reflectance band will shift to lower wavelengths as the angle of incidence increases [26]. The reason behind that is the change of the optical path that the wave will travel inside the filter. Consequently, constructive interference will occur for a different wavelength that satisfies the condition of 3.8. Figure 3.10 shows the reflection peak change when the angle of incidence is 60°. More specifically, at zero degrees the reflection occurs at 500nm and for higher angle of incidence the reflection shifts to 420nm.

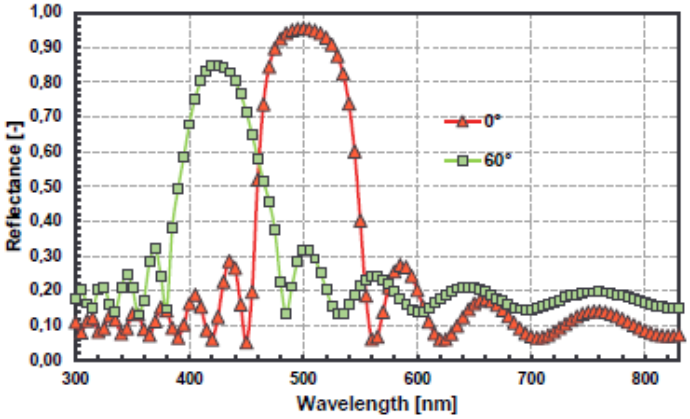

Figure 3.10 Angle of incidence dependence on the reflectance [7]

4 Model methodology

4.1 Introduction of the model

4.1.1 Introduction

The aim of the model is to predict the performance of PV modules in terms of temperature, energy yield and efficiency considering the angle of incidence and angular absorptance. The model is spectrally resolved and has been developed for comparing different module designs with optic filters and without optic filters. The model is user friendly and can effortlessly give results based on the user's requirements, module design and color, since all the parameters are variable and easy to be changed. The model can give results for different locations for a specific day of a year, range of days of a year, a month of a year and for a whole year. Additionally, the model has been designed for modules which are free mounted, attached on a roof or on a façade, with or without an air gap on the back side. Differential energy balance equations expressed in SI units, with unknown temperatures have been created to satisfy those scenarios and are solved using finite difference methods. A detail explanation will be given on how those equations have been formed and which parameters were considered.

The model is a one-dimensional (1D) model which neglects exchanges through the edges of the PV module and each layer is considered isothermal. The reason why the model is only 1D is because the temperature differences inside the layers are not expected to diverge significantly. This is because the geometry is not complex, and the layer thickness is relatively small. Moreover, the conditions are assumed to be the same along the length dimension of the module; (y axis). Also, by selecting a 1D approach, the computational time is optimized and ensures a good accuracy for the results. The forced and free convection are considered at the front and back surface. The emissivity of the sky is calculated from ambient temperature and shading effects of surrounding elements are not considered. Moreover, spectral absorptance, reflectance and transmittance values are considered for all the layers whereas for the crystalline silicon (cSi) thermalization losses are also calculated. Multiple reflections within the layers and recycling of light are also considered. Finally, the properties such as thermal conductivity, capacity and density are considered constant.

4.1.2 Designs

The model considers the PV modules mounting scenarios shown in Figure 4.1 .The reason why the model considers these specific configurations, is because these are the most common commercially available applications of PV modules [27], [28]. Moreover, in this way the model is interactive with the user and can give realistic results for different designs. Nowadays, BIPV installations are very popular since they improve the aesthetics of PV modules. Nevertheless, the operating conditions and the constrains of the module are changing based on the mounting design. For this reason, different equations and different assumptions have been made in order to simulate those scenarios. A detail explanation will be following in the next chapter.

The first design, shown in Figure 4.1 a) represents a free mounted module which is tilted in an open area. This configuration is simulated with the vision that such system can be found in solar parks, public areas or on buildings with flat roofs. This design allows convection and radiation on both front and back surfaces of the module. Moreover, the developed model can simulate this configuration for modules with and without optic filters. In addition, the angle and orientation are variable in the model, and it can be adjusted based on the user needs. The advantage of this design compared to the rest designs, is that it's orientation can be optimized for the maximum energy yield although, the main disadvantage is that is not a BIPV solution.

The following design, shown in Figure 4.1 b) represents an integrated PV module on a roof (BIPV) whereas design Figure 4.1 d) represents the design for an integrated PV module on a facade. These configurations are aimed to simulate the performance of modules which are attached on tilted roofs and on facades. The design allows convection and radiation exchange only in the front layer and conduction exchange between the roof and the back layer for design b) and conduction exchange between the façade and the back layer for design d). The model can simulate these layouts for different angles, orientations and materials of the roof. For the scenario of a module with or without optic filter on a façade, the angle is fixed at 90 degrees, but the orientation and the materials of the façade wall are variables based on the design. These designs have the important advantage of ensuring good aesthetics of the modules. The reason why these designs are more commercially attractive is because for the case where the attached modules are colored, they are not even visible if their color matches the color of the roof or the façade. Another important advantage is that they can utilize the free area that the roof and façade provide. Also, they give the flexibility of creating colorful buildings with color patterns and innovative architecture. The main disadvantage of these configurations is that the module is attached on a roof or a façade and therefore there is no convection at the back side which allows energy exchange with the air. Moreover, for design b) the module is tilted based on the roof angle and that means that for already constructed roofs the module will not have the optimum angle. Although, for future projects, the roof angle can be optimized to give better energy yield of the module. For the design d) the disadvantage is that the module is fixed at 90 degrees and therefore the angle of the module is not optimum, and an important amount of incident irradiance is expected to be reflected.

The next designs Figure 4.1 c) and Figure 4.1 e) represent a PV module on a roof and on a façade with an air gap between accordingly. The idea behind these designs, is to test what is the impact on having an air gap on roof and façade installations since the air gap will allow convection exchange at the back side. The air gap thickness is a variable between 10cm until 50 cm and can be adjusted based on the design. The gap is chosen to be limited to 10cm because for a smaller air gap thickness the resistance will be very high and therefore the wind flow will not be effective for convection exchange. On the hand, the gap is limited to 50cm because then for higher thicknesses the design will not be aesthetically attractive. Also, the wind speed is expected to move freely for the size of 50cm. Overall, the idea is to give the optimum thickness of air gap for the highest energy yield results. The advantage of this design is that the convection at the back side is not blocked as for the case of BIPV on a roof and façade. Although, BIPV designs give a more aesthetical solution. As already mentioned before, also for this design the module angle is dependent on the roof and façade angle and therefore the module is not optimally oriented.

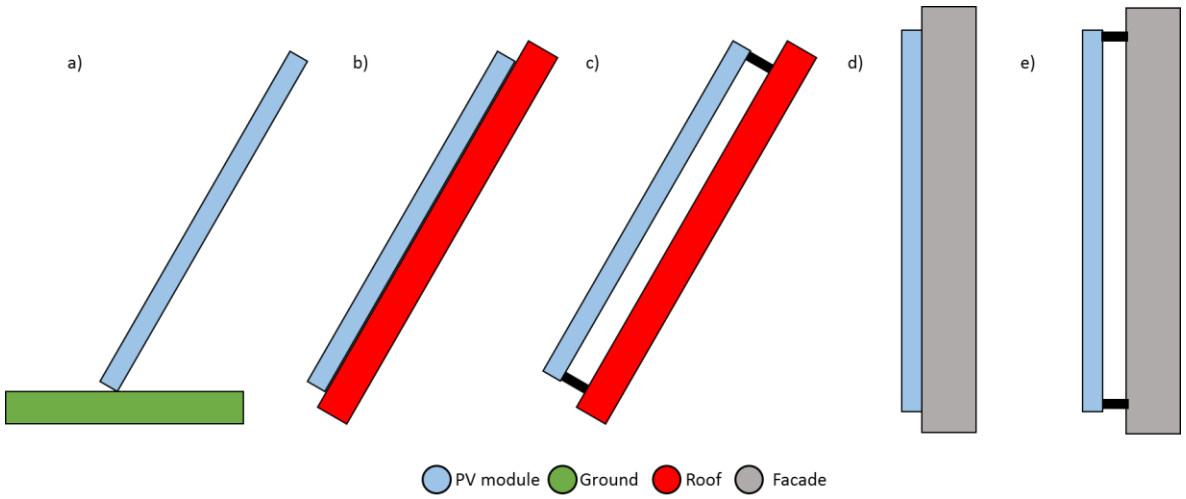

Figure 4.1 Model main designs; a) free mounted module, b) module attached on a roof, c) module attached on roof with air-gap, d) module attached on a façade, c)module attached on façade with air-gap

4.2 Thermal model

4.2.1 Methodology Introduction

To start with, equations have been formed for 4 different types of nodes with different boundaries which are front surface node, inside nodes, crystalline silicon node and back surface node. The total number of nodes and the representative equations can be defined automatically in the model based on the total number of layers of the simulated module. Also, for the cases of a roof and façade applications, an extra node is considered for the roof or the façade wall. Each node is applied in the middle of each layer and its temperature is considered as an average for the whole layer. This is a good approximation because as has been mentioned before, the thickness of the layers is small to allow important changes to the temperature. Important to mention is that for the optic filter layers, in order to avoid many nodes for such small thicknesses, one single node is applied at the middle of the layer stack representing in that way the total optic filter. The material properties of the optic filter are calculated as an equal resistance based on the individual properties of each material of the optic filter. The mathematical expressions of equation 4.1, 4.2 and 4.3 are formed to give the equivalent properties of the optic filter. Where *d* is the thickness of the layer, *k* is the conduction coefficient, C_p the specific heat capacity and ρ the density.

$$k_{Optic\ filter} = \frac{d_{OF}}{\sum_{layer=1}^{n}\left(\frac{d_{layer}}{k_{layer}}\right)} \quad 4.1$$

$$Cp_{optic\ filter} = \frac{\sum_{layer=1}^{n}\left(d_{layer}Cp_{layer}\right)}{d_{optic\ filter}} \quad 4.2$$

$$\rho_{optic\ filter} = \frac{\sum_{layer=1}^{n}(d_{layer}\rho_{layer})}{d_{optic\ filter}} \quad 4.3$$

In addition, the same equations have been applied for the scenarios where wall/roof is included. Based on the number of the layers and each material, a representative C_p and ρ is calculated.

$$Cp_{wall/roof} = \frac{\sum_{layer=1}^{n}(d_{layer}Cp_{layer})}{d_{wall/roof}} \quad 4.4$$

$$\rho_{wall/roof} = \frac{\sum_{layer=1}^{n}(d_{layer}\rho_{layer})}{d_{wall/roof}} \quad 4.5$$

The energy balance equation 4.6 is applied for each layer and considers the exchange energy between the layers and the environment [29]. Based on the layer and the type of node that is applied, the equation is formed accordingly. Initially, from the way that the equation is analyzed for each node, the energy direction of heat transfer is assumed to be positive and towards the node and therefore positive energy storage. Afterwards, the direction is corrected based on the temperature difference of the studied node and the heat exchanged with other nodes or the environment. Detail analysis will follow for better understanding. In Equation 4.6, *dt* is the time step, *T* the temperature and *dx* the thickness of the layer.

$$\rho Cpdx\frac{{T_i}^t - {T_i}^{t-1}}{dt} = \sum energy\ exchange \quad 4.6$$

In the case of front surface, surface node is applied, and the energy balance equation considers absorption, convection, conduction and radiation heat transfer energies as shown in Figure 4.2 a). The sketch illustrates the energies heat transfer which are considered when the equation of energy is analyzed for a front surface node. The surface node equation is:

$$\rho Cpdx\frac{{T_i}^t - {T_i}^{t-1}}{dt} = absorption_i + conduction_{i+1\to i} + convection_i + radiation_i \quad 4.7$$

In the case inside layer, inside node is applied and absorption and conduction heat transfer are considered. Conduction heat exchange is considered for both previous and following layers. An example is shown in Figure 4.2 b) where the inside node interacts with the neighboring nodes. The final equation is:

$$\rho Cpdx\frac{{T_i}^t - {T_i}^{t-1}}{dt} = absorption_i + conduction_{i+1\to i} + conduction_{i-1\to i} \quad 4.8$$

For the crystalline Silicon layer, cSi node is applied where thermalization and electrical losses and conduction heat transfer are considered in the equation. P_e is the output electricity based on the potential electricity calculated from the band gap and n_t is the efficiency from the potential electricity to the actual

power output. In more detail, Figure 4.2 c) presents the energy heat transfer towards the c-Si node and the actual power output are presented.

$$\rho Cpdx\frac{T_i^{\,t}-T_i^{\,t-1}}{dt}=thermalization_i+conduction_{i+1\to i}+conduction_{i-1\to i}+(1-n_t)P_e \qquad 4.9$$

For the back surface, back surface node is applied with the following equation. Here, the same heat transfer energies are considered as for the front surface node.

$$\rho Cpdx\frac{T_i^{\,t}-T_i^{\,t-1}}{dt}=absorption_i+conduction_{i+1\to i}+convection_i+radiation_i \qquad 4.10$$

For the case where the module is mounted on a roof or on a façade without air gap, for the back layer inside node is applied. The difference is that conduction heat transfer is considered between the node of the layer and the node of the roof or wall of the façade.

$$\rho Cpdx\frac{T_i^{\,t}-T_i^{\,t-1}}{dt}=absorption_i+conduction_{wall/roof\to i}+conduction_{i-1\to i} \qquad 4.11$$

Finally, when the module is mounted on a roof or on a façade with an air gap, the energy balance equation considers absorption, convection, conduction and radiation heat transfer energies as shown in Figure 4.2 d). The radiation heat transfer is considered between the back layer and the roof or the façade.

$$\rho Cpdx\frac{T_i^{\,t}-T_i^{\,t-1}}{dt}=absorption_i+conduction_{wall/roof\to i}+convection_i+radiation_{wall/roof\to i} \qquad 4.12$$

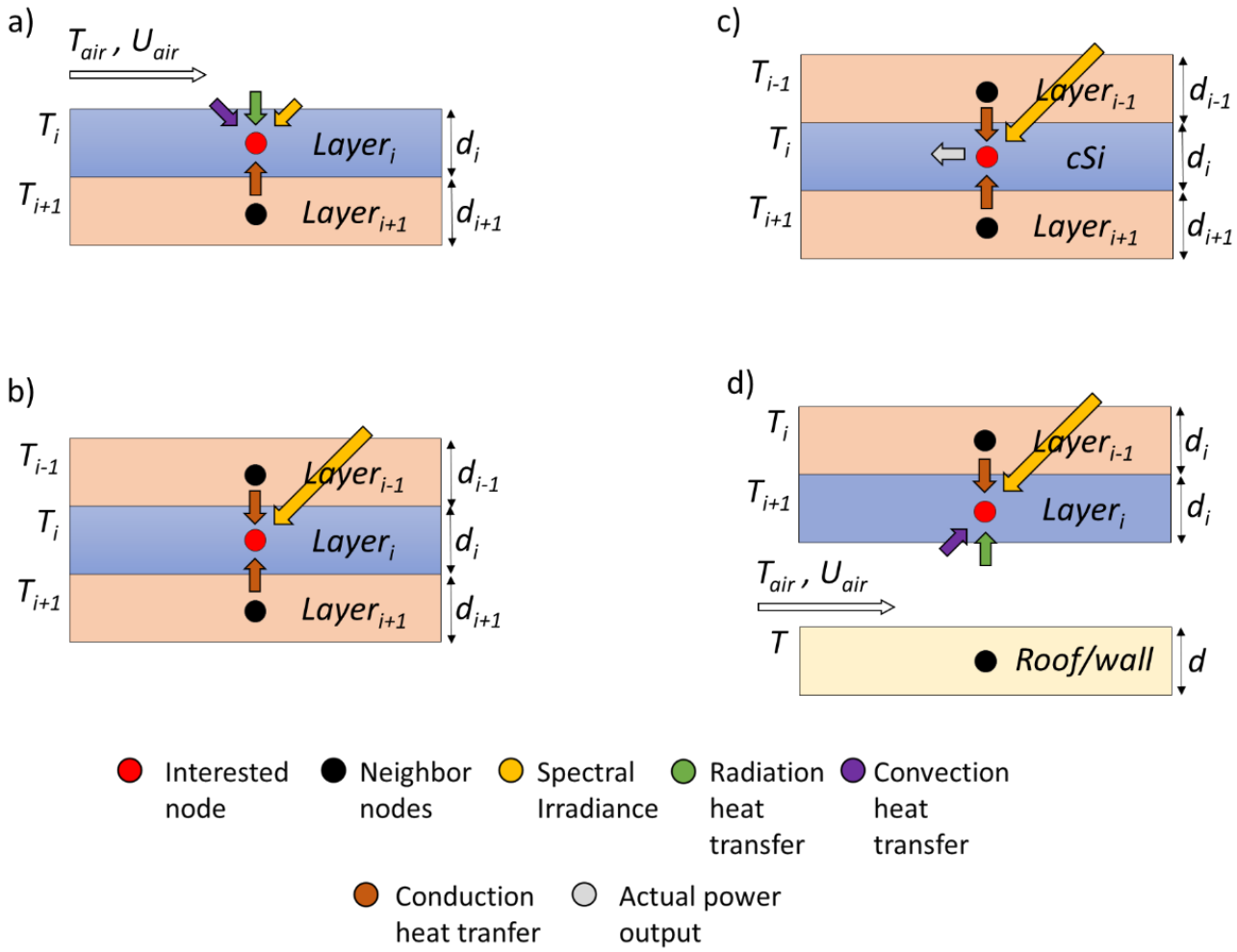

Figure 4.2 Sources of heat energy transfer considered for each node; a) front surface, b) inside node, c) cSi node, d) back node with air gap

The discretization of the energy balance equations is by employing an implicit method. The implicit method solves the finite difference equation by evaluating the unknowns; temperatures at the new time step while, the explicit method uses the previous time step values of each node. As can be seen from equation 4.13, the differential equation is solved by considering the temperature of the previous time step of each node, whereas, the equation 4.14 evaluates the temperatures at the new time where *R* is the thermal resistance. The implicit method was chosen since the explicit method has some limitations with the time step (dt). That means small values of time step are required and large number of time intervals are needed to obtain an accurate solution. On the other hand, implicit method reduces the computational time and maintains a good accuracy with flexibility for the time step [29].

$$\rho C p dx \frac{T_i^{\,t} - T_i^{\,t-1}}{dt} = \frac{T_i^{t-1} - T_{i+1}^{t-1}}{R} \qquad 4.13$$

$$\rho C p dx \frac{T_i^{\,t} - T_i^{\,t-1}}{dt} = \frac{T_i^{t} - T_{i+1}^{t}}{R} \qquad 4.14$$

After the discretization of the differential equations, the equations must be solved simultaneously. Therefore, Gauss-Seidel iteration / matrix inversion is used. To obtain a solution, the number of equations needs to match the number of unknowns [29].

The inversion method expresses the *N* finite difference equations as shown in equation 4.15 , where a_{11}- a_{NN} and C_1- C_N are known constant coefficients.

$$\begin{aligned} a_{11}T1 + a_{12}T2 + a_{13}T_3 + \cdots + a_{1N}T_N &= C_1 \\ a_{21}T1 + a_{22}T2 + a_{23}T_3 + \cdots + a_{2N}T_N &= C_2 \\ &\vdots \\ a_{N1}T1 + a_{N2}T2 + a_{N3}T_3 + \cdots + a_{NN}T_N &= C_N \end{aligned} \qquad 4.15$$

Using matrix notation, the equations can be expressed as:

$$[A]\,[T] = [C] \qquad 4.16$$

Where the matrix *A* contains the constant coefficient elements and its dimensions are equal to the number of equations and unknowns (*NxN*). The vector *T* contains the unknown temperatures and the vector C the constant values.

$$A \equiv \begin{bmatrix} a_{11}\ a_{12} \dots\ a_{1N} \\ a_{21}\ a_{22} \dots\ a_{2N} \\ \vdots \\ a_{N1}\ a_{N2} \dots\ a_{NN} \end{bmatrix} \qquad T \equiv \begin{bmatrix} T_1 \\ T_2 \\ \vdots \\ T_N \end{bmatrix} \quad C \equiv \begin{bmatrix} C_1 \\ C_2 \\ \vdots \\ C_N \end{bmatrix} \qquad 4.17$$

To find the solution the vector *T* is mathematically expressed as shown in equation 4.18, where $[A]^{-1}$ is the inverse of *A* from equation 4.19.

$$[T] = [A]^{-1}[C] \qquad 4.18$$

$$[A]^{-1} \equiv \begin{bmatrix} b_{11}\ b_{12} \dots\ b_{1N} \\ b_{21}\ b_{22} \dots\ b_{2N} \\ \vdots \\ b_{N1}\ b_{N2} \dots\ b_{NN} \end{bmatrix} \qquad 4.19$$

Finally, the unknowns are solved, and the solution can be computed as follows:

$$\begin{aligned} T_1 &= b_{11}C_1 + b_{12}C_1 + \cdots + b_{1N}C_N \\ T_2 &= b_{21}C_1 + b_{22}C_2 + \cdots + b_{2N}C_N \\ &\vdots \\ T_N &= b_{N1}C_1 + b_{N2}C_2 + \cdots + b_{NN}C_N \end{aligned} \qquad 4.20$$

4.2.2 Irradiance model

For the irradiance model, spectral Direct normal and Diffused irradiance is used with the spectrum as a function of wavelength. The data was taken from SMARTS 295 software Dr. Christian Gueymard [30], which provides data of *DNI* and *DHI* based on the relative air mass. More specifically, the spectral range was selected from 280nm to 4000nm with a step of 5nm and the air mass from 1 until 38 with a step of 1. Using spectral irradiance for different air mass (*AM*), this allows an accurate calculation of the actual reflection, transmission and absorption energy for each wavelength. Based on the accuracy of the *AM* decimal points and the wavelength range that the user wants, the data is then linearly interpolated to give spectral irradiance for more values between *AM* 1-38. Figure 4.3 shows the spectral DNI for *AM1*.5 which is interpolated compared to the spectral DNI for *AM1*.5 manually downloaded from SMARTS software. The two lines perfectly match for the wavelength range 280-4000 nm. More specifically, the average deviation of the two graphs was calculated as 0.002 W/m^{2}nm.

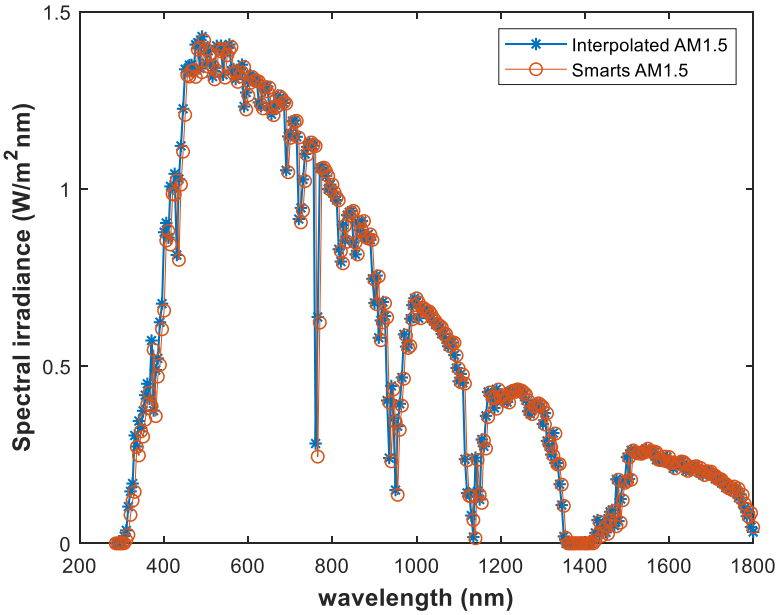

Figure 4.3 Comparison between SMARTS and simulated Spectral irradiance for AM1.5

In order to determine the *AM* for the simulations and therefore the *DNI* and *DHI* for each time step, equation 4.21 was used to calculate the air mass from the altitude vector of the sun as according to the time period that the user will select [31],[32]. Since the *AM* from the equation fluctuates between 1 and 38, the *DNI* and *DHI* are set to be zero when the altitude of the sun is zero. With the aforementioned method, irradiance data can be formed which are representative for a clear sky scenario based on the altitude of the sun. Figure 4.4 shows the altitude of the sun for the day of 21st of June and 21st of December for Delft location. At the same time, the representative air mass is calculated through the days based on the formula of equation 4.21. The formula is calibrated so that it takes values between 1 up until 38. Also, it can be realized that since the altitude of the sun changes according to the date, the *AM* changes as well significantly. Consequently, it is important to consider the *AM* as a variable.

Finally, since *DNI* and *DHI* are distribution data and give the power per 1nm wavelength range, both DNI and *DHI* are manually integrated with the wavelength step that the user will select to give the value of how much power is entering per wavelength range. For example, if the wavelength step is set 5, then manual integration is performed to give the irradiance for a wavelength range of 5nm in W/m^2.This transformation is needed to determine the absorption energy values. For the current project, the wavelength range that is selected for the simulations is 280-1800 nm with a step of 5nm [33] . This covers the absorption wavelength range that is expected, and it was verified that by using up to 3000nm wavelength the results are not changing a lot. Moreover, this wavelength range and step optimizes the computational time and ensures that the important wavelengths are considered. Significant to mention is that the step was chosen per 5nm because the energy yield results were underestimated by selecting higher step; for example, a step of 15nm which means the accuracy was heavily influenced.

$$AM = \frac{1}{sin\,(as) + 0.50572 * (96.07995 - (90 - as)))^{-1.6364}} \qquad 4.21$$

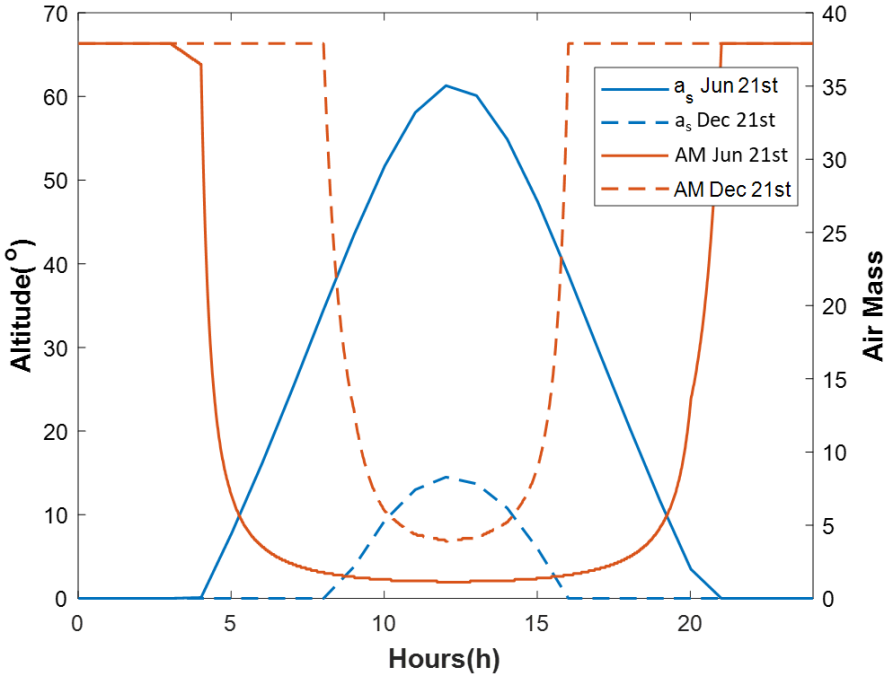

Figure 4.4 Altitude of the sun and according Air mass on the 21st of June and 21st of December in Delft

Following, with the aim to achieve more logical results and correct the simulated *DNI* and *DHI*, a strategy was developed in order to consider clouds influence. Firstly, the first approach was to consider clouds by creating an equation which multiplies with zero the *DNI* when the clouds concentration is 8 *oktas* (overcast), and with 1 when the clouds concentration is 0 *oktas* (clear sky). The values of the cloud's concentration were taken from Meteonorm. However, by comparing the values of the simulated *DNI* with the measured value from Meteonorm, it was found that this method was not giving accurate effect of the clouds. Even though sometimes there was an overcast, still values of *DNI* were able to be measured since clouds did not fully obstruct the sunlight. Therefore, a new approach was developed which manipulates the area of the simulated direct and diffuse spectral irradiance based on the according values from Meteonorm. By that way, the effect of clouds is considered as a grey filter which decreases or increases

equally the spectrum for the whole range of wavelengths for an according air mass. Figure 4.5 illustrates the differences between measured and simulated *DNI* and *DHI* for Delft on the 21st of June. More specifically, the average deviation from the measured data is 0.47 W/m^2 for DNI and 0.54 W/m^2 for *DHI*.

The total spectral irradiance incident on the module is calculated by considering diffused, direct and albedo spectral irradiance. The angle of incidence is time depended and is calculated from the equation 4.22 which considers the position of the sun; (a_s , A_s) and the orientation and tilted angle of the module; (a_M, A_M). For the negative values of the cosine of the *AOI* the value was set to be zero because it is considered that the sun is behind the module. For the direct irradiance incident on the module the equation 4.23 is used. To calculate the diffuse irradiance on the module, the Sky view factor (*SVF)* was considered as shown in the equation 4.24. For the albedo irradiance, equation 4.26 was used which considers the Sky view factor of the module and the albedo (a) of the ground. Finally, by adding those values, the total irradiance incident on the module is calculated from equation 4.27 as function of wavelength [31].

$$cosAOI = \cos(a_M)\cos(a_s)\cos(A_M - A_s) + \sin(a_M)\sin(a_s) \quad (4.22)$$

$$G_{Direct} = DNI\ cos(AOI) \quad (4.23)$$

$$G_{Diffuse} = f(SVF, DHI) = \frac{1 + \cos(\theta_M)}{2}\ DHI, \qquad \theta_M: module\ tilt\ angle \quad (4.24)$$

$$GHI = G_{Direct} + G_{Diffuse} \quad (4.25)$$

$$G_{Albedo} = GHI\ a\ (1 - SVF) \quad (4.26)$$

$$G_{Module} = G_{Direct} + G_{Diffuse} + G_{Albedo} \quad (4.27)$$

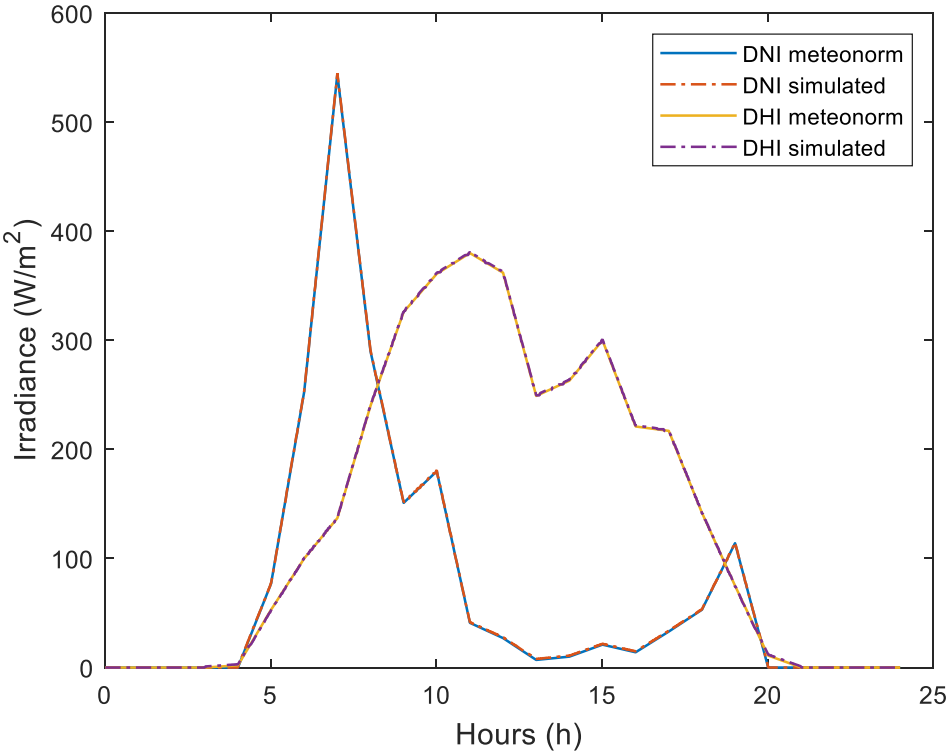

Figure 4.5 Comparison between measure DNI and DHI from Meteonorm and simulation

4.2.3 Absorption model

The absorption values of each layer are determined from the GenPro4 model developed by R.Santbergen [34]. GenPro4 is an optical model which combines wave and ray optics in a computational efficient way. The model calculates the ratio of the incident light that is absorbed in each layer and the fraction of the reflected and transmitted light of the solar cell as a function of wavelength by considering scattering and light trapping at the interfaces. The model can give optical results for both flat and textured interfaces. Considering optically flat surfaces, the reflection and transmission values are calculated based on Fresnel and Lambert-Beer law equations respectively. A single ray can be reflected multiple times and each reflection needs to be considered. At each interface four q_i fluxes are defined as illustrated in Figure 4.6 and related by a set of linear equations which can be solved numerically and determine the R, T and A. For the case where the optical filters have thicknesses comparable to the length of sunlight (coherence layers) and interference effect take place, the GenPro model uses a different calculation algorithm by expressing the fluxes into complex amplitudes of electromagnetic waves [34].

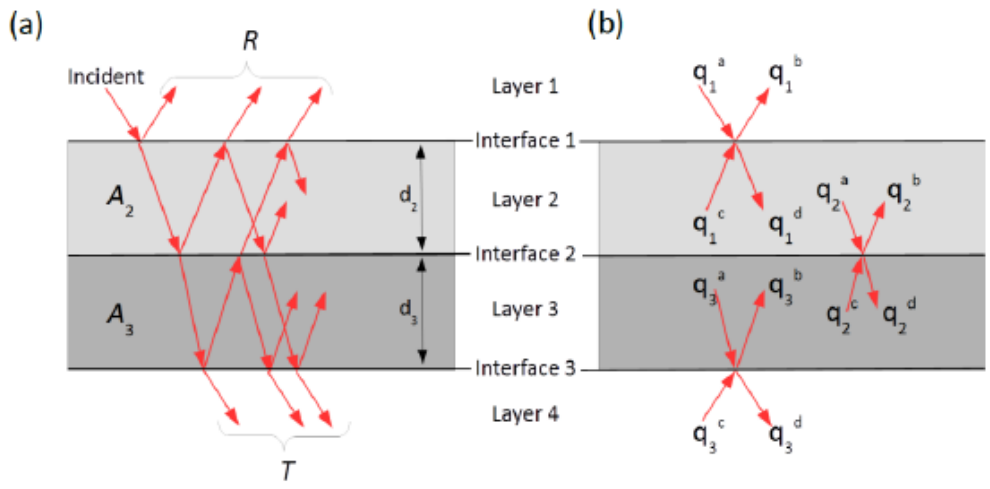

Figure 4.6 Representation of the number of layers and interfaces of a specific multilayer structure. The multiple optical paths and fluxes are presented which are used to calculate the R, T and A for each layer [34]

In the case of textured interfaces, the reflected and transmitted light propagation is not predictable since the propagation is scattered and distributed over a range of angles as shown in Figure 4.7. Because of that, the resolution is more complex, and the hemisphere is divided into several angular intervals each of them representing a corresponding sub-flux [34].

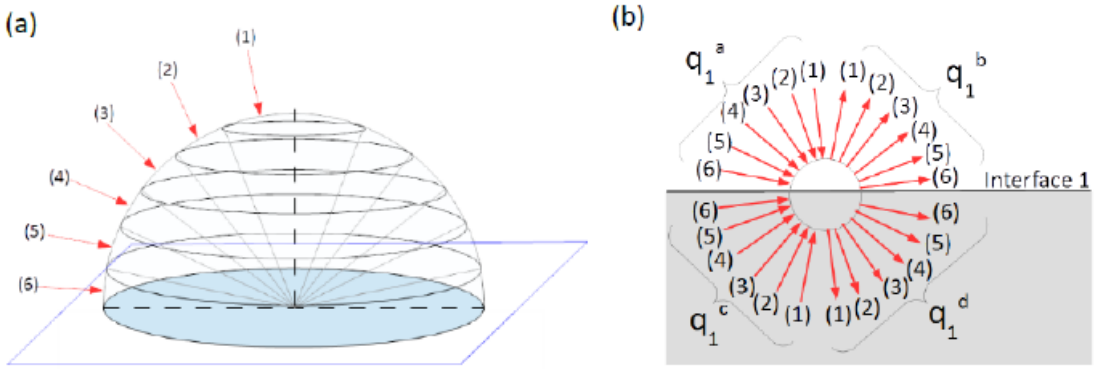

Figure 4.7 Representation of the sub-fluxes for an interface 1 where the hemispherical direction is divided into angular intervals [34]

With the optical output values of the model, the absorption irradiance for each wavelength can be calculated by multiplying the absorption values with the incident spectral irradiance for the corresponding wavelength. Therefore, it can be precisely defined how much of the incident irradiance will effectively produce electricity or heat inside the solar cell and eventually increase the working temperature.

Especially for optic filters, an important factor which influences significantly the R, T and A is the angle of incident between the light and the surface of the module as discussed in section 4.1. For this reason, from the altitude of the sun and the tilted angle of the PV module, the angle of incident is calculated as explained before; equation 4.22, and values of absorption reflection and transmission are observed depending on the AOI. The number of angular steps of the AOI can be adjusted from the user between 5 for fast calculations and 30 for accurate calculations to match exactly the settings of angular intervals from

GenPro4. For the current project, 15 angular intervals were selected which means the absorption values are calculated for every 6 degrees of AOI. This number was chosen because, this is a relatively accurate number for observing absorption results and not significant changes of the absorption are expected between less than 6 degrees. Moreover, by choosing this number of angular intervals the computational time is optimized well by ensuring good accurate results. Important mentioning is that, the absorption for the step of every 6 degrees is assumed to be the same so that absorption values for every angle of incident can be observed. Based on the angle of incidence vector, which is time dependent the according values of absorption are determined. Important mentioning is that for the times where the AOI is 90 degrees the absorption values were set to be zero for all the wavelength range.

For the total layer energy absorption for each time step, the absorption of each layer is calculated based on the spectral irradiance incident on the module multiplied with the according absorption values. The result gives the units Watt/m for each wavelength. Following by sum all the values, the total layer absorption can be determined for each layer. For the layers except of the crystalline silicon, that is considered only thermal source. While, for the crystalline silicon, the absorption energy per wavelength is divided to thermalization losses and potential electricity energy. This potential electricity before electrical losses due to recombination is based on the crystalline silicon bang gap, which is Temperature depended as shown in equation 4.28 [35].

The E_o is the energy band gap at 0 K and a and δ are material constants. According to P.Varshni [35], the variation of the energy band gap with respect to the temperature is expected due to the shift of the position of the conduction and the valence bands. This is happening firstly, due to the temperature dependence of the dilation of the lattice where the effect is linear with the temperature at high temperatures. Secondly, the major influence comes from the temperature dependent electron lattice interaction. The dependence of the band gap with temperature was considered since as it can be seen from the Figure 4.8, it decreases with the increase of the cSi temperature. That means, for higher temperatures the thermalization losses are expected to increase.

$$Band\ gap(eV) = \frac{E_o - (a \times (T_{cSi})^2)}{(T_{cSi} + \delta)} \quad Band\ gap(J) = \frac{1.11 - (4.73 \times 10^{-4} \times (T_{cSi})^2)}{(T_{cSi} + 636) \times (1.60217 \times 10^{-19})} \qquad 4.28$$

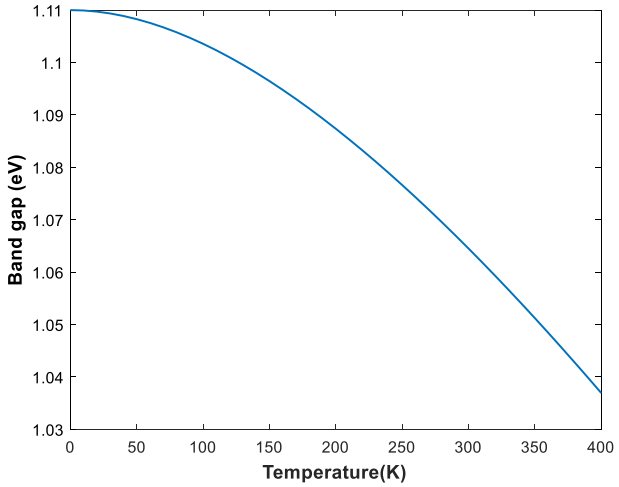

Figure 4.8 Band gap energy of cSi based on its temperature

More specifically, the photon energy is calculated for each wavelength using the equation 4.29 [31]. Then, based on the absorption per wavelength from equation 4.30 and equation 4.31 the thermalization and electricity energy are calculated according to the number of absorbed photons per wavelength [36]. These calculations were considered to define specifically which proportion of the incident irradiance will lead to heat source and which will effectively give potential electricity. Important to mention is that, after multiplying the potential electricity with the efficiency, the remaining part of electricity is add up as an extra thermal source.

$$Photon\ Energy = \frac{h\,c}{\lambda} \qquad h = 6.626 \times 10^{-34}\ , \qquad c = 3 \times 10^{8} \tag{4.29}$$

$$Thermalization(W/m^2) = (absorption_{cSi}/\ Photon\ \ Energy) \times (Band\ gap - Photon\ Energy) \tag{4.30}$$

$$Electricity\ Power\ (W/m^2) = (absorption_{cSi}/\ Photon\ \ Energy) \times (Band\ gap) \tag{4.31}$$

4.2.4 Convection model

4.2.4.1 Natural convection

Convection is a mechanism of heat transfer due to the movement of fluids where the heat is transferred by vibrations though the solid or fluid and is expressed mathematically by equation 4.32 . The convection heat transfer is one most important heat exchange mechanism that is taken into consideration for the model. Both natural and forced convection are included to the model and the total convection coefficient is defined as shown the equation 4.33 [29], where h is the convection coefficient and A the surface area.

$$Q_{conv} = h_{conv} A (T - T) \tag{4.32}$$

$$h_{conv} = \left({h_{free}}^{3} + {h_{forced}}^{3}\right)^{1/3} \tag{4.33}$$

The free convection occurs when there is a temperature difference and therefore fluid motion is present due to buoyancy forces. Since the behavior of natural convection is dependent on the orientation of the plate with respect to gravity, the h_{free} coefficient is calculated differently for different configurations of the module.

For the scenario of a free mounted PV module, there are three possible configurations; a module tilted at 0, 90 and between 0 and 90 degrees. Different equations are applied for the front and back surface of the module to determine the convection coefficient.

For the case where the module is tilted at 0 degrees and with no restriction to flow, the equations which are used are following [37],[38]. Based on the Rayleigh number (Ra) the average Nusselt number (Nu) is calculated via equations 4.34, 4.37, 4.38. Where, L is the characteristic length, g is the gravitational force, β is the volumetric thermal expansion coefficient, υ is the kinematic viscosity and α thermal diffusivity.

$$Ra_L = \frac{g\,(L/4\,)^3\beta\,(T_s - T_\infty)}{\upsilon\alpha} \tag{4.34}$$

The Nusselt is given by:

$$\overline{Nu}_{Lchar} = \frac{\bar{h}\,(L/4)}{k} \tag{4.35}$$

$$\overline{Nu}_{Lchar} = \left(\overline{Nu}^{10}{}_{Lchar,\ lam} + \overline{Nu}^{10}{}_{Lchar,\ turb}\right)^{1/10} \tag{4.36}$$

Where the laminar Nusselt number is:

$$\overline{Nu}_{Lchar,lam} = \frac{1.4}{ln\left(1 + \frac{1.4}{0.835\ C_{lam}{Ra_{Lchar}}^{0.25}}\right)} \qquad C_{lam} = \frac{0.671}{\left[1 + \left(\frac{0.492}{Pr}\right)^{9/16}\right]^{4/9}} \tag{4.37}$$

And the turbulent Nusselt number is:

$$\overline{Nu}_{Lchar,turb} = C_{turb,U}{Ra_{Lchar}}^{1/3} \qquad C_{turb,U} = 0.14\left(\frac{1 + 0.0107\ Pr}{1 + 0.01\ Pr}\right) \tag{4.38}$$

Where Pr is the Prandtl number.

For the back surface the following equation 4.39 is used to calculate the Nusselt number.

$$\overline{Nu}_{Lchar} = \frac{2.5}{ln\left\{1 + \frac{2.5}{0.527{Ra_{Lchar}}^{0.20}}\left[1 + \left(\frac{1.9}{Pr}\right)^{0.9}\right]^{2/9}\right\}} \tag{4.39}$$

For the case where the module is vertical, the natural convection is correlated with the Rayleigh number; defined by equation 4.40 and the average Nusselt number; defined by equation 4.41 which are dependent on based on the length in the vertical direction. The following equations are used to calculate the natural convection for the front and back surface.

$$Ra_L = \frac{g\ L^3\beta\ (T_s - T_\infty)}{\upsilon\alpha} \tag{4.40}$$

$$\overline{Nu_L} = \frac{\bar{h}\,L}{k} \tag{4.41}$$

The average Nusselt number is calculated using the empirical formula:

$$\overline{Nu_L} = \left(\overline{Nu}^6{}_{L,lam} + \overline{Nu}^6{}_{L,turb}\right)^{1/6} \tag{4.42}$$

Where the laminar Nusselt number is:

$$\overline{Nu}_{L,lam} = \frac{2.0}{ln\left(1 + \frac{2.0}{C_{lam} {Ra_L}^{0.25}}\right)} \qquad C_{lam} = \frac{0.671}{\left[1 + \left(\frac{0.492}{Pr}\right)^{9/16}\right]^{4/9}} \tag{4.43}$$

And the turbulent Nusselt number is:

$$\overline{Nu}_{L,turb} = \frac{C_{turb,V}\ {Ra_L}^{1/3}}{1 + (1.4 \times 10^9)\frac{Pr}{Ra_L}} \qquad C_{turb,V} = \frac{0.13\ Pr^{0.22}}{(1 + 0.61\ Pr^{0.81\ })^{0.42}} \tag{4.44}$$

For tilted modules between 0 and 90 degrees, the same equations have been used as for the scenario at zero degrees. Although, the gravity force is modified to include the angle of the module:

$$Ra_L = \frac{g \cos(\theta_M)\ L^3 \beta\ (T_s - T_\infty)}{\upsilon \alpha} \tag{4.45}$$

For the inclined back surface, the Rayleigh number is calculated by equation4.46, where also the *g* is modified. Then equation 4.47 determines the Nusselt number[39], [40].

$$Ra_L = \frac{g \cos(90 - \theta_M)\ L^3 \beta\ (T_s - T_\infty)}{\upsilon \alpha} \tag{4.46}$$

$$Nu_b = \left[0.825 + \frac{0.387\ Ra^{1/6}}{\left[1 + \left(\frac{0.492}{Pr}\right)^{9/16}\right]^{8/27}}\right]^2 \tag{4.47}$$

For the scenario where the module is tilted with a gap on a roof or on a façade the calculations for the front surface are the same as for the case where the module is free mounted. Although, the calculations for the back surface are different account the effect of a reduced airgap. The space of the gap and the length of the module are used to define the Nusselt number; equation 4.48 [38]. The space *S* can be adjusted based on the design, whereas the *L* is equal to 1 since the results are per area. Important to mention is that the values of the air gap should not be less than 0.1 cm. This is an assumption that has been made because otherwise the ratio of *S/L* will be very small, and the results will give very high free convection values [41].

$$Nu = \frac{Ra_L}{24}\frac{S}{L}\left[1 - exp\left(\frac{-35}{Ra}\frac{L}{S}\right)\right]^{0.75} \tag{4.48}$$

$$Ra_L = \frac{g \cos(\theta_M)\ (L/4\ )^3 \beta\ (T_s - T_\infty)}{\upsilon \alpha} \tag{4.49}$$

$$Nu = \frac{h\ S}{k_{air}} \tag{4.50}$$

4.2.4.2 Forced convection

Forced convection is a mechanical heat transfer mechanism due to the movement of a fluid. The forced convection coefficient depends on the wind speed of the fluid and empirical linear correlations give an estimation of the expected value. For the determination of the h forced convection coefficient, the angle between the incident wind speed and the angle of the module and the wind direction; (leeward and windward) are considered.

To characterize the direction of the wind speed on the surface (ϑ), the equation 4.51 is used which calculates the wind angle of incident based on the wind direction and the normal direction of the PV module. This equation was formed to determine whether the wind speed flows in the front surface or towards the back surface of the module. This is This is needed given that different equations are needed when the wind speed is leeward or windward to a surface [39],[42].To define the direction, if the calculated angle is less than ± 90 then the wind direction on the front surface is windward and on the back surface is leeward and if the calculated angle is more than ± 90, then the wind direction on the front surface is leeward and on the back surface is windward.

$$\vartheta = abs(A_m - A_{wind}) \tag{4.51}$$

Equation 4.52 used for the case of Leeward direction

$$h = 5.7\ U \cos\left(\theta_{wind}\right) \tag{4.52}$$

and equation4.53 for windward direction

$$h = 0.848\ k \left(\cos(\theta_{wind})\ U \frac{Pr}{v}\right)^{0.5} d^{0.5} \tag{4.53}$$

For the remaining scenarios where the module is tilted between 0 and 90 degrees the same methodology is followed.

For the determination of the back forced convection during the scenario where the module is attached on a roof or a façade with an air gap, wind speed data are needed inside the air gap. That has been the most complex scenario since data for the wind speed inside the channel related to the ambient wind speed have not been found. For this reason, an equation has been formed to satisfy this necessity. An approximation has been made which considers the wind speed zero inside the air gap for 0.01 m gap and equal to the ambient wind speed when the gap is 0.5 m. Considering these assumptions, the wind speed inside the air gap is considered to be linearly correlated to the width of the air gap. Consequently, the equation 4.54 estimates the wind speed inside the air gap compared to the ambient wind speed and width of the air gap.

$$u = \frac{Uair\ xb}{(0.5 - 0.01)}\ (s - 0.01) \tag{4.54}$$

Figure 4.9 shows the effect of air gap for a windy day at Delft on the 28th of January for. The different thicknesses of the air gap influence the total convection coefficient at the back side. More specifically, the

total convection coefficient has the shape and approximately same values as the forced convection. This is because the effect of free convection is not that important as the effect of forced convection during a windy day and therefore the bigger the air gap the higher the convection energy exchange. On the other hand, it can be seen from Figure 4.10 which shows the effect of air gap at Delft on the 8th of July, that since the wind speed values are not very high, the total convection coefficient is higher in the middle of the day when the air gap is 0.1m. Therefore, it is expected that for not windy days the effect of natural convection will be more important. All in all, considering those two figures and the results, that become the motivation on testing these configurations with different air gaps and investigate what is the effect of different air gaps in terms of energy yield and temperature.

Important to mention is that for the scenario where the module is attached on the roof or façade, the back forced convection is assumed to be zero.

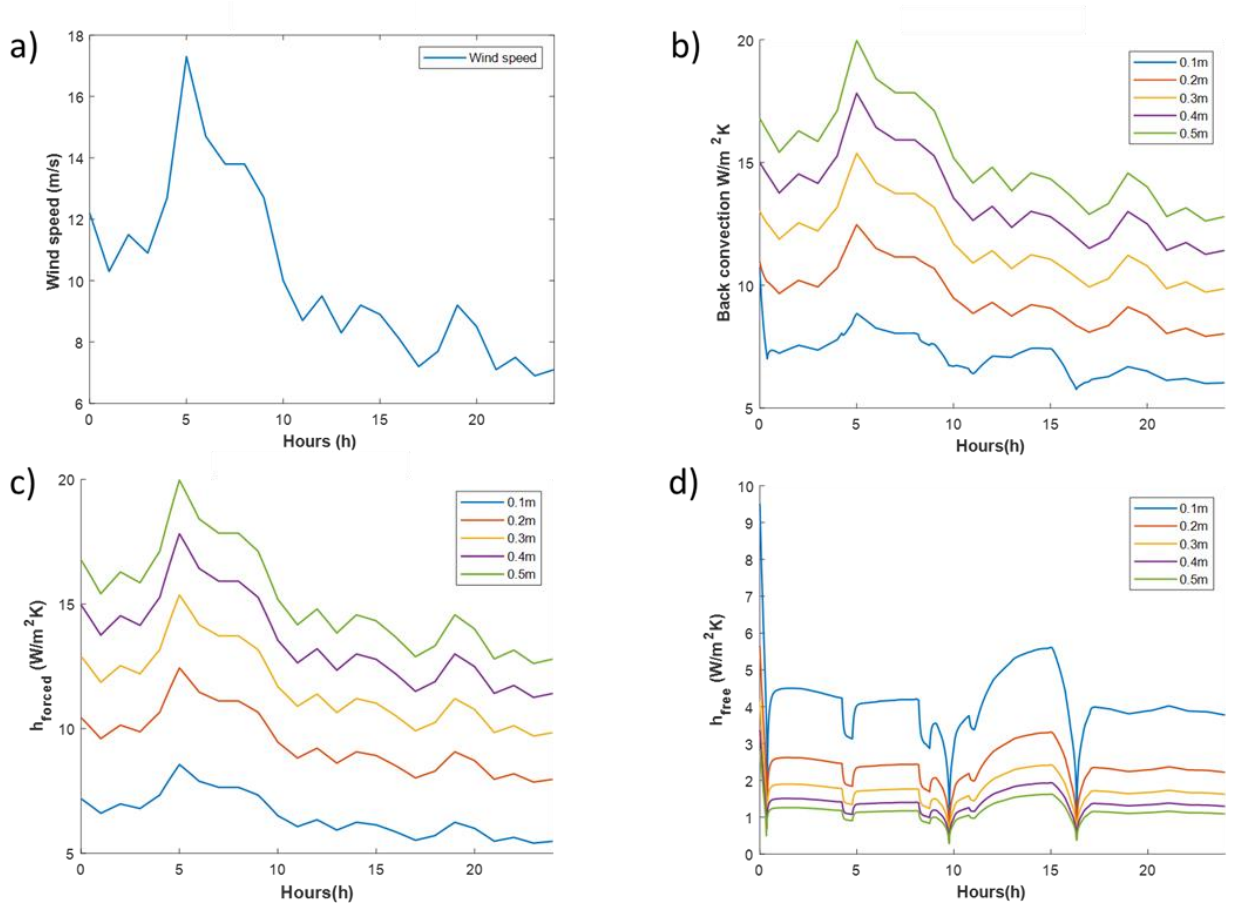

Figure 4.9 Figure a) wind speed on the 28th of January Delft , for 0.1-0.5 meters air gap the figures present the convection at the back side : Figure b) the total convection at the back side is plotted , Figure c) the forced convection is presented and Figure d) the free convection is plotted

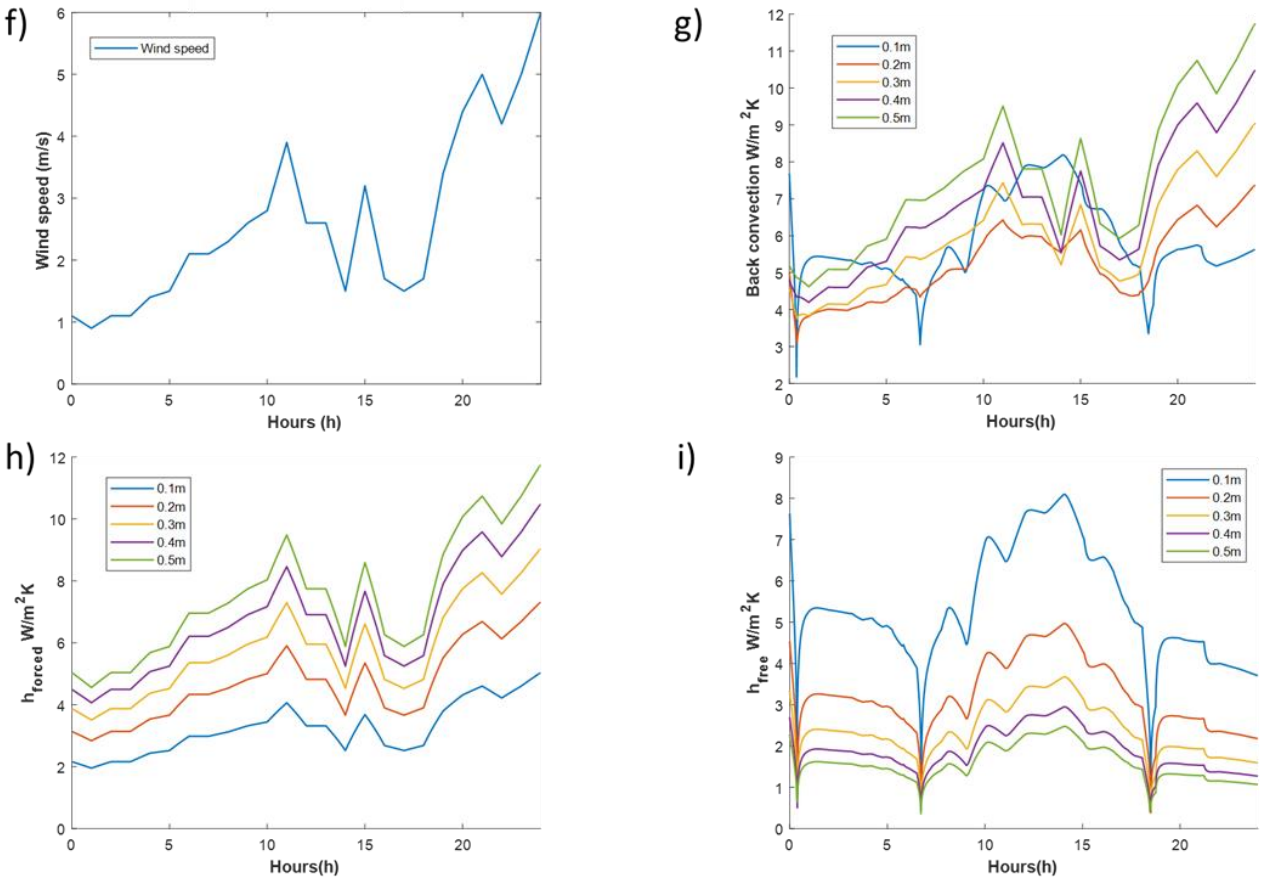

Figure 4.10 Figure f) wind speed on the 8th of July Delft , for 0.1-0.5 meters air gap the figures present the convection at the back side : Figure g) the total convection at the back side is plotted , Figure h) the forced convection is presented and Figure i) the free convection is plotted

4.2.5 Conduction model

Conduction heat transfer is a thermal energy which occurs when gradient temperature difference exists in a medium or between media. The conduction refers to transfer of energy from more energetic to less energetic particles due to interaction between the particles. The conduction heat transfer is expressed with equation 4.55 known as Fourier's law. The heat transfer rate is proportional to the temperature gradient. The thermal conductivity k is a material characteristic [29].

$$Q_{conduction} = kA\frac{dT}{dx} = kA\frac{T_i - T_{i+1}}{dx} \qquad 4.55$$

For the model, the conduction between layer nodes is proportional to the temperature difference between the layers, their thickness and the materials conductivity. Since the layer temperature is homogeneous, the energy flux is assumed to pass between the nodes of the layer and the neighboring layers. For each layer, a resistance is formed as shown in equation 4.56 and therefore equation 4.55 is converted to equation 4.57.

$$R = \frac{\frac{d_i}{2}}{k_i} + \frac{\frac{d_{i+1}}{2}}{k_{i+1}} \quad 4.56$$

$$Q_{conduction} = \frac{T_i - T_{i+1}}{R} \quad 4.57$$

For the scenarios of integrated modules on a roof and on a façade, a total conduction coefficient is calculated based on the materials forming the wall on a façade and the roof. Using the equation 4.58, based on the thickness and conduction coefficient of each material a resistance is calculated that represents the whole structure. Finally, the total resistance used for the conduction equation is calculated from equation 4.59, with respect to the total thickness of the wall and the roof and the thickness and conduction coefficient of the back layer of the module. The total resistance is calculated in a way that the two nodes are applied at the center of the wall/roof and the back layer of the module .Finally, using the equation 4.60 the conduction exchange formula can be used in the equation of the wall/roof and back layer node accordingly.

$$R_{facade/roof} = \sum_{layer=1}^{n} \left(\frac{d_{layer}}{k_{layer}} \right) \quad 4.58$$

$$R_{facade/roof \leftrightarrow back\ layer} = \frac{\frac{d_{wall/roof}}{2}}{R_{facade/roof}} + \frac{\frac{d_{back\ layer}}{2}}{k_{back\ layer}} \quad 4.59$$

$$Q_{conduction} = \frac{T_{wall/roof} - T_{back\ layer}}{R_{facade/roof \leftrightarrow back\ layer}} \qquad Q_{conduction} = \frac{T_{back\ layer} - T_{wall/roof}}{R_{facade/roof \leftrightarrow back\ layer}} \quad 4.60$$

4.2.6 Radiation model

The radiation energy is emitted from an object that is temperature is nonzero and the energy is transported by electromagnetic waves. Radiation originates from a source such as the sun or from surface to surface. The limit to the emissive power is prescribed by the Stefan-Boltzmann law as shown in equation 4.61 which represents the energy emitted from a blackbody [29]. Where σ is the Stefan – Boltzman constant

$$Q_{radiation} = \sigma T^4 \quad 4.61$$

Whereas, the heat flux emitted by a real surface is described by the equation 4.62, where ϵ is a radiative property of the emitter surface. The values of ϵ fluctuate between 0 and 1 and the number is a measure on how efficient the emission is compared to a perfect emitter.

$$Q_{radiation} = \epsilon \sigma T^4 \quad 4.62$$

For the model, radiation energy exchange is considered for the front and backside layers with the sky and ground. Moreover, since the module is not entirely exposed to the sky and ground because of the inclination angle θ, sky-view and ground view factors are implemented to the equations[43],[44].

$$Q_{radiation} = \epsilon F \sigma (T^4 - T^4) + \epsilon F \sigma (T^4 - T^4) \quad 4.63$$

$$F_{front \leftrightarrow sky} = 0.5\ (1 + cos\theta_M) \quad 4.64$$

$$F_{front \leftrightarrow ground} = 0.5\ (1 - cos\theta_M) \quad 4.65$$

$$F_{back \leftrightarrow sky} = 0.5\ (1 - \sin\ (90 - \theta_M)) \quad 4.66$$

$$F_{back \leftrightarrow ground} = 0.5\ (1 + s\sin\ (90 - \theta_M)) \quad 4.67$$

The factors are developed in such a way to calculate the proportion of radiation exchange to the sky and to the ground accordingly. Although, for the case where the module is at zero degrees, it is assumed that the radiation exchange to the sky and the ground is zero.

Additionally, important to mention is that the radiation with the sky is assumed to be with the ambient temperature. This is because it was found that the radiation exchange considering the sky temperature was overestimated. A detail explanation will be given while presenting the validation results

For the scenarios where the module is on a façade or on a roof with an air gap, the radiation exchange of the back layer of the module is considered with the node of the façade/roof. The total radiation transferred from the one node q1 must be equal to the total radiation transferred to the other node –q1. The equation 4.68 is used to calculate the radiation exchange assuming that the nodes represent parallel planes. Since the air gap is very small and 1D approach is used, the view factor is considered equal to 1 for both nodes[29], [45].

$$Qradiation_{wall/roof \leftrightarrow back\ layer} = \frac{\sigma\left({T_{wall/roof}}^4 - {T_{back\ layer}}^4\right)}{\frac{1}{\varepsilon_{wall/roof}} + \frac{1}{\varepsilon_{back\ layer}} - 1} \quad 4.68$$

$$Qradiation_{wall/roof \leftrightarrow back\ layer} = \frac{\sigma\left({T_{back\ layer}}^4 - {T_{wall/roof}}^4\right)}{\frac{1}{\varepsilon_{wall/roof}} + \frac{1}{\varepsilon_{back\ layer}} - 1} \quad 4.69$$

The formulas of radiation exchange need to be linearized since for the energy balance equations everything must be expressed on Temperature to the power of one. From the Solar book [31], the equation can be linearized as follows:

$$(a^4 - b^4) = (a^2 + b^2) + (a + b)(a - b) \quad 4.70$$

Therefore:

$$hr_{sky} = \varepsilon_i \sigma \left({T_i}^2 + {T_{sky}}^2 \right) + (T_i + T_{sky}) \quad 4.71$$

$$hr_{ground} = \varepsilon_i \sigma \left({T_i}^2 + {T_{ground}}^2 \right) + (T_i + T_{ground}) \quad 4.72$$

$$Q_{radiation,i} = F hr_{sky} ({T_i}^2 - {T_{sky}}^2) + F hr_{ground} ({T_i}^2 - {T_{ground}}^2) \quad 4.73$$

For the scenario of a module on the façade or on a roof with air gap the equation for the back side is linearized as follows:

$$hr_{wall/roof \leftrightarrow back\ layer} = \varepsilon_i \sigma \left({T_{wall/roof}}^2 + {T_{back\ layer}}^2 \right) + (T_{wall/roof} + T_{back\ layer}) \quad 4.74$$

And therefore, the radiation exchange equation simplifies as follows:

$$Qradiation_{wall/roof \leftrightarrow back\ layer} = \frac{hr_{wall/roof \leftrightarrow back\ layer} \left({T_{wall/roof}}^2 - {T_{back\ layer}}^2 \right)}{\frac{1}{\varepsilon_{wall/roof}} + \frac{1}{\varepsilon_{back\ layer}} - 1} \quad 4.75$$

$$Qradiation_{wall/roof \leftrightarrow back\ layer} = \frac{hr_{wall/roof \leftrightarrow back\ layer} \left({T_{back\ layer}}^2 - {T_{wall/roof}}^2 \right)}{\frac{1}{\varepsilon_{wall/roof}} + \frac{1}{\varepsilon_{back\ layer}} - 1} \quad 4.76$$

4.3 Electrical model

To obtain accurate results in terms of thermal performance and energy yield an electrical model needs to be implemented. The electrical model was developed by Ándres Calcabrini is a two-diode model that has been successfully validated and provides accurate results for I-V curves for different temperatures and absorbed potential irradiance on the solar cell. It is very important to include such model since the increased solar cell temperature leads to a shift in the I-V curve as shown in Figure 4.11. Also, the efficiency is needed for each time step, to calculate the correct temperature of the cell; the thermal model is highly connected to the electrical model via equation 4.9. More specifically, with an increase in temperature, the short circuit current increases slightly but the open voltage decreases significantly and therefore the efficiency will also decrease. On the other hand, for higher irradiance, the short circuit current increases significantly whereas the voltage increases by a small factor. Consequently, since the I-V curve shifts according to irradiance and temperature, the maximum power point (MPP) is also influenced which means the efficiency changes and the output power.

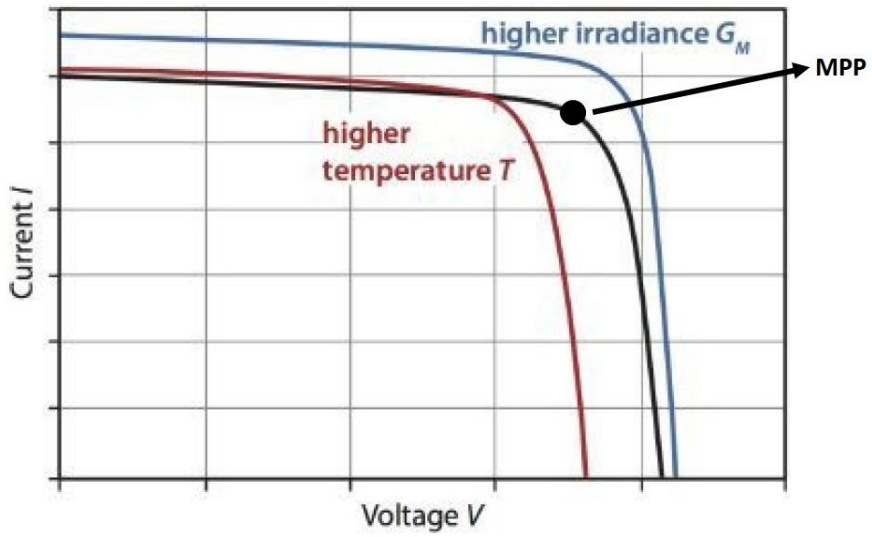

Figure 4.11 Effect of temperature and irradiance on the I-V solar cell [31]

From the electrical model, I-V curves have been extracted for different combinations of temperature and absorbed irradiance values. Consequently, a 2D matrix has been developed with the power density with respect to temperature and irradiance combinations. This matrix has been implemented to the model.

In the model, the irradiance but also the working temperature of the cell fluctuates and therefore, it is very important to consider these changes and determine in each time step the representative I-V curve. As have been discussed in section 4.2.3, in each time step the thermalization and electricity power are calculated according to the number of absorbed photons per wavelength. The electricity power is considered until this step as the potential electricity if recombination losses are assumed to be zero. In the electrical model, the potential electricity and the temperature of the cell are used as inputs to extract the correct I-V. Therefore, from the I-V curve obtained in each time step, the maximum power point is calculated and at the same time the efficiency is defined from the ratio of potential electricity to the MPP.

4.4 Color model

For each time step of the simulation, the obtained color based on the angle of incident needs to be calculated. This will give an understanding on how the reflected light of the optic filter changes as the altitude of the sun and eventually the angle of incidence changes for a certain period. To define the resulting color, the computational model developed by Juan Camilo Ortiz during his Master thesis project [1] was used. The model transforms the optical information of the reflectance spectrum into color coordinates and finally into an actual visible color which is displayed on a screen. More specifically, the model uses the Color matching functions of the International Commission on Illumination [46]. The CIE has defined color-mapping functions which are based on the chromatic response of a standard observer. From the color-mapping function and the optical information, the color model calculates and eventually translates the chromaticity coordinates to RGB color coordinates. Finally, a gamma correction is applied, and the final color is observed. The gamma correction is applied to transform the linear sRGB to nonlinear since human eye sensitivity is nonlinear. More detail information can be found from [7], [8].

5 Validation

The model was validated in terms of thermal performance from measurements that were taken from Juan Camilo Ortiz. For the validation, two mini modules that have been fabricated by Juan Camilo Ortiz and Simona Villa were used and installed at the monitoring station at TU Delft for a week; from the 19th of June until 26 of June 2020. The structure of the modules is illustrated from Figure 5.1. More specifically, the optic filter of the colored mini module is consisted of ten periods of 0.09µm SiO_2 (n_H) and 0.09µm SiN_3 (n_L). With this optic filter configuration, the observed color is bright orange as shown in Figure 5.2. The angle of the mini modules is set to zero degrees.

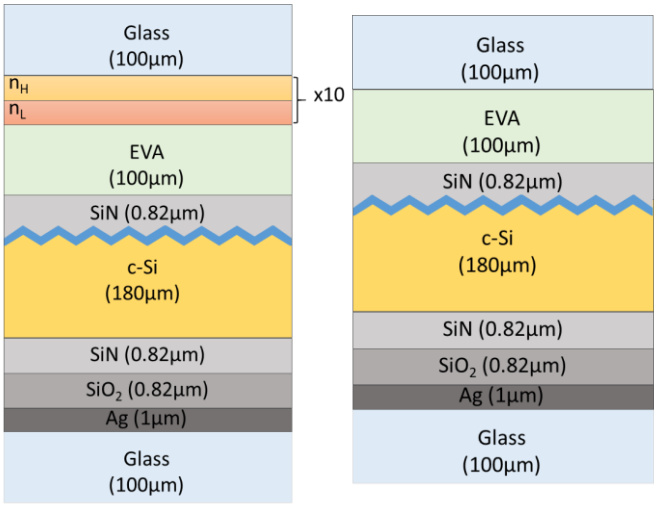

Figure 5.1 Mini modules structure. Module stack on the left shows the layers for a mini module with optic filter and the right stack without optic filter

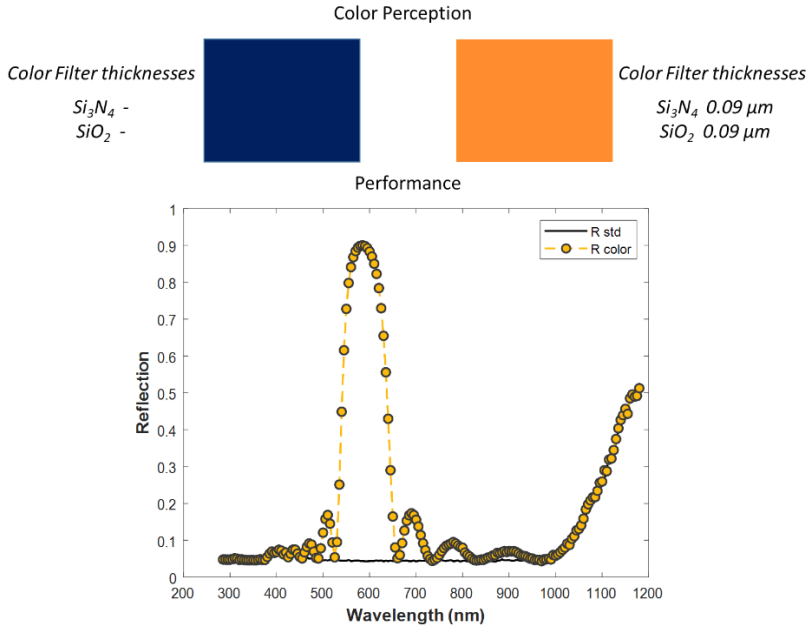

Figure 5.2 Color perception from the colored mini module and standard module, Figure on the bottom illustrates the reflection performance per wavelength of the colored and standard module

The model has been validated for three days 24th 25th and 26th of June. The weather data measured for this period are presented in Figure 5.3. Important to mention is that, further information of the wind direction have not been measured for this specific period and location and therefore, data have been used from Meteonorm. Because of that, differences are expected when the wind speed direction changes. Moreover, the spectral irradiance is not measured but data from Smarts have been used for the validation.

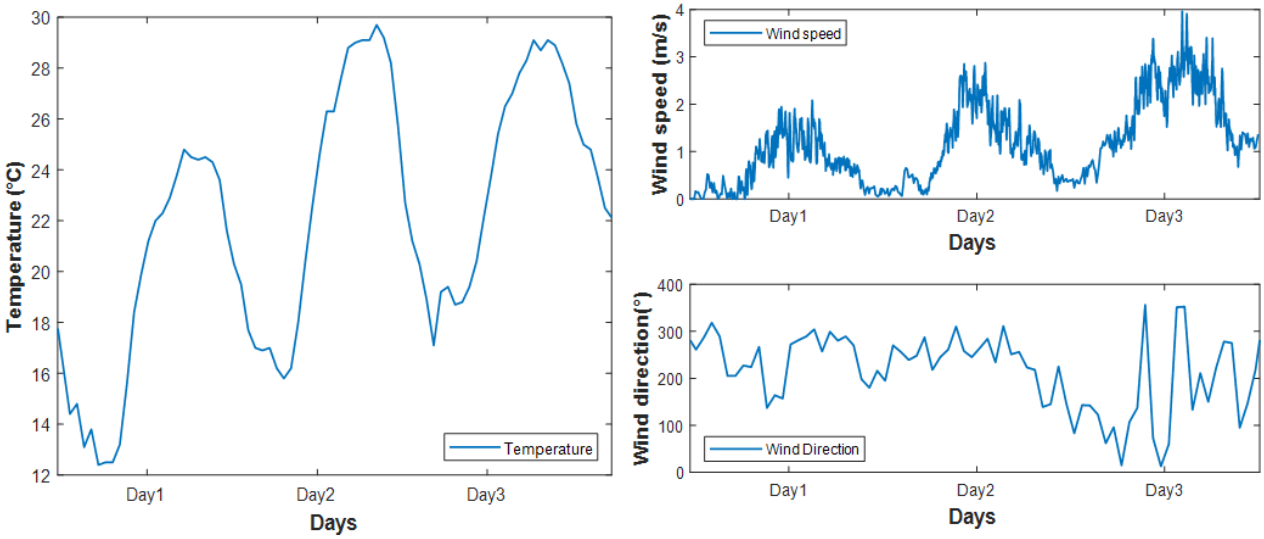

Figure 5.3 Weather data for 24th,25th and 26th of June. Figure on the left illustrates the temperature profile and the figure on the right shows the wind speed and wind direction accordingly. The wind direction is taken from Meteonorm

The result of the validation is presented in Figure 5.4. To observe this final validation results, the convection at the back and front side of the module had to be changed. A factor of 0.65 has been used for both sides so that the simulated graph meets as much as possible the reference graph. More specifically, the simulated results changed +1 degree with the applied factor. The correction was applied since the convection equations are empirical and are overestimating the convections. Moreover, the simulated module is a mini module and therefore, the hydraulic perimeter is much more different than a module which is 10 cm x10 cm. Important to mention s that, there was a fault from PicoLog data collector and data between the 2nd and the middle of the 3rd day was missing.

The top graph presents the results for a standard mini module and the bottom graph for the colored mini modules. It can be concluded for the standard modules' validation, that the trend of the measured and validated data merge during the operating hours but there is a difference during the night. This can be explained from radiation heat exchange, as the radiation of the module is considered with the ambient and not sky temperature. Important to mention is that radiation with the sky has been tested as well but, during the operating hours the radiation effect was overestimated. Therefore, since it is more important to predict the temperature behavior during working hours the assumption with the ambient radiation has been made. Moreover, the measured model during the morning has a gradual increase of temperature and then a sudden jamb follows. This is mainly because the module was under shadow and suddenly the sun appeared and that behavior is observed, although, in the current model shadow effects are not considered. More specifically, the RMSD was calculated 5.20 degrees. The high value of RMSD is a result of the high deviations during the morning and the night. More specially, during the working hours the deviation between the measured and the simulated results is on average 1.5 degrees.

Regarding the mini colored modules validation, it can be concluded that the temperature trend is again similar with a variance during the night. Although, during the pick of the day, a difference of is observed. This is associated to the fact that the SMARTS spectrum irradiance data used for the simulation do not provide the exact values for the real spectrum irradiance that has been incident on the module for the given period. Therefore, this deviation was expected as the power per wavelength has some errors compared to the real power. More specifically, the RMSD was calculated 4.79 degrees. The high value of RMSD is a result of the high deviations during the morning and the night. More specially, during the working hours the deviation between the measured and the simulated results is on average 2 degrees.

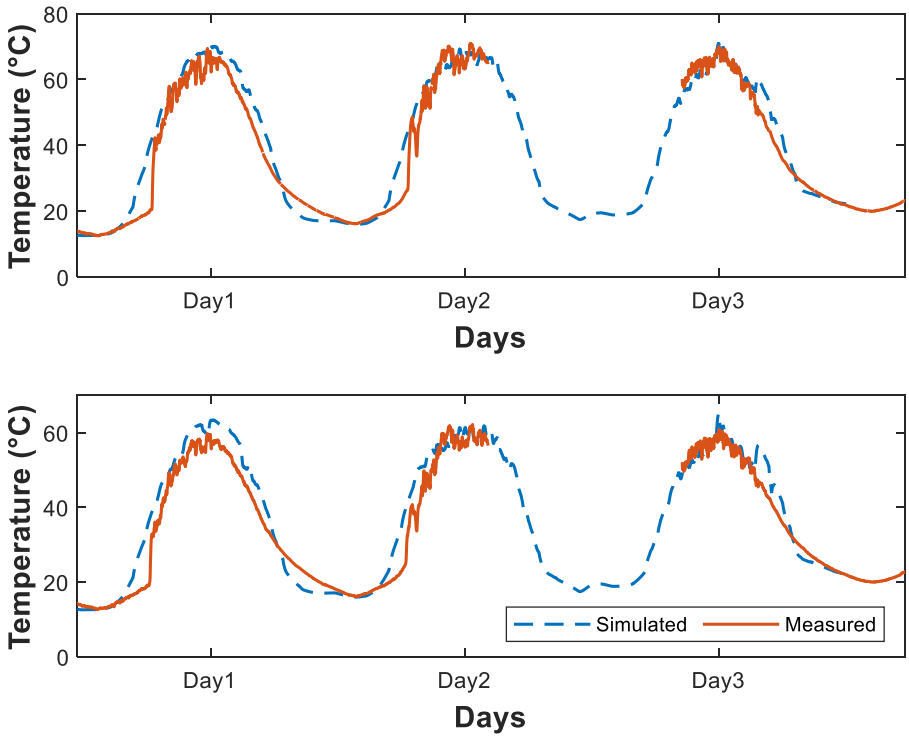

Figure 5.4 Temperature distribution of simulated and measured data for 3 consecutive dates; 24th 25th and 26th of June 2020.

6 Results

6.1 Introduction

In this chapter optic, thermal and electrical results will be presented for 5 different configurations as presented in Figure 4.1. The simulated modules are the mini modules shown in Figure 5.1. For each configuration, two scenarios have been tested. The first scenario corresponds to the date on the as highest temperature that was found for the optimum angle of a free mounded module for each location. As a worst-case scenario, a date with clouds has been simulated.

The results are divided into five sections based on the module configuration. In each section results for the two weather scenarios of each location are presented in terms of daily temperatures, energy yield and I-V curves for standard module and ten selected colors. Finally, in each section energy yield results are given for a whole year for a standard module and the ten selected colors. The daily results have been simulated with a time step of 60sec, however for the yearly results the time step is per hour (3600 sec).

6.2 Main inputs parameters

The model is developed in a way that all the inputs are reconfigurable and can be changed easily according to the preferences of the user. For the current thesis results, the inputs for each module configuration are presented in the following tables. Table 6-1, shows the coordinates of Delft and Dubai locations. These two locations were chosen because they have different climates. Dubai is closer to the equator and therefore, the behavior of the optic filters is expected to deviate from the behavior in Delft. In Table , the module orientation is presented based on the location and the module configuration. The optimum angle for each location was found from [47]. Table 6-4, Table 6-5 and Table 6-6 , present the materials of the module, roof and façade respectively[28] and finally, Table 6-7 shows the selected days for each weather scenario.

The main weather scenarios have been selected for High irradiance and low irradiance in order to test the performance of the optic filter under a normal and worst-case scenario. The weather data can be found in Appendix B in Figure A 11,Figure A 14,Figure A 16,Figure A 19 for each location and scenario respectively.

Information regarding the wavelength reflection range and the reflected color based the angle of incidence for the selected colors can be found in Appendix A.

Location	Delft, Netherlands	Dubai, United Arab Emirates
Altitude (°)	52.01	25.20
Longitude (°)	4.35	55.27
GMT (h)	-1	-4

Table 6-1 Location coordinates for Delft and Dubai

Cell dimensions	Number of cells
Number of cells	6 (2x3) connected in series
Dimension of the cell (cm^2)	4.5 x 3.5

Table 6-2 Module dimensions

Configuration	Free mounted	Roof/Roof air gap	Façade/Façade air gap
Tilted angle Delft (°)	32	35	90
Tilted angle Dubai (°)	25	20	90
Orientation	South	South	South

Table 6-3 Orientation of the module and inclination angle for each configuration

	Density (kg/m^3)	Thermal conductivity (W/mK)	Specific heat capacity (J/kgK)	Emissivity
Glass	2700	1.8	750	0.84
Optic filter	2.6	2.659	808	0
EVA	960	0.35	2090	0
SiN	3000	20	0.7	0
cSi	2300	149	836	0
SiO_2	2500	1.4	730	0
Ag	2730	209	963	0.03

Table 6-4 Material properties of the module [48]

Roof			
Materials	Clay	Insulation	Wool
Thicknesses (cm)	20	3.5	5
Density (kg/m^3)	1600	7.7	2300
Conduction (W/m^2K)	0.975	0.0433	0.14
Specific heat capacity (J/m^2K)	878	700	350
Emissivity	0.91	-	-

Table 6-5 Material properties of the roof [48], [28]

Façade			
Materials	Concrete	Insulation	Wood
Thicknesses (cm)	20	3.5	5
Density (kg/m^3)	2000	7.7	350
Conduction (W/m^2K)	0.113	0.0433	0.099
Specific heat capacity (J/m^2K)	1000	700	2380
Emissivity	0.91	-	-

Table 6-6 Material properties of the façade [48], [28]

Scenarios	Highest Temp & Irradiance	Cloudy day
Delft	5/5/2005	19/1/2005
Dubai	3/9/2005	1/1/2005

Table 6-7 Selected days for each scenario

6.3 Color matrix

Figure 6.1 a) illustrates the observed color simulated from the colored mini modules for different optic filter combinations of SiN_x and SiO_2. Since different optic filters thicknesses yield similar colors, it can be noticed that the matrix is divided into groups with the shades of 10 main colors; Blue, Turquoise, Green, Dark Green, Yellowish, Orange, Dark Orange, Red, Purple and Pink. The dark colors have not selected because are not aesthetically attractive and are linked to low color saturation provided of the optic filters .Therefore, the matrix has been divided in color groups as shown in Figure 6.1 b). The color table was simulated for all the optic filter combinations for a whole year to define which is the best optic filter for each main color. The optimum optic filter that has been selected for each color group is defined based on which combination of SiN and SiO_2 has the highest energy yield for a whole year. Consequently, the optimum optic filter thicknesses for each color have been found for each location and configuration

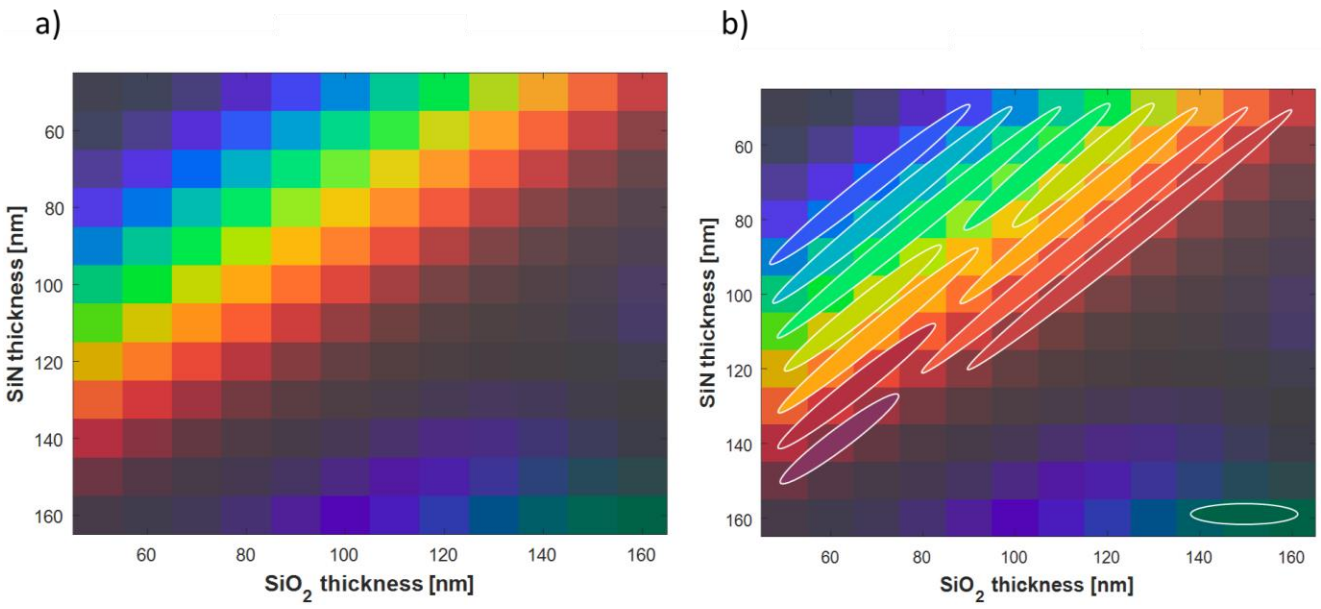

Figure 6.1 Figure a) Observed color for different combinations of optic filter, Figure b) division of the matrix into 10 main colors

6.3.1 Optic filter selection based on location

The simulation was performed for a free mounted module in Delft with an angle of 32degrees. The results of the total energy yield (kWh/m^2) are illustrated in Figure 6.2 a) and fluctuate between 82 and 64 kWh/m^2 for 50nm of SiN/SiO_2 and 110nm SiN/120nm SiO2 respectively. For each group of color, different energy yields are observed for each optic filter combination. The maximum energy was calculated and the optimum optic filter thicknesses for each color are presented in Table 6-8. These specific optic filter thicknesses have been used for the results and have been compared with the standard module in terms of temperature, yield energy and efficiency.

Figure 6.2 b), presents the maximum temperature drop for each color with respect to the standard module. The temperature drops have been measured from the peak of the temperature distributions on the 5th of May; Figure 6.2 c). Different optic filters have different cooling behavior since different reflections are occurred. More specifically, it can be noticed that the combination of thicknesses between

70-110nm SiN and 80-120 nm of SiO_2 have the highest impact on the reduction of the working temperature by approximately 6 degrees.

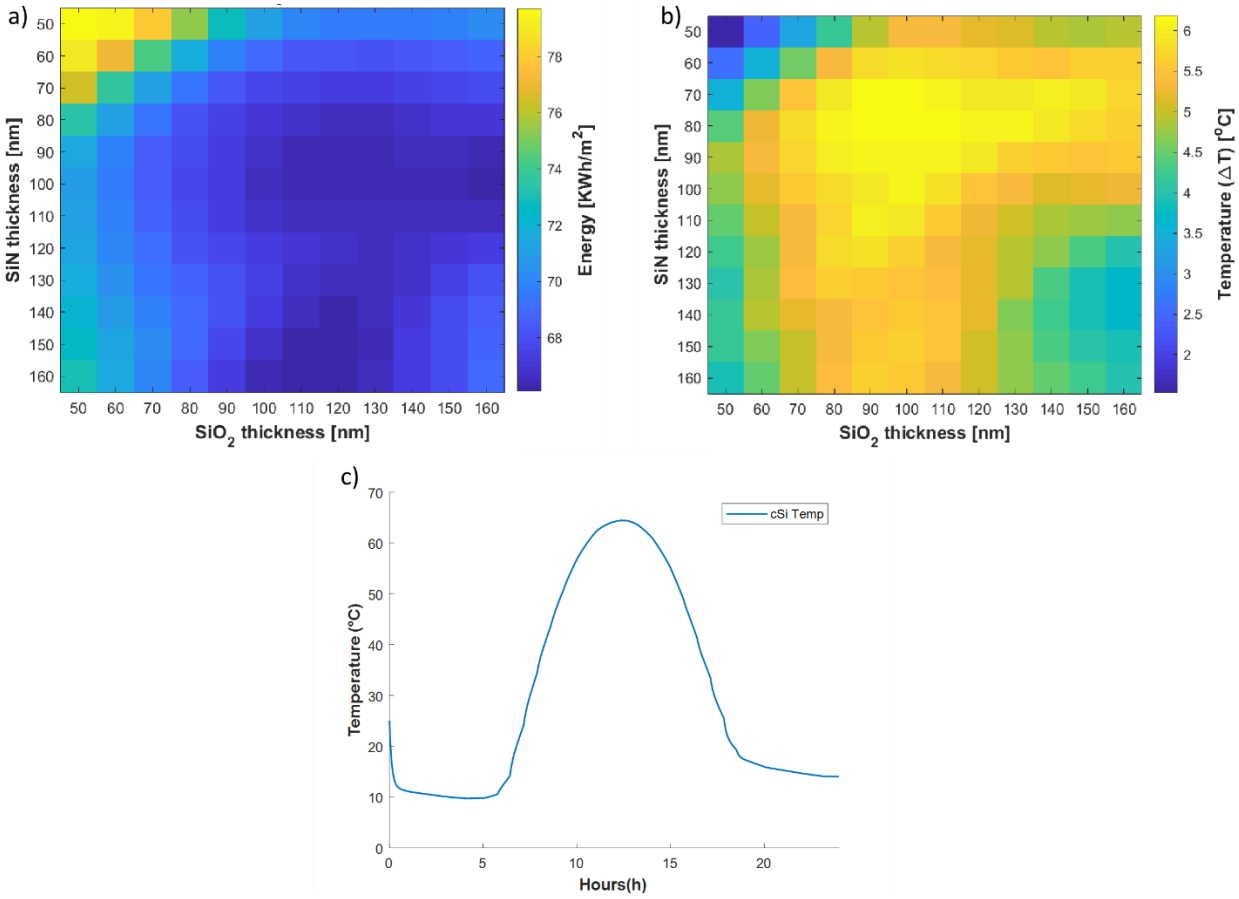

Figure 6.2 Figure a) Energy yield (kWh/m²) for each optic filter combination in Delft 2005 Figure b) Maximum temperature difference for each optic filter combination from the standard module on Figure c) on the 5th of May.

	Blue	Turquoise	Green	Dark green	Yellowish	Orange	Dark orange	Red	Purple	Pink
Si_3N_4	0.05	0.05	0.11	0.16	0.12	0.13	0.05	0.05	0.15	0.14
SiO_2	0.09	0.1	0.05	0.16	0.05	0.05	0.15	0.16	0.05	0.05

Table 6-8 Optimum combination of optic filters for each color based on the highest energy yield

Figure 6.3 a) illustrates the results of energy yield for different optic thicknesses for a module in Dubai tilted at 25 degrees. The energy yield is much higher than Delft, which is expected since the module in Dubai receives more irradiance. More specifically, the maximum energy yield is approximately 145 kWh/m² for an optic filter design of 50nm SiN and SiO_2 and the minimum energy is around 120 kWh/m² for 110nm SiN/120nm SiO2. It was found that the optimum thicknesses resulting the maximum energy yield are the same values that have been calculated for Delft. Therefore, the same optic filter thicknesses have been tested for Dubai as shown in Table 6-8. That means that the performance of the optic filters has an almost linear effect on current generation from different locations due to changes in the incident irradiance and the angle of incidence. However, the relative differences among the optic filters remain the same.

Figure 6.3 b) shows the according maximum temperature drop for Dubai. The reason why the temperature drop for each optic filter is smaller than in Delft is because the selected day has slighter less irradiance compared to Delft. From the figure, the combination of thicknesses between 60-80nm SiN and 80-90 nm of SiO_2 have the highest impact on the working temperature at approximately 6 degrees.

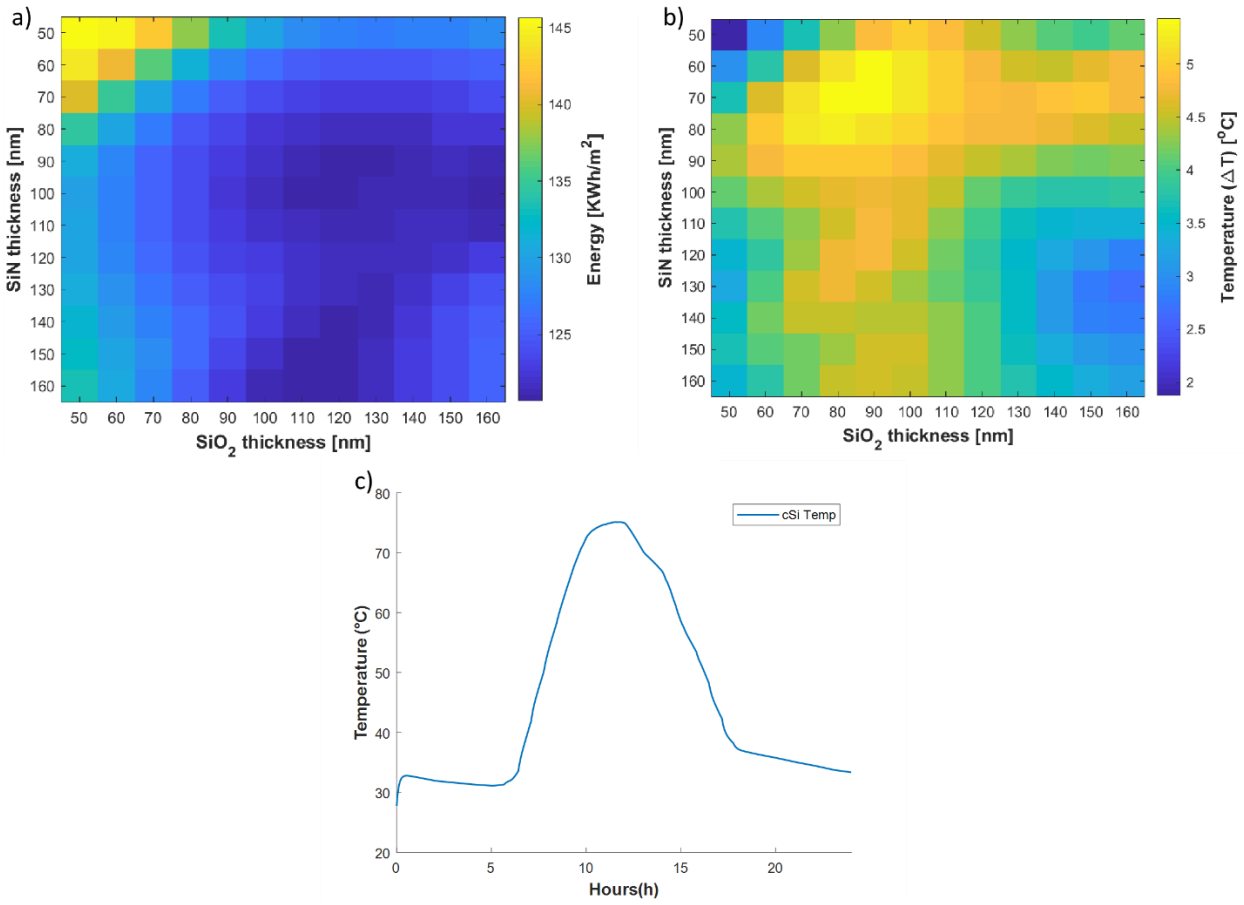

Figure 6.3 Figure a) Energy yield (kWh/m^2) for each optic filter combination in Dubai 2005 Figure b) Maximum temperature difference for each optic filter combination from the standard module on Figure c) on the 3rd of September .

6.4 Free mounted module

6.4.1 Temperature results

In this chapter, the results for free mounted modules are discussed for both colored and standard modules. The module in Delft is set at 32 degrees and the module in Dubai at 25 degrees, both oriented south. The results are presented in a way that comparison of a standard module and colored module is illustrated.

6.4.1.1 Highest temperature

Figure 6.4 illustrates the temperature distribution for the whole day on the 5th of May and the differences between the maximum temperature of a standard and the colored modules. From Figure 6.3 a) the maximum temperature is at around 65 degrees and it drops significantly with optic filters. More specifically, from Figure 6.3 b) , the table shows that the turquoise color cools the most the module by around 5.5 degrees whereas the dark green module decreases the least the temperature at around 4 degrees. All in all, it can be concluded that the optic filters since are reflecting with the visible wavelength range, they decrease the working temperature of the module. The maximum temperature difference is observed during the peak of the graph since at that time the AOI is the minimum and the irradiance incident on the module the highest.

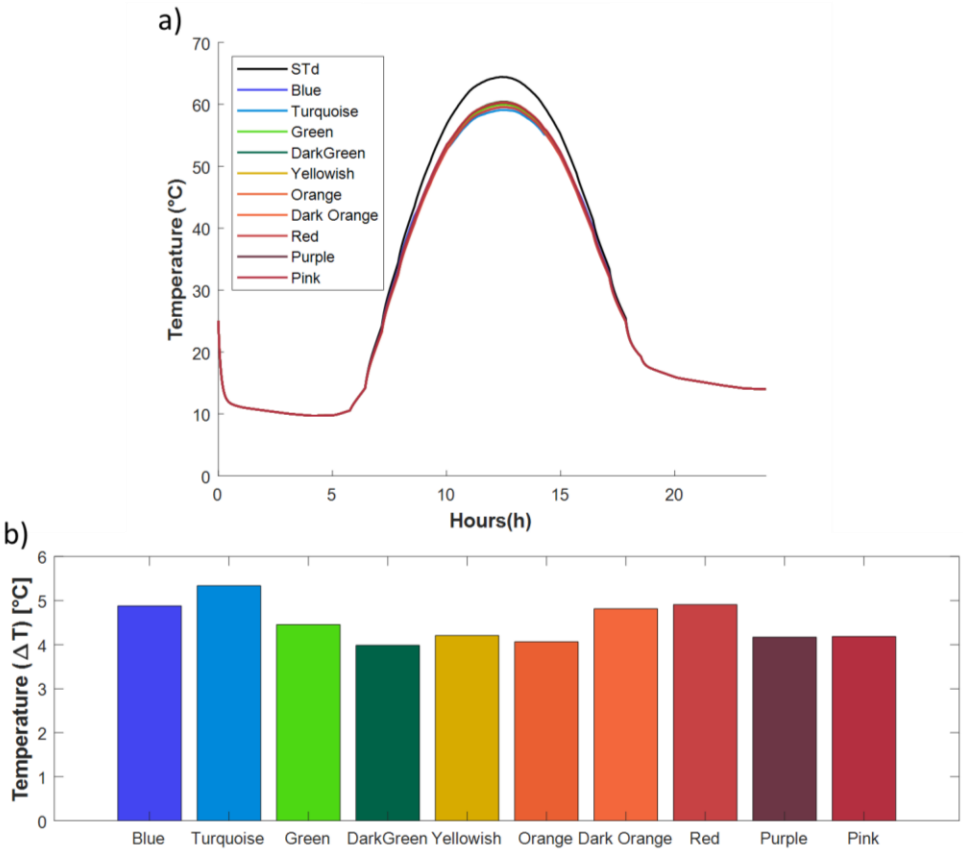

Figure 6.4 Figure a) Temperature distribution for the standard module and the 10 main colors on the 5th of May in Delft Figure b) Temperature difference for each color from the maximum temperature of the standard module

In Figure 6.5 a) , the power distribution is illustrated whereas in Figure 6.5 c) the energy yield for this day is presented. Comparing the plots, it can be noticed that the dark green optic filter gives the lowest energy yield. However, at the same time the dark green module has also the lowest temperature drop. The reason behind this, is the wavelength range that is reflected from the dark green filter; Appendix A, the reflection for a dark green optic filter is plotted. The optic filter is designed to reflect at 1050nm which is a wavelength range with low photon energies and therefore the reflected irradiance does not have a high impact on the energy yield. Although, a second reflection appears at 520nm and a third reflection at around 350nm. Eventually the third reflection results to an addition irradiance reflection in the range where the photon energy is very close to the bandgap. That is in comparison with the turquoise filter that reflects a smaller range between 420-520 nm and therefore the energy yield is higher. The highest temperature drop is observed since the filter reflects photons which are parasitically absorbed.

The blue optic filter has a slightly higher energy yield at around 0.5kWh/m^2 although, the remaining colors have similar values of energy yield.

Regarding the I-V curve from Figure 6.5 b), the voltage influence due to the temperature drop is very small compared to the current drop due to the reflection of irradiance for each optic filter. The dark green mini module has a slightly smallest efficiency as can be seen from the I-V curve, and the blue optic filter the highest among the colored modules. More specifically, the overall efficiency for the standard module is at around 18% Figure A 12.

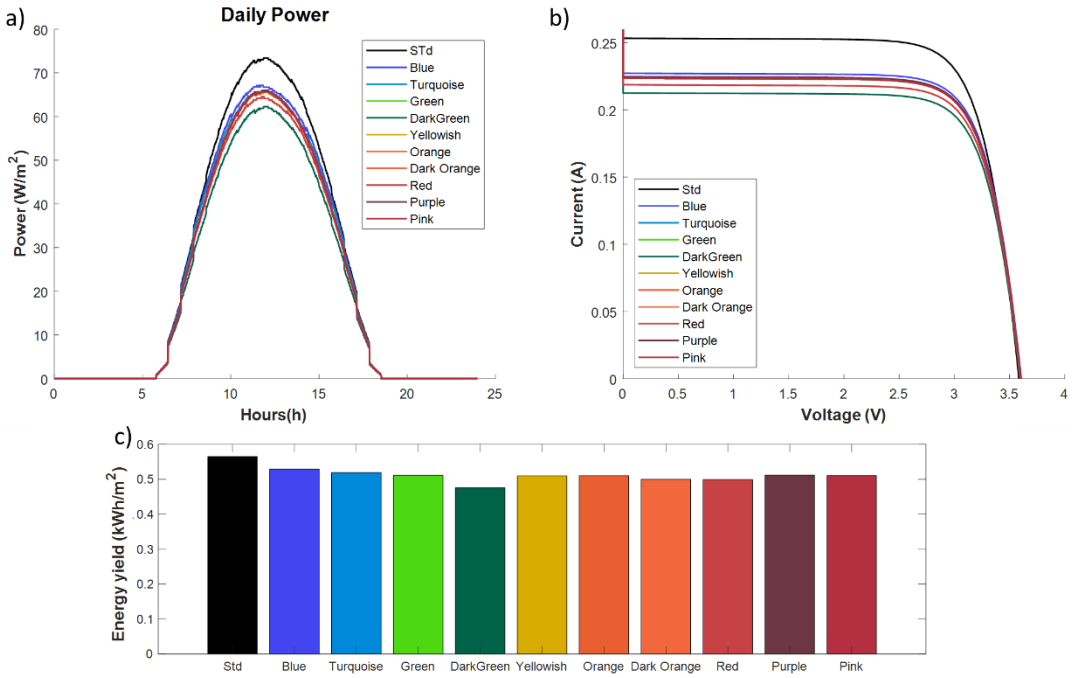

Figure 6.5 Figure a) Power distribution for the standard module and the 10 main colors on the 5th of May in Delft, Figure b) Efficiency distribution, Figure c) Energy yield difference for each color from the total energy yield of the standard module

Figure 6.6 illustrates the temperature results for a standard module in Dubai and the respecting temperature difference at the highest peak. The blue and turquoise colored modules have a similar performance in terms of temperature with a drop at around 6 degrees from the standard module. All in

all, the temperature drop of the remaining colors is lower than in Delft and this is because the selected day in Dubai has a lower irradiance than Delft ;Figure A 11 & Figure A 14. The dark green module has again the lowest temperature drop of 3 degrees.

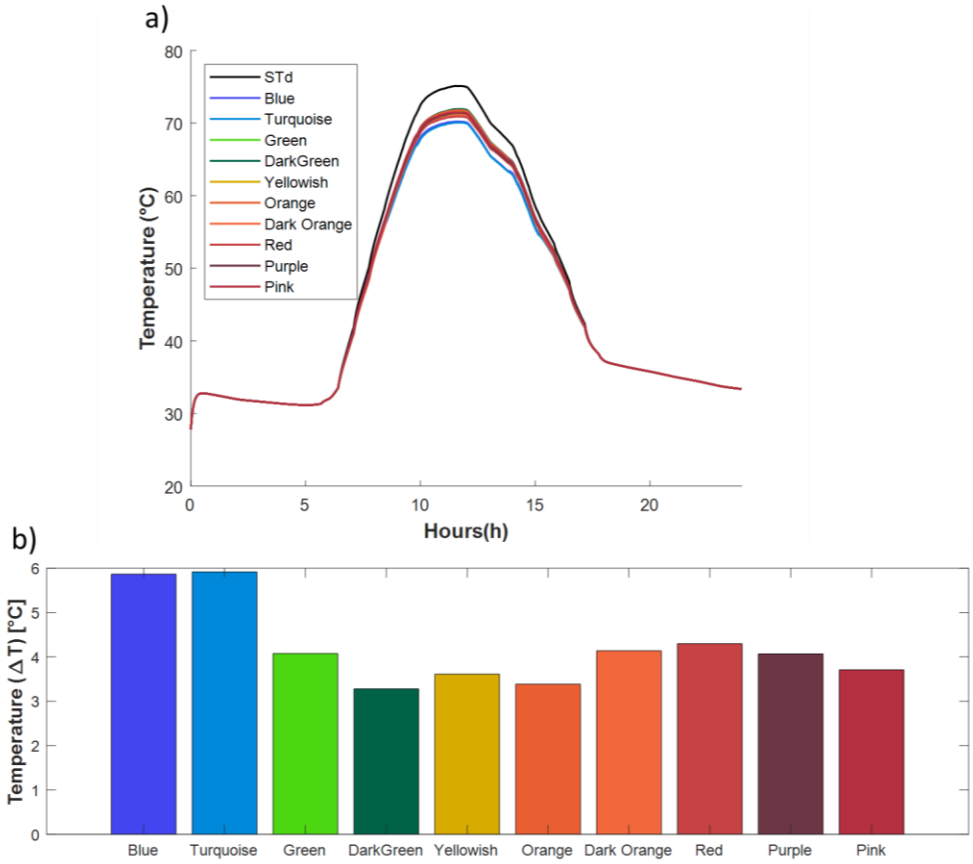

Figure 6.6 Figure a) Temperature distribution for the standard module and the 10 main colors on the 3rd of September in Dubai, Figure b) Temperature difference for each color from the maximum temperature of the standard module

From Figure 6.7 a) and c), the energy yield is approximately same for all the colored modules with a very small increase of the blue color and a slight drop from the dark green module. The standard module has an energy yield around 0.37 kWh/m^2 and the colored modules approximately 0.35kWh/m^2.

Regarding the I-V curve, the V_{oc} voltage is less than 3.5 Volts which is much lower than the previous plot of Delft; Figure 6.5. This is because the ambient temperature is very high ;Figure A 14 and that has an important impact on the overall cell temperature which is almost 10degrees higher at the peak than the standard module at Delft. The I_{sc} is the lowest for the dark green module whereas the remaining colored modules have a similar value. More specifically, the efficiency of the modules during the peak of irradiance is arround 17%; Figure A 15.

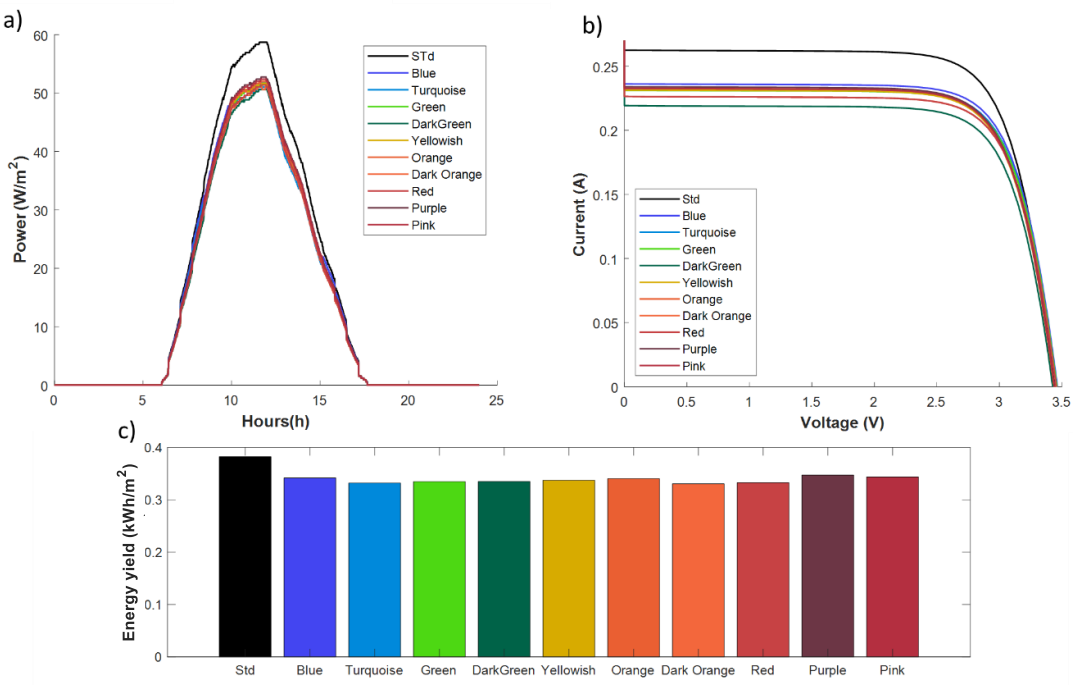

Figure 6.7 Figure a) Power distribution for the standard module and the 10 main colors on the 3rd of September in Dubai, Figure b) Efficiency distribution, Figure c) Energy yield difference for each color from the total energy yield of the standard module

6.4.1.2 Cloudy day

The temperature behavior of the modules for a cloudy day at Delft is illustrated in Figure 6.8. It can be concluded from both plot a) and b) that the effect of optic filters is insignificant for such scenario. This is because the optic filters are highly dependent on irradiance, therefore for significantly low irradiance the thermal effect of the optic filters is reduced. The irradiance information can be found in Figure A 16.

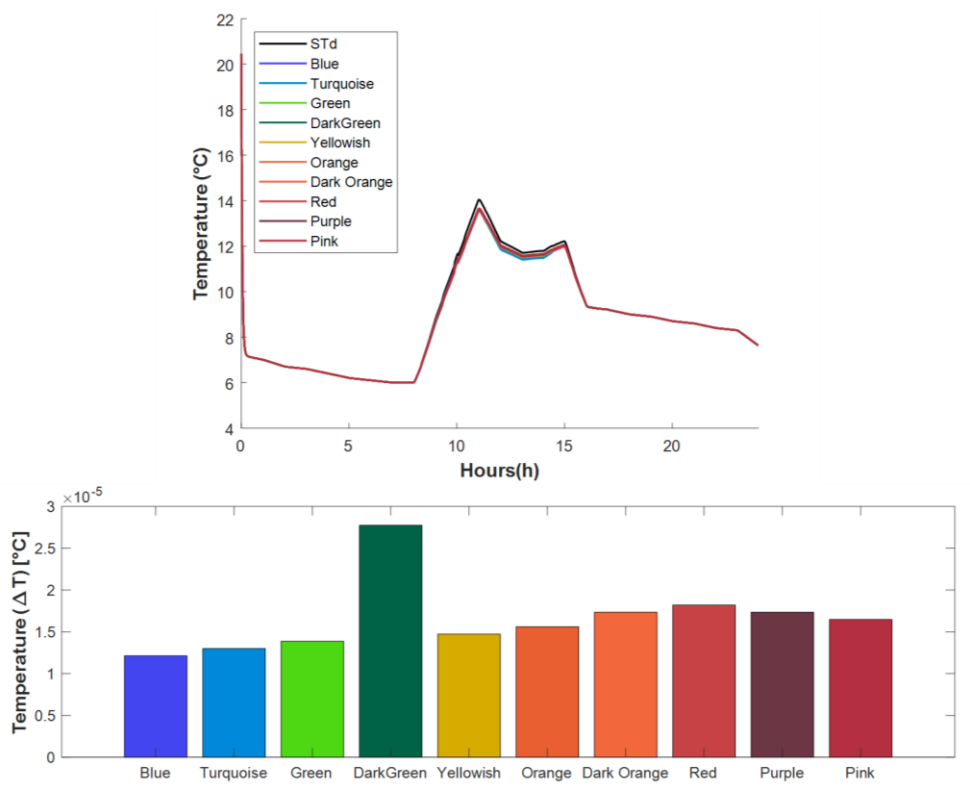

Figure 6.8 Figure a) Temperature distribution for the standard module and the 10 main colors on the 19th of January in Delft, Figure b) Temperature difference for each color from the maximum temperature of the standard module

From the power and energy yield results presented in Figure 6.9, the same observation can be concluded as the energy yield drop is very small from the standard module of 0.07kWh/m^2.

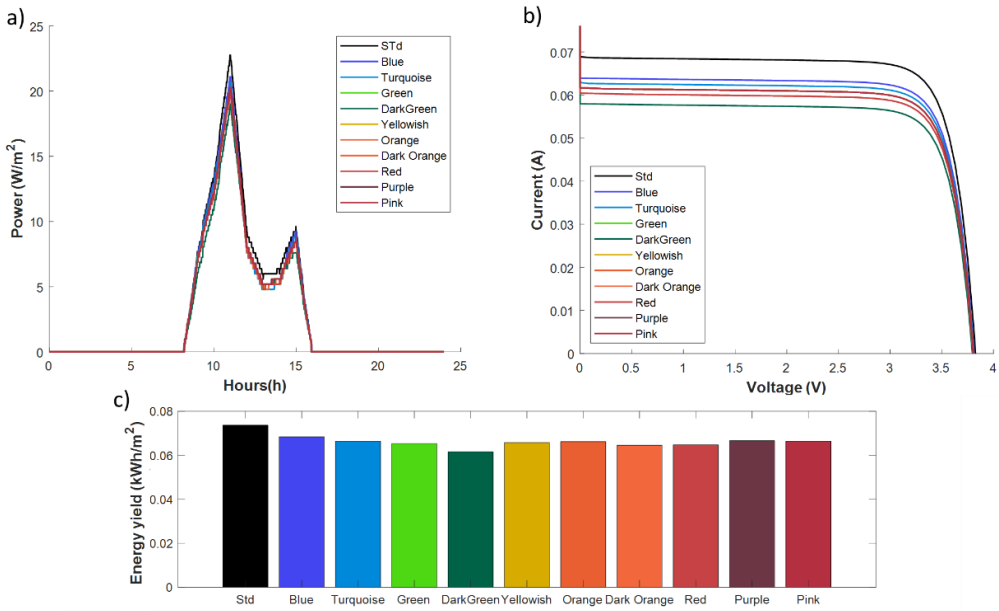

Figure 6.9 Figure a) Power distribution for the standard module and the 10 main colors on the 19th of January in Delft, Figure b) Efficiency distribution, Figure c) Energy yield difference for each color from the total energy yield of the standard module

The temperature behavior for the worst-case scenario in Dubai is illustrated in Figure 6.10. As have been noticed for the worst-case scenario in Delft, the value of temperature difference of the optic filters in Dubai has been decreased significantly. Although, the colored bar plot has the same trend as for the high temperature scenario but with smaller values. This behavior is also visible from Figure 6.11 where the energy yield is lower, and the trend is the same. More specifically, the energy yield of the standard module is around 0.12kwh/m^2. Further information for the weather data can be found from Figure A 19.

Comparing the two worst-case scenarios, Dubai has a relatively higher irradiance than Delft therefore, the performance of the optic filter is better, and differences can still be observed.

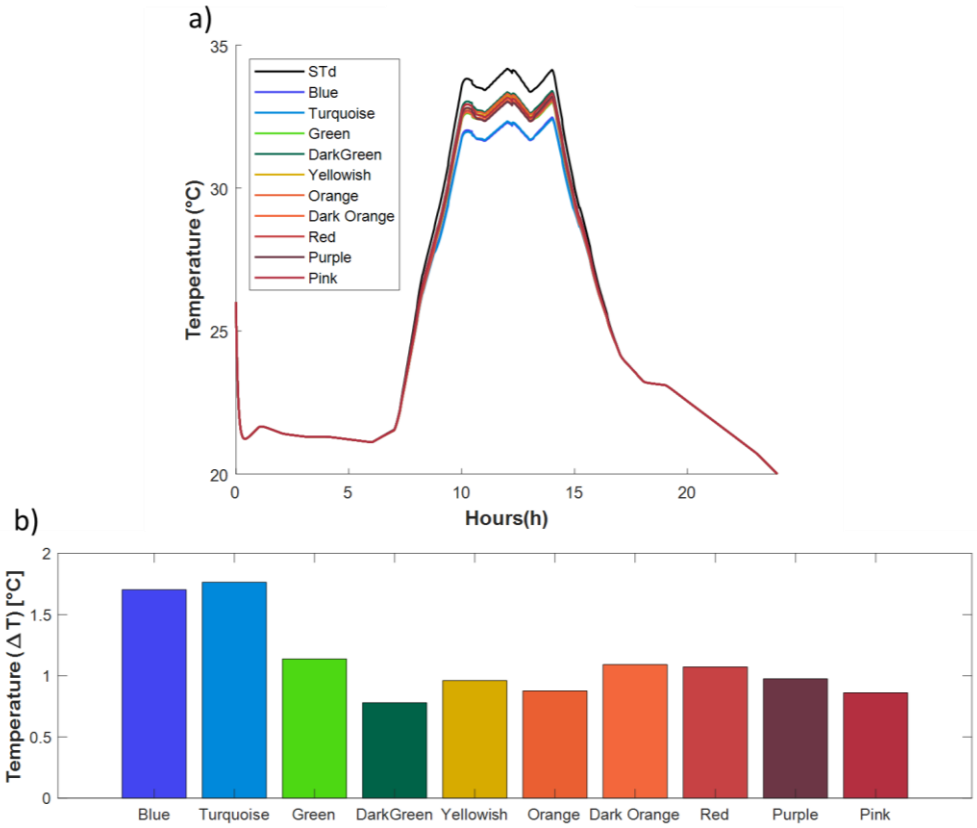

Figure 6.10 Figure a) Temperature distribution for the standard module and the 10 main colors on the 1st of January in Dubai, Figure b) Temperature difference for each color from the maximum temperature of the standard module

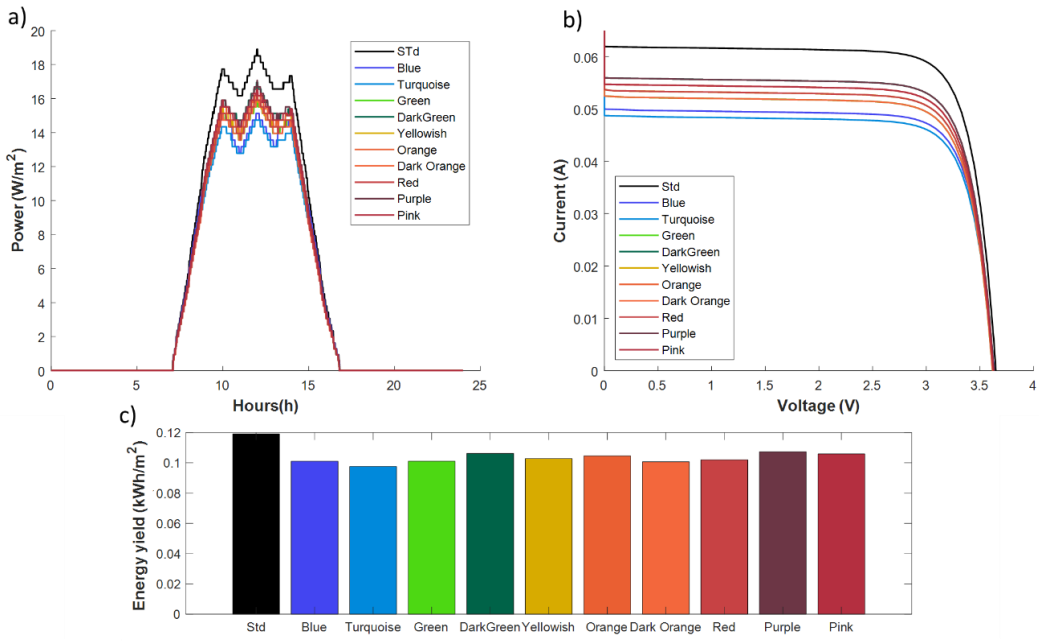

Figure 6.11 Figure a) Power distribution for the standard module and the 10 main colors on the 1st of January in Dubai, Figure b) Efficiency distribution, Figure c) Energy yield difference for each color from the total energy yield of the standard module

6.4.2 Energy yield

Figure 6.12 presents the energy yield results for the year of 2005 in Delft. The standard module has an energy yield of around 80kWh/m^2 whereas the remaining colored modules have similar energy yield results. More specifically, on average the selected optic filters have an energy yield value 10kWh/m^2 lower than the standard module. In Table 6-9 , the exact values of the energy yield are presented for all the mini modules. From these values, the dark green module has the worst performance of 68.90 kWh/m^2 energy yield whereas the blue module has highest of 72.86 kWh/m^2 energy yield.

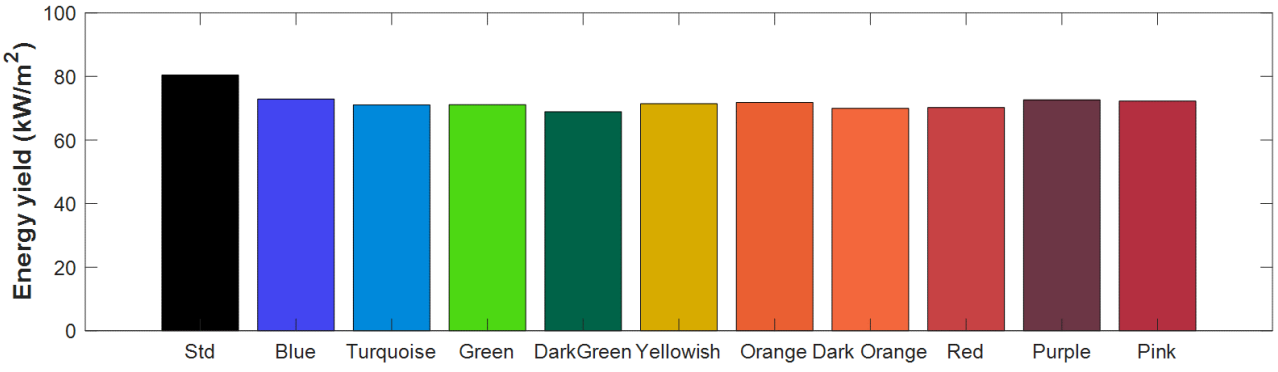

Figure 6.12 Energy yield per color for a free mounted module at 32 degrees in Delft

	Std	Blue	Turquoise	Green	Dark Green	Yellowish	Orange	Dark Orange	Red	Purple	Pink
kWh/m²	80.00	72.86	71.06	71.12	68.90	71.41	71.83	69.96	70.22	72.61	72.23

Table 6-9 Energy yield per color for a free mounted module at 32 degrees in Delft

In Figure 6.13 the energy yield values are presented for Dubai in 2005. As have been already concluded, the energy yield differences among the colored module is similar. More specifically, the energy yield of the standard module is approximately 150kWh/m^2 and the average drop of the colored modules is around 10kWh/m^2. The corresponding drop in Dubai is equal to just 6% of reduced yield where in Delft is equal to 12.5%. Table 6-9 shows the exact energy yield values for all the tested modules. The module with the weakest performance is again the dark green module with 125.72kWh/m^2 energy yield. The blue module has the highest energy yield of 133.35kWh/m^2

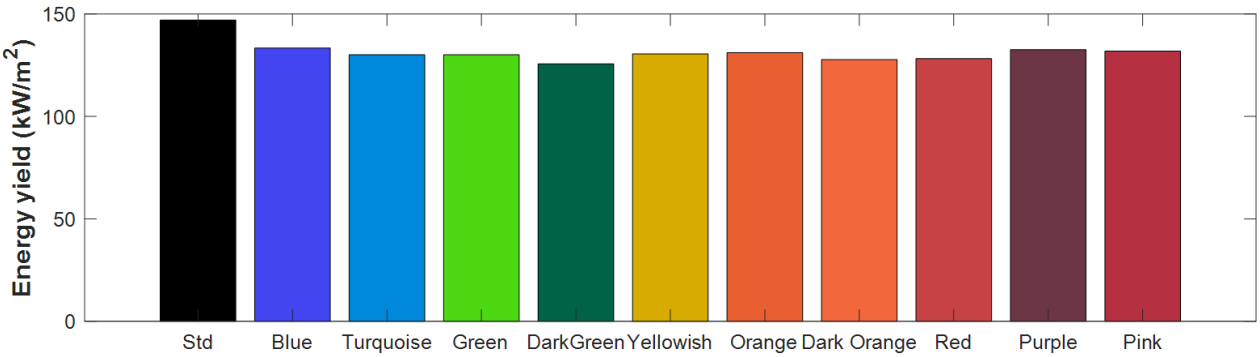

Figure 6.13 Energy yield per color for a free mounted module at 25 degrees in Dubai

	Std	Blue	Turquoise	Green	Dark Green	Yellowish	Orange	Dark Orange	Red	Purple	Pink
kWh/m²	146.91	133.35	130.1	130.00	125.72	130.59	131.10	127.77	128.25	132.62	131.8

Table 6-10 Energy yield per color for a free mounted module at 25 degrees in Dubai

6.5 Mounted module on a roof

In this section, the results for the configuration where the module is attached on a roof are presented. Temperature, power, energy yield results and I-V curves will be displayed for both standard and colored mini modules. Moreover, energy yield results will be discussed for the year of 2005.

6.5.1 Temperature results

6.5.1.1 Highest temperature

To start with, Figure 6.14 illustrates the temperature profiles of the modules and the temperature difference at the peak with respect to the standard module. Firstly, it is obvious that the temperature has been increased significantly compared to the free mounted module scenario. More precisely the working temperature has been increased almost 25 degrees compared to the previous scenario where the module was free mounted at 32 degrees[49]. That is because the convection at the back side is blocked and conduction takes place with the roof that is highly insulated. Therefore, the heat has no exit and eventually it leads to a significant increase of the module working temperature. Regarding the color bar, the same trend as for the scenario of free mounted module but scaled up is observed. The maximum temperature

drop is from the turquoise colored module at approximately 8.5 degrees and the minimum drop is 6.5 degrees from the dark green module.

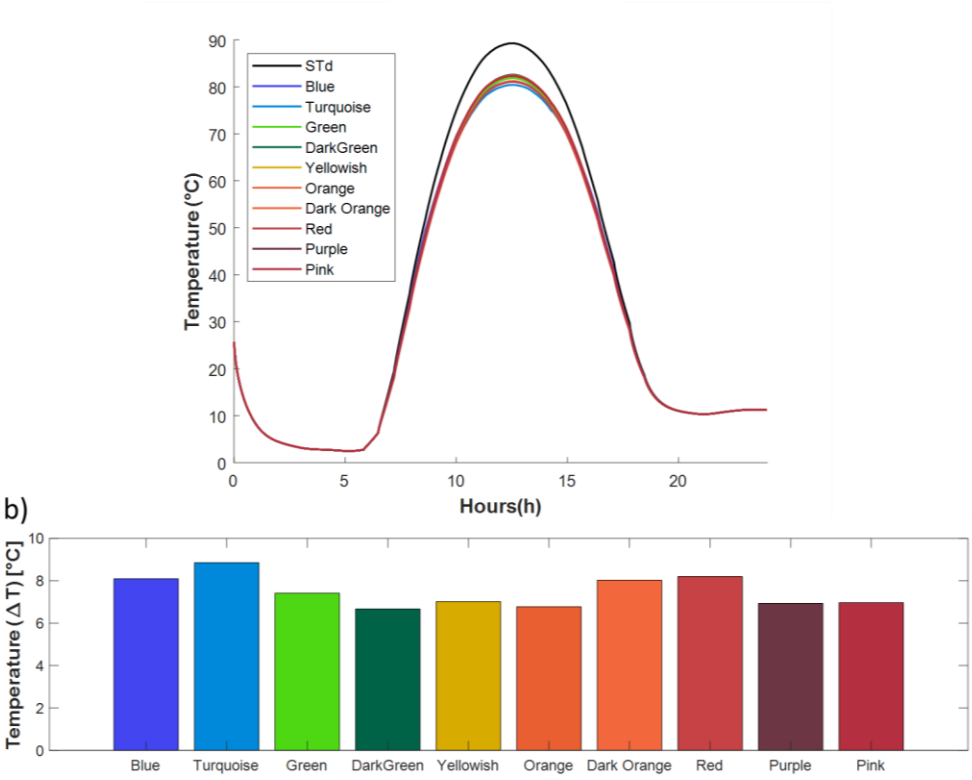

Figure 6.14 Figure a) Temperature distribution for the standard module and the 10 main colors on the 5th of May in Delft Figure b) Temperature difference for each color from the maximum temperature of the standard module

Figure 6.15 a) and c) present the power distribution and energy yield on the 5th of May. It can be noticed that indeed the energy yield has been decreased since the working temperature of the module has increased significantly. For relatively the same incident irradiance on the module, for the standard module the I_{sc} current has remain the same, although, the V_{oc} voltage has a drop from 3.7V to 3.3V; Figure 6.15 b) & Figure 6.5 b). Important to notice is that the colored modules are increasing the voltage from 3.3 to 3.42V whereas the current decreases to the power of 10^{-2}. Overall, the efficiency with colored modules increases from 16% to almost 16.3% as shown in Figure A 23. That is because for this case the drop of the temperature has a more significant impact on the I-V curve. Consequently, the total energy yield for each module has been decreased equally at around 1kWh/m^2.

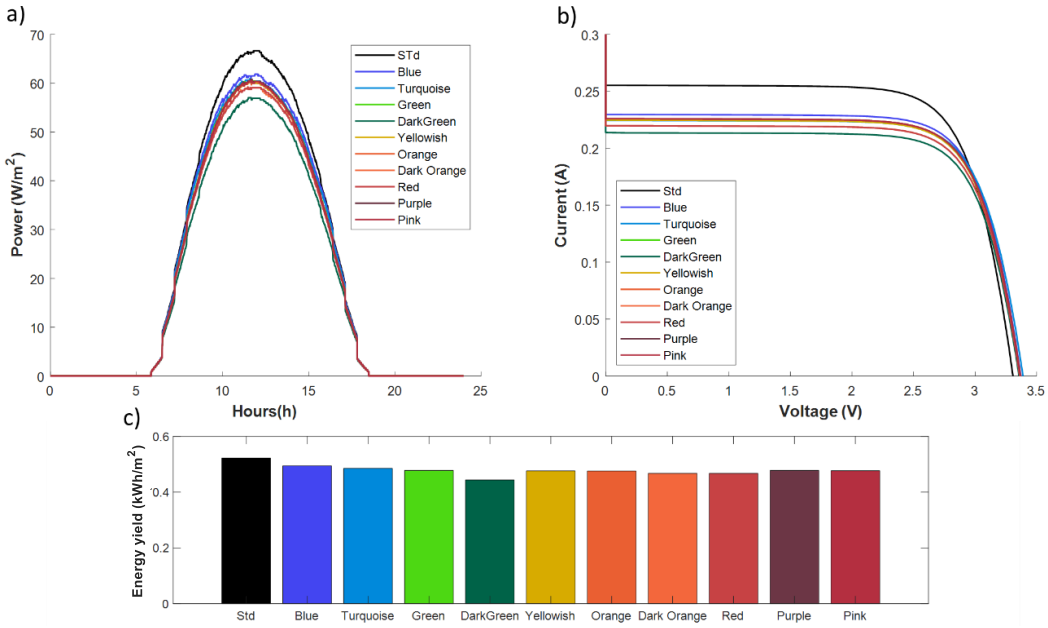

Figure 6.15 Figure a) Power distribution for the standard module and the 10 main colors on the 5th of May in Delft, Figure b) Efficiency distribution, Figure c) Energy yield difference for each color from the total energy yield of the standard module

Figure 6.16 shows the results for the installation in Dubai on the 3rd of September. The same observation can be observed, since the temperature increase is very high when the module is attached on the roof. More specifically, the temperature at the peak has increased almost 20degrees. In Figure 6.16 c) the same trend is observed as for the free mounted module, although the temperature decrease has been scaled up. The turquoise color module decreases the temperature by 8.5 degrees whereas the dark green color module at around 6 degrees.

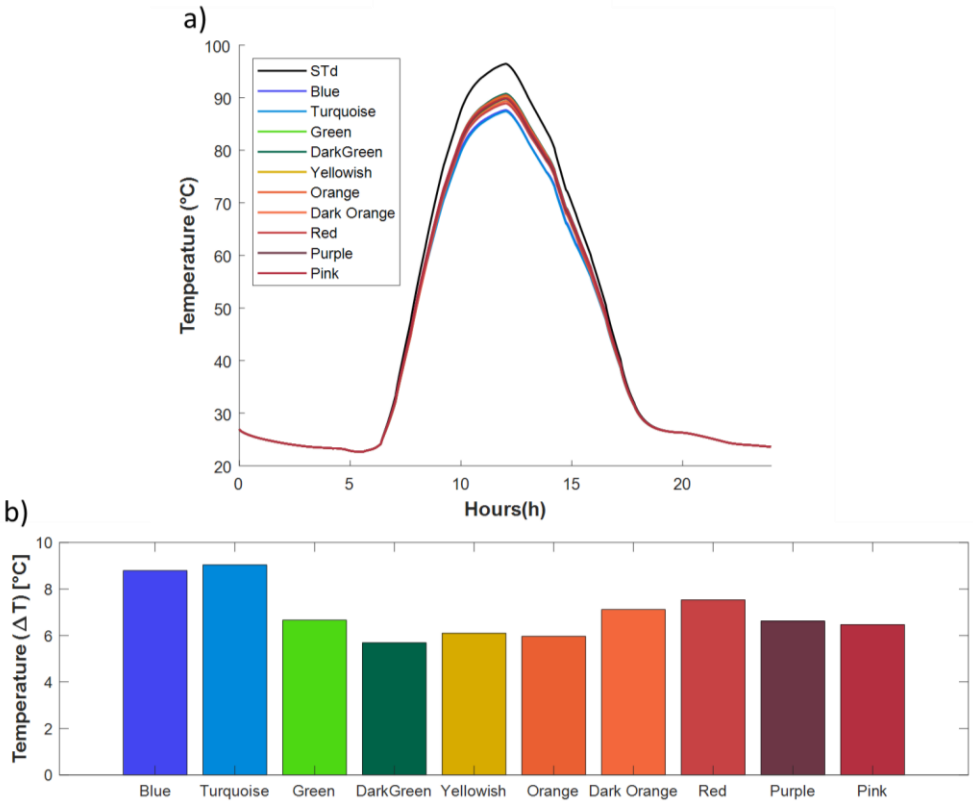

Figure 6.16 Figure a) Temperature distribution for the standard module and the 10 main colors on the 3rd of September in Dubai, Figure b) Temperature difference for each color from the maximum temperature of the standard module

Figure 6.17 a) and c) show the power and energy yield for this day in Dubai. Same results are observed since the energy yields has been decreased compared to the according free mounted modules. More precisely, the voltage has dropped from 3.4 V to 3.2 V for the standard module. The colored modules have a positive effect on the voltage of around 0.1V increase compared to the standard module. Therefore, since the increase of voltage is more than the decrease of I_{sc}, the overall efficiency is increasing with the colored modules from 15.8% to 16%. Overall, the energy yield for the same day has decreased approximately 1kWh/m^2 and the same trend among colors is observed compared to the free mounded module.

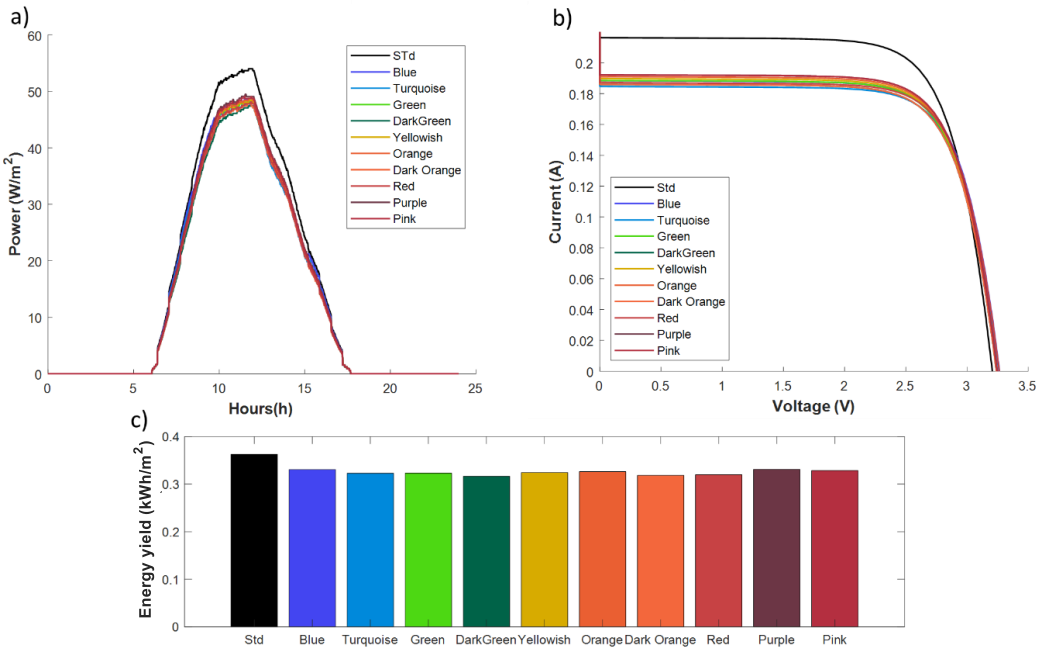

Figure 6.17 Figure a) Power distribution for the standard module and the 10 main colors on the 3rd of September in Dubai, Figure b) Efficiency distribution, Figure c) Energy yield difference for each color from the total energy yield of the standard module

6.5.1.2 Cloudy day

Figure 6.18 illustrates the temperature results for the worst-case scenario in Delft for a mounted module on a roof. The optic filter performance is influence from the decrease of the irradiance. Although, higher temperatures are observed compared to the worst-case scenario of the free mounted module Figure 6.10.

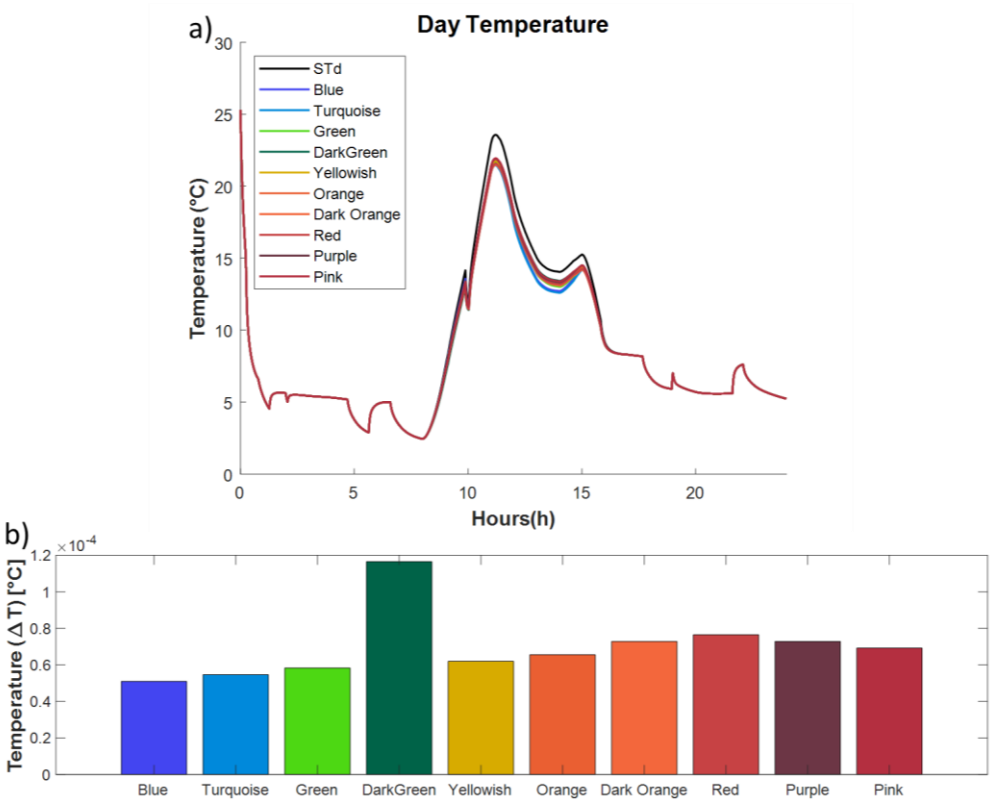

Figure 6.18 Figure a) Temperature distribution for the standard module and the 10 main colors on the 19th of January in Delft, Figure b) Temperature difference for each color from the maximum temperature of the standard module

From the power and energy yield of Figure 6.11, it can be observed that the drop of the irradiance has a significant impact on the total energy of the day. More specifically, the I_{sc} current of the standard module drops from 0.26 A to 0.07 A. Similar results are observed as for the worst-case scenario of a free mounted module; Figure 6.9. The average efficiency of the all the modules is around 19%; Figure A 29.

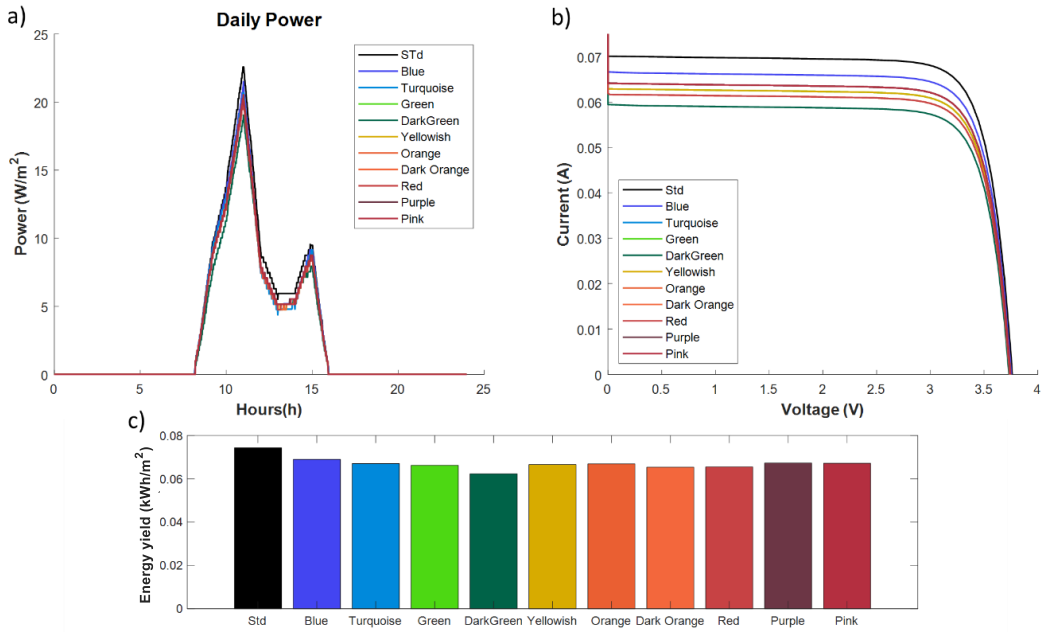

Figure 6.19 Figure a) Power distribution for the standard module and the 10 main colors on the 19th of January in Delft, Figure b) Efficiency distribution, Figure c) Energy yield difference for each color from the total energy yield of the standard module

Figure 6.20 shows the temperature results for a mounted module on a roof on the 1st of January in Dubai. The effect of irradiance has decreased significantly the temperature for all the modules, although the performance of the optic filters is not influenced as much as the according worst-case scenario in Delft. This is because the irradiance is much higher at the peak compared to Delft; Figure A 28 & Figure A 31. More precisely, the maximum temperature of the day is still relatively high, and the standard module reaches almost 45 degrees which is 10 degrees higher than the according scenario of a free mounted module. In addition, the maximum temperature drop is 5 degrees for the blue and turquoise colored modules.

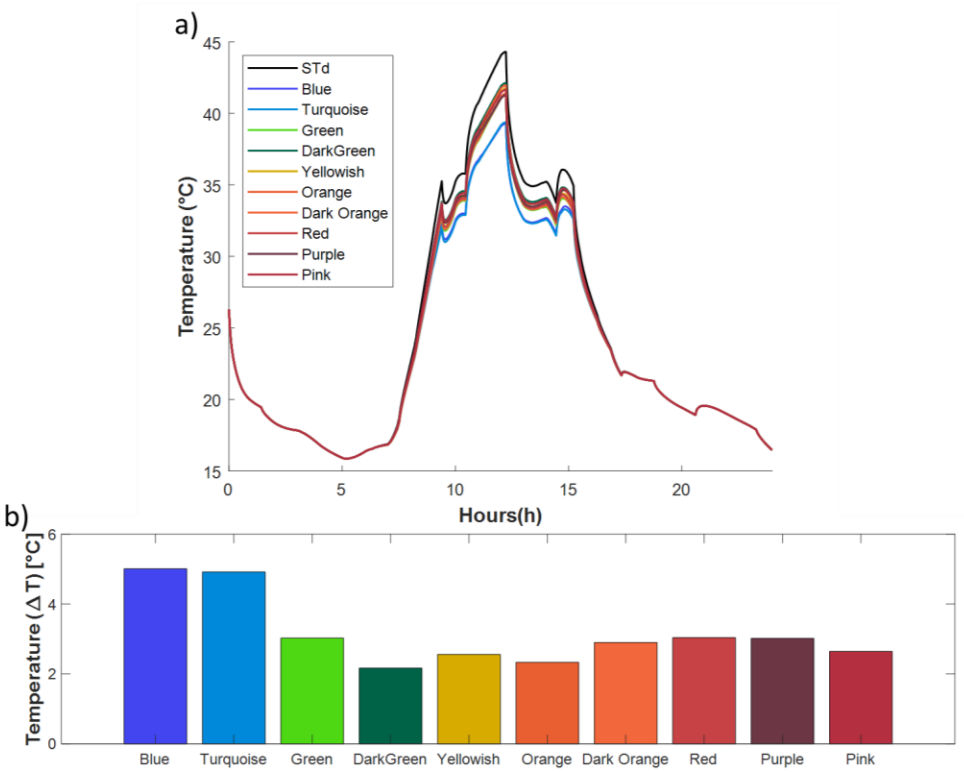

Figure 6.20 Figure a) Temperature distribution for the standard module and the 10 main colors on the 1st of January in Dubai, Figure b) Temperature difference for each color from the maximum temperature of the standard module

Figure 6.21 a) and c) shows the power and energy yield distribution. The energy yields for all the modules have a drop compared to the free mounted modules. A small difference can be observed from the I-V curve Figure 6.21 b) where the voltage drops to 3.55 Volts. Although, no differences on the V_{oc} can be observed from the different optic filters. Therefore, the differences between the energy yields from the standard module are due to the I_{sc} drop. The overall average efficiency is similar for all the modules at around 18%;

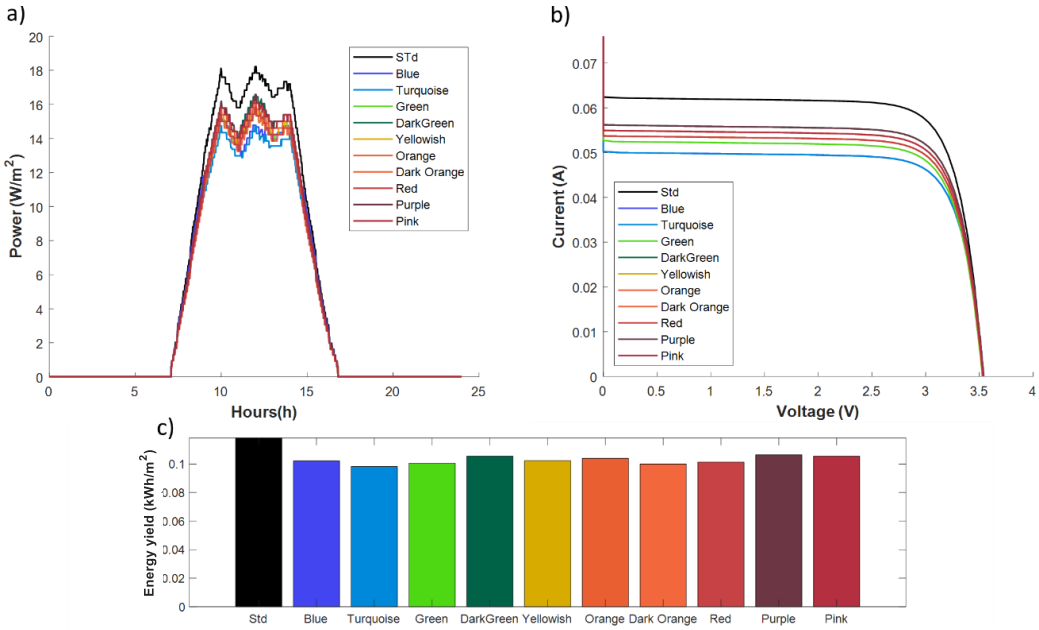

Figure 6.21 Figure a) Power distribution for the standard module and the 10 main colors on the 1st of January in Dubai, Figure b) Efficiency distribution, Figure c) Energy yield difference for each color from the total energy yield of the standard module

6.5.2 Energy yield

Figure 6.22 shows the energy yield of the colored modules attached on a roof in Delft for the whole year. From Table 6-11 the exact values can be found. The total energy yield of the standard mini module is 79.16 kWh/m^2 and the lowest energy yield comes from the dark green module and is 67.89 kWh/m^2. Overall, the energy yield difference among the different colored module is relatively small and maintains the same trend as for the free mounded module. Although, compared to the energy yields observed for the free mounded module, the corresponding energy yield for each presented module is reduced. That is because the attached module as it has no convection at the back side, it is exposure to higher working temperatures during the year, which can reach values of 25 degrees higher as it was confirmed in Figure 6.14 .

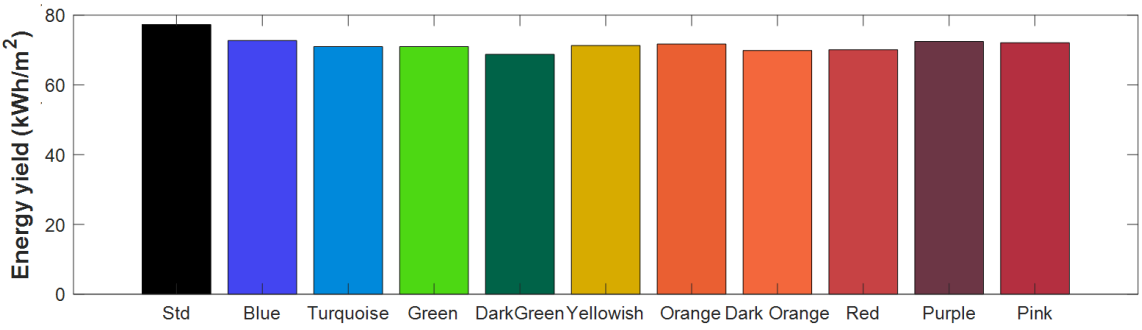

Figure 6.22 Energy yield per color for a module attached on a roof in Delft

	Std	Blue	Turquoise	Green	Dark Green	Yellowish	Orange	Dark Orange	Red	Purple	Pink
kWh/m²	79.16	71.85	70.13	70.12	67.89	70.40	70.81	69.02	69.25	71.57	71.20

Table 6-11 Energy yield per color for a module attached on a roof in Delft

The corresponding Figure 6.23, presents the energy yield results for the modules attached on a roof in Dubai whereas in Table 6-12, the exact values can be found. All in all, the same observations can be made, since also for Dubai the energy yields have been decreased compared to the according free mounted modules. As explained before, that is because the module is experiencing higher working temperatures. The standard module delivers 141.20 kWh/m^2 for the according year and the dark green module still produces the least amount of energy. Comparing the different colored modules, the same trend is observed as for the free mounted module, although, the energy yield is smaller for each module.

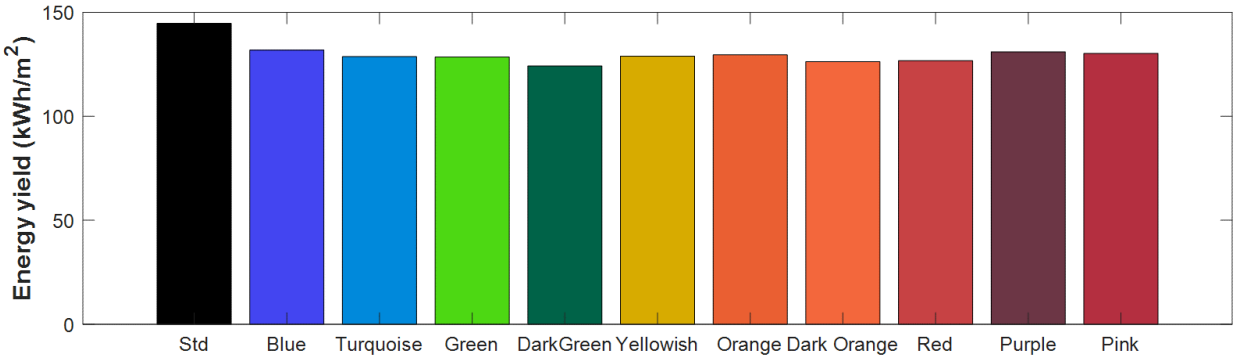

Figure 6.23 Energy yield per color for a module attached on a roof in Dubai

	Std	Blue	Turquoise	Green	Dark Green	Yellowish	Orange	Dark Orange	Red	Purple	Pink
kWh/m²	141.20	129.20	126.20	125.80	121.6	126.20	126.80	123.70	124.10	128.20	127.50

Table 6-12 Energy yield per color for a module attached on a roof in Dubai

Comparing both energy yields in Dubai and Delft, the colored modules behave the same with respect to one another although, in Dubai the overall energy is much higher for all the modules. Moreover, comparing the different colors, it can be concluded that the dark green module delivers the least amount of energy while the blue module delivers the highest. However, the energy yields of the purple and pink modules do not deviate much from the energy yield of the blue module. The remaining colors have a relatively similar behavior. In addition, it can be noticed that indeed the performance of the optic filters changes for each location based on the temperature and irradiance although, the trend between the colors remains the same.

6.6 Tilted air gap

In this chapter, the results for modules attached on a roof with an air gap are discussed for both colored and standard modules. This chapter aims to investigate if the air gap will change the performance of the modules and eventually decrease the working temperature. Before an explanation of the selected air gap thickness will be given. The results are presented in a way that comparison of a standard module and colored module is illustrated.

6.6.1 Selection of the air gap

For the selection of the air gap thickness, energy yield results have been simulated for both locations for air gaps between 0.10, 0.20, 0.30, 0.40 and 0.5 m as shown in Table 6-13 and Table 6-14. As can be seen from the tables, the 0.5 m air gap gives the highest energy yield for both locations. That is because the convection heat exchange is the highest as the forced convection for that thick air gap is presented for the wind speed equal to the ambient. The 0.1m air gap leads to the lowest energy yield since the free convection dominates over forced convection. That is because, both locations are relatively windy, and forced convection can maintain lowest working temperatures than the natural convection. It can be also observed, that as soon as the thickness increases to 0.2m the energy yield is smaller since the free convection has been decreased and the wind speed in the channel is still very small compared to the ambient. As soon as the air gap continues to increase, the forced convection increases and the natural convection decreases. From 0.3m the forced convection already overcomes the natural convection.

Thickness air gap (m)	0.1	0.2	0.3	0.4	0.5
Energy Yield (kWh/m^2)	144.6144	144.5756	144.9089	145.2398	145.5320

Table 6-13 Energy yield output for a year in Dubai 2005 based on different air gaps

Thickness air gap (m)	0.1	0.2	0.3	0.4	0.5
Energy Yield (kWh/m^2)	79.2126	79.0471	79.1208	79.2433	79.3555

Table 6-14 Energy yield output for a year in Delft 2005 based on different air gaps

At this point, it can be concluded that in terms of energy yield, the optimum choice is the air gap of 0.5m. However, if the aesthetics parameter is considered, the overall optimum choice is the air gap of 0.1m. The air gap thicknesses of 0.1 and 0.2m can be considered as more aesthetically pleasing and the air gap of 0.1m is better since it is application is more aesthetic and it leads to less energy yield losses than 0.2. On the other hand, from values of 0.3m until 0.5m air gap, the installation will be very limited. Considering therefore those parameters, the selected air gap is 0.1m since it combines in an optimum way aesthetics and energy yield. The 0.1m air gap will be used also for the façade scenario with air gap.

6.6.2 Temperature results

6.6.2.1 Highest temperature

Figure 6.24 shows the temperature results for the standard and colored mini modules on the 5th of May in Delft. As a first observation, the working temperature of the modules has decreases significantly

compared to the scenario where the module was attached on a roof. More specifically, the peak temperature of the standard and colored modules has decreased almost 20degrees Celsius. This is a very important conclusion as the working temperature is very important to remain as low as possible in order to maintain a good performance of the modules and maximize as much as possible the energy yield.

Another remark, is that the trend of the temperature drop from the standard module is the same as for the previous scenarios but is has been decreased almost 2degrees Celsius compared to the according plot for the attached on a roof scenario of Figure 6.16. The highest temperature decrease is observed for the turquoise mini module with 7 degrees and the smallest decrease of 5 degrees occurs with the dark green module.

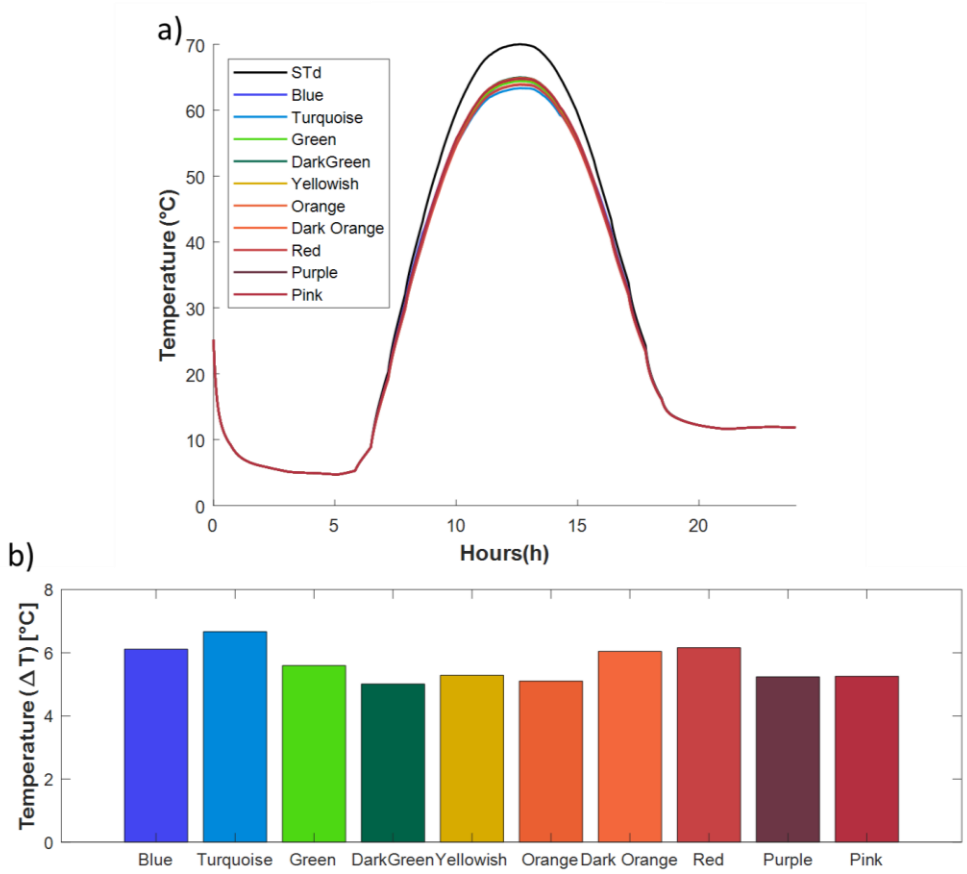

Figure 6.24 Figure a) Temperature distribution for the standard module and the 10 main colors on the 5th of May in Delft Figure b) Temperature difference for each color from the maximum temperature of the standard module

From the power distribution plot and energy yield graph from Figure 6.25 a) and c) it can be noticed that the air gap has a positive impact on the energy yield. More precisely, the energy yield of the standard module has increased from 0.35kWh/m^2 Figure 6.16, to almost 0.55 kWh/m^2. The same can be observed for the remaining colored modules as the energy yield for all the colors has been rise. The same trend of temperature difference is still observed, with the blue colored module producing 0.5kWh/m^2 and the dark green 0.45kWh/m^2 which is the lowest value from the bar plot. The remaining colors have values of energy yield in between. Regarding the I-V curve from Figure 6.25 c), the voltage has been increased for the standard module from 3.3V for an attached module to 3.5V with an air gap. With the optic filters, the

voltage increases to 3.6V and the I_{sc} drops with a factor of 10^{-2}. Overall, the efficiency has been increased to 17% and is relatively the same for all the modules.

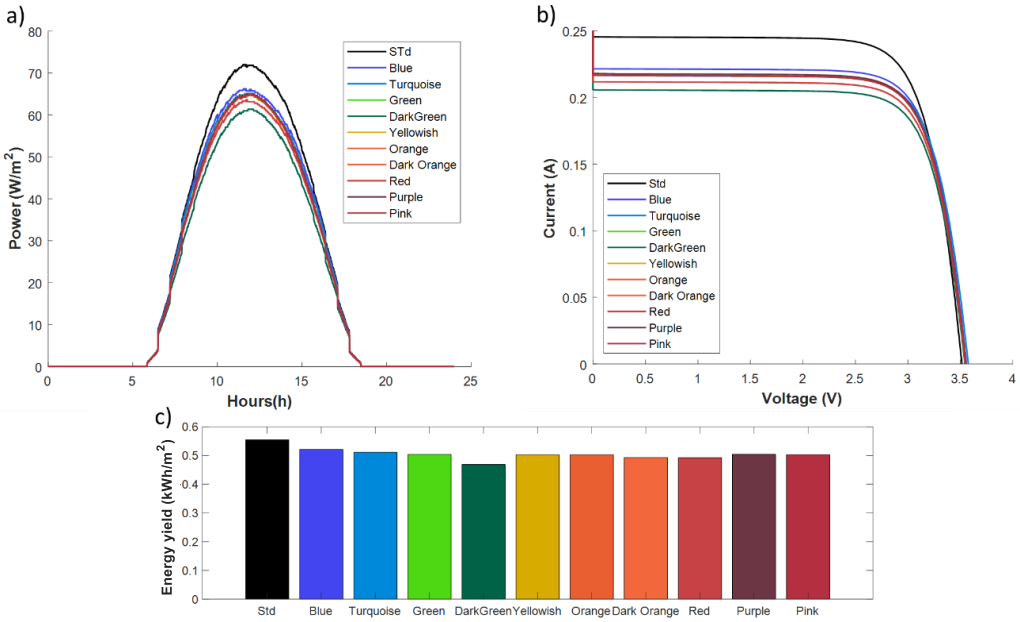

Figure 6.25 Figure a) Power distribution for the standard module and the 10 main colors on the 5th of May in Delft, Figure b) Efficiency distribution, Figure c) Energy yield difference for each color from the total energy yield of the standard module

Figure 6.26 illustrates the according results for Dubai location. As have been noticed before, the working temperature of the modules decreases significantly up to 15 degrees compared to the according values when the module is attached on a roof; Figure 6.17. Regarding Figure 6.26 b), the trend of the bar plot among the different colored modules remains the same as for the previous scenarios in Dubai, with a decrease of 2 degrees compared to the plot of attached module. The turquoise colored module decreases the most the temperature up to 7 degrees where the dark green module decreases the working temperature by 4 degrees.

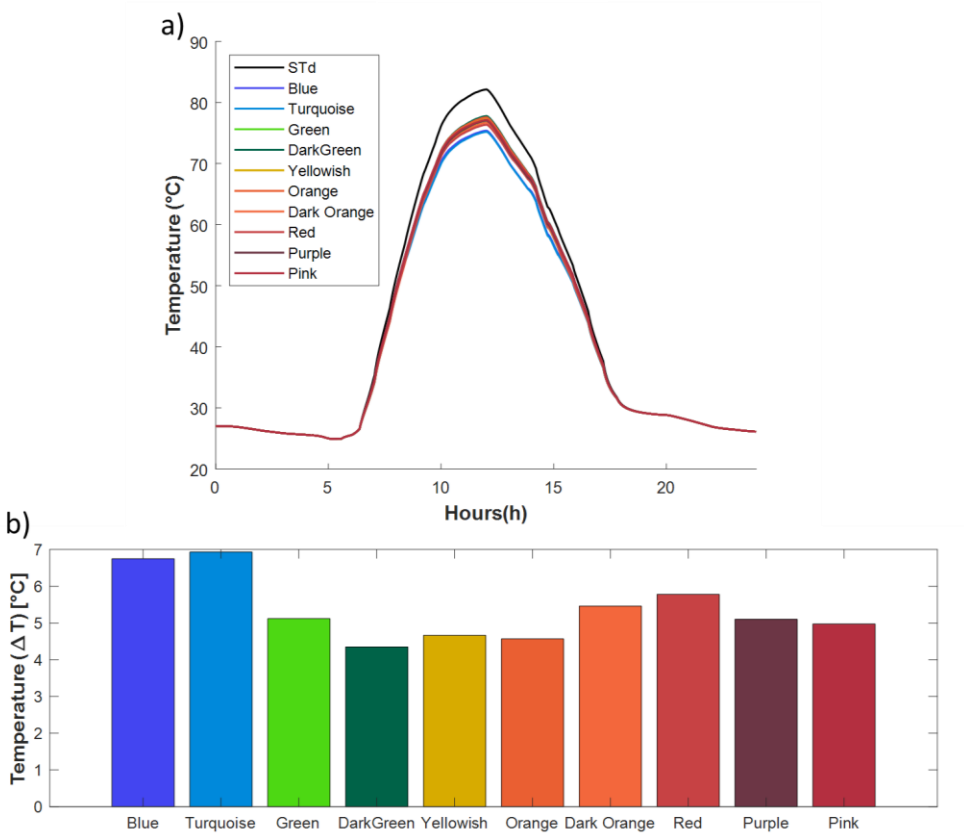

Figure 6.26 Figure a) Temperature distribution for the standard module and the 10 main colors on the 3rd of September in Dubai Figure b) Temperature difference for each color from the maximum temperature of the standard module

In Figure 6.27 a) and b) the corresponding power distribution and energy yield for a day are presented. The energy yield for the standard module increases from 0.35kWh/m^2 when it is attached to almost 0.38kWh/m^2. The energy yield plot remains with the same trend as the previous presented plots in Dubai with the dark green module generating the least amount of energy. The remaining colors have energy yield values in between. The V_{oc} of the standard module has been increased to 3.4 V where the colored modules are increasing the voltage at around 0.05 V. The overall efficiency is around 16% for all the modules during the noon.

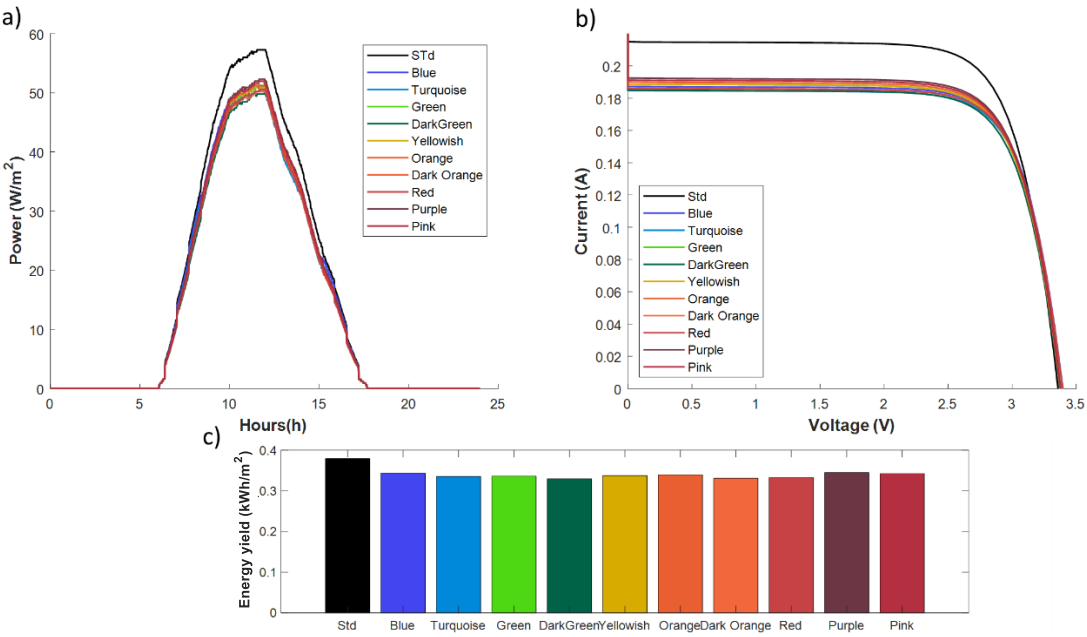

Figure 6.27 Figure a) Power distribution for the standard module and the 10 main colors on the 3rd of September in Dubai, Figure b) Efficiency distribution, Figure c) Energy yield difference for each color from the total energy yield of the standard module

6.6.2.2 Cloudy day

In Figure 6.28 a) and b) temperature information are presented for the worst-case scenario in Delft for a module attached on a roof with air gap. As it was noticed from the aforementioned worst-case scenarios, the impact of the corresponding optic filters on the working temperature of the module is insignificant when the irradiance is very low. Even though, the dark green module has the highest difference of temperature drop albeit small.

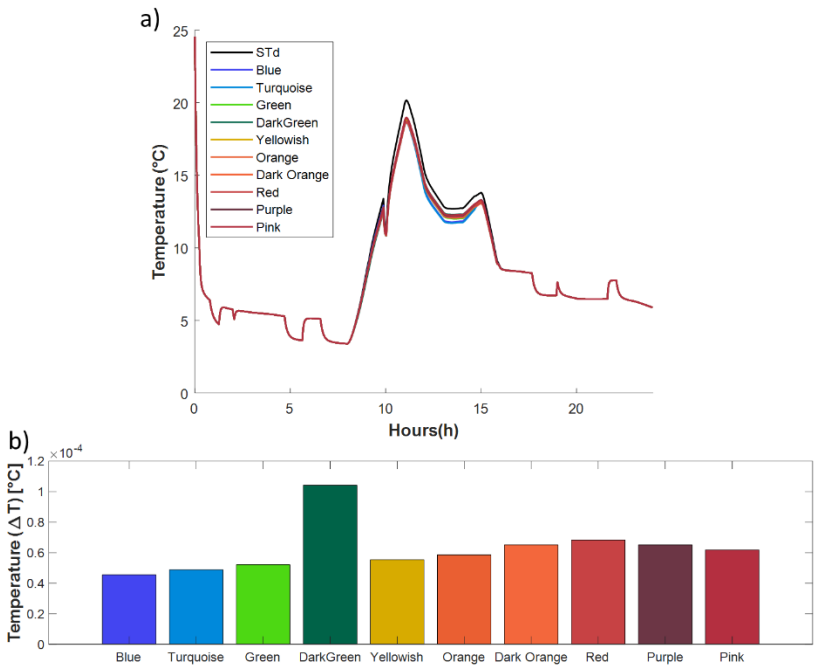

Figure 6.28 Figure a) Temperature distribution for the standard module and the 10 main colors on the 19th of January in Delft Figure b) Temperature difference for each color from the maximum temperature of the standard module

The differences observed in terms of energy yield for the colored modules are insignificant compared to the energy yield of the standard module; Figure 6.29 a) and c). Since the effect of colored modules on the temperature is very small, the result V_{oc} remains the same as presented in Figure 6.29 b).On the other hand, a minimal decrease can be observed in the I_{sc} values where the standard module has 0.09 A and the dark green module 0.06 A.

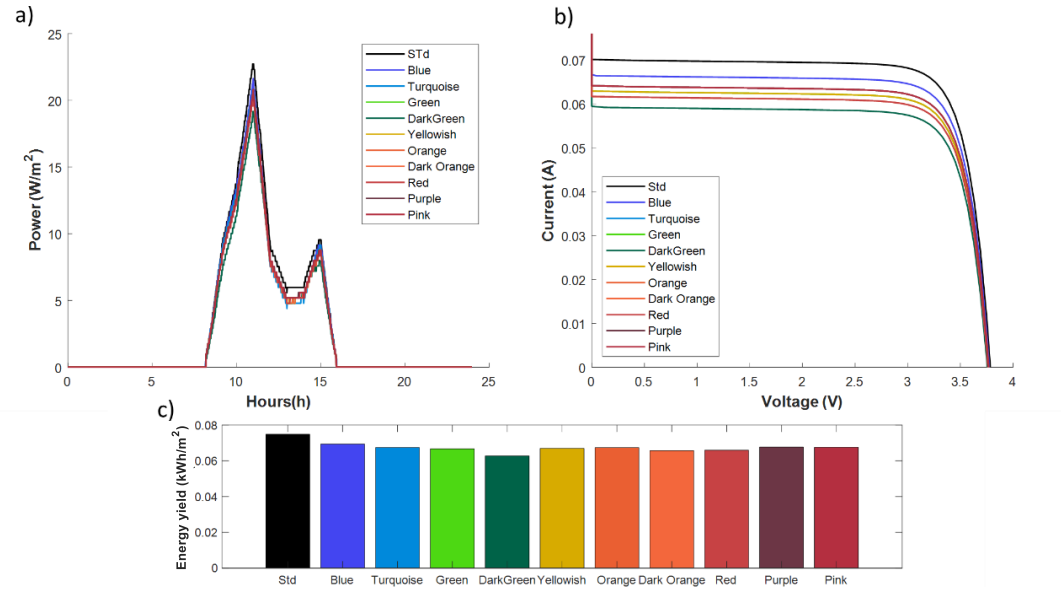

Figure 6.29 Figure a) Power distribution for the standard module and the 10 main colors on the 19th of January in Delft, Figure b) Efficiency distribution, Figure c) Energy yield difference for each color from the total energy yield of the standard module

For the worst-case scenario in Dubai since the irradiance is relatively high, differences on the working temperature can be observed as illustrated in Figure 6.30. Comparing the behavior of the attached module and the results with the implementation of air gap, the maximum of the working temperature of the standard mini module has decreased around 5 degrees where the effect of the optic filters has the same trend but scaled approximately by 1 degree.

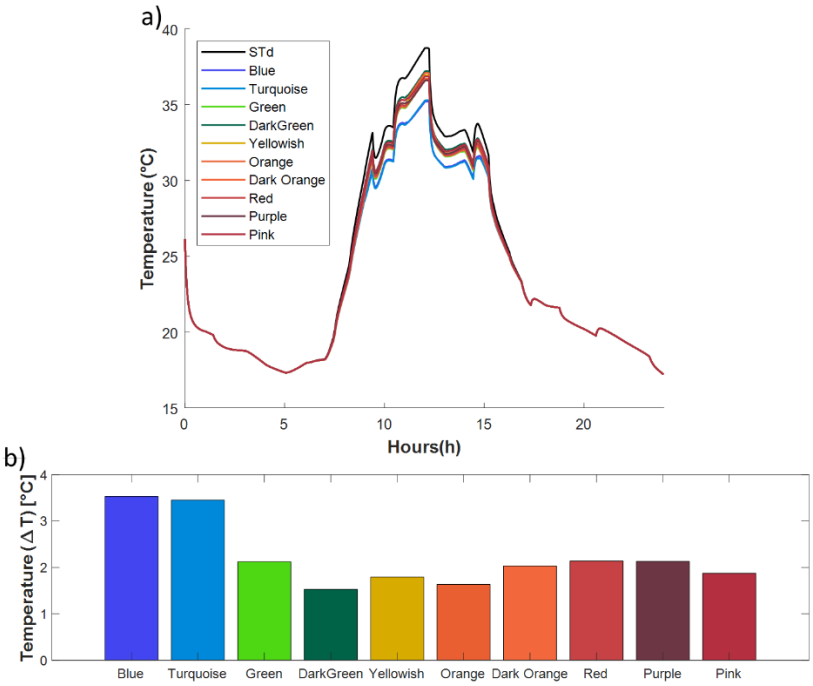

Figure 6.30 Figure a) Temperature distribution for the standard module and the 10 main colors on the 1st of January in Delft Figure b) Temperature difference for each color from the maximum temperature of the standard module

Figure 6.31 a), b) and c) present the power, energy yield and I-V for the worst-case scenario in Dubai. It can be concluded that a small effect among the optic filters is observed. The standard module has energy yield of around 0.12 kWh/m^2 where the lowest energy yield of 0.09 kWh/m^2 is delivered from the turquoise color. From the I-V curve small differences can be observe in terms of I_{sc} as the V_{oc} remains the same for all the modules.

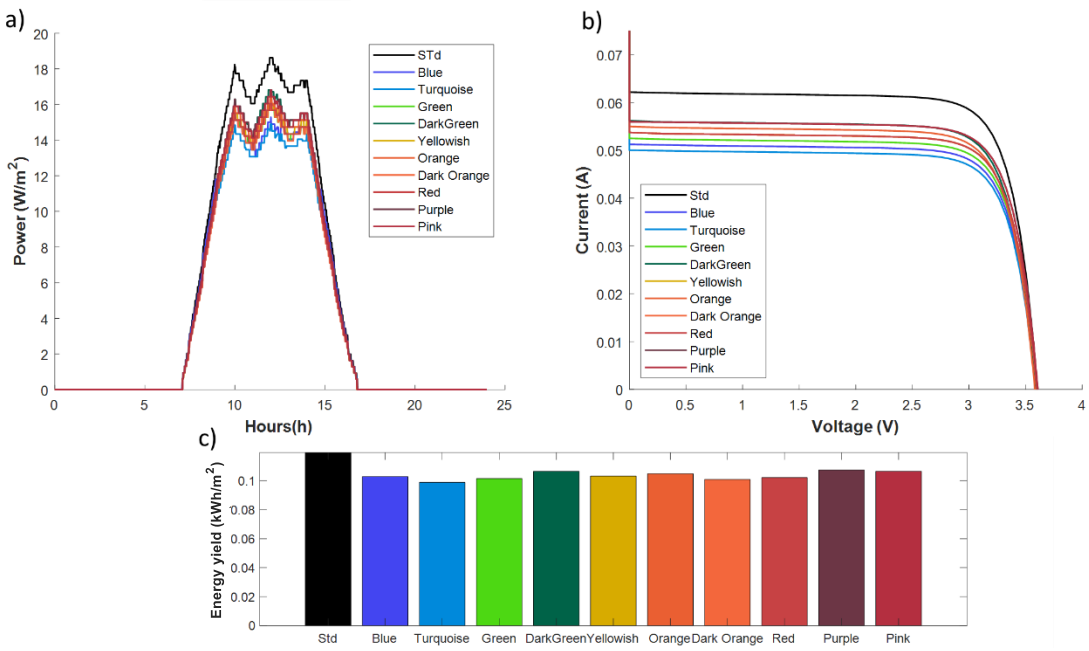

Figure 6.31 Figure a) Power distribution for the standard module and the 10 main colors on the 1st of January in Dubai, Figure b) Efficiency distribution, Figure c) Energy yield difference for each color from the total energy yield of the standard module

6.6.3 Energy yield

In this chapter the energy yield results for the whole year of 2005 are presented for Delft and Dubai for the different colored and standard modules. The Figure 6.32 and Figure 6.33 show in colored bars the generated energy yield for Delft and Dubai respectively where from Table 6-15 and Table 6-16 the exact values are presented.

Generally, the energy yield is higher than the scenario where the module is attached on a roof without air gap. More precisely, the standard module generates 79.71kWh/m^2 when the air gap is implemented and 79.16kWh/m^2 when no air gap is considered. All in all, the general behavior among the optic filters is observed although the plot is scaled up in terms of generated energy compared to the Figure 6.22. The color with the best performance is again the blue mini module with an energy yield of 72.68 kWh/m^2 and the dark green color still delivers the least amount of energy of 68.74 kWh/m^2.

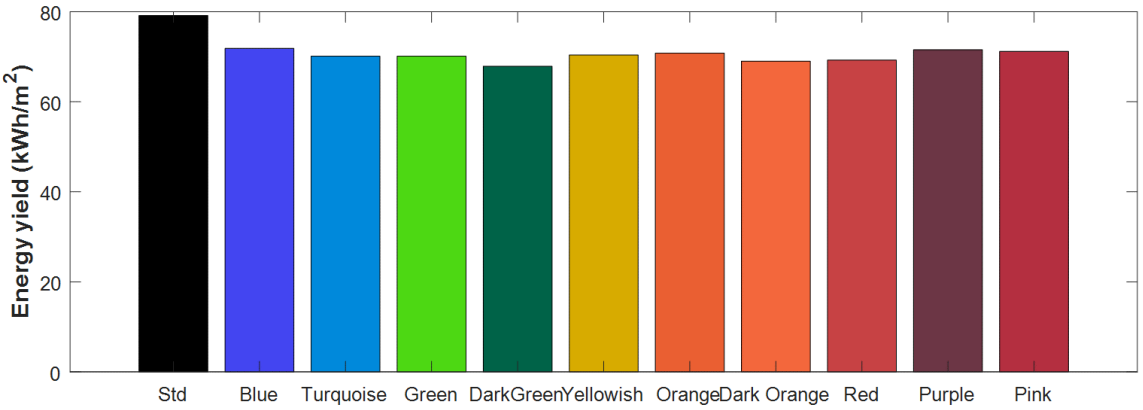

Figure 6.32 Energy yield per color for a module attached on a roof with air gap in Delft

	Std	Blue	Turquoise	Green	Dark Green	Yellowish	Orange	Dark Orange	Red	Purple	Pink
kWh/m²	79.71	72.68	70.94	70.98	68.74	71.24	71.7	68.84	70.08	72.44	72.08

Table 6-15 Energy yield per color for a module attached on a roof in Delft

Regarding the energy yield of the modules installed in Dubai, the energy yield is much higher compared to Delft. This was expected since the total irradiance incident on the modules is significantly higher compared to Delft. The same observations can be made, as the energy yield for all the modules is higher than the scenario of the attached module on the roof. More specifically, for the standard module the energy yield increases from 141.20 to 144.7 kWh/m^2. Similar increase has been observed for the whole range of colored module presented in Figure 6.33. It can be concluded again, that the blue colored module delivers the highest amount of energy yield for a whole year 131.90 kWh/m^2 where the dark green generates the least energy yield of 124.20 kWh/m^2. Generally, the energy yield for each color does not have an enormous deviation from the energy yield of the standard module.

Comparing the two plots Figure 6.32 and Figure 6.33 with the respecting plot for the scenario of the roof without an air gap Figure 6.22 and Figure 6.23 , it can be concluded that the implementation of the air gap has a positive impact of the total energy yield for both locations and colors. However, higher differences are observed in Dubai, since the temperature increase is much higher when the convection at the back side is blocked. In both locations, dark green module has the worst performance and blue colored module the best. The remaining colors are fluctuating in between with relatively small deviations.

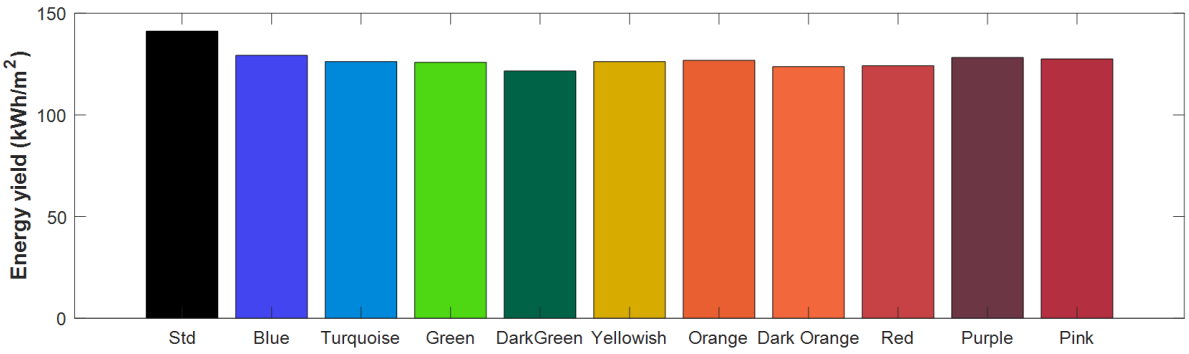

Figure 6.33Energy yield per color for a module attached on a roof in Dubai

	Std	Blue	Turquoise	Green	Dark Green	Yellowish	Orange	Dark Orange	Red	Purple	Pink
kWh/m²	144.7	131.90	128.70	128.50	124.20	128.90	129.60	126.30	126.80	131.00	130.30

Table 6-16 Energy yield per color for a module attached on a roof in Dubai

6.7 Façade

In this section the results of the scenario where the module is installed on a façade without air gap will be presented. The results in terms of temperature, energy yield, power and I-V curves will be shown and discussed for both locations for colored and standard modules.

6.7.1 Temperature results

6.7.1.1 Highest temperature

Figure 6.34 illustrates the temperature results of a module installed on a south-oriented façade in Delft. The peak of the temperature for the standard module is approximately 75 degrees where high temperature drop is observed for the dark orange module of 6 degrees. The plot of Figure 6.34 b) which presents the values of the temperature difference from the standard module, has a different distribution compared to the previous plots. The impact of each optic filter on the working temperature has changed. More specifically, the turquoise color, which was characterized before for its good cooling performance, for this scenario in comparison with the remaining colors, it has a smaller effect of 4 degrees. On the other hand, the performance of dark green color has a better impact on the working temperature with a drop of 5.5 degrees. The colors with the higher temperature decrease are dark orange and red, with almost 6 degrees. The blue color has the smallest temperature drop of 3 degrees. Generally, this difference in performance is observed since the module now is at 90degrees. The optic filter performance is highly dependent on the angle of incidence of the irradiance and the amount of the irradiance. In May the sun in Delft is relatively in a high altitude, therefore, high angle of incident is observed between the module on the façade and the incident light. Consequently, the performance of the optic filters is affected, and the reflection shifts in wavelength range accordingly.

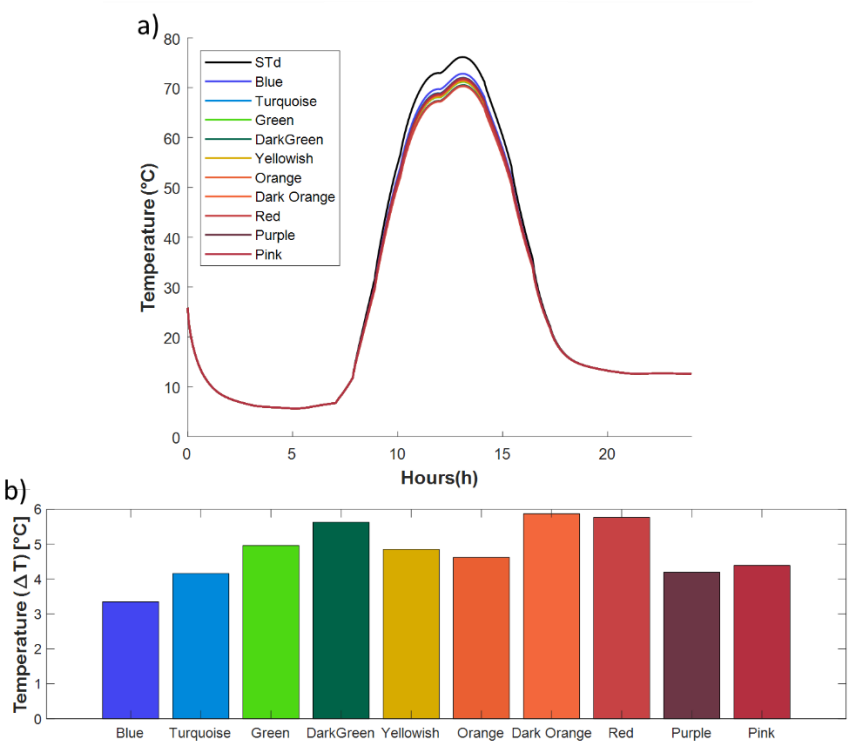

Figure 6.34 Figure a) Temperature distribution for the standard module and the 10 main colors on the 5th of May in Delft Figure b) Temperature difference for each color from the maximum temperature of the standard module

Figure 6.35 a) and c) show the power distribution and the energy yield respectively. The standard module generates approximately 0.25 kWh/m^2 whereas the blue module delivers 0.24kWh/m^2 energy yield. This small difference in energy yield occurs since the irradiance on the module is relatively small. Also as have been discussed before, the angle of incidence is expected to be very high. The dark green module has the smallest amount of energy yield of approximately 0.23 kWh/m^2. In general, the energy yield difference between the colors with respect to the standard module is insignificant. From the I-V curve in Figure 6.35 b), it can be seen that a very small increase in V_{oc} is observed as well as a relatively small decrease of the I_{sc}. The efficiency at the highest temperature is approximately 16% for both modules; Figure A 47.

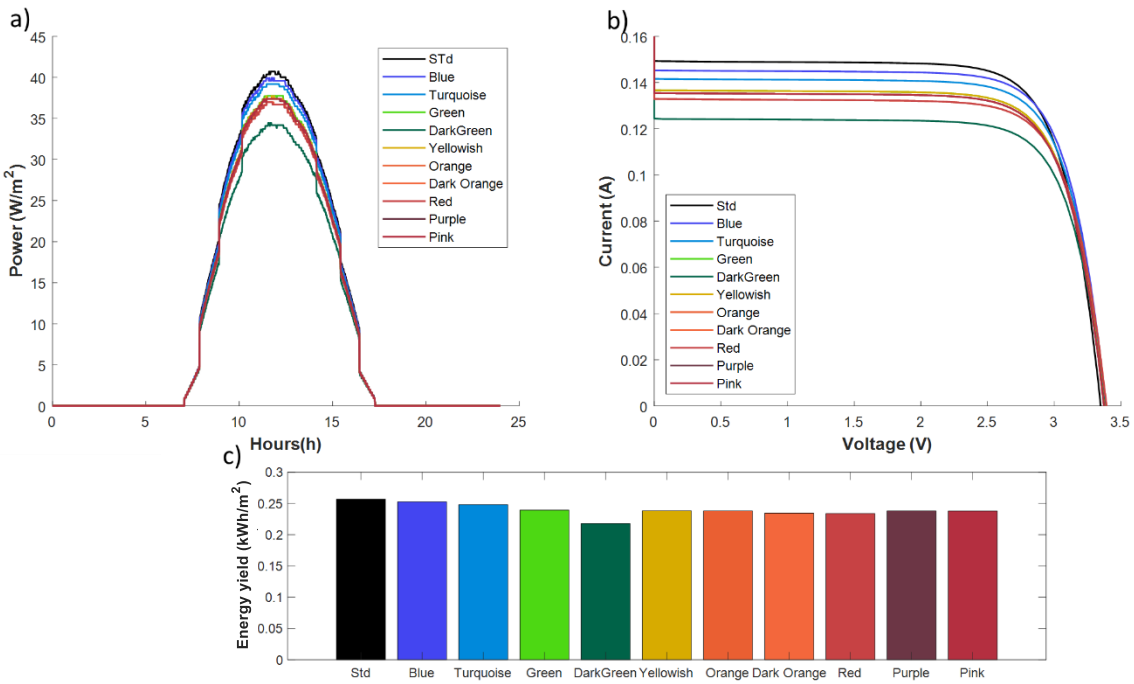

Figure 6.35 Figure a) Power distribution for the standard module and the 10 main colors on the 5th of May in Delft, Figure b) Efficiency distribution, Figure c) Energy yield difference for each color from the total energy yield of the standard module

The following Figure 6.36, shows the temperature results for the modules installed on a façade in Dubai. The maximum working temperature of the standard module is 62 degrees and the highest difference in temperature is observed with the turquoise module by 3 degrees. The temperature difference for all the modules is relatively small compared to the previous scenarios and that is because for this selected day the incident irradiance on the module is comparatively small. Therefore, the performance of the optic filters is influenced. In general, the same trend of temperature drop is observed but scaled down. The dark green module has the smallest decrease on the working temperature of 1.7 degrees.

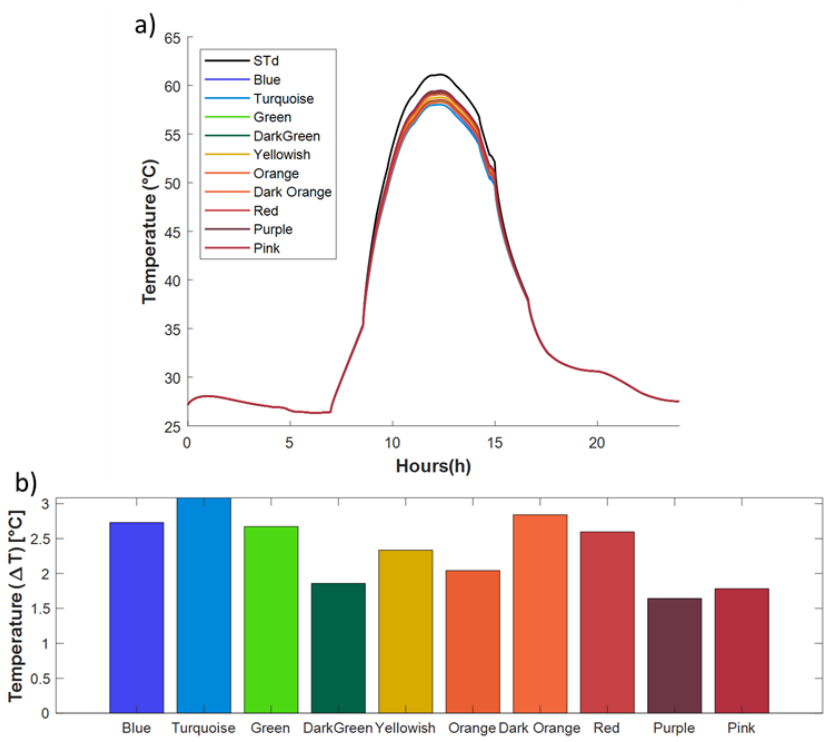

Figure 6.36 Figure a) Temperature distribution for the standard module and the 10 main colors on the 5th of May in Delft Figure b) Temperature difference for each color from the maximum temperature of the standard module

In Figure 6.37, the power energy yields, and I-V curves are presented for the modules on a façade in Dubai. The energy yield for this specific day from the standard module is around 0.1 kWh/m^2, which is comparatively very small. On September, the sun altitude in Dubai is very high and therefore, the angle of incidence between the module on the facade and the sun increases. That is the reason why differences between the standard module and the colored modules are difficult to be distinguished.

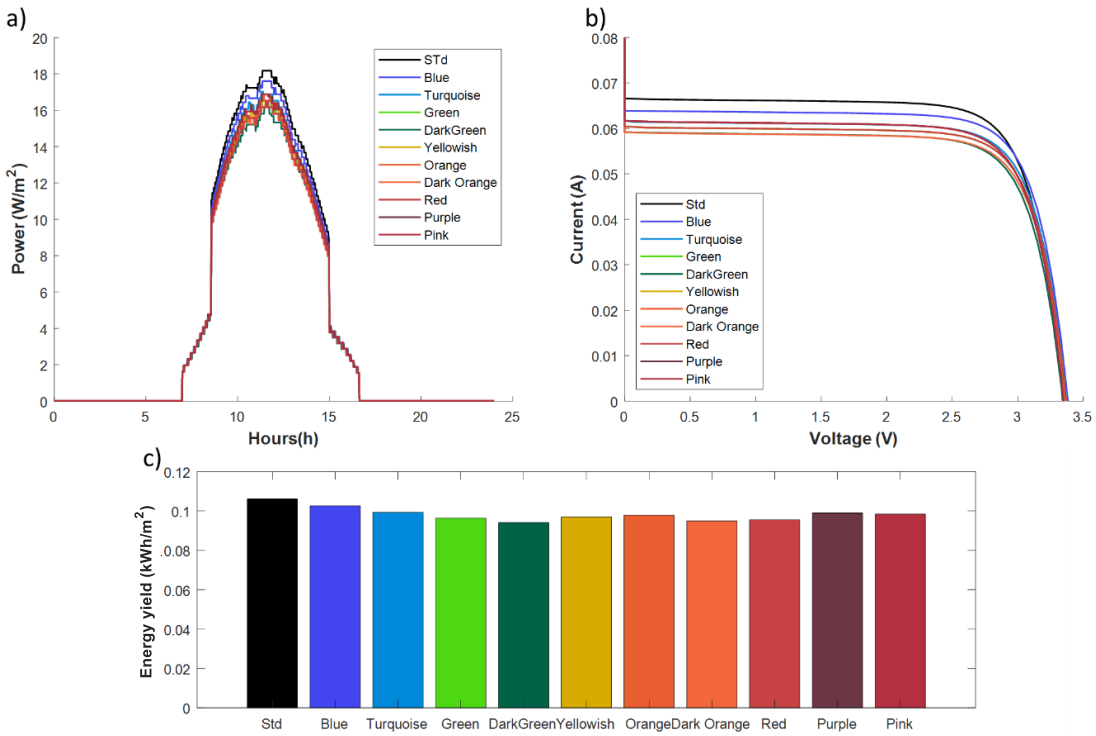

Figure 6.37 Figure a) Power distribution for the standard module and the 10 main colors on the 3rd of September in Dubai, Figure b) Efficiency distribution, Figure c) Energy yield difference for each color from the total energy yield of the standard module

6.7.1.2 Cloudy day

Figure 6.38 presents the temperature results on the 19th of January in Delft where the selected day represents the worst-case scenario. The standard module has a temperature peak at 26 degrees and the differences in temperature between the standard module and the optic filters is constant at 0.8 degrees.

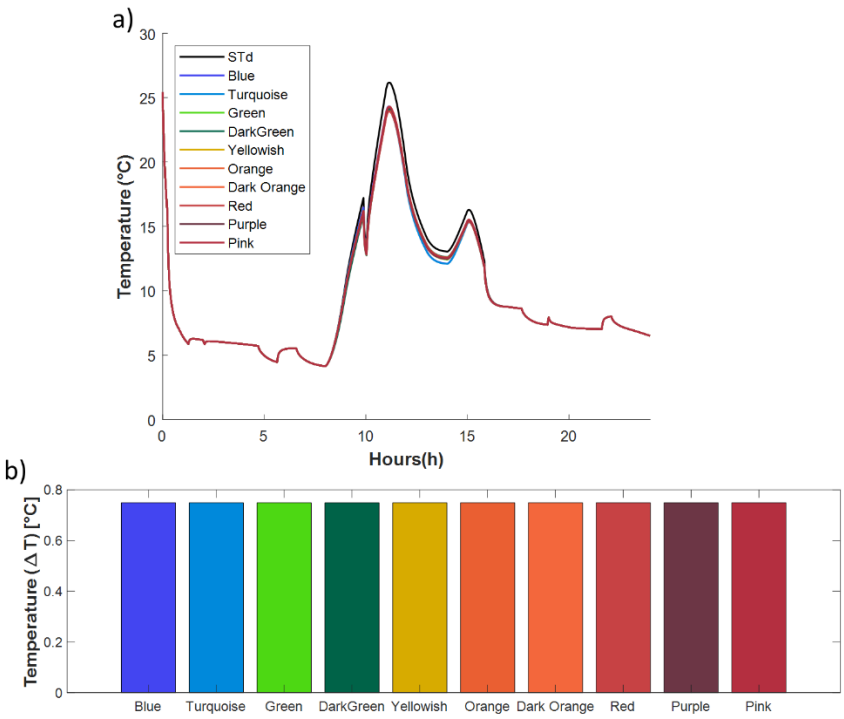

Figure 6.38 Figure a) Temperature distribution for the standard module and the 10 main colors on the 19th of January in Delft , Figure b) Temperature difference for each color from the maximum temperature of the standard module

From the power and energy yield results in Figure 6.39 a) and c), a small difference is observed in terms of energy yield between the standard and the colored modules. That is a result of the I_{sc} current drop between the different colors from the standard module; Figure 6.39 b). The standard module produces 0.07 kWh/m^2. However, all the colors have an energy yield around 0.06 kWh/m^2 except for the dark green optic filter where the energy yield is 0.057 kWh/m^2.

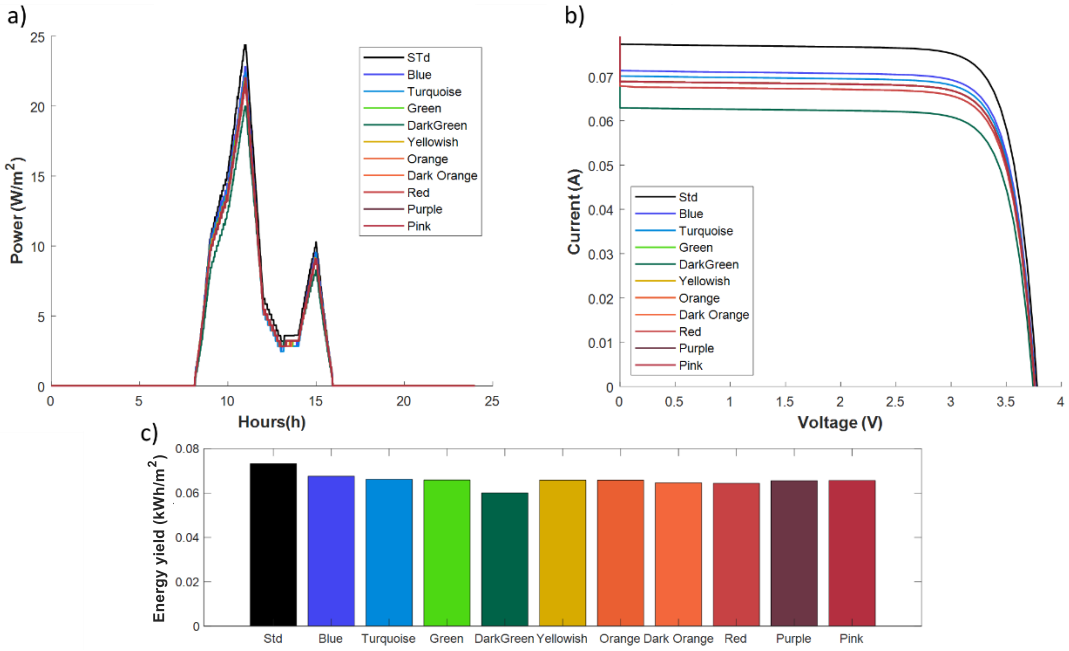

Figure 6.39 Figure a) Power distribution for the standard module and the 10 main colors on the 19th of January in Delft, Figure b) Efficiency distribution, Figure c) Energy yield difference for each color from the total energy yield of the standard module

Figure 6.40 shows the temperature results for the 1st of January in Dubai where the selected day represents the worst-case scenario. The maximum temperature of the standard module is 37 degrees where the temperature decreases at around 3 degrees with the turquoise colored module. The dark green module has again the smallest temperature decrease of 1.2 degrees.

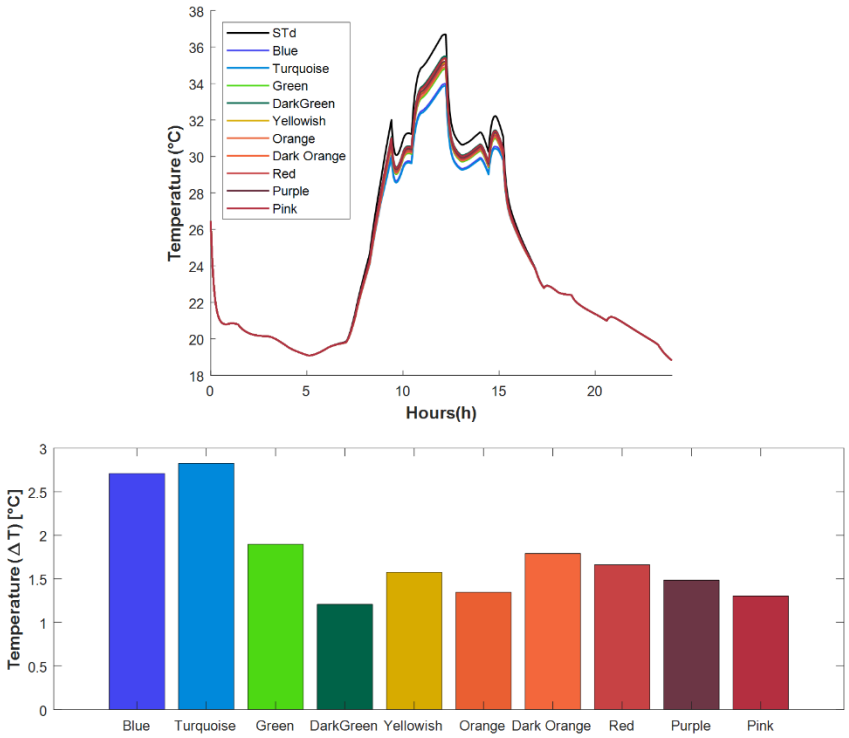

Figure 6.40 Figure a) Temperature distribution for the standard module and the 10 main colors on the 1st of January in Dubai, Figure b) Temperature difference for each color from the maximum temperature of the standard module

From the energy yield results presented in Figure 6.41, the energy yield for this specific day is small. More specifically, the energy yield of the standard module is around 0.07 kWh/m^2 however, results in around 0.07 kWh/m^2 are observed for the colored modules.

In general, it can be concluded that the impact of the optic filters on the performance of the module is insignificant for the cases where the irradiance is very small, and the angle of incidence is very high.

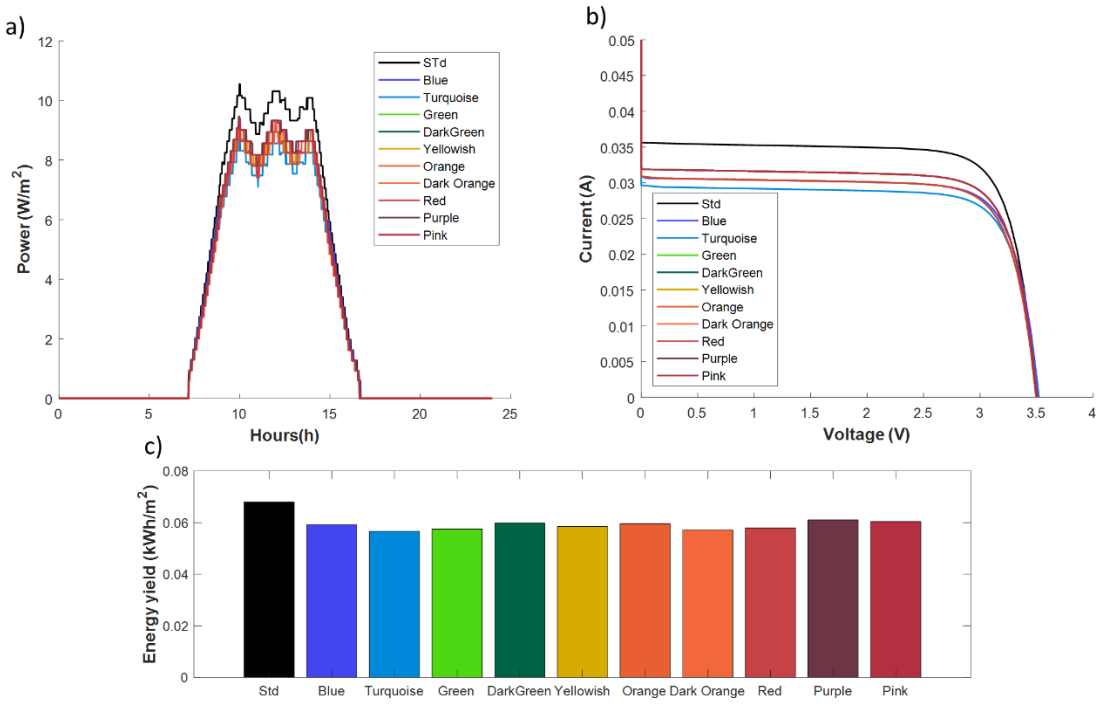

Figure 6.41 Figure a) Power distribution for the standard module and the 10 main colors on the 1st of January in Dubai, Figure b) Efficiency distribution, Figure c) Energy yield difference for each color from the total energy yield of the standard module

6.7.2 Energy yield

In Figure 6.42 the energy yield results for 2005 are illustrated for standard and colored modules attached on a façade in Delft. From the Table 6-17, the exact values are presented. The energy yield from the standard module is around 46.76 kWh/m^2 where the highest energy yield among the colored modules is observed with the blue module with 44.21 kWh/m^2 generation which is equal to 5.7% lower than the standard module. The smallest energy is observed with the dark green module of approximately 42.01 kWh/m^2 which is equal to 8% lower energy yield compared to standard module.

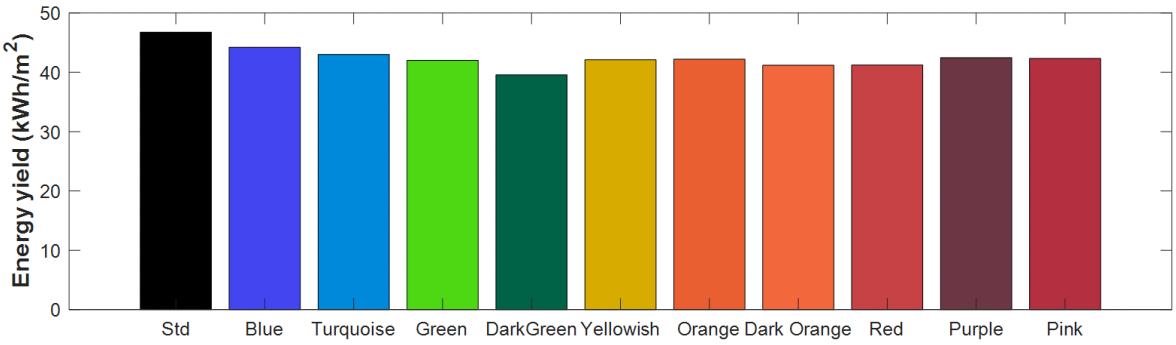

Figure 6.42 Energy yield per color for a module attached on a façade in Delft

	Std	Blue	Turquoise	Green	Dark Green	Yellowish	Orange	Dark Orange	Red	Purple	Pink
kWh/m²	46.76	44.21	42.99	42.01	39.57	42.09	42.20	41.18	41.21	42.45	42.34

Table 6-17 Energy yield per color for a module attached on a façade in Delft

Figure 6.43 shows the according results for Dubai and the exact values can be found from Table 6-18. The total energy yield of the standard module is around 56.18 kWh/m^2. Among the colored modules, the blue module generates the highest amount of energy yield of 54.02 kWh/m^2 which is equal to 4% lower than the standard module. The dark module generates the least energy of 47.92 kWh/m^2 which is equal to 15% lower energy yield compared to standard module.

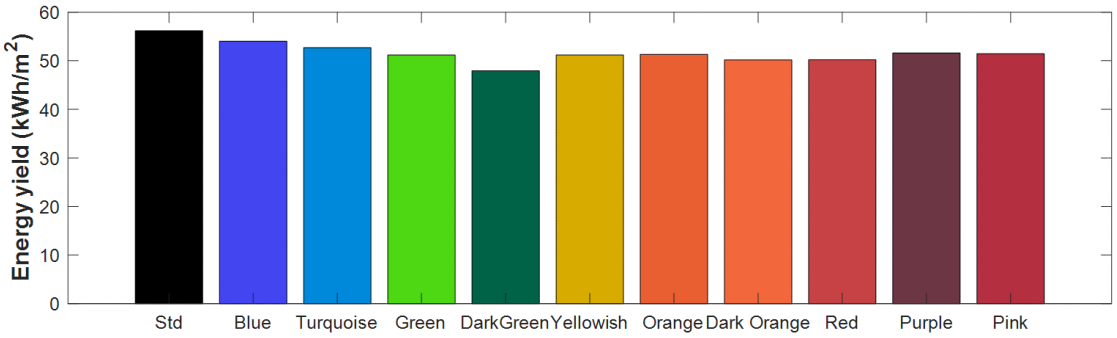

Figure 6.43 Energy yield per color for a module attached on a façade in Dubai

	Std	Blue	Turquoise	Green	Dark Green	Yellowish	Orange	Dark Orange	Red	Purple	Pink
kWh/m²	56.18	54.02	52.69	51.17	47.92	51.19	51.31	50.18	50.20	51.60	51.44

Table 6-18 Energy yield per color for a module attached on a façade in Dubai

All in all, comparing the two locations, it can be concluded that the energy yield in Dubai for both standard and colored modules is higher. That is because the module in Dubai experience more irradiance in a year compared to a module in Delft. Also, the sun altitude in Dubai does not reach as high values as for Delft. Regarding the colored modules, the same trend of energy yield is observed with a different scale based on the location. That confirms again that the performance changes for different locations but the percentage of difference between the optic filters remains the same.

6.8 Air gap façade

The same results that have been observed for the scenario where the modules are attached on a façade will be presented for the installation on a façade with an air gap in the Appendixes. The reason for that is because the same observation can be made as for the conclusions between roof installation with and without air gap. More specifically, for all the dates that have been studied for both locations, the implementation of air gap, allows in both sides' convection heat exchange and therefore, the working temperature of the module decreases.

Energy yield results will be presented in order to understand what the real impact of the air gap in terms of total energy is.

6.8.1 Energy yield

In Figure 6.44 the energy yield for each simulate module attached on a façade with air gap is presented for Delft where from Table 6-19 the values are presented. Overall, the behavior of the plot appears the same as in the previous according plots. In comparison with the Figure 6.42, the air gap increases significantly the energy yield for all the tested modules. The standard mini module generates 47.47 kWh/m^2 while the blue colored module produces 44.81 kWh/m^2 which is the highest value among the colored modules. The dark green module continuous to produce the least amount of energy which in this case is 40.10 kWh/m^2. The remaining colored modules are fluctuating in between those values and not extreme deviations can be noticed.

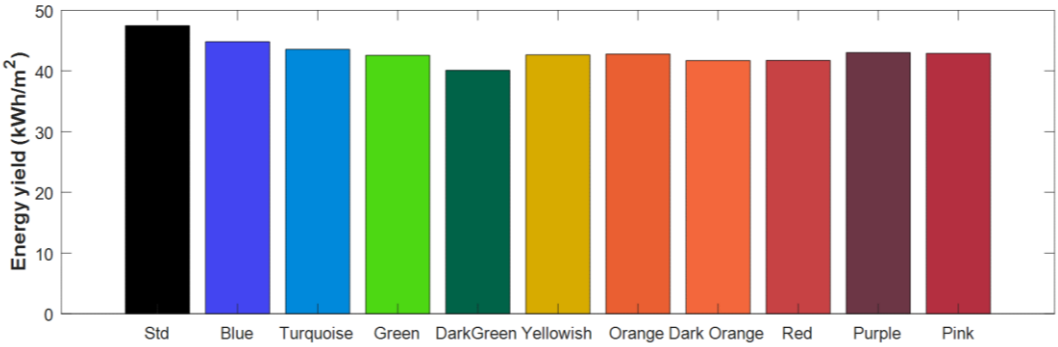

Figure 6.44 Energy yield per color for a module attached on a façade with an air gap in Delft

	Std	Blue	Turquoise	Green	Dark Green	Yellowish	Orange	Dark Orange	Red	Purple	Pink
kWh/m²	47.47	44.81	43.55	42.56	40.10	42.64	42.77	41.72	41.74	43.02	42.9

Table 6-19 Energy yield per color for a module attached on a façade with an air gap in Delft

The same results are presented for Delft in Figure 6.45 and Table 6-20. From the colored plot it is obvious that the performance of the colored modules compared to the standard module remains the same but scaled down. That is an observation that seems to appear in all the cases and scenarios. Also, comparing the results with Figure 6.43, the air gap has a positive effect in the total energy yield. The standard module generates 57.01 kWh/m^2 where, the highest amount of energy 54.71 kWh/m^2 is generated from the blue module and the smallest amount of energy 48.52 kWh/m^2 is produced from dark green module.

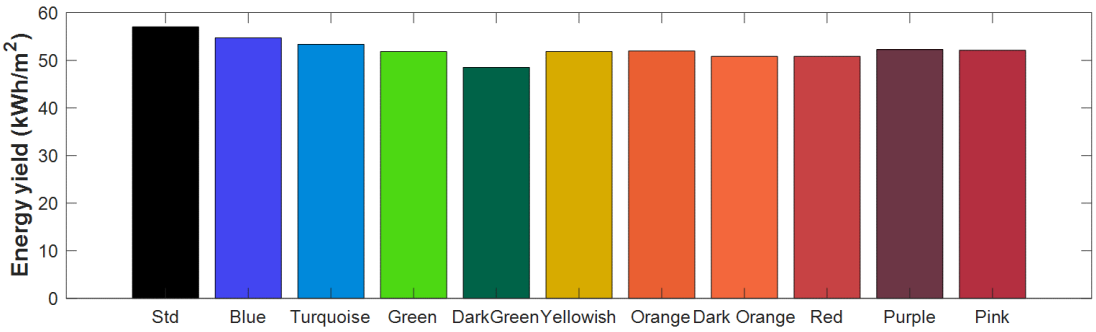

Figure 6.45 Energy yield per color for a module attached on a façade in Dubai

	Std	Blue	Turquoise	Green	Dark Green	Yellowish	Orange	Dark Orange	Red	Purple	Pink
kWh/m²	57.01	54.71	54.35	51.82	48.52	51.83	51.96	50.80	50.82	52.27	52.10

Table 6-20 Energy yield per color for a module attached on a façade with an air gap in Dubai

Comparing the current results, in Dubai the overall generation is higher for façade installations for all the tested modules. In both locations the performance of the colored modules in comparison to the standard module appears the same as the blue module is proved again as the highest generator while the dark green module the smallest generator of energy. Regarding the rest colors, it seems that not that high deviations are observed as they deliver close values energy yield.

7 Conclusions

The optical performance and the angular resilience of the optic filters in modules has been investigated. Although, information regarding the real impact on performance and the change in terms of energy yield are still not yet examined. In this view, the aim of this thesis is to fully assess what is the real impact of optic filters compared to a module without optic filter under real operational conditions. A complete spectrally resolved thermal model in MATLAB has been developed that considers angular dependence of optic filters on both appearance and performance. The model provides information of temperature, efficiency and energy yield results for different optic filters and locations. The model considers different installations of modules; BAPV and BIPV on façade and roof. Finally, the model was validated for three consecutive days on 24th 25th and 26th of June 2020. Also, the optimum thicknesses of the optic filters have been found for ten main colors. The colored matrix was divided and the optimum selection among different thicknesses that observe the same color was based on which gives the maximum energy yield. In this chapter the main results will be addressed divided by topic and recommendations for future work will follow.

7.1 Validation

The model has been validated for two mini modules with optic filter (0.09nm SiN and 0.09 SiO_2) and without optic filter that were fabricated from Juan Camilo Ortiz and Simona Villa. The measurements were carried out at the monitoring station at TU Delft. Regarding the validation of a module without optic filter, it was observed that during the working hours the simulated data perfectly matched the measured data with an average difference of 1 degree. The relative RMSD value was found to be 5.20 degrees. The value was calculated that high, because a deviation was observed during the time where the sun rises and sets. That is because the simulated model does not consider any shading effects.

The validation of the colored optic filter had a deviation from the measured data on average 2 degrees. This difference is associated to the fact that the SMARTS spectrum irradiance data used for the simulation do not provide the exact values for the real spectrum irradiance that has been incident on the module for the given period. Therefore, this deviation was expected as the power per wavelength has some errors compared to the real power. The values of RMSD was calculated 4.79 degrees for the colored modules. As mentioned before, this is a result of the deviations observed during the morning and night.

7.2 Optimization of optic filter thicknesses

The colored matrix Figure 6.1, was divided in ten main colors as provided in table 20 and simulated for a whole year in both locations and configurations in terms of energy yield. It was found that the optic filters thicknesses that are presented in the table below are the optimum designs for their corresponding color in terms of energy yield. It was found that the optimum thicknesses resulting the maximum energy yield are the same for both locations and installations. That means that the performance of the optic filters changes from different locations since the incident irradiance and the angle of incidence changes however, the relative differences among the optic filters remain the same.

	Blue	Turquoise	Green	Dark green	Yellowish	Orange	Dark orange	Red	Purple	Pink
Si_3N_4	0.05	0.05	0.11	0.16	0.12	0.13	0.05	0.05	0.15	0.14
SiO_2	0.09	0.1	0.05	0.16	0.05	0.05	0.15	0.16	0.05	0.05

Table 7-1 Optimum combination of optic filters for each color based on the highest energy yield

7.3 Temperature results

The temperature results have been simulated for two main locations; Delft and Dubai for the aforementioned optic filters and a standard mini module. The performance was tested for a day with that the maximum temperature of the module observed in Delft and Dubai; 5th of May and 3rd of September accordingly. Also, a worst-case scenario was studied on the 19th of January and 1st of January in Delft and Dubai accordingly.

- For all the locations and scenarios, it was found that the turquoise optic filer cools the most the module, while the dark green decreases the temperature the least. The remaining colors where every time fluctuation in between them. Moreover, for the worst-case scenario it has been found that the effect of optic filters on temperature is insignificant.
- More specifically, for a free mounted module in Delft it was found that the temperature drops from 65 degrees to 59.5 degrees with the turquoise optic filter. Although in Dubai for the same configuration the module was cooled from 75 degrees to 69 degrees.
- For the free mounted modules configuration for the worst-case scenario in Delft the impact of optic filter is insignificant although for Dubai still small decrease can be observed with 1.75 degrees drop of the turquoise filter and up to 1 degree for the remaining colors.
- For the mounted module on a roof scenario, the temperature of the standard module increases to 90 degrees in Delft and almost 98 degrees in Dubai. In comparison with the according values of a standard module that is 25 degrees higher in Delft and 20 degrees in Dubai. The performance of the optic filters on the working temperature is therefore higher. The turquoise color cools the working temperature by approximately 9 degrees. The remaining colors are decreasing the working temperature in the range of 6-7.5 degrees.
- With the introduction of the 0.1 m air gap, the working temperature of the standard module decreases by 20 degrees in Delft and by 15 degrees in Dubai. Therefore, it has been proved that the air gap which eventually allows convection heat exchange at the back side, having an important impact on the temperature. The temperature difference observed with the different colored modules has decreased by 1 degree; turquoise color cools the working temperature by approximately 7 degrees.
- Same observations have been concluded for façade installations as the temperature decreases with the implementation of 0.1 m air gap.
- In addition, it was noticed that indeed the performance of the optic filters changes for each location based on the temperature and irradiance although, it changes linearly and therefore the percentage change between each color remains the same.

7.4 Efficiency and energy yield

- Regarding the daily efficiency it was found that during the maximum temperature the efficiency difference between standard module and colored modules never excited 1%.
- It has been also observed that for the free mounted modules the voltage influence due to the temperature drop is very small compared to the current drop due to the reflection of irradiance for each optic filter.
- For the scenario where the module is attached on a façade during the highest temperature scenarios, the V_{oc} voltage of the standard module has a drop from 3.7V to 3.3V in Delft whereas in Dubai from 3.4 V to 3.2 V. The colored modules are increasing the voltage whereas the current decreases to the power of 10^{-2} therefore, the efficiency increases from 16% to almost 16.3% in Delft and from 15.8% to 16% in Dubai.
- In terms of energy yield results, in general not significant differences have been observed among the different colors. Although, for all the cases the energy yield is smaller than the standard module. Overall, the blue module has proved to deliver the highest amount of energy yield and the dark green module that least. More specifically, on average the selected optic filters have an energy yield value 10kWh/m^2 lower than the standard module. However, for bigger installations the decrease among different colors needs to be investigated more careful in terms of kWh as the values are presented in kWh/m^2.
- Important to mention is that the energy yield on façade and roof installations increases significantly for both standard and colored module when the air gap is introduced. For example, for the standard module installation on a façade the energy yield increases from 79.16 kWh/m^2 to 79.71 kWh/m^2 in Delft and from 141.20 kWh/m^2 to 144.70 kWh/m^2 in Dubai.

8 Recommendations

This work has the purpose to create a complete spectrally resolved thermal model in MATLAB to provide some insight on the real impact of optic filters on performance and the change in terms of energy yield. As far as there is room for improvement the following recommendations are considered:

- Validation of the model needs to be established for different colored modules and locations. Also, the model needs to be tested for cloudy conditions in order to assess the change on the performance of optic filters and the impact on the working temperature of the module.
- Moreover, the model needs to be improved in terms of shadow effects since at the moment they are not accounted for.
- The radiation exchanged of the module with the ambient temperature is constant per wavelength. A nice approach would be to distinguish the difference in emissivity for different wavelengths.
- The impact of the clouds in the spectrum irradiance is considered as a grey filter that equally decreases the spectrum irradiance per wavelength. A more detailed cloud model can produce will give better estimation of the spectrum irradiance under cloudy conditions.
- Moreover, variable material properties would be nice to be implemented based on temperature as sometimes the temperature of the module increases significantly.
- The real impact of optic filters on performance has been evaluate for mini modules, therefore the next step it to test the impact on performance in large scale modules.
- Finally, as have been found from Simona's thesis, random textured glass tackles the problem of angular resilience as it improves the AOI dependence of the optic filter in terms of observed color. Therefore, the optical model needs to be improved to replicate such approach.

Appendix A Reflection and color distribution for each optic filter

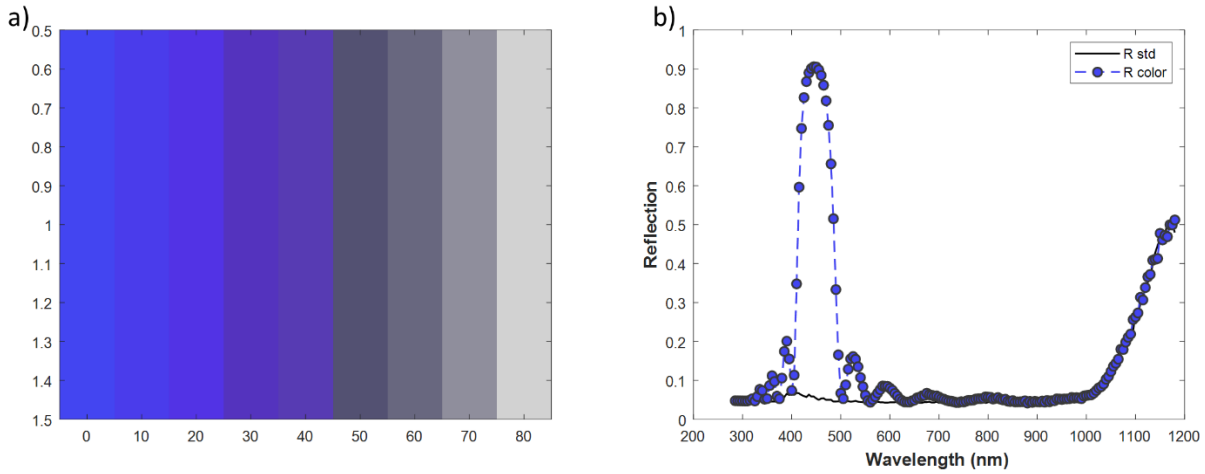

Figure A 1 Figure a) shows the reflected color based on the angle of incidence for a blue optic filter in the mini module Figure b) illustrates the reflection per wavelength at zero degrees

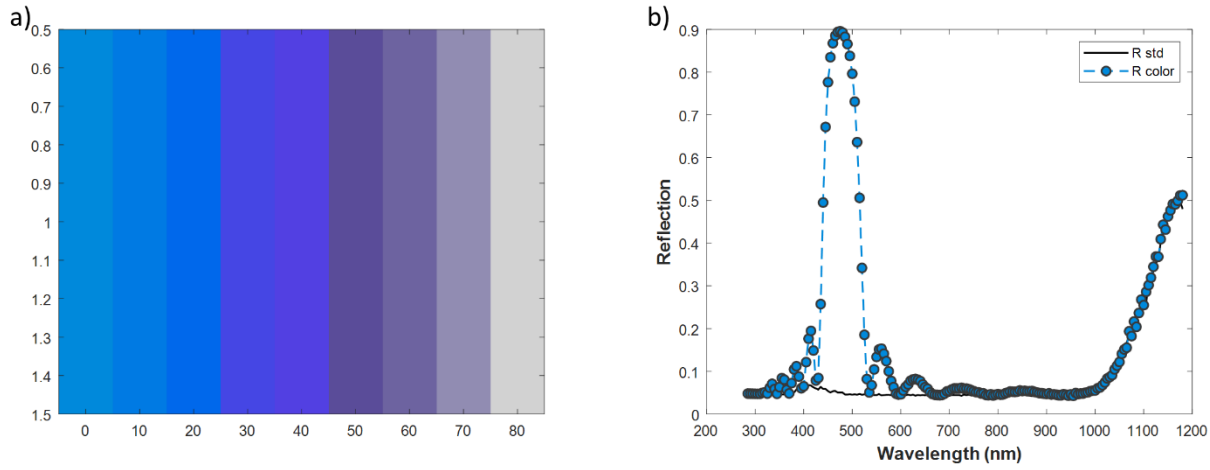

Figure A 2 Figure a) shows the reflected color based on the angle of incidence for a turquoise optic filter in the mini module Figure b) illustrates the reflection per wavelength at zero degrees

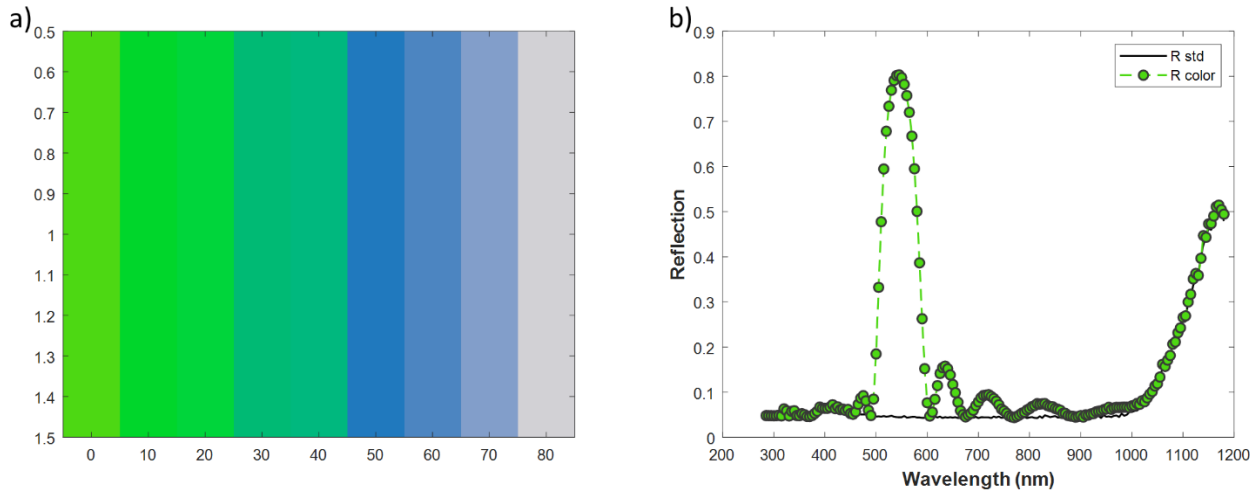

Figure A 3 Figure a) shows the reflected color based on the angle of incidence for a green optic filter in the mini module Figure b) illustrates the reflection per wavelength at zero degrees

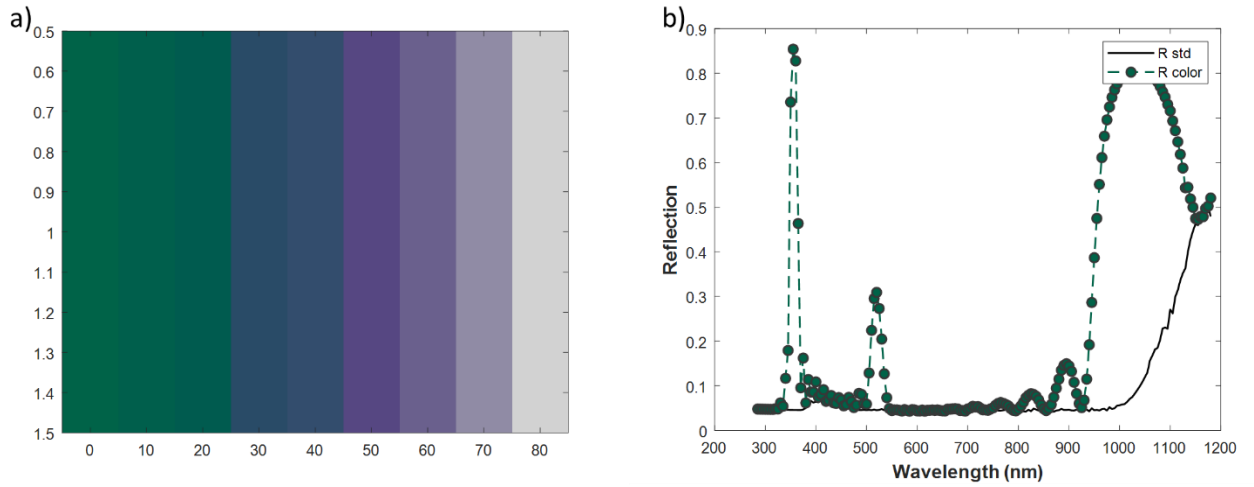

Figure A 4 Figure a) shows the reflected color based on the angle of incidence for a mini module with a dark green optic, Figure b) illustrates the reflection per wavelength at zero degrees

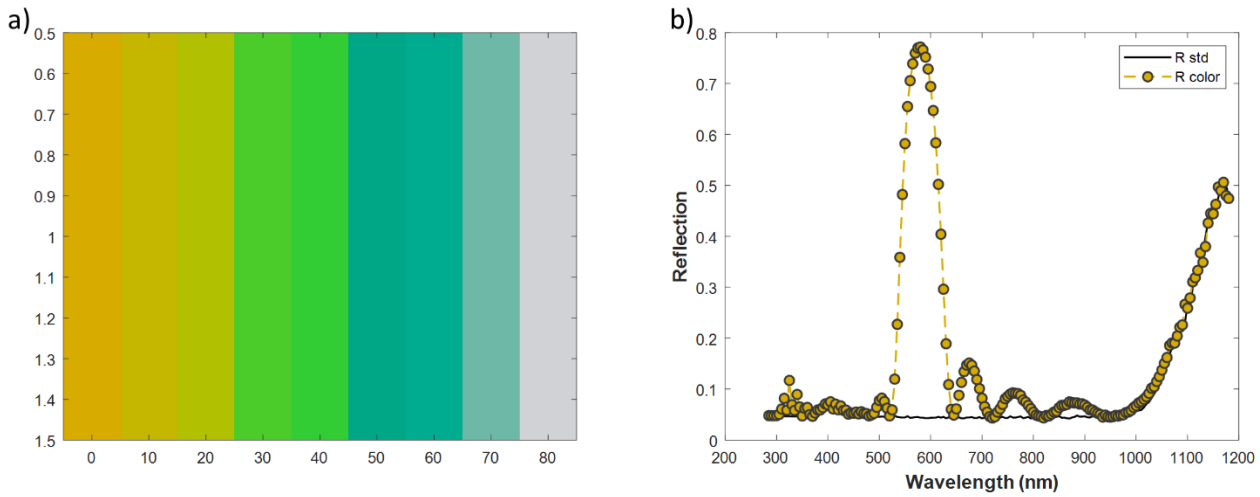

Figure A 5 Figure a) shows the reflected color based on the angle of incidence for a mini module with a yellowish optic, Figure b) illustrates the reflection per wavelength at zero degrees

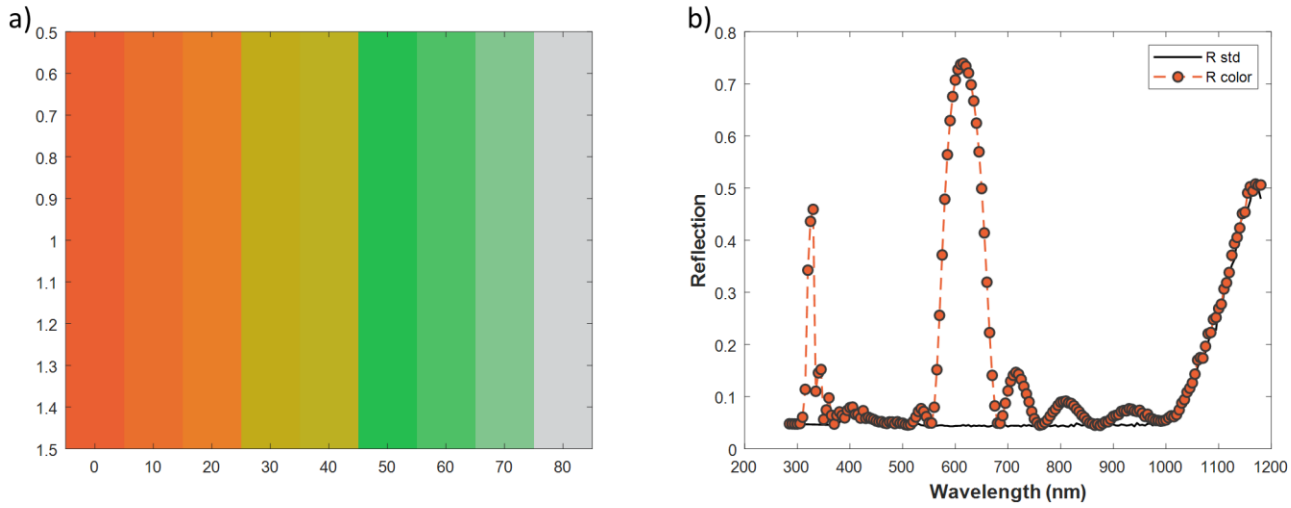

Figure A 6 Figure a) shows the reflected color based on the angle of incidence for a mini module with a orange optic, Figure b) illustrates the reflection per wavelength at zero degrees

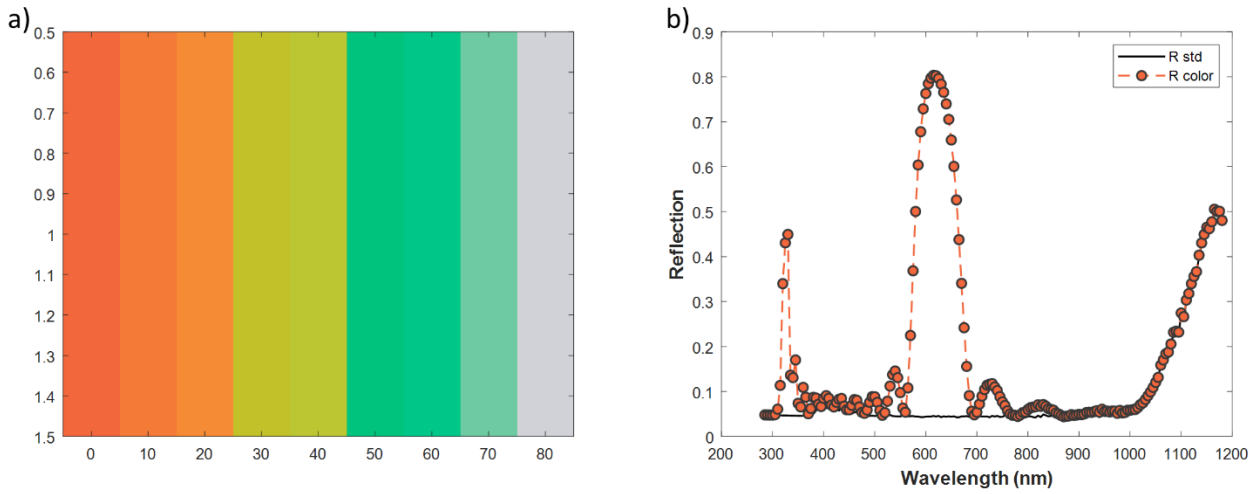

Figure A 7 Figure a) shows the reflected color based on the angle of incidence for a mini module with a dark orange optic, Figure b) illustrates the reflection per wavelength at zero degrees

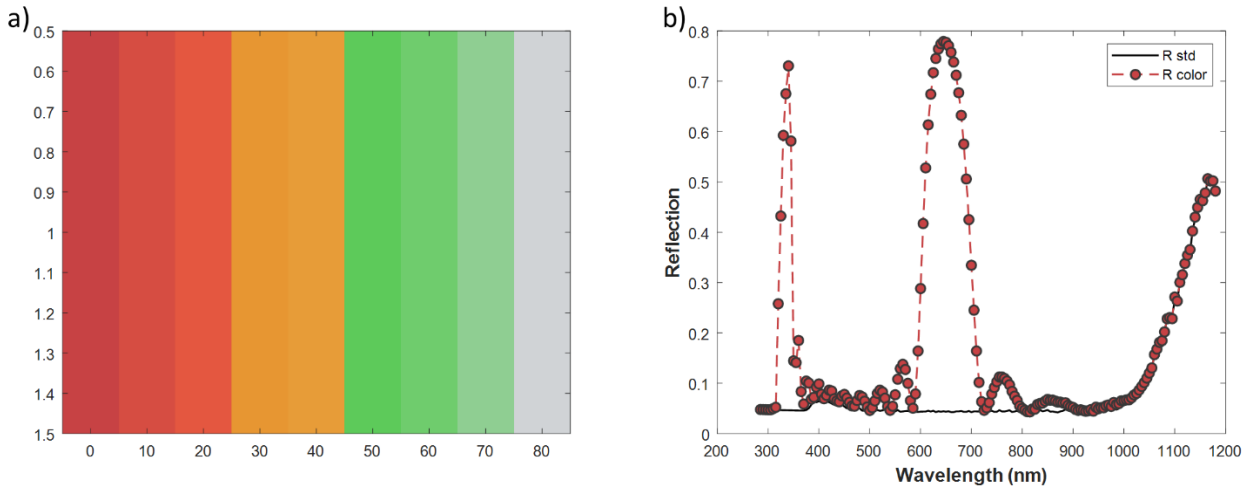

Figure A 8 Figure a) shows the reflected color based on the angle of incidence for a mini module with a red optic, Figure b) illustrates the reflection per wavelength at zero degrees

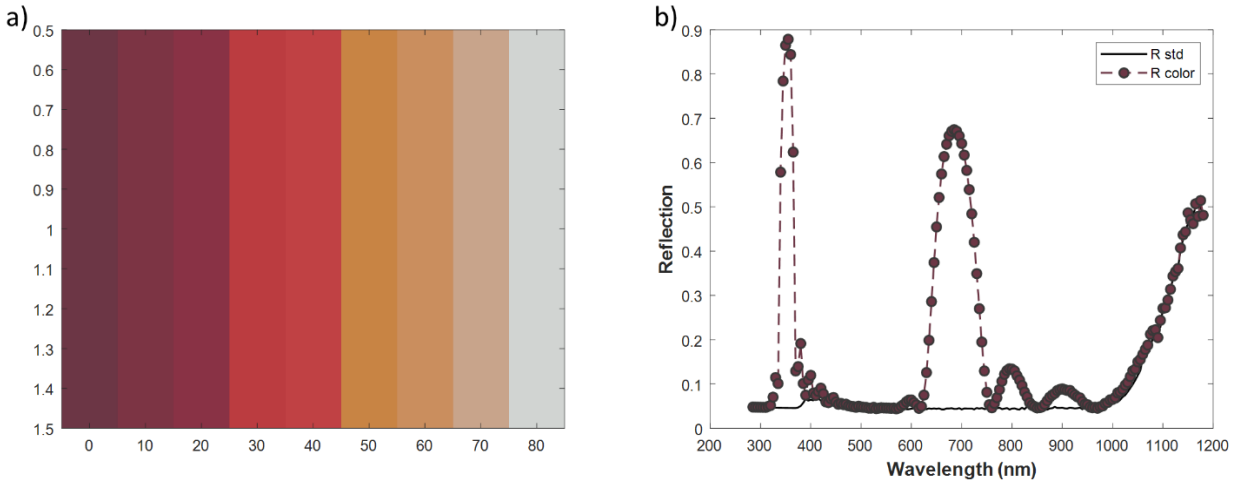

Figure A 9 Figure a) shows the reflected color based on the angle of incidence for a mini module with a purple optic, Figure b) illustrates the reflection per wavelength at zero degrees

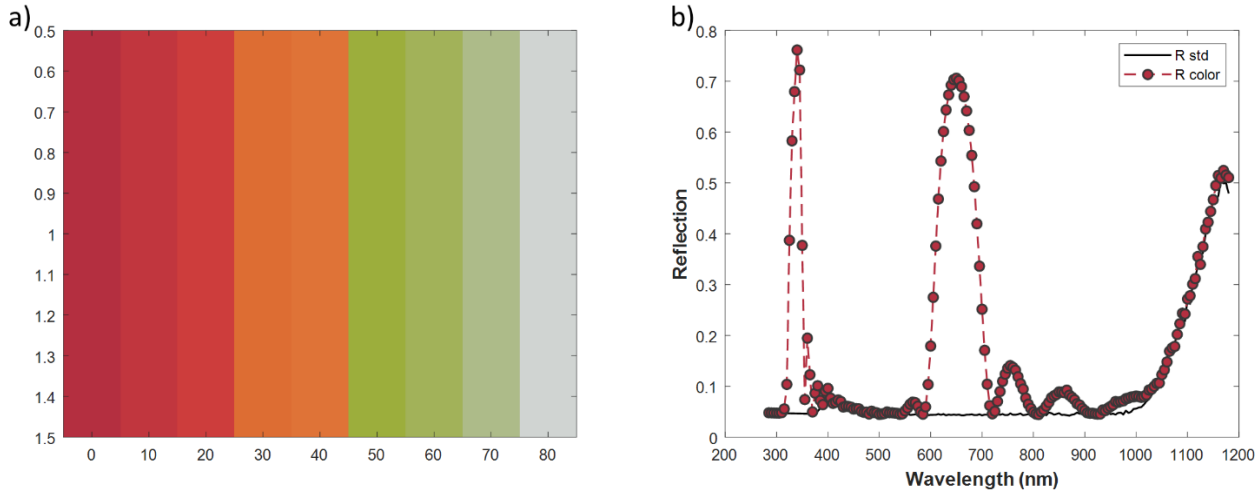

Figure A 10 Figure a) shows the reflected color based on the angle of incidence for a mini module with a pink optic, Figure b) illustrates the reflection per wavelength at zero degrees

Appendix B Weather data of scenarios

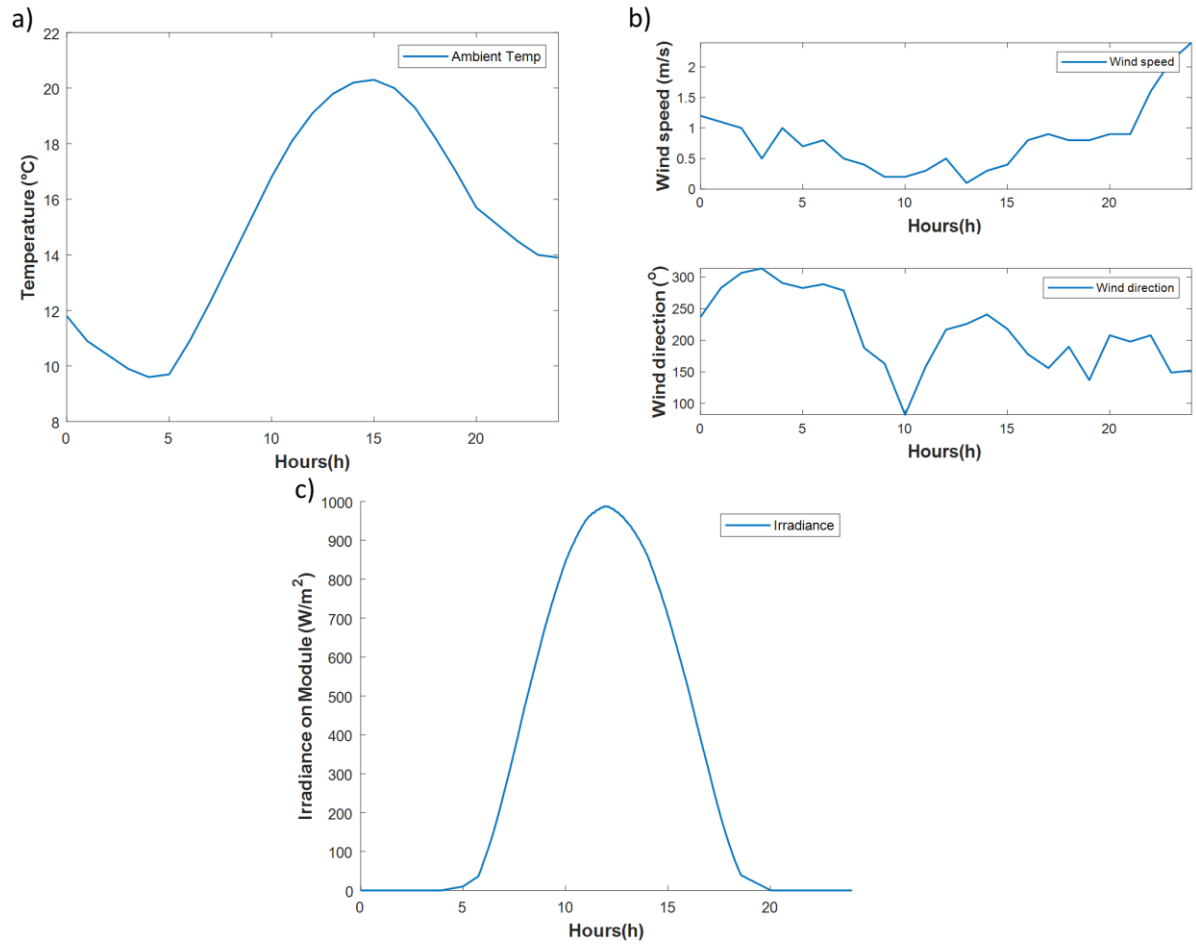

Figure A 11 Delft weather data on the 5th of May; Figure a) Ambient Temperature distribution , Figure b) Wind speed and Wind direction, Figure c) Total incident irradiance on the module

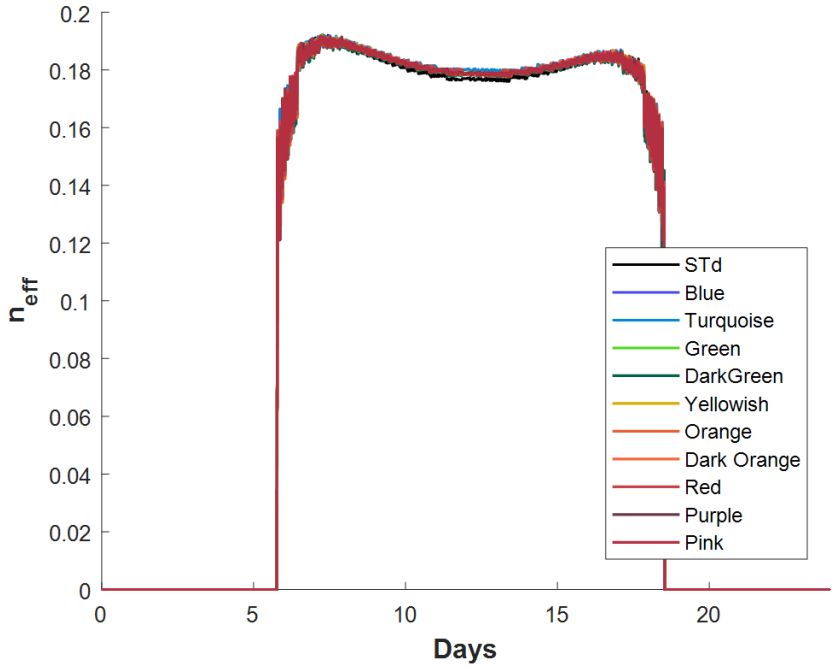

Figure A 12 Efficiency distribution for a free mounted module at 32 degrees on the 5th of May at Delft

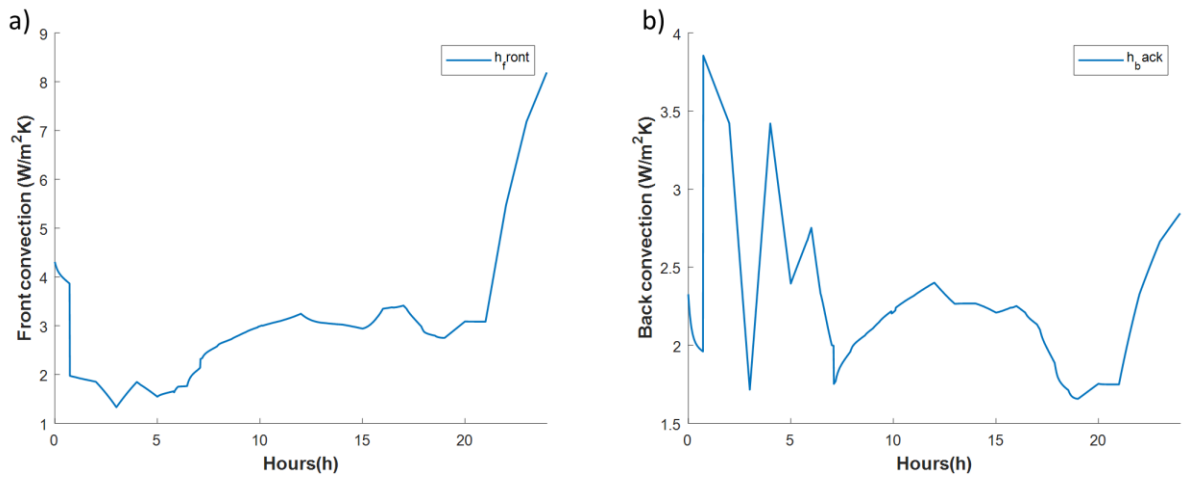

Figure A 13 Figure a) Total convection on the front, Figure b) Total convection on the back side for a free mounted module at 32 degrees on the 5th of May at Delft

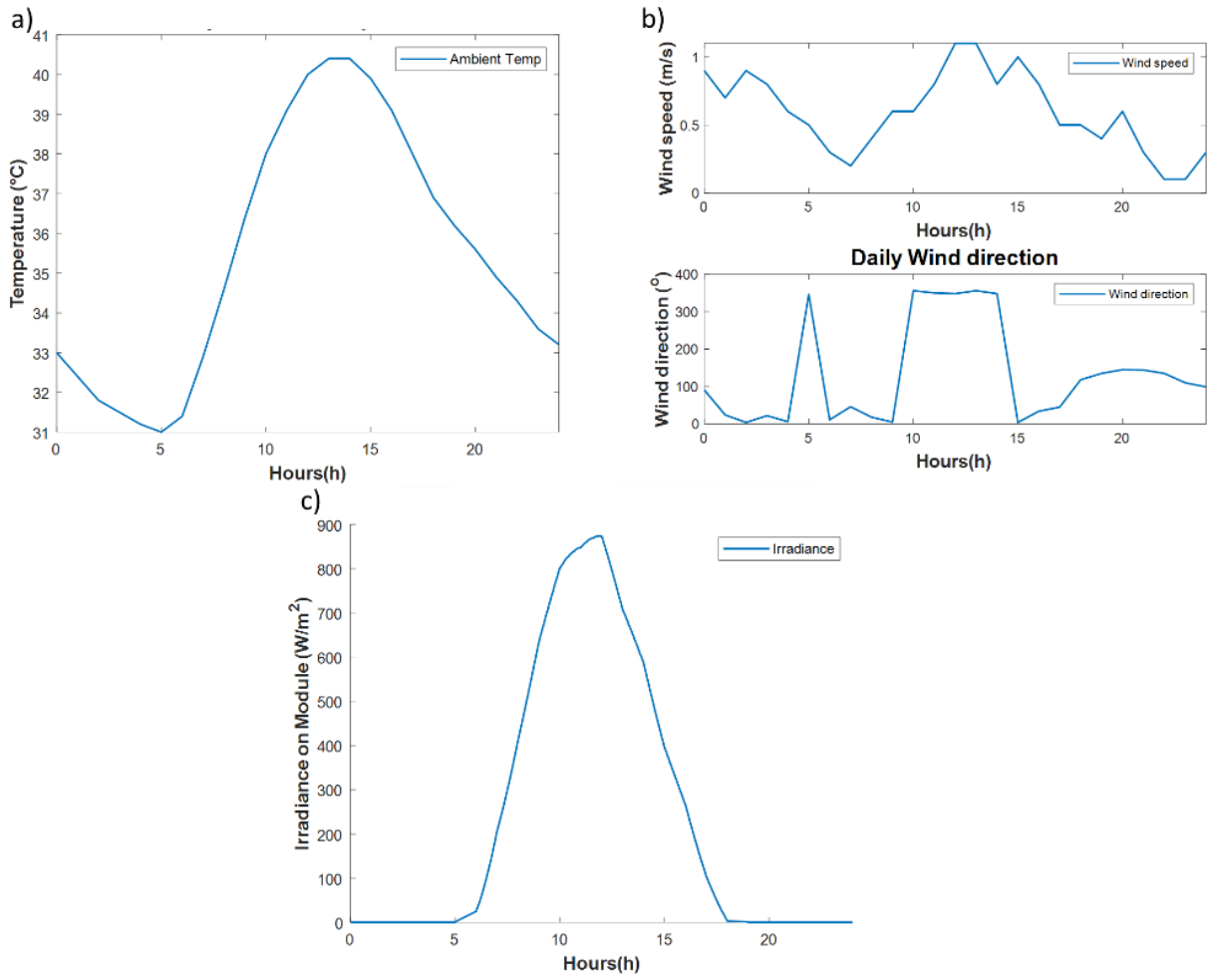

Figure A 14 Dubai weather data on the 3rd of September; Figure a) Ambient Temperature distribution , Figure b) Wind speed and Wind direction, Figure c) Total incident irradiance on the module

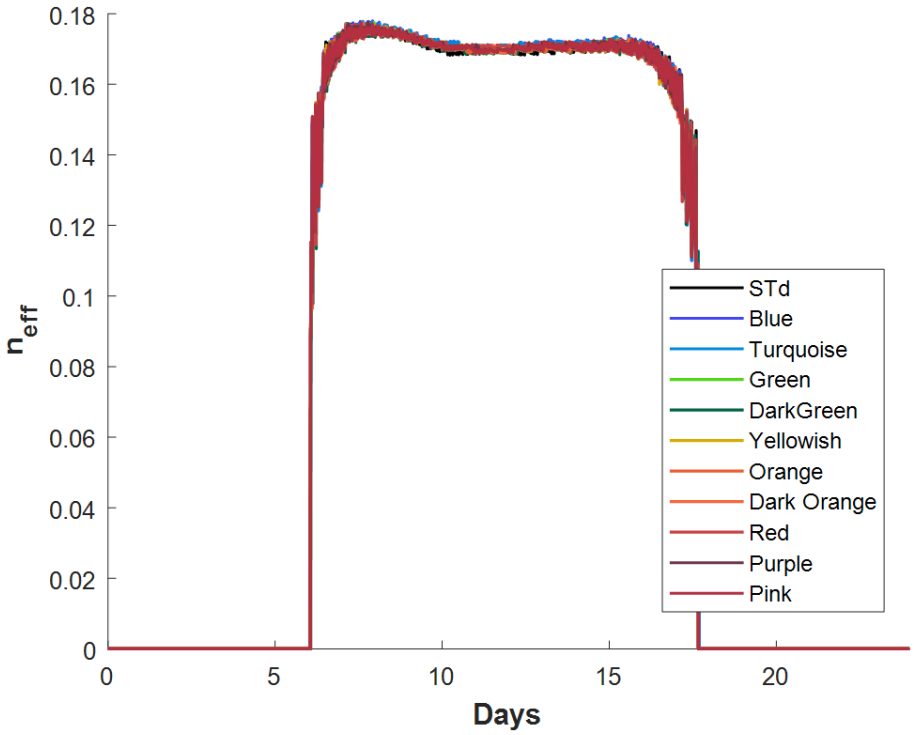

Figure A 15 Efficiency distribution for a for a free mounted module at 25 degrees on the 3rd of September at Delft

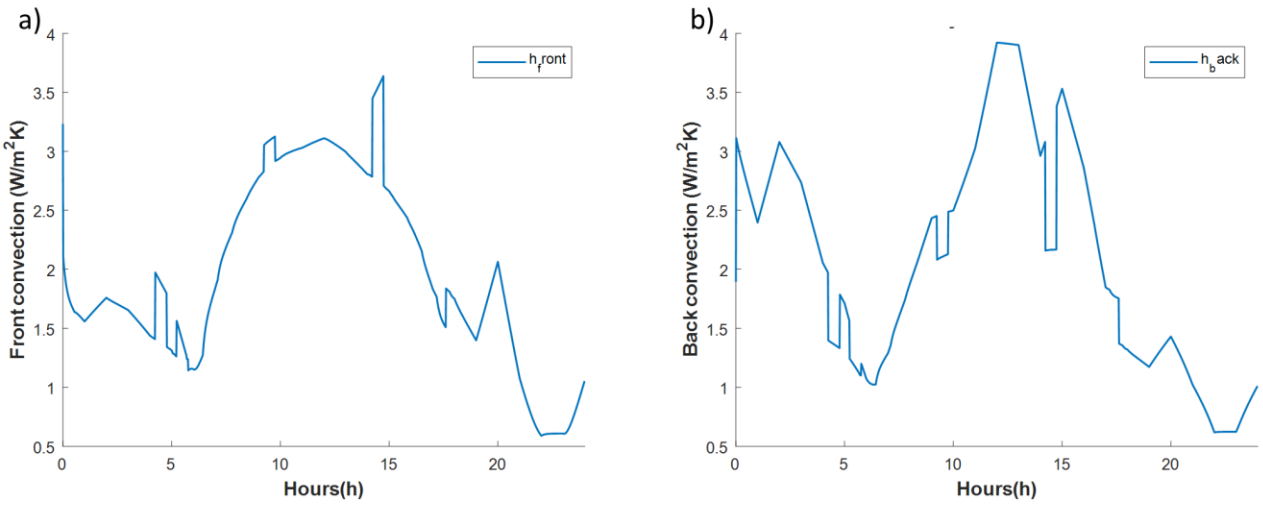

Figure 0.1 Figure a) Total convection on the front, Figure b) Total convection on the back side for a for a free mounted module at 25 degrees on the 3rd of September in Dubai

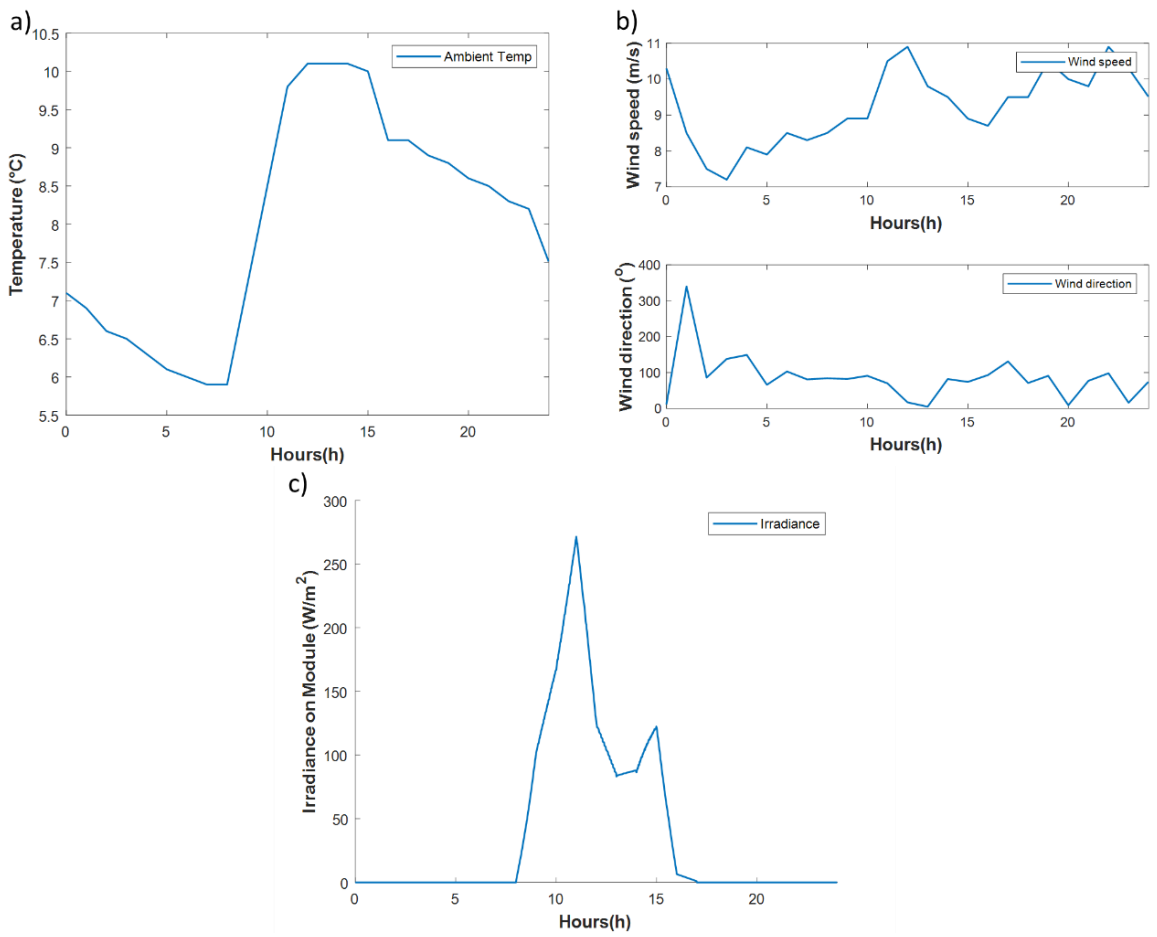

Figure A 16 Delft weather data on the 19th of January; Figure a) Ambient Temperature distribution , Figure b) Wind speed and Wind direction, Figure c) Total incident irradiance on the module

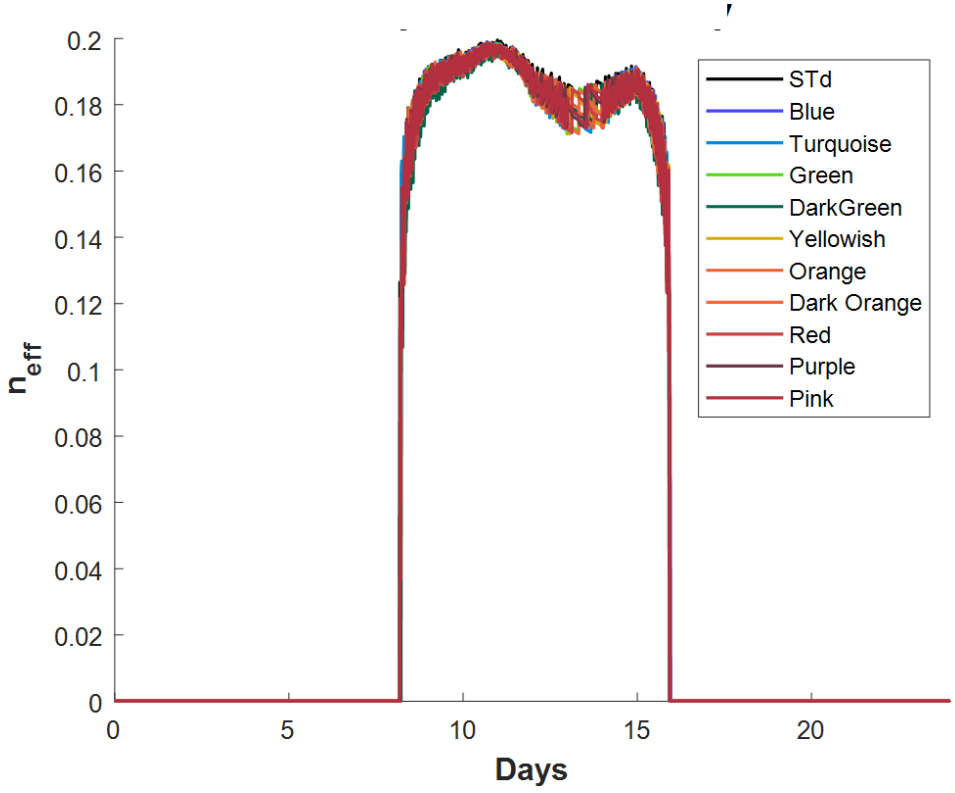

Figure A 17 Efficiency distribution for a for a free mounted module at 32 degrees on the 19th of January in Delft

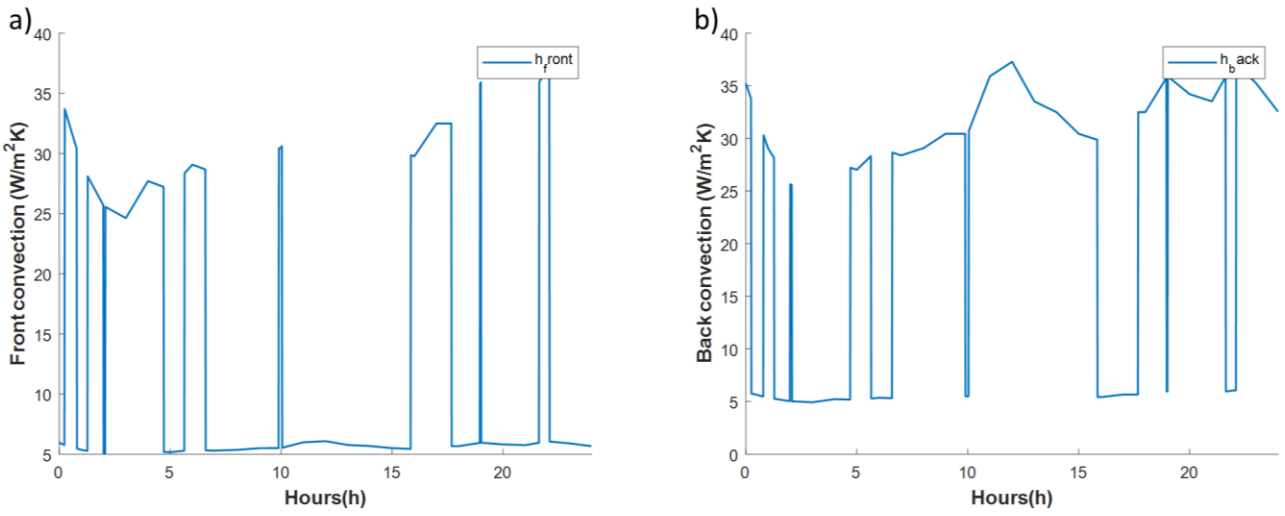

Figure A 18 Figure a) Total convection on the front, Figure b) Total convection on the back side for a free mounted module at 32 degrees on the 19th of January in Delft

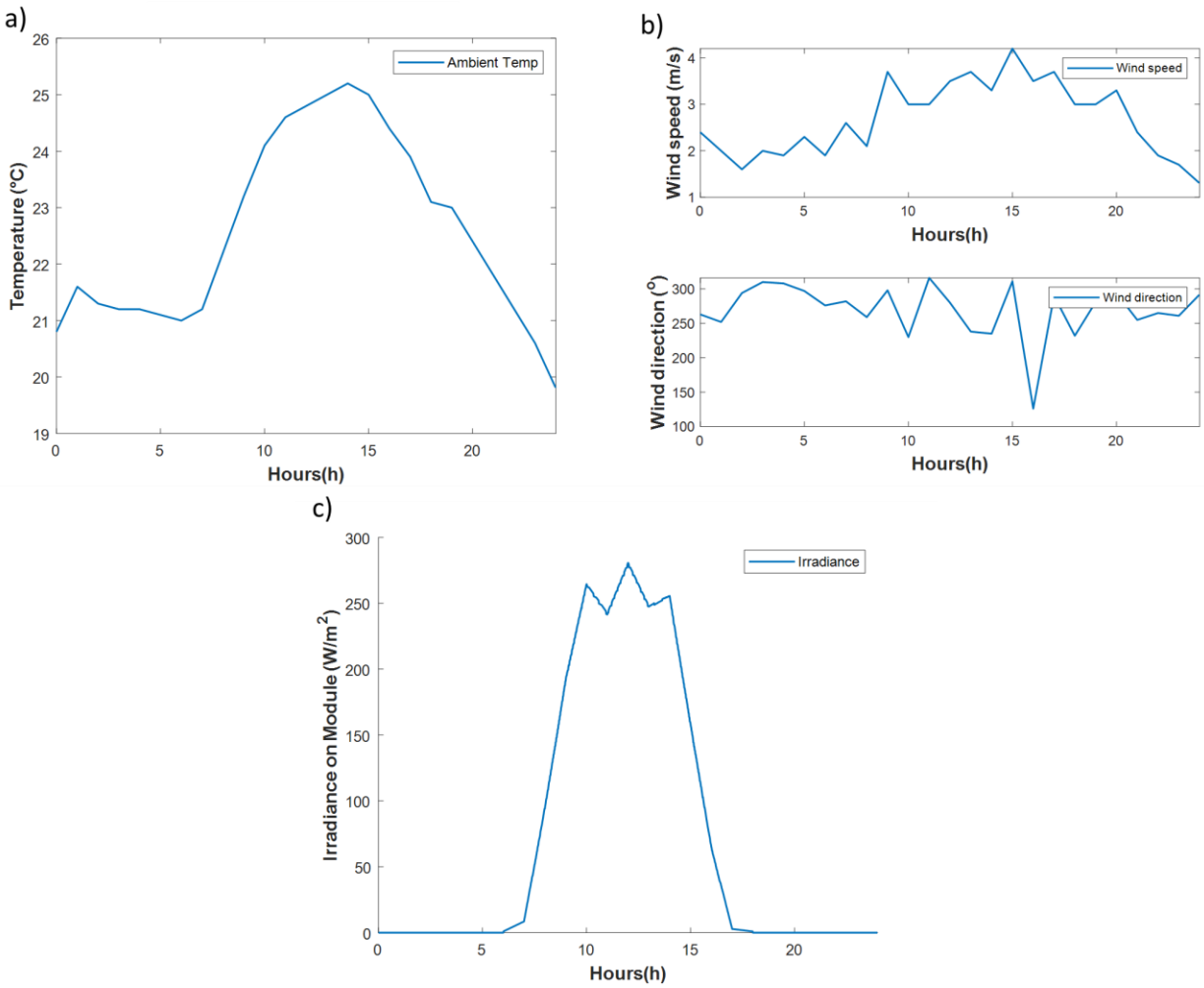

Figure A 19 Dubai weather data on the 1st of January; Figure a) Ambient Temperature distribution , Figure b) Wind speed and Wind direction, Figure c) Total incident irradiance on the module

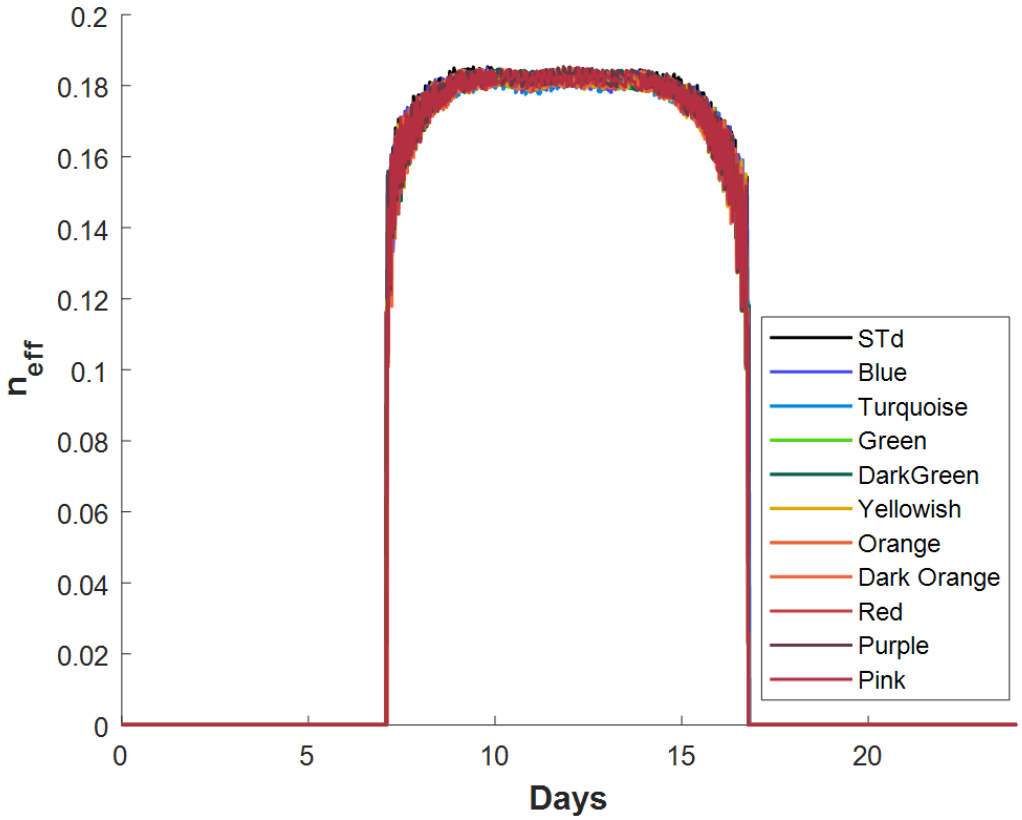

Figure A 20 Efficiency distribution for a for a free mounted module at 25 degrees on the 1st of January in Dubai

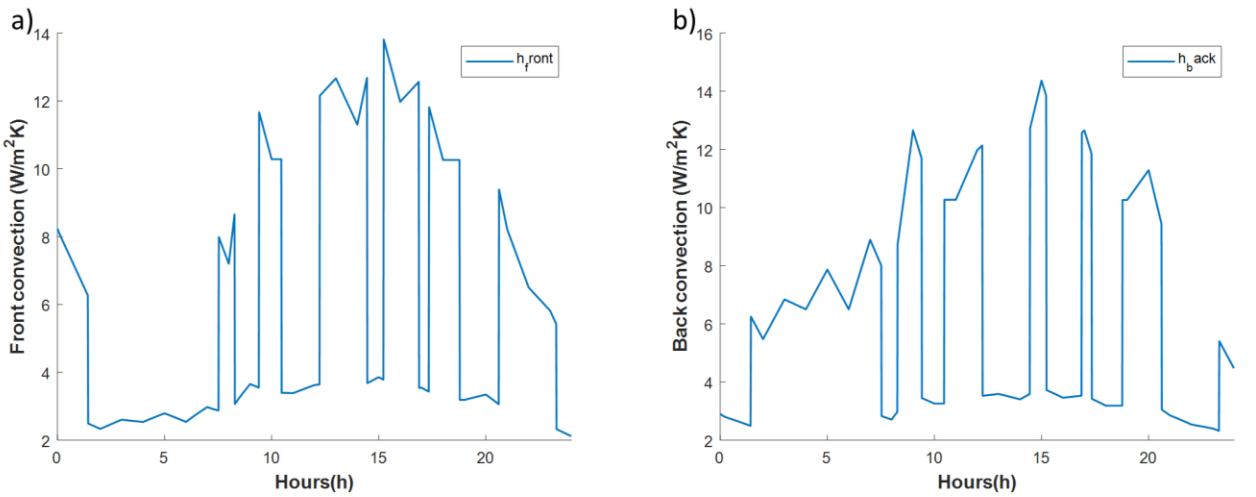

Figure A 21 Figure a) Total convection on the front, Figure b) Total convection on the back side of the module on the 1st of January in Dubai

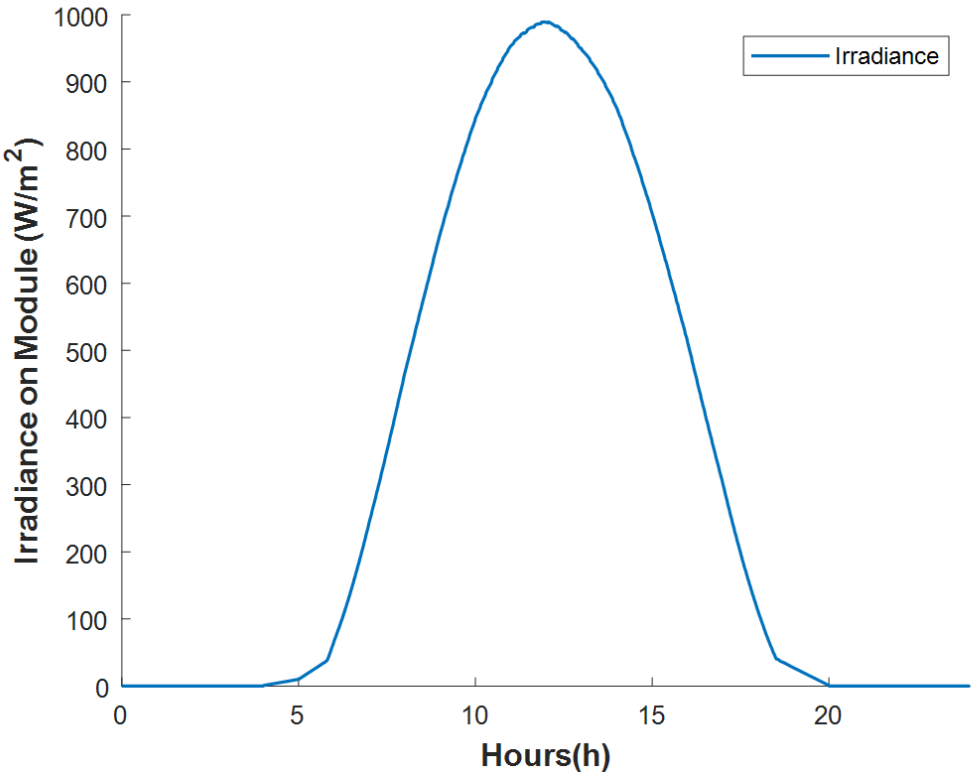

Figure A 22 Total incident irradiance on the module attached on a 35 degrees roof on the 5th of May

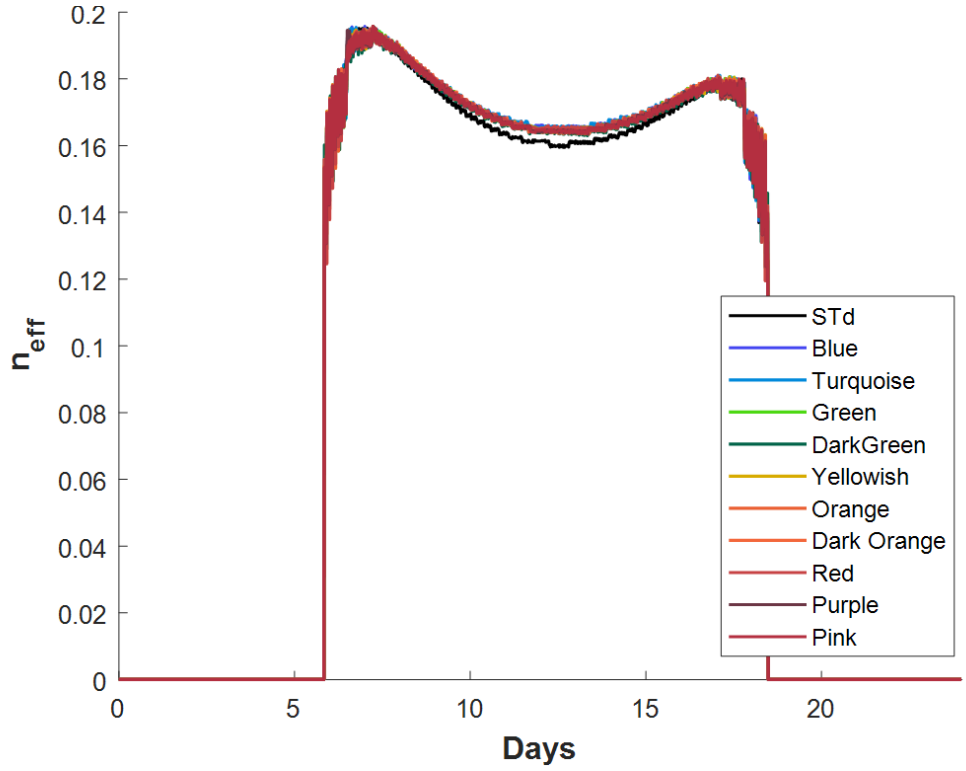

Figure A 23 Efficiency distribution for the modules attached on a 35 degrees roof on the 5th of May at Delft

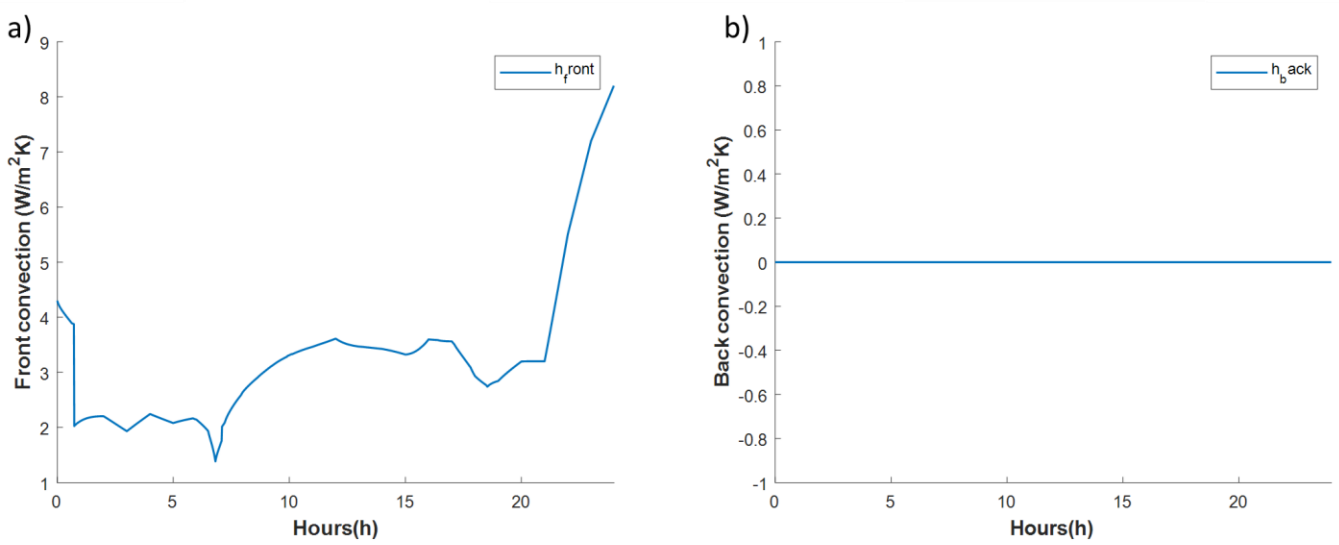

Figure A 24 Figure a) Total convection on the front, Figure b) Total convection on the back side of for the modules attached on a 35 degrees roof on the 5th of May at Delft

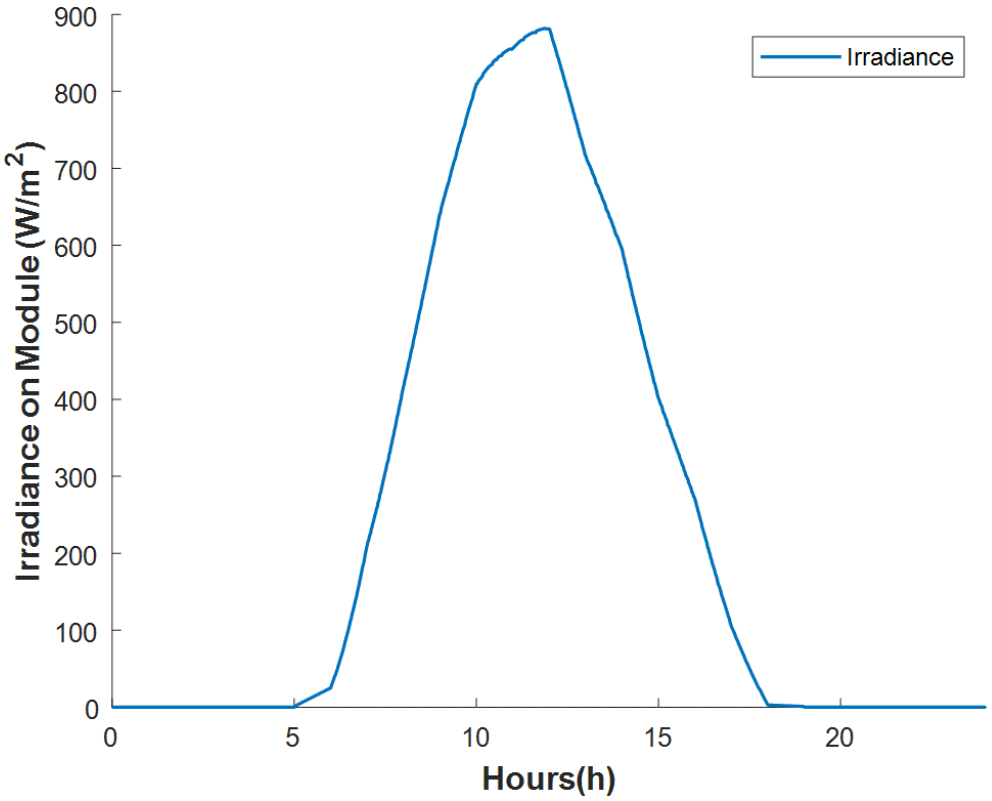

Figure A 25 Total incident irradiance on the module attached on a 20 degrees roof on the 3rd of September in Dubai

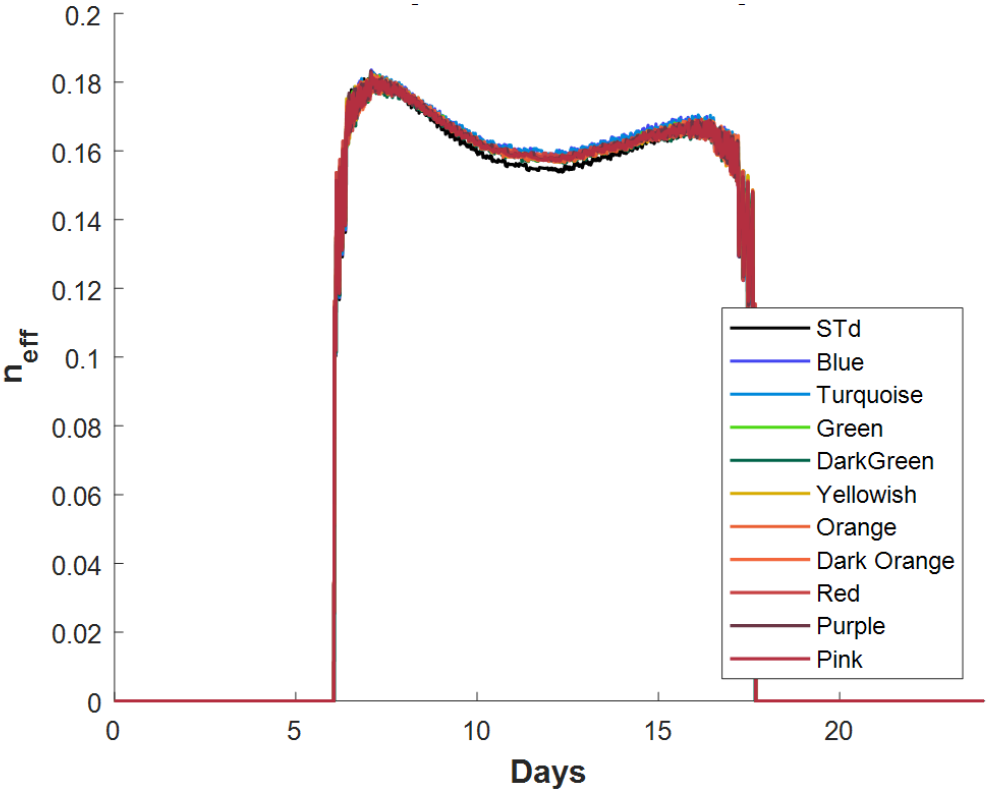

Figure A 26 Efficiency distribution for the modules attached on a 20 degrees roof on the 3rd of September in Dubai

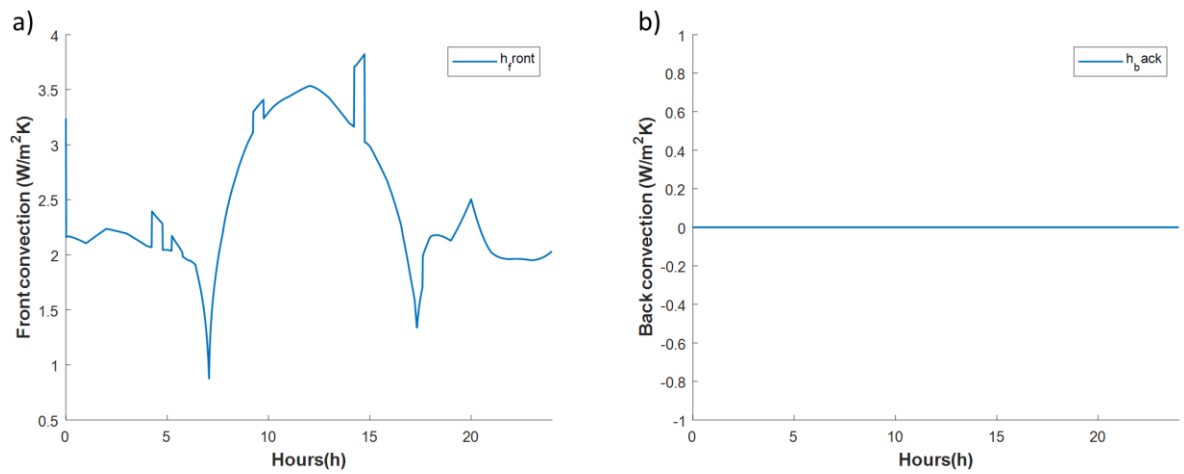

Figure A 27 Figure a) Total convection on the front, Figure b) Total convection on the back side of for the modules attached on a 20 degrees roof on the 3rd of September in Dubai

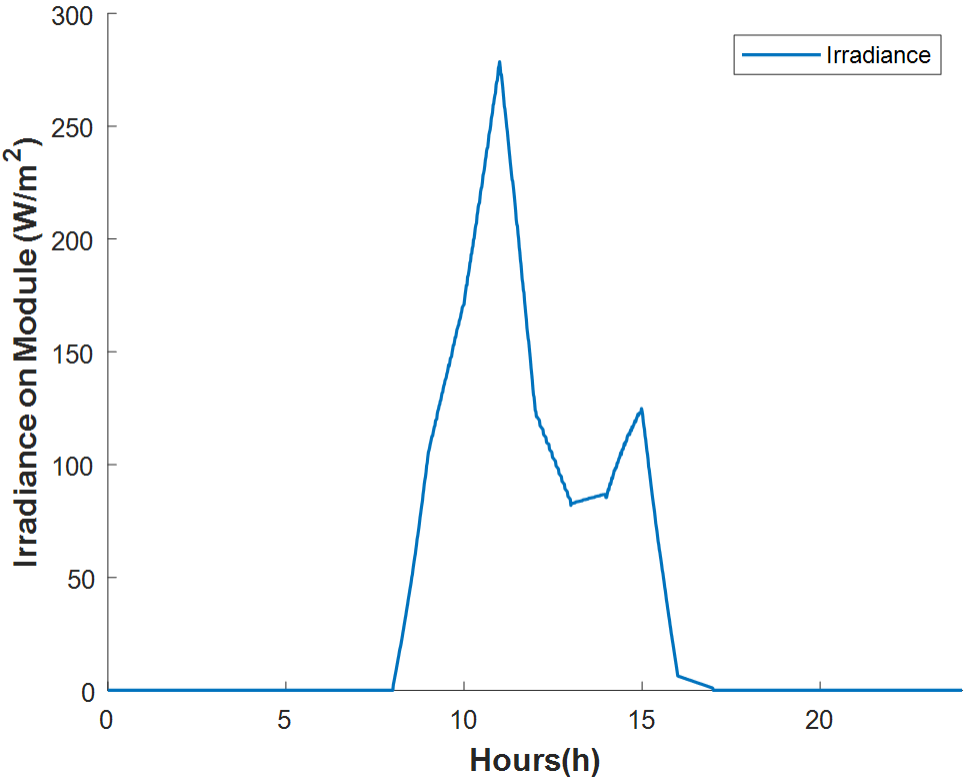

Figure A 28 Total incident irradiance on the module attached on a 35 degrees roof on the 19th of January Delft

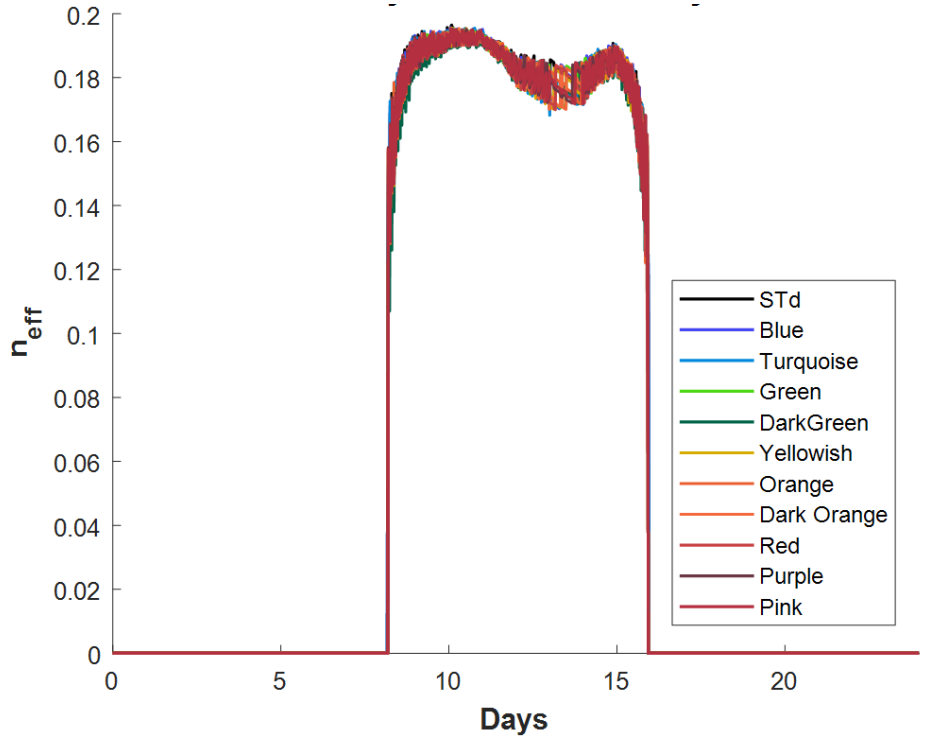

Figure A 29 Efficiency distribution for the modules attached on a 35 degrees roof on the on the 19th of January

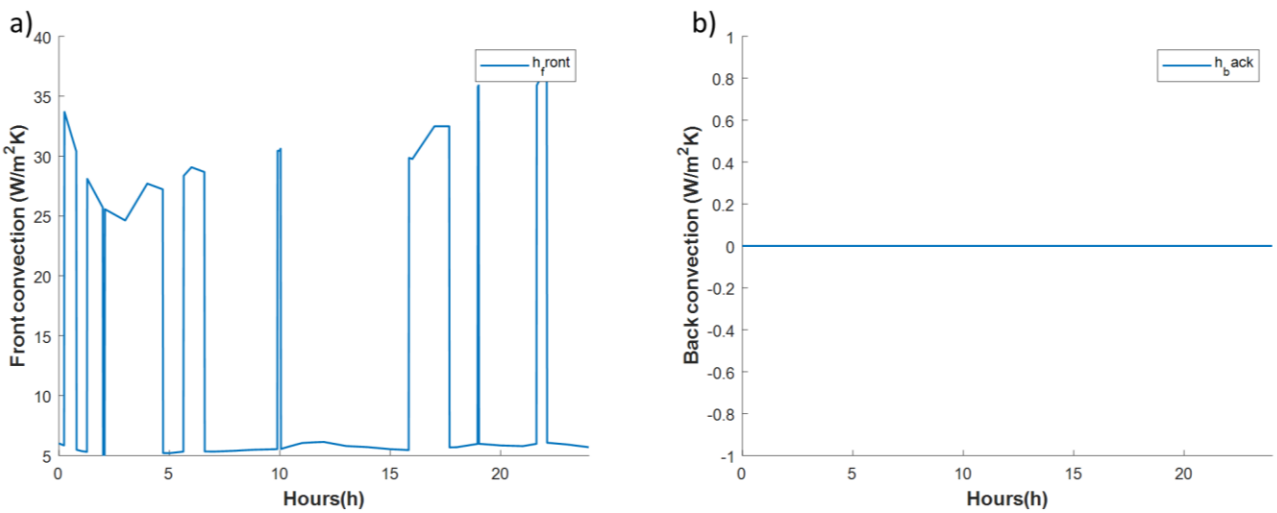

Figure A 30 Figure a) Total convection on the front, Figure b) Total convection on the back side for the modules attached on a 35 degrees roof on the 19th of January Delft

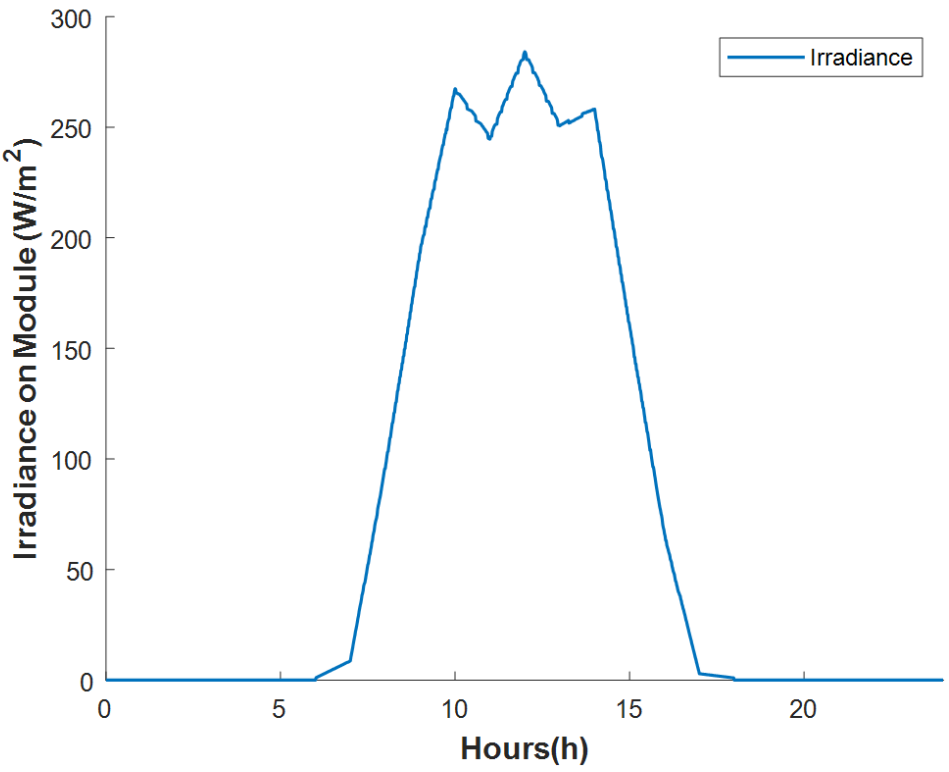

Figure A 31 Total incident irradiance on the module attached on a 20 degrees roof on the 1st of January Dubai

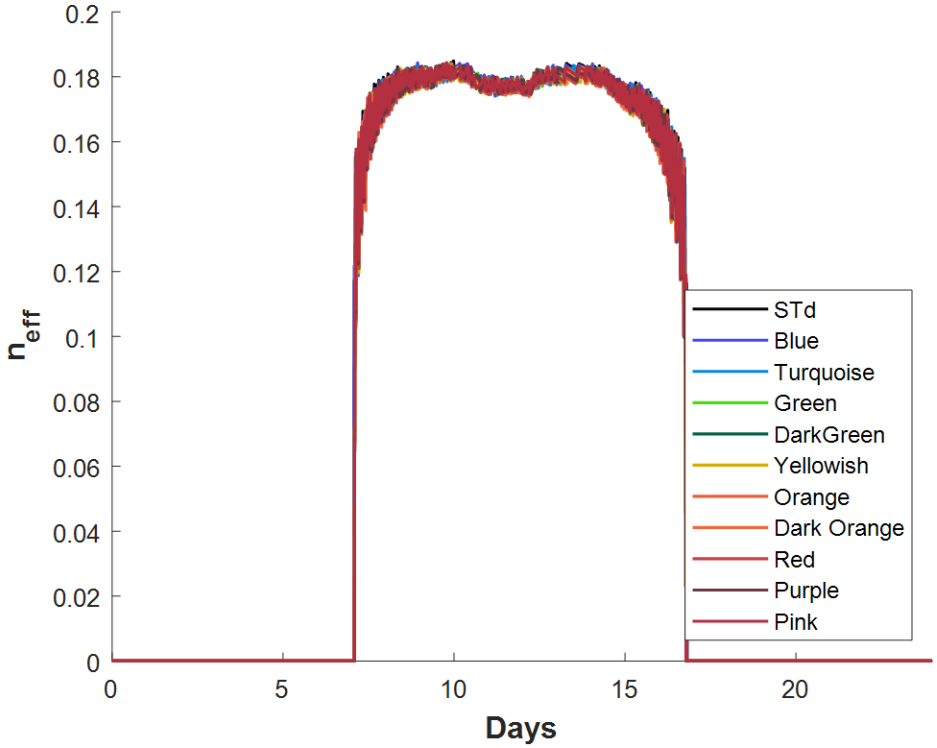

Figure A 32 Efficiency distribution for the modules attached on a 35 degrees roof on the 1st of January

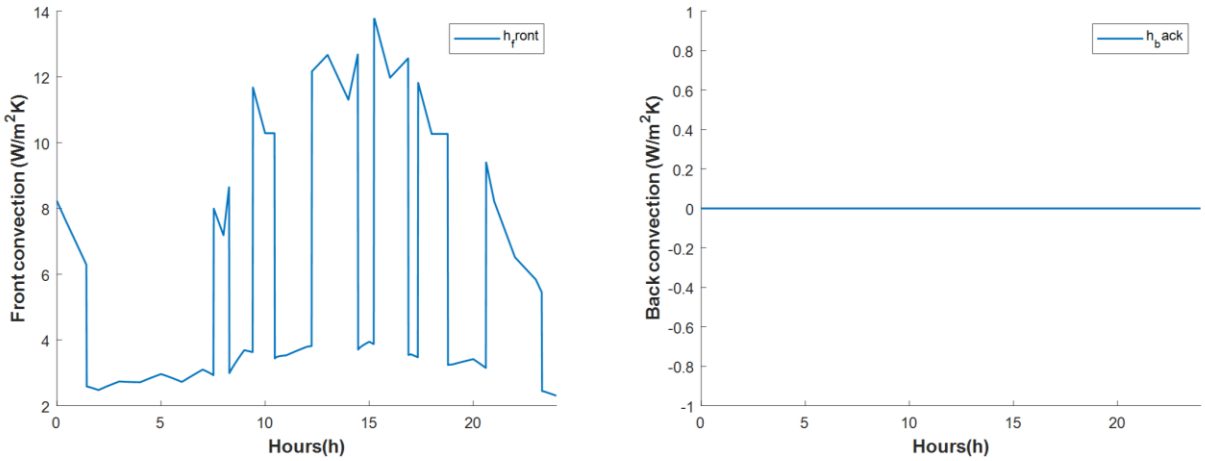

Figure A 33 Total convection on the front, Figure b) Total convection on the back side for the modules attached on a 35 degrees roof on the 1sh of January Dubai

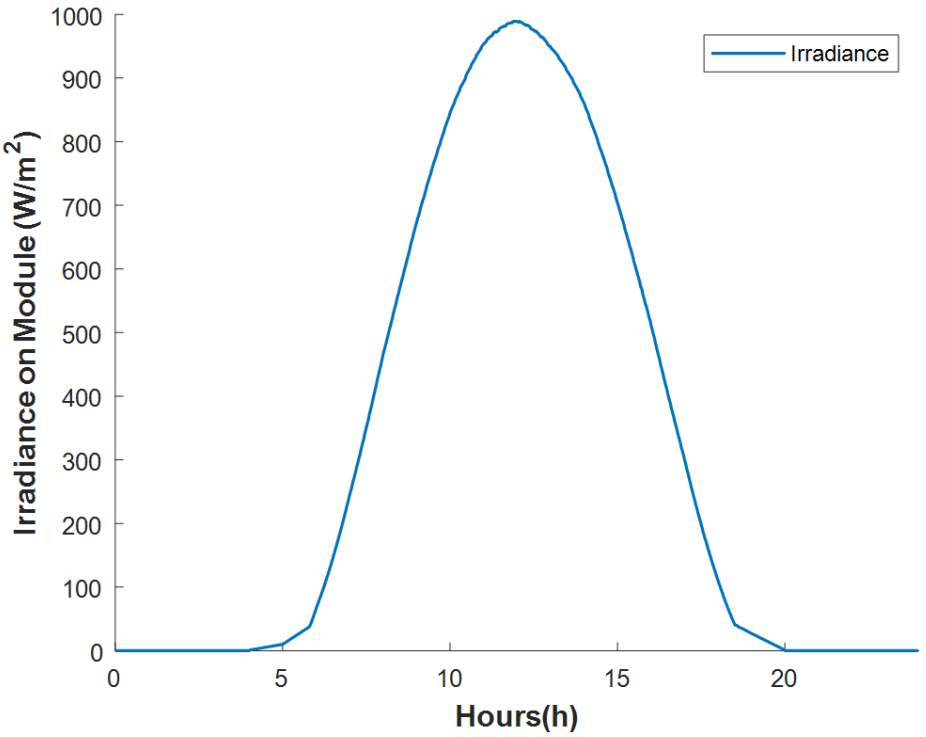

Figure A 34 Total incident irradiance on the module installed on 35 degrees roof with air gap on the 5th of May Delft

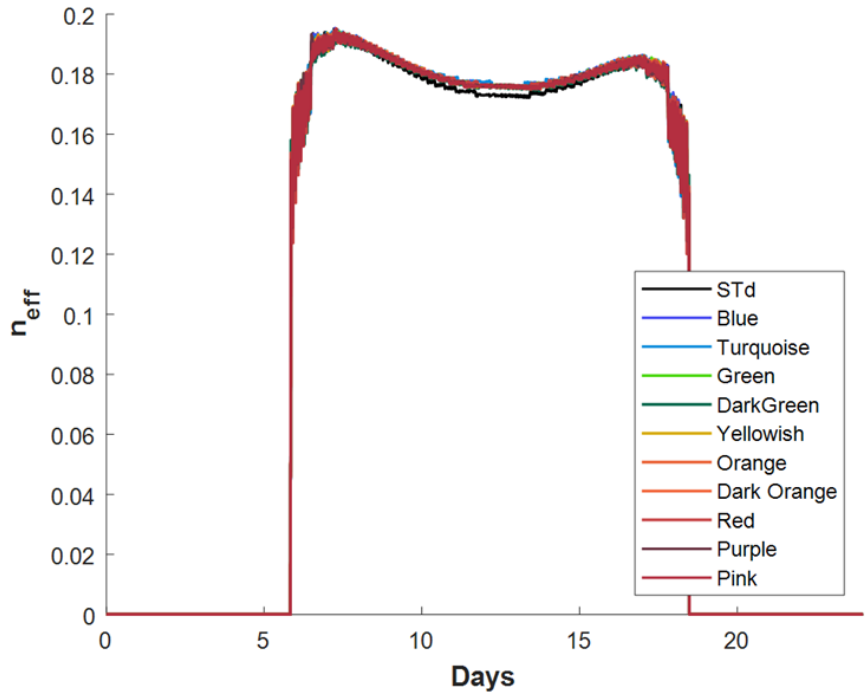

Figure A 35 Efficiency distribution for the modules attached on 35 degrees roof with air gap on the 5th of May in Delft

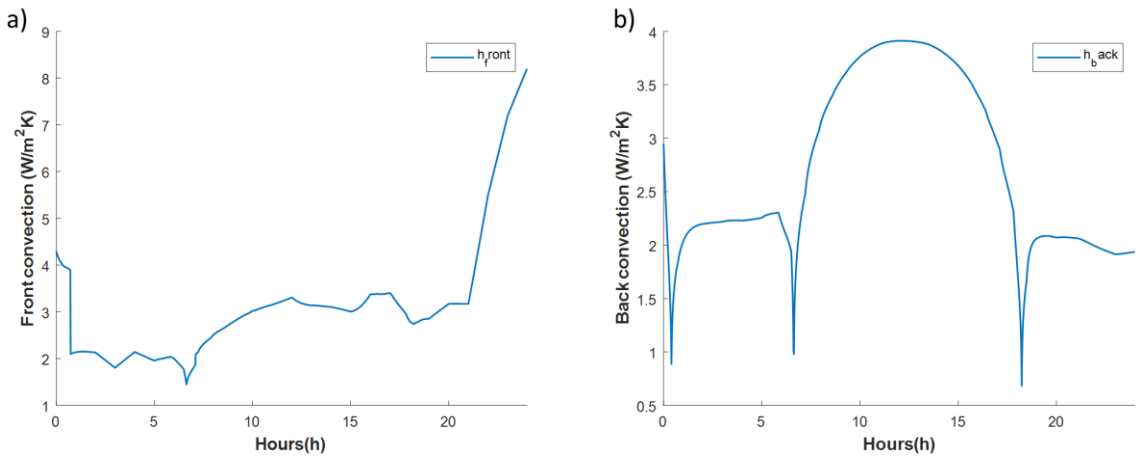

Figure A 36 Total convection on the front, Figure b) Total convection on the back side of the modules attached on 35 degrees roof with air gap on the 5th of May in Delft

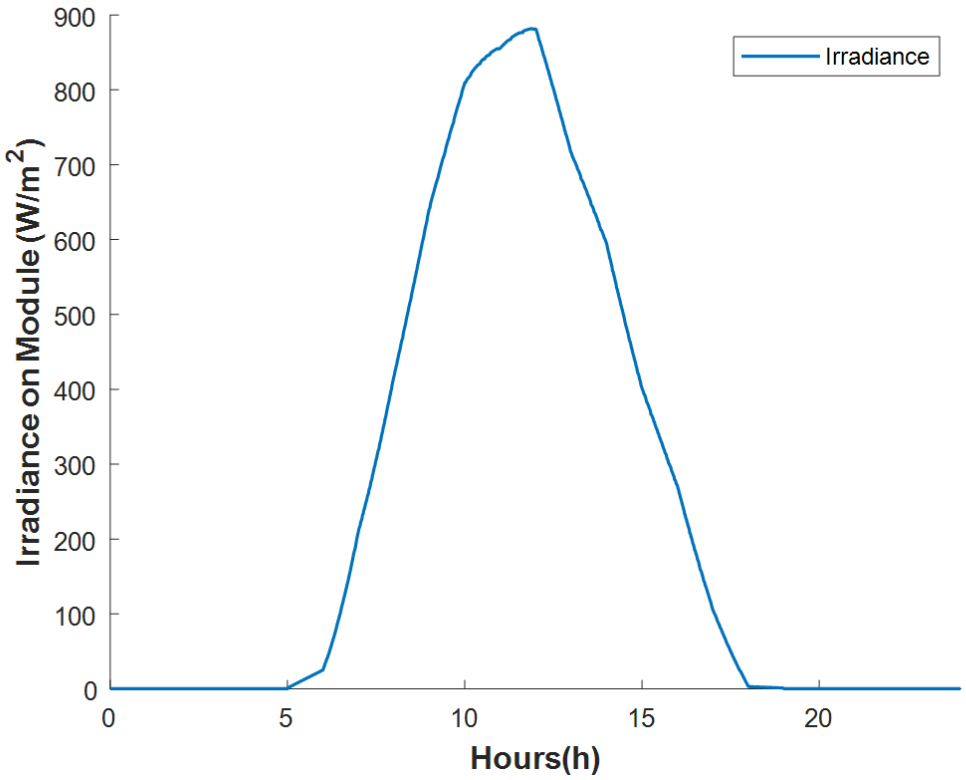

Figure A 37 Total incident irradiance for the modules attached on 20 degrees roof with air gap on the 3rd of September in Dubai

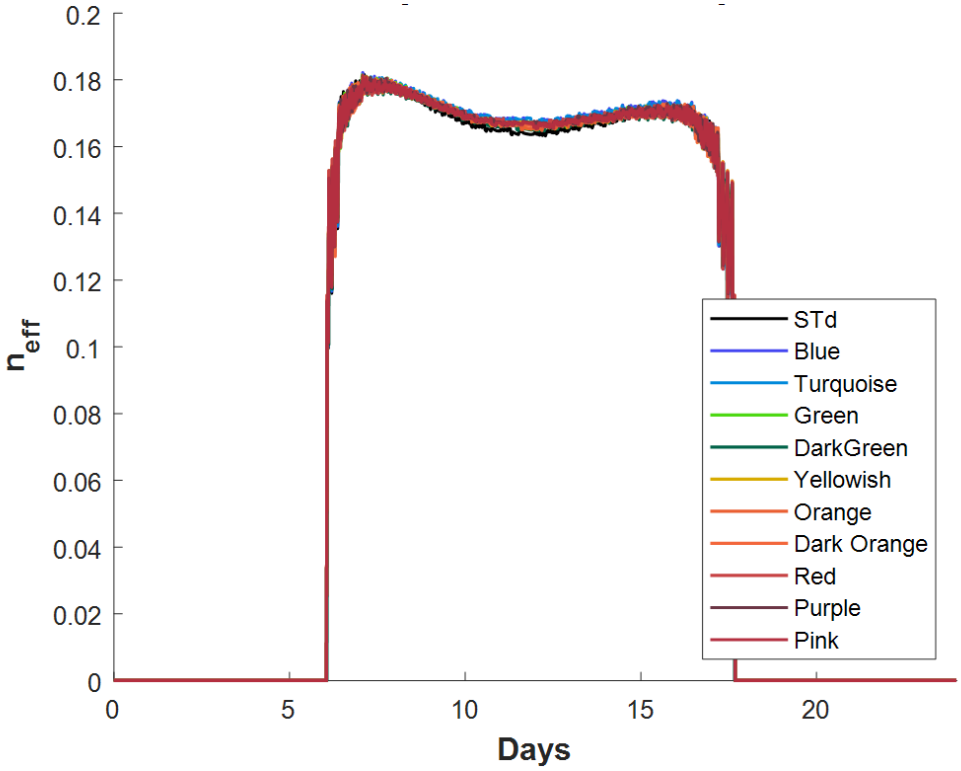

Figure A 38 Efficiency distribution for the modules attached on 20 degrees roof with air gap on the 3rd of September in Dubai

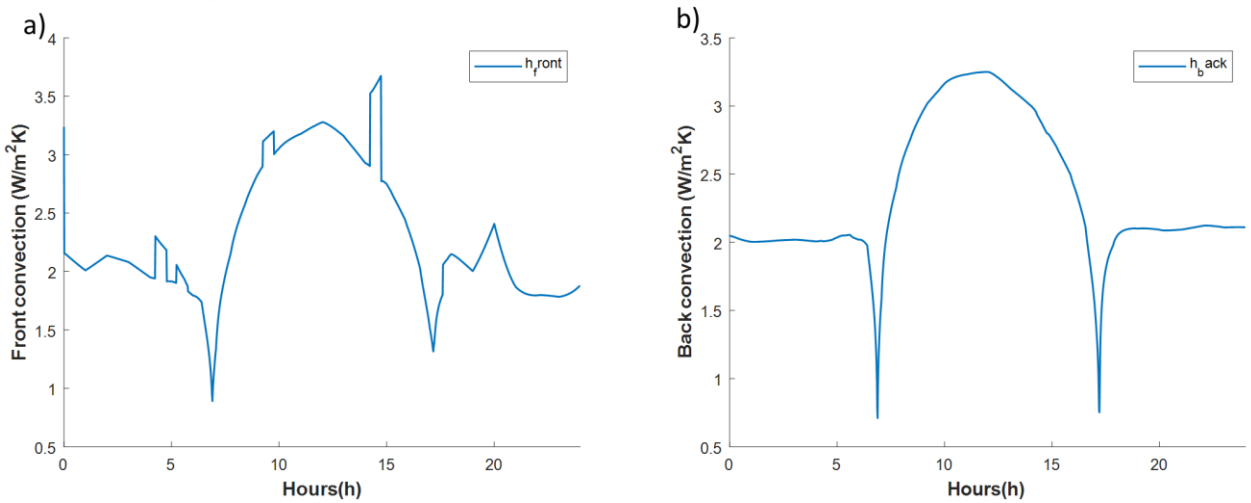

Figure A 39 Total convection on the front, Figure b) Total convection on the back side of the module attached on 20 degrees roof with air gap on the 3rd of September in Dubai

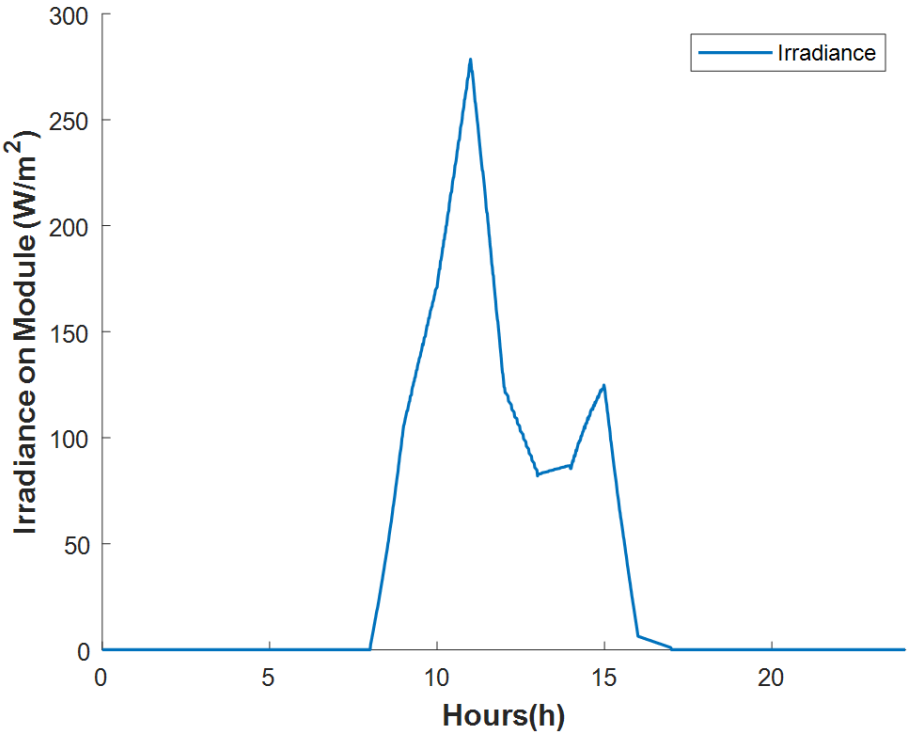

Figure A 40 Total incident irradiance for the modules attached on 35 degrees roof with air gap on the 19th of January in Delft

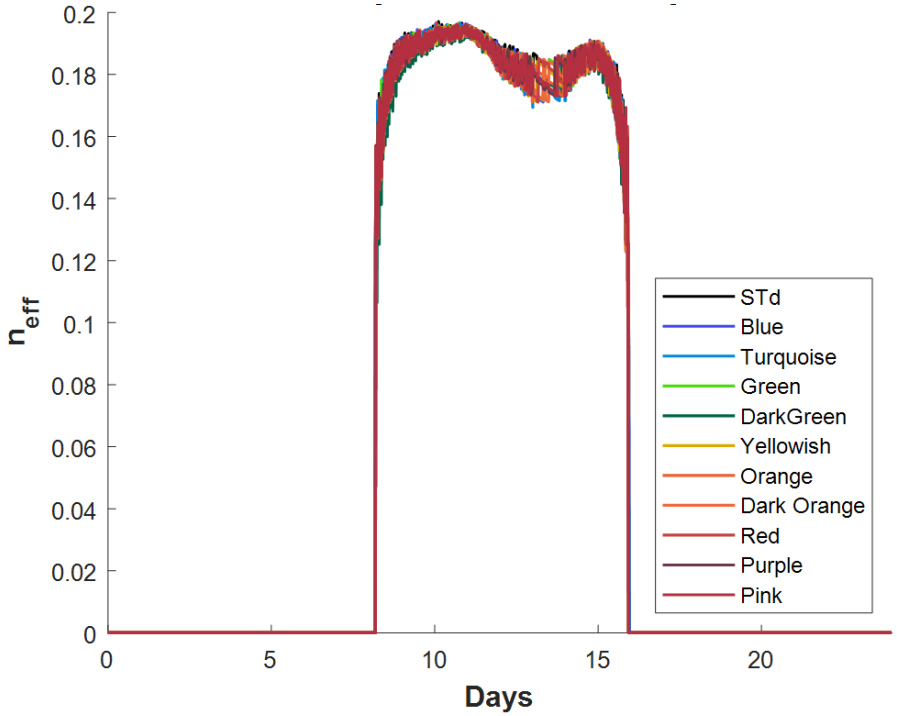

Figure A 41 Efficiency distribution for the modules attached on 35 degrees roof with air gap on the 9th of January in Delft

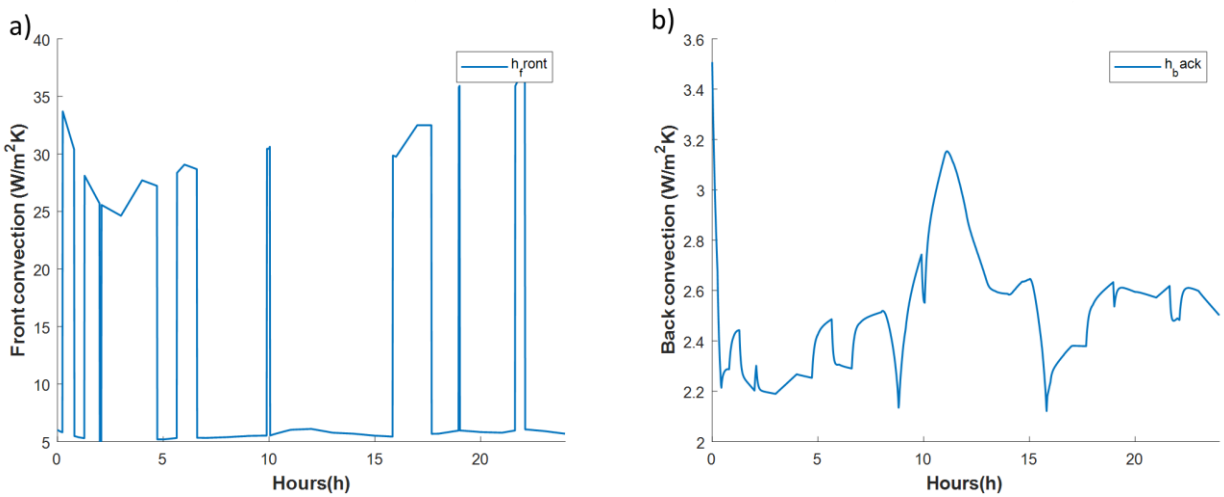

Figure A 42 Total convection on the front, Figure b) Total convection on the back side of the module attached on 35 degrees roof with air gap on the on the 19th of January in Delft

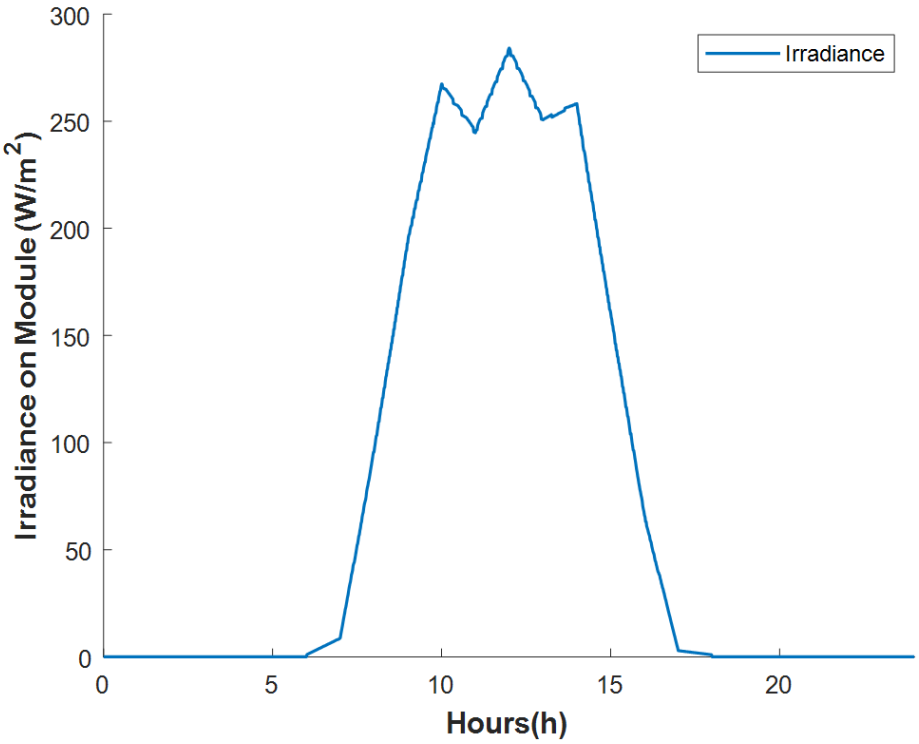

Figure A 43 Total incident irradiance for the modules attached on 35 degrees roof with air gap on the 1st of January in Dubai

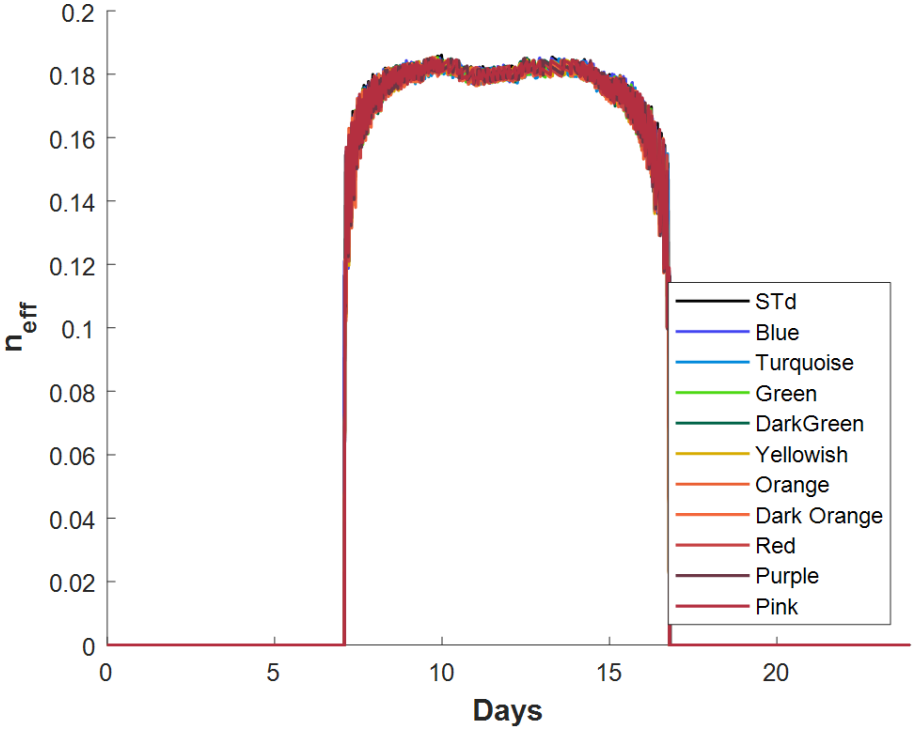

Figure A 44 Efficiency distribution for the modules attached on 20 degrees roof with air gap on the 1th of January in Dubai

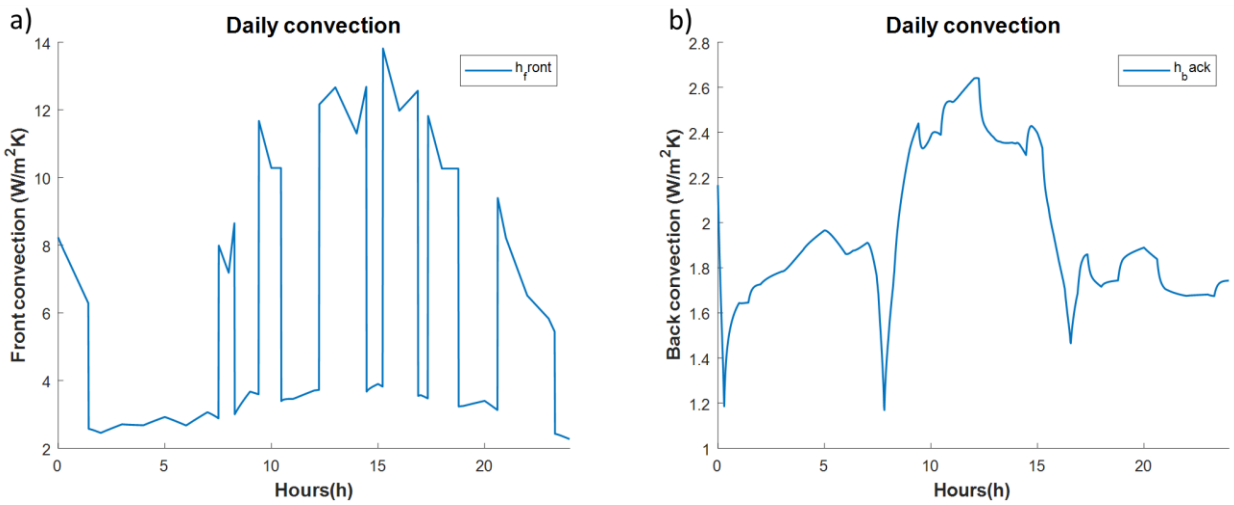

Figure A 45 Total convection on the front, Figure b) Total convection on the back side of the module attached on 20 degrees roof with air gap on the on the 1th of January in Dubai

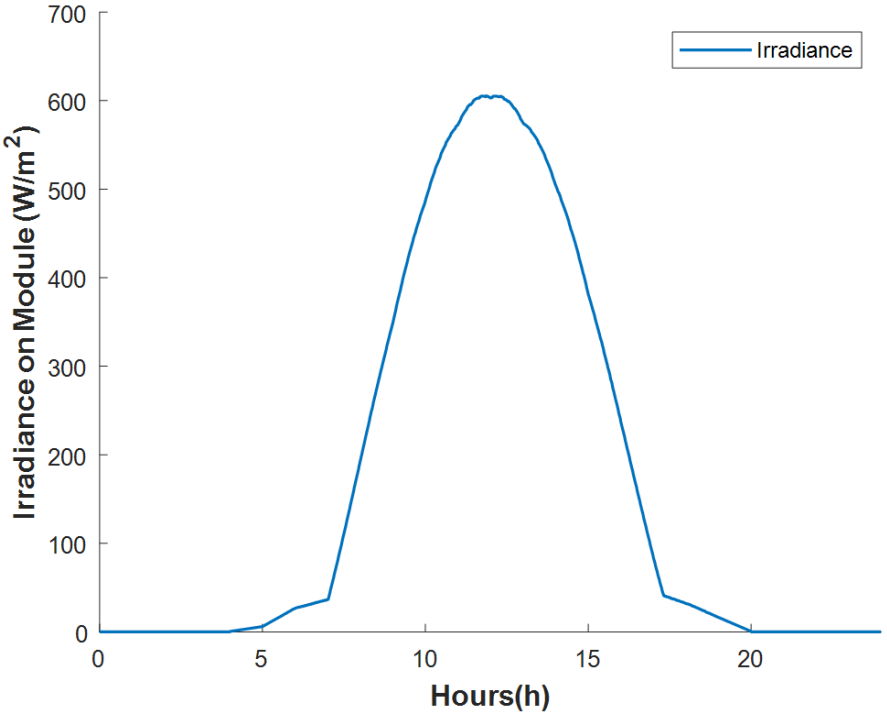

Figure A 46 Total incident irradiance for the modules attached on a façade on the 5th of May in Delft

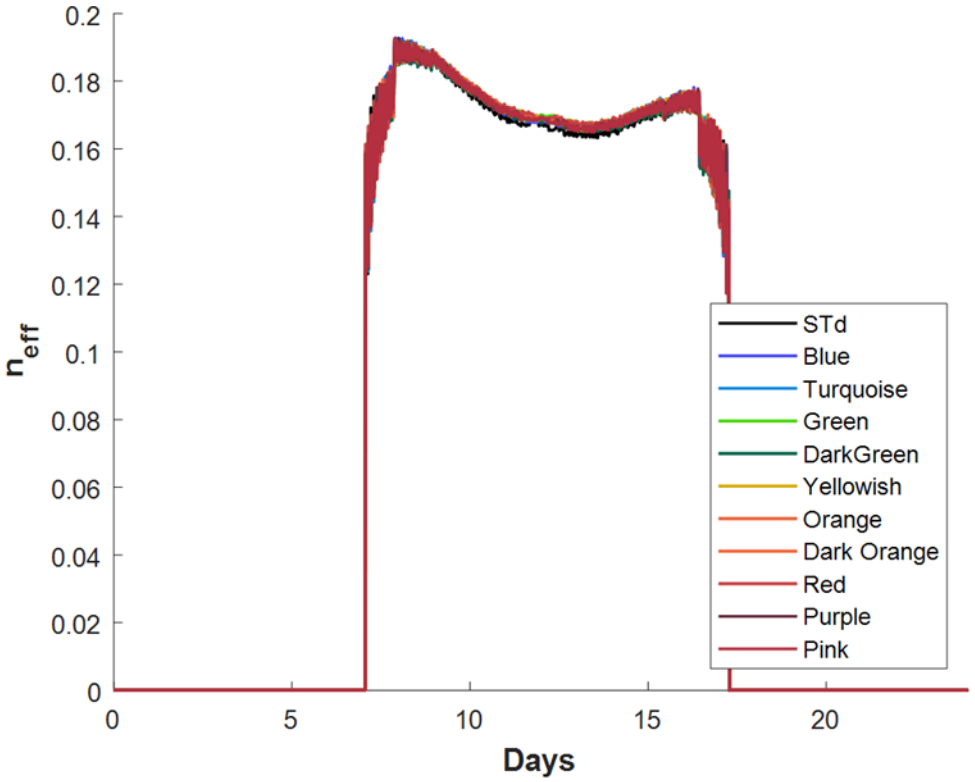

Figure A 47 Efficiency distribution for the modules attached on a façade on the 5th of May in Delft

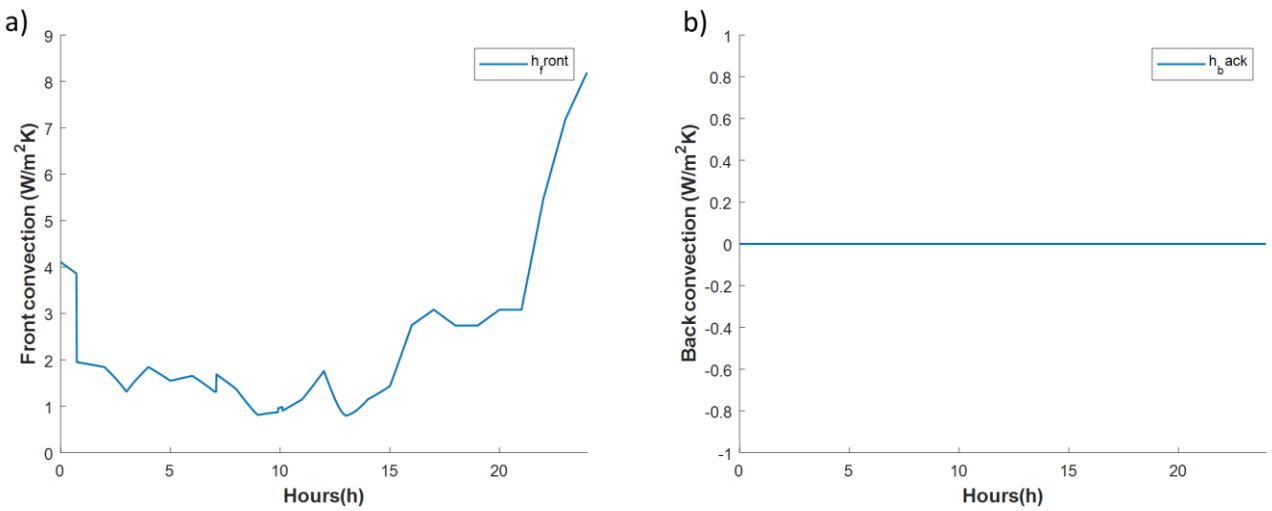

Figure A 48 Total convection on the front, Figure b) Total convection on the back side of the module attached on a façade on the 5th of May in Delft

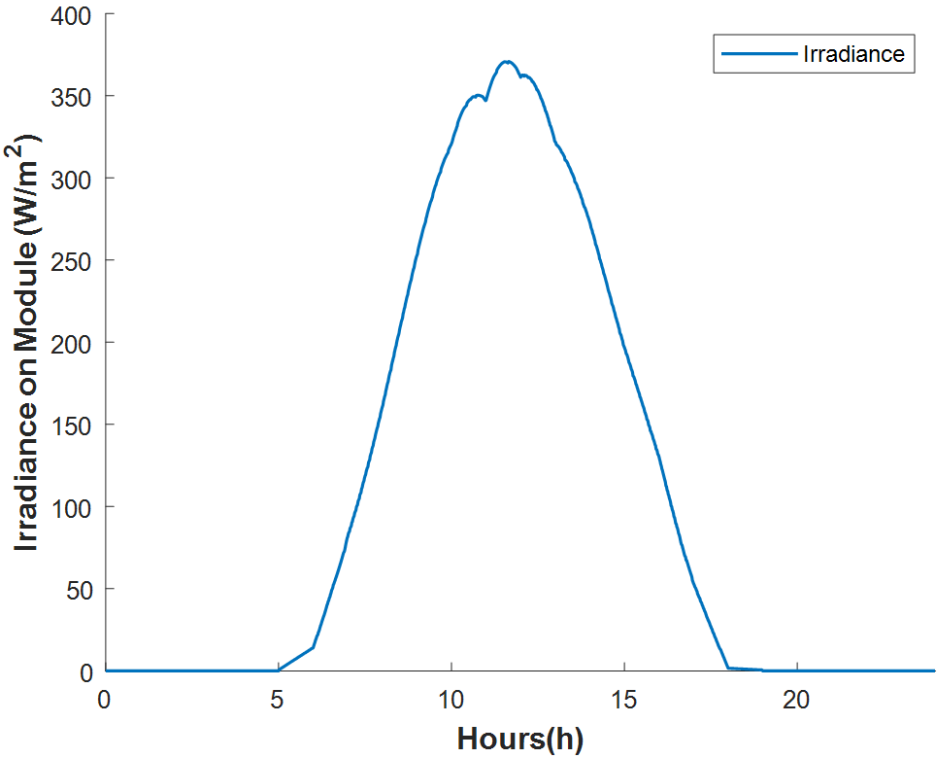

Figure A 49 Total incident irradiance for the modules attached on a façade on the 3rd of September in Dubai

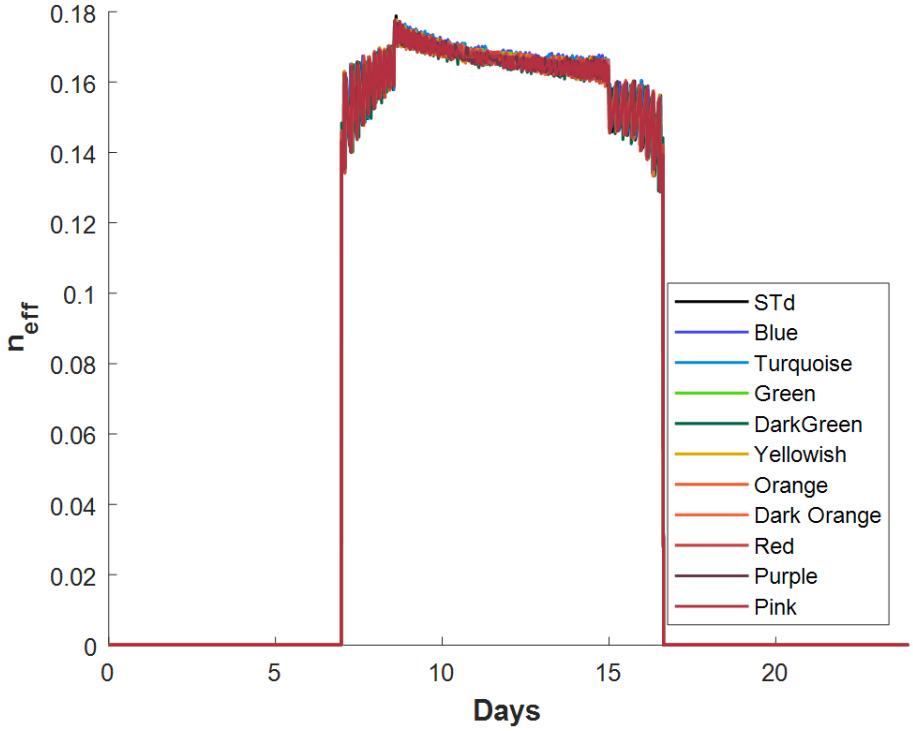

Figure A 50 Efficiency distribution for the modules attached on a façade on the 3rd of September in Dubai

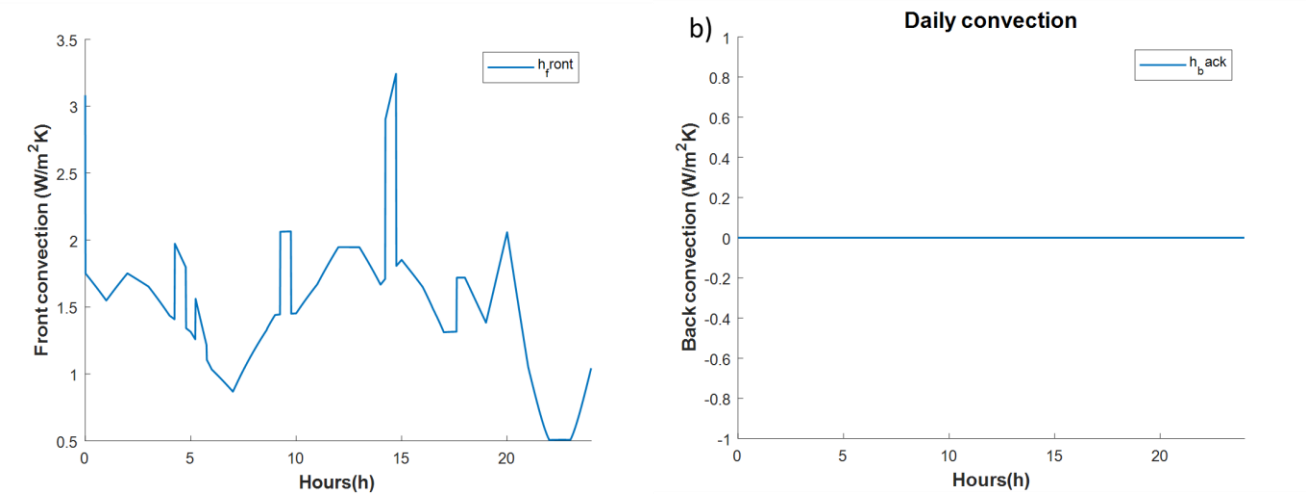

Figure A 51 Total convection on the front, Figure b) Total convection on the back side of the module attached on a façade on the 3rd of September in Dubai

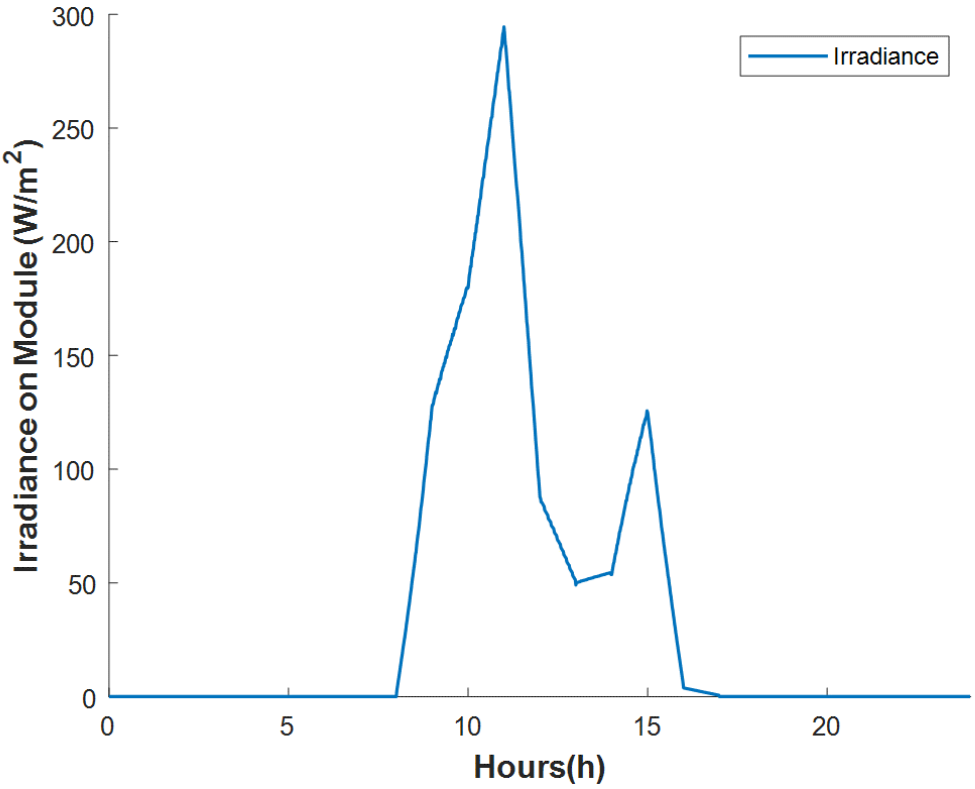

Figure A 52 Total incident irradiance for the modules attached on a façade on the 19th of January in Delft

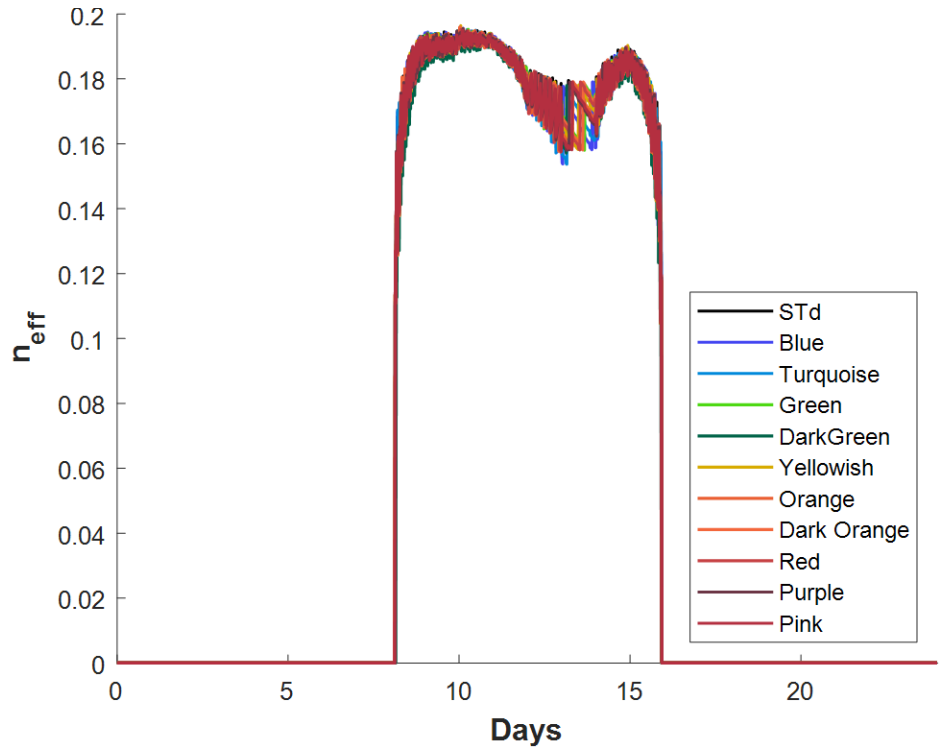

Figure A 53 Efficiency distribution for the modules attached on a façade on the 19th of January in Delft

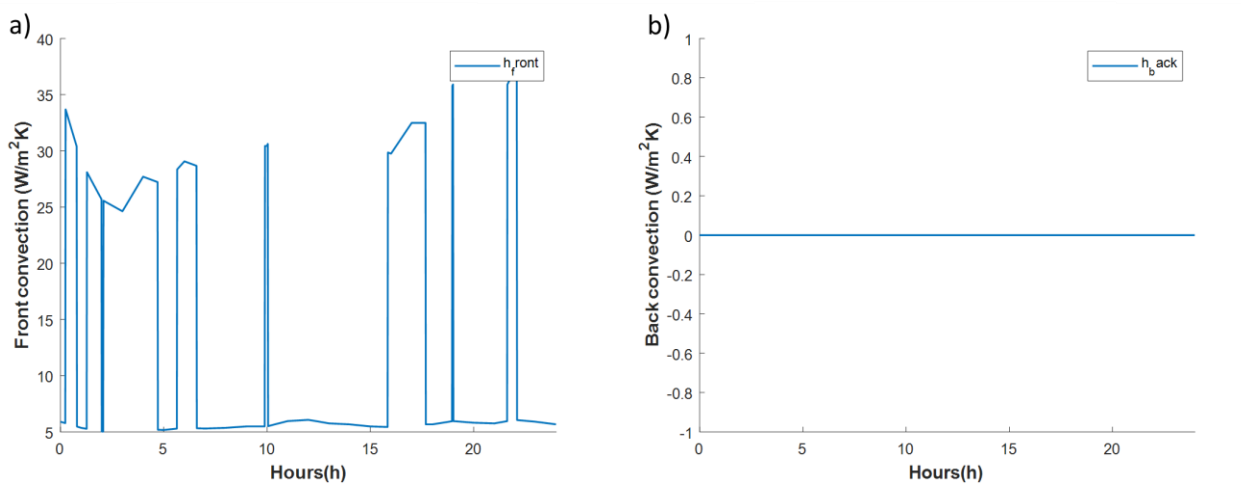

Figure A 54 Total convection on the front, Figure b) Total convection on the back side of the module attached on a façade on the 19th of January in Delft

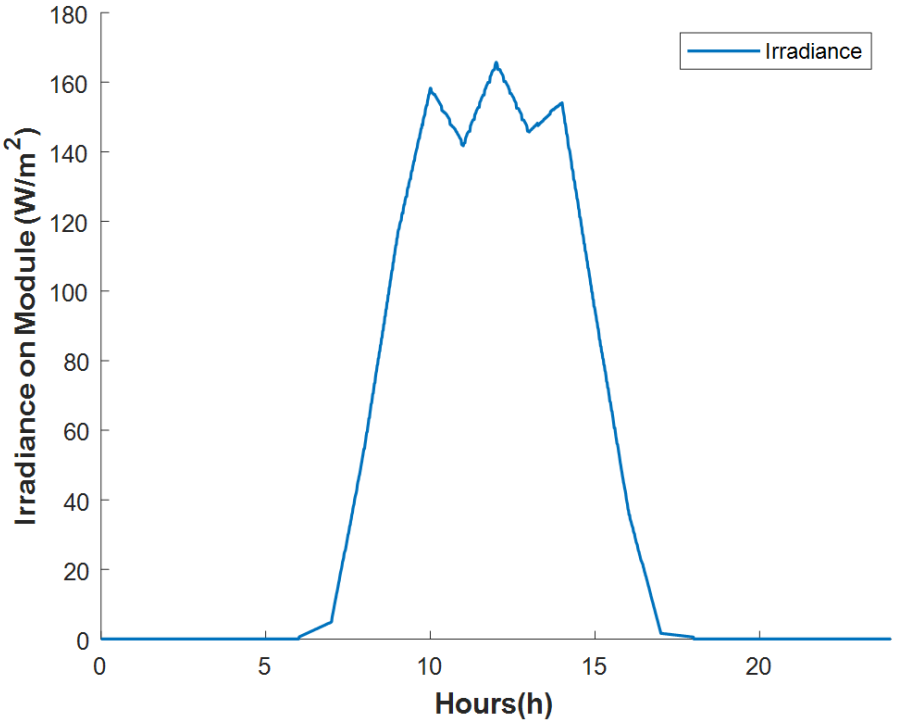

Figure A 55 Total incident irradiance for the modules attached on a façade on the 1st of January in Dubai

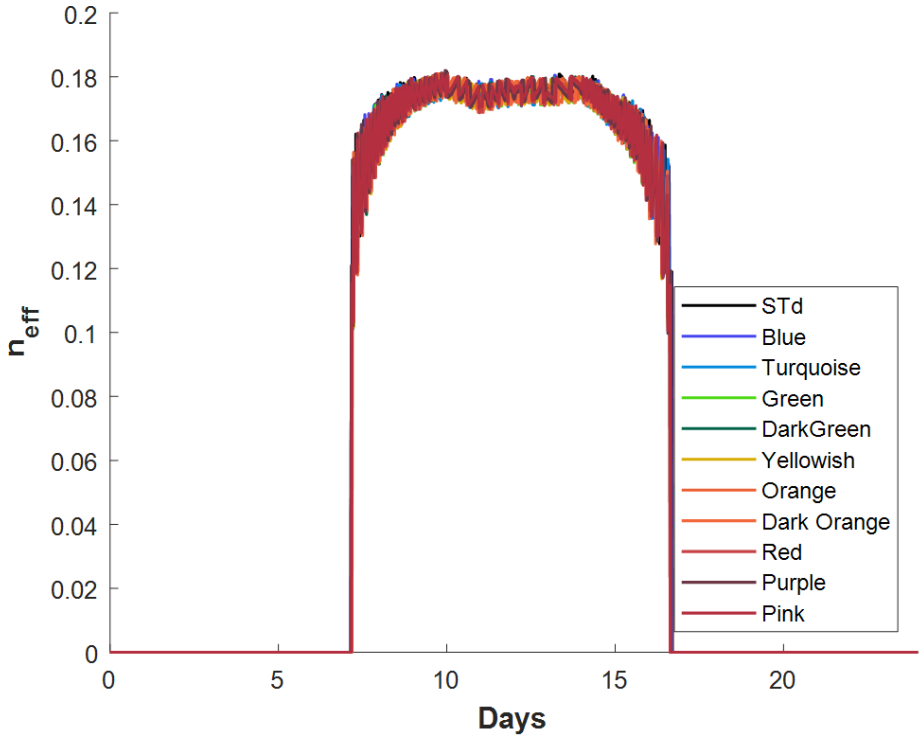

Figure A 56 Efficiency distribution for the modules attached on a façade on the 1st of January in Dubai

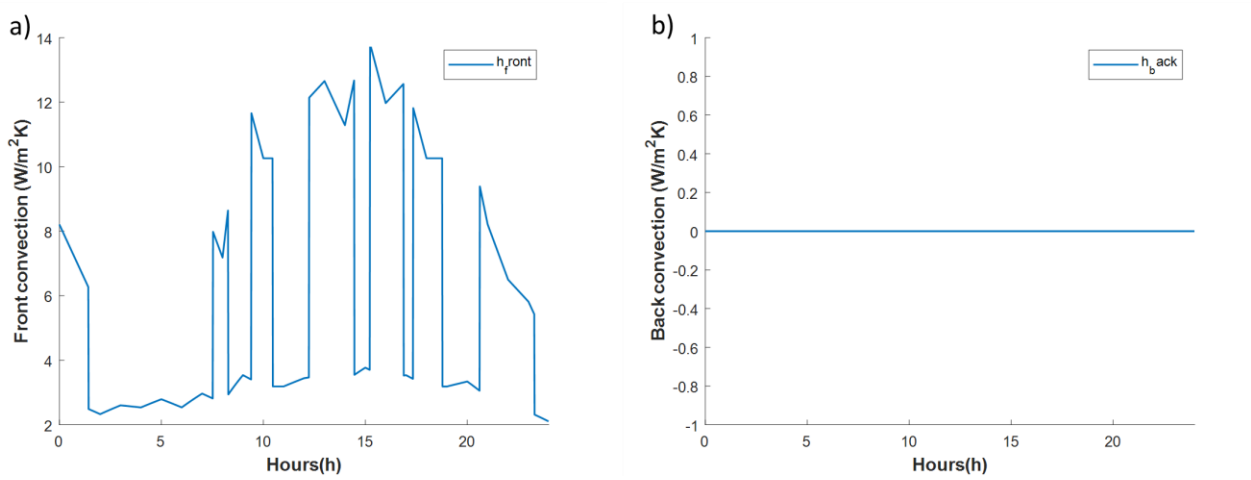

Figure A 57 Total convection on the front, Figure b) Total convection on the back side of the module attached on a façade on the 1st of January in Dubai

Appendix C Results of the façade with an air gap

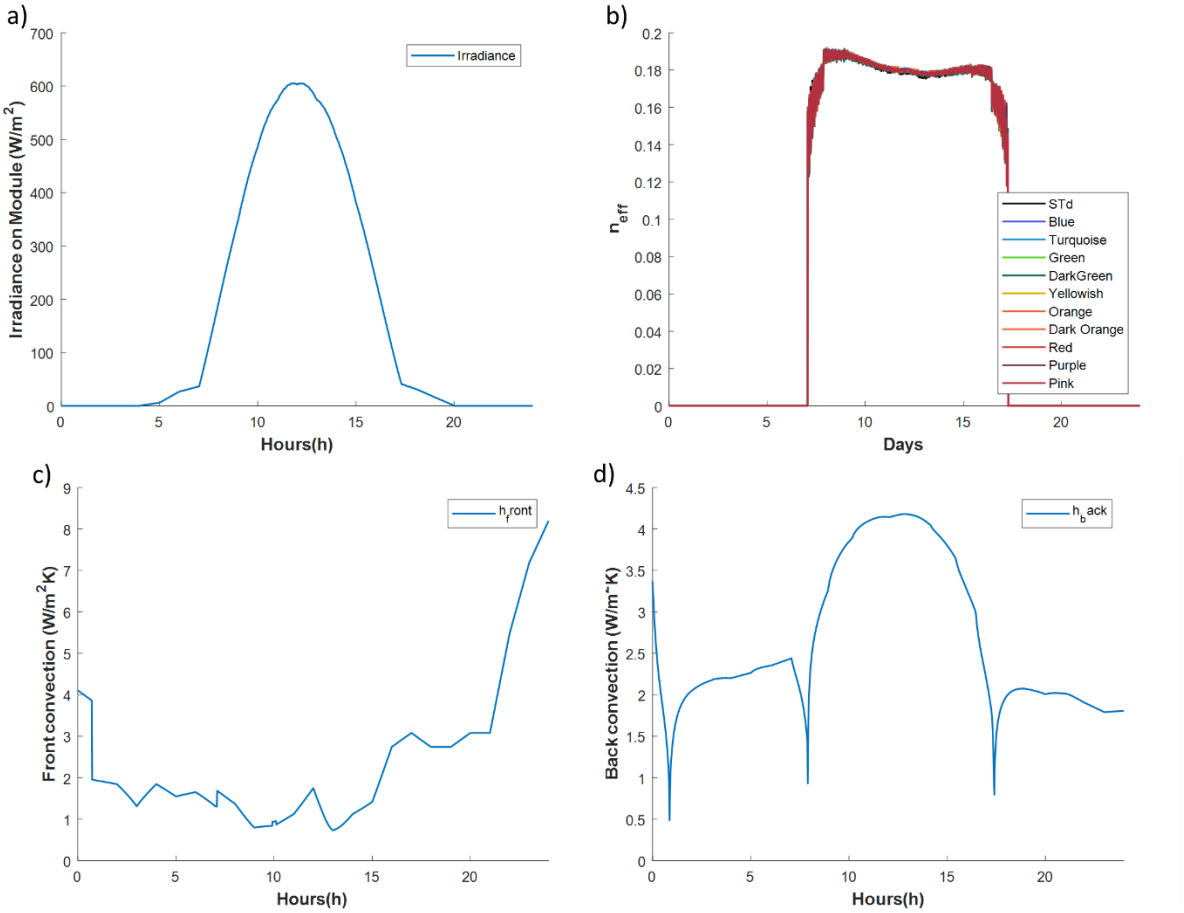

Figure A 58 Figure a) Total incident irradiance for the modules attached on a façade with an air gap on the 5th of May in Delft, Figure b) Efficiency distribution for the modules attached on a façade on the 5th of May in Delft, Figure c) Total convection on the front, Figure b) Total convection on the back side of the module attached on a façade with an air gap on the 5th of May in Delft

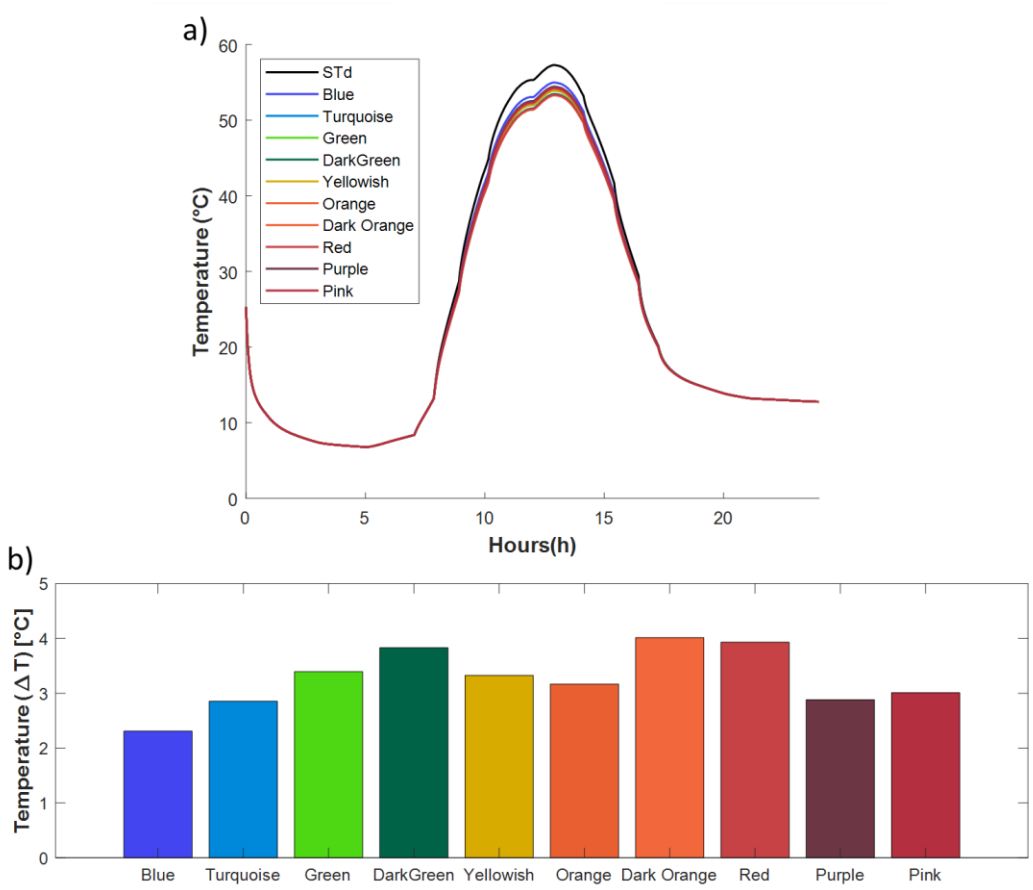

Figure A 59 Figure a) Temperature distribution for the standard module and the 10 main colors attached on a façade with an air gap on the 5th of May in Delft, Figure b) Temperature difference for each color from the maximum temperature of the standard module

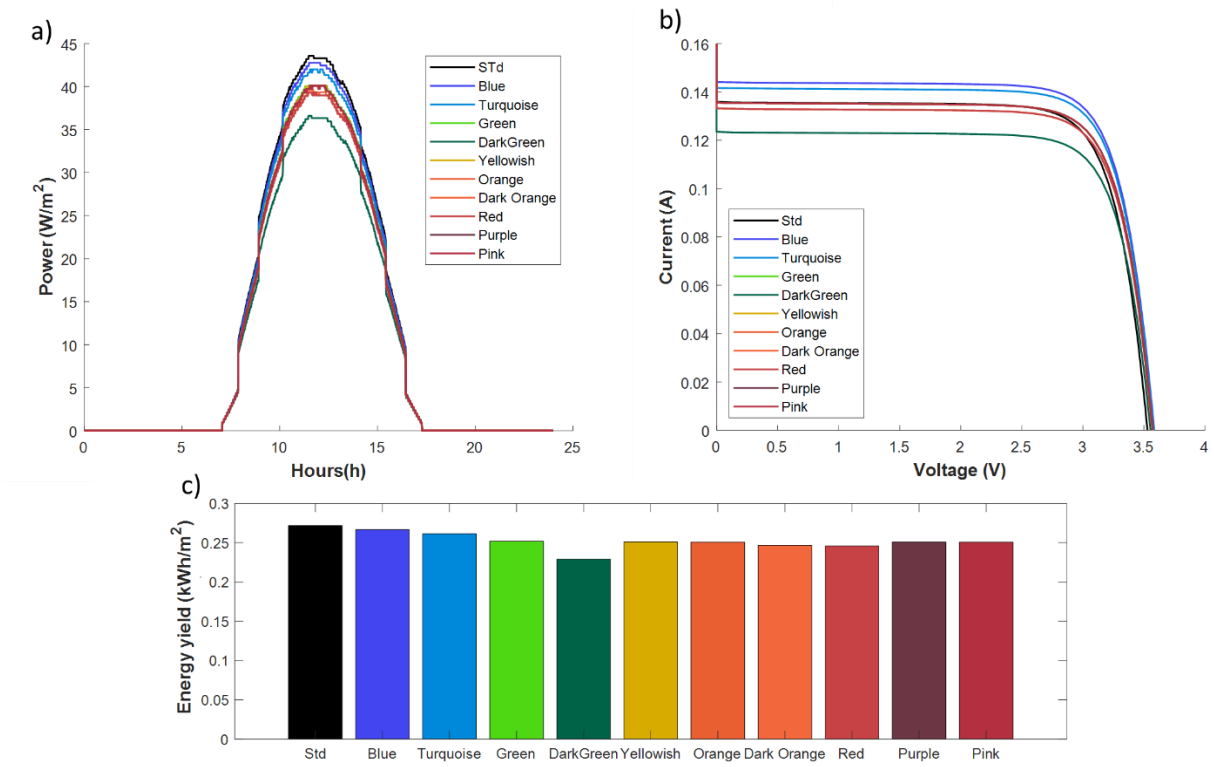

Figure A 60 Figure a) Power distribution for the standard module and the 10 main colors attached on a façade with an air gap on the 5th of May in Delft, Figure b) Efficiency distribution, Figure c) Energy yield difference for each color from the total energy yield of the standard module

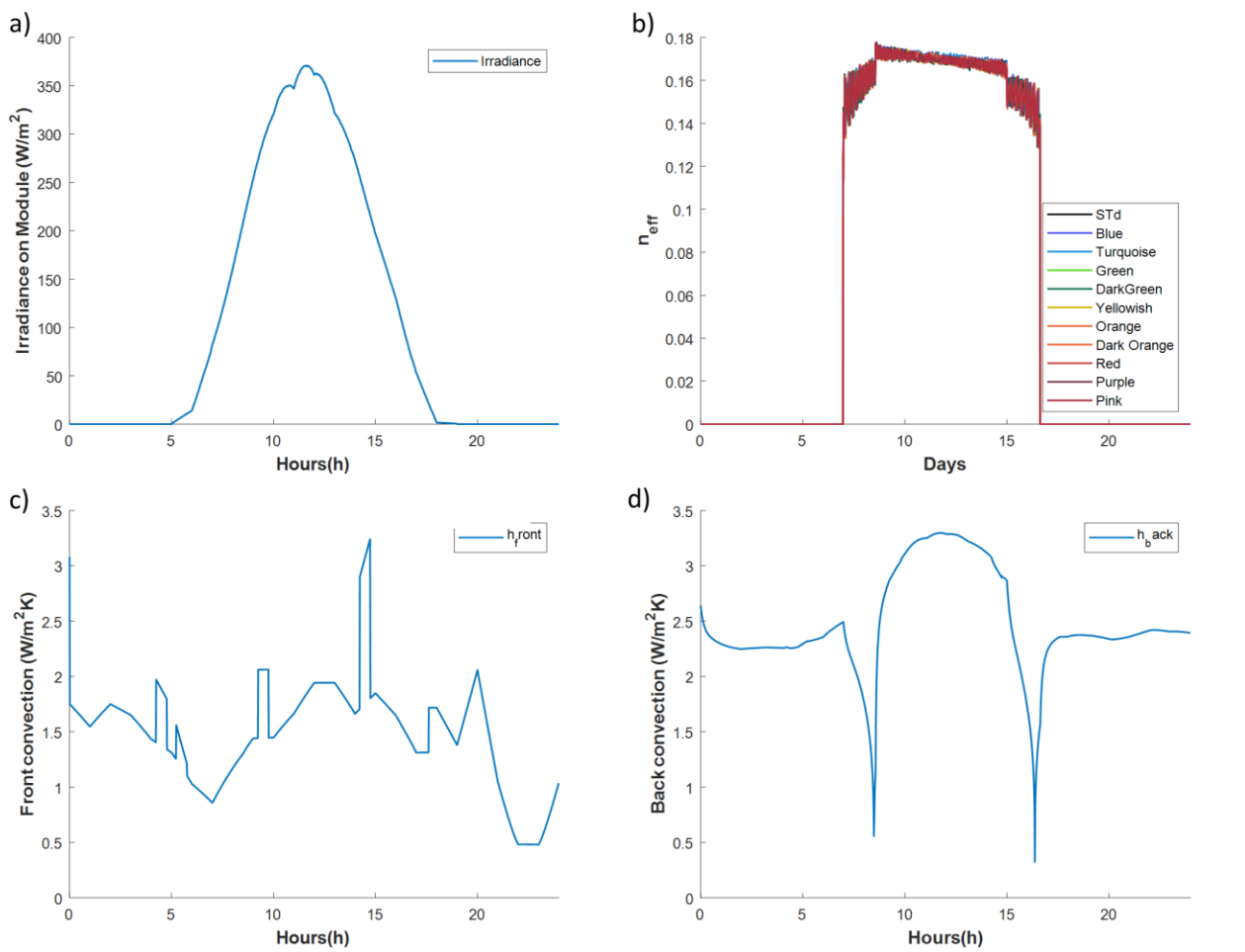

Figure A 61 Figure a) Total incident irradiance for the modules attached on a façade with an air gap on the 3rd of September in Dubai, Figure b) Efficiency distribution for the modules attached on a façade on the 3rd of September in Dubai, Figure c) Total convection on the front, Figure b) Total convection on the back side of the module attached on a façade with an air gap on the 3rd of September in Dubai

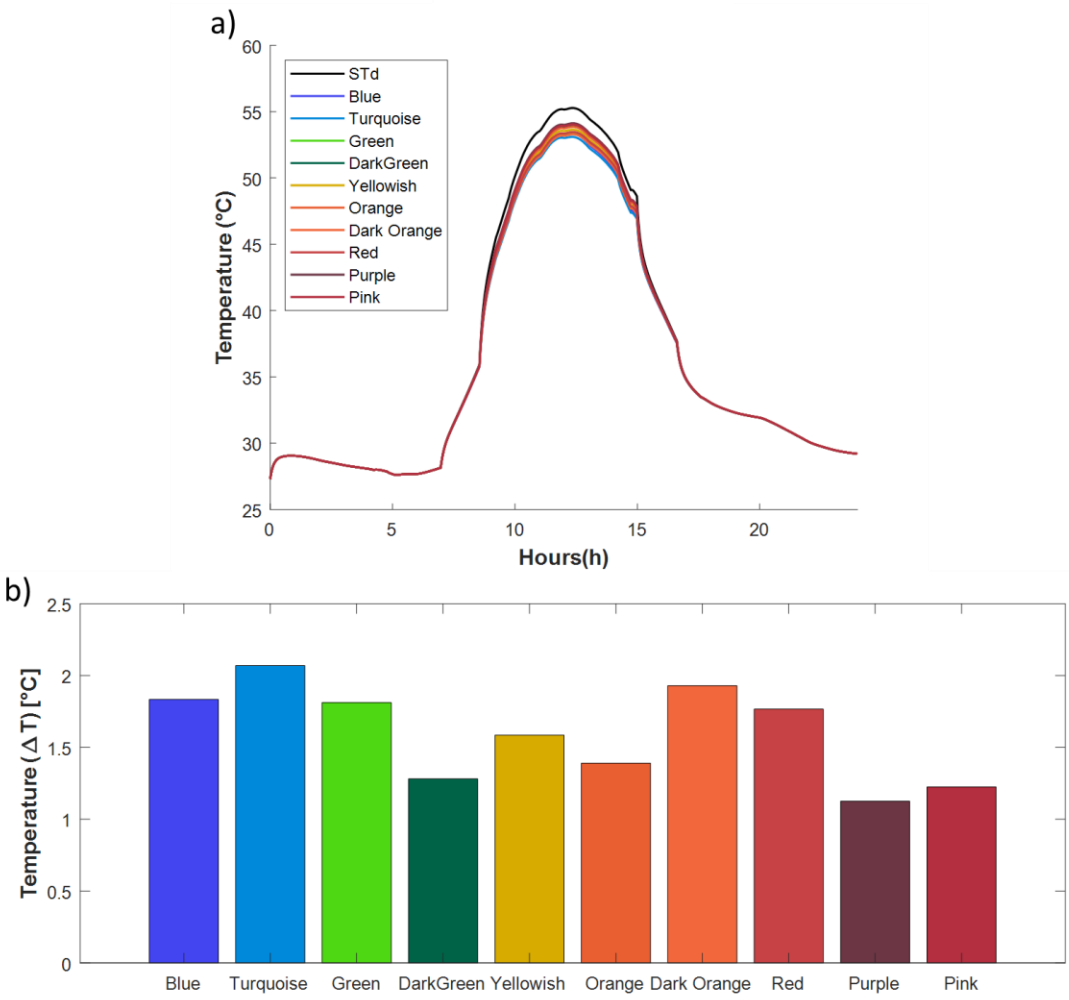

Figure A 62 Figure a) Temperature distribution for the standard module and the 10 main colors attached on a façade with an air gap on the 3rd of September in Dubai, Figure b) Temperature difference for each color from the maximum temperature of the standard module

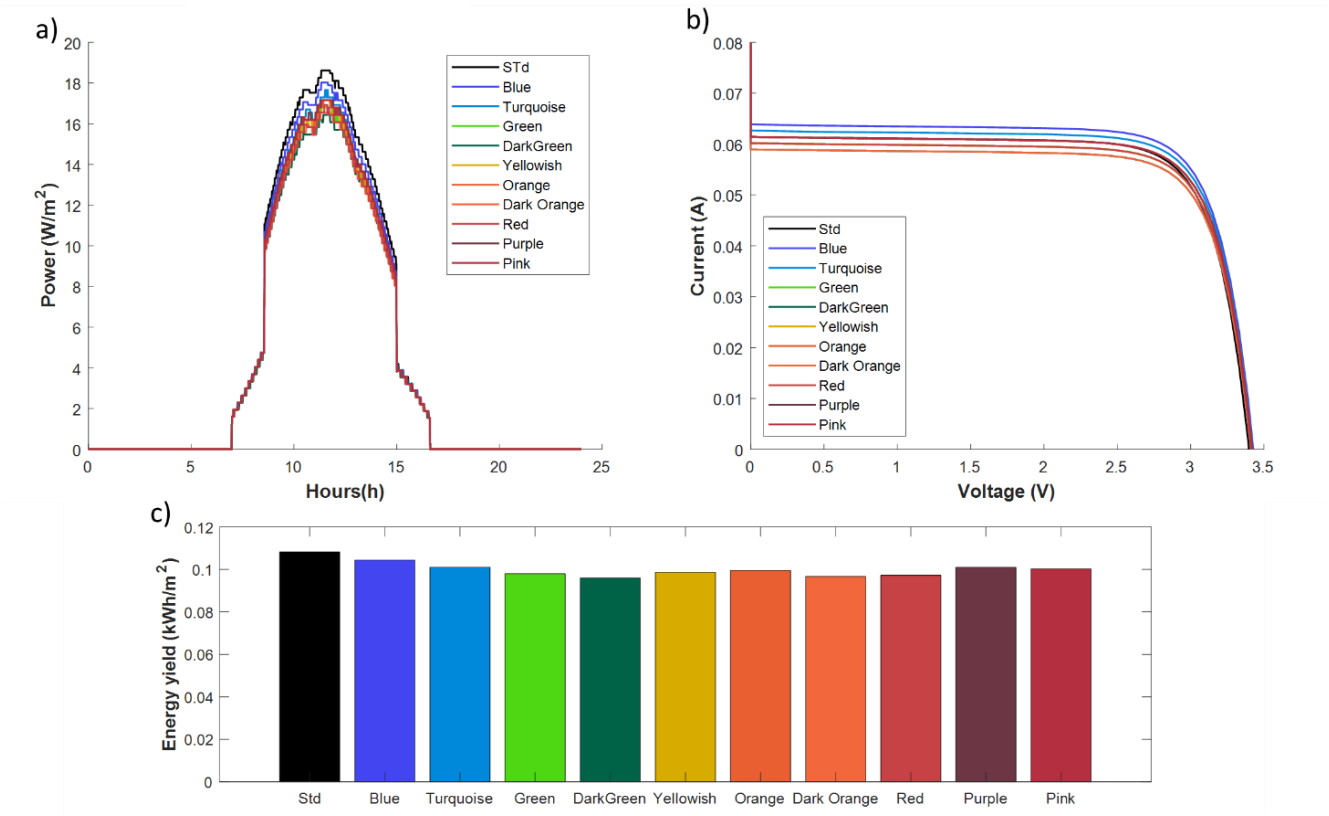

Figure A 63 Figure a) Power distribution for the standard module and the 10 main colors attached on a façade with an air gap on the 3rd of September in Dubai, Figure b) Efficiency distribution, Figure c) Energy yield difference for each color from the total energy yield of the standard module

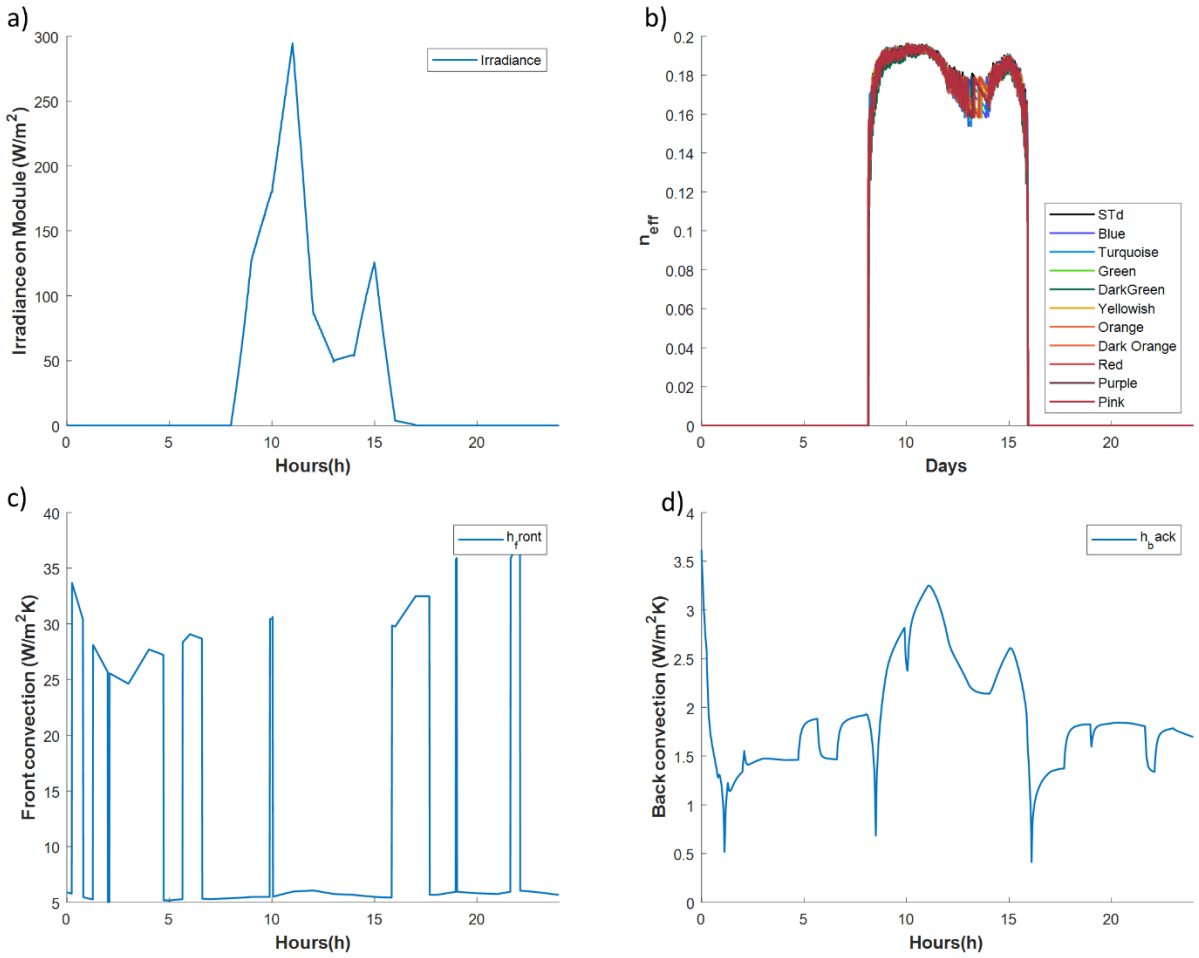

Figure A 64 Figure a) Total incident irradiance for the modules attached on a façade with an air gap on the 19th of January in Delft, Figure b) Efficiency distribution for the modules attached on a façade on the 19th of January in Delft, Figure c) Total convection on the front, Figure b) Total convection on the back side of the module attached on a façade with an air gap on the 19th of January in Delft

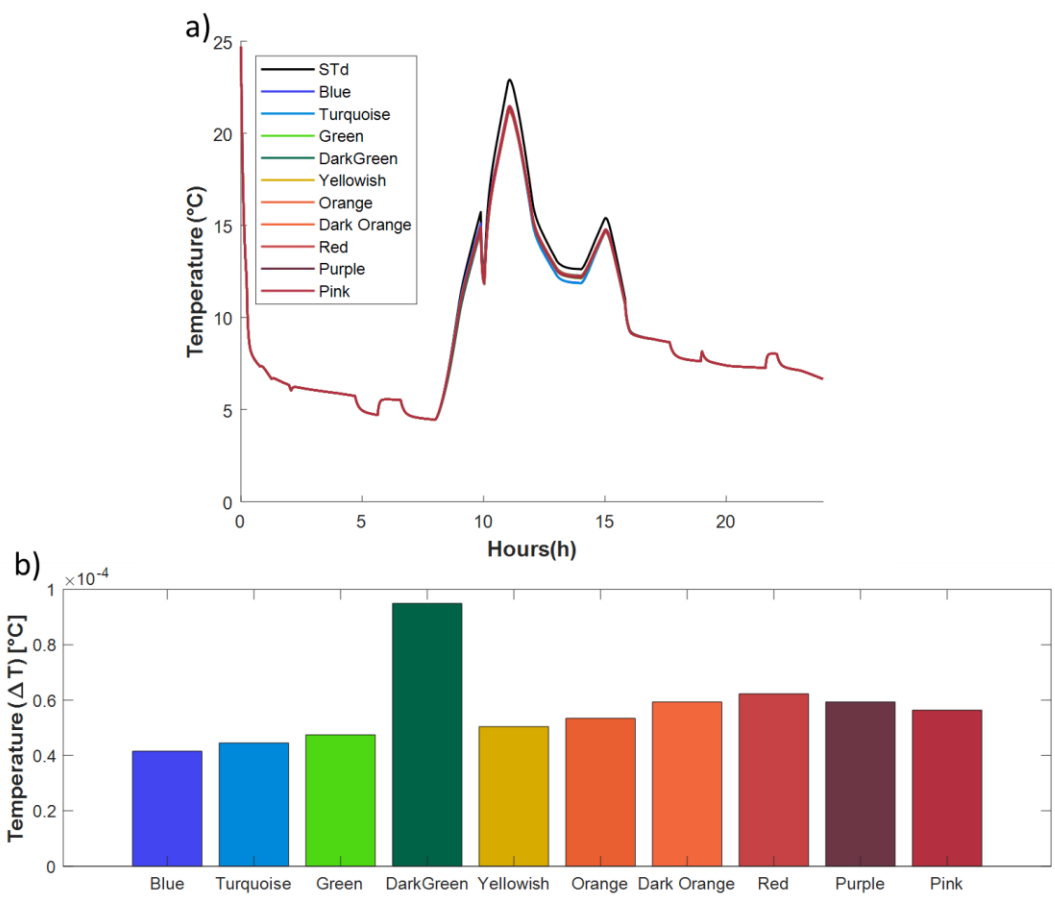

Figure A 65 Figure a) Temperature distribution for the standard module and the 10 main colors attached on a façade with an air gap on the 19th of January in Delft, Figure b) Temperature difference for each color from the maximum temperature of the standard module

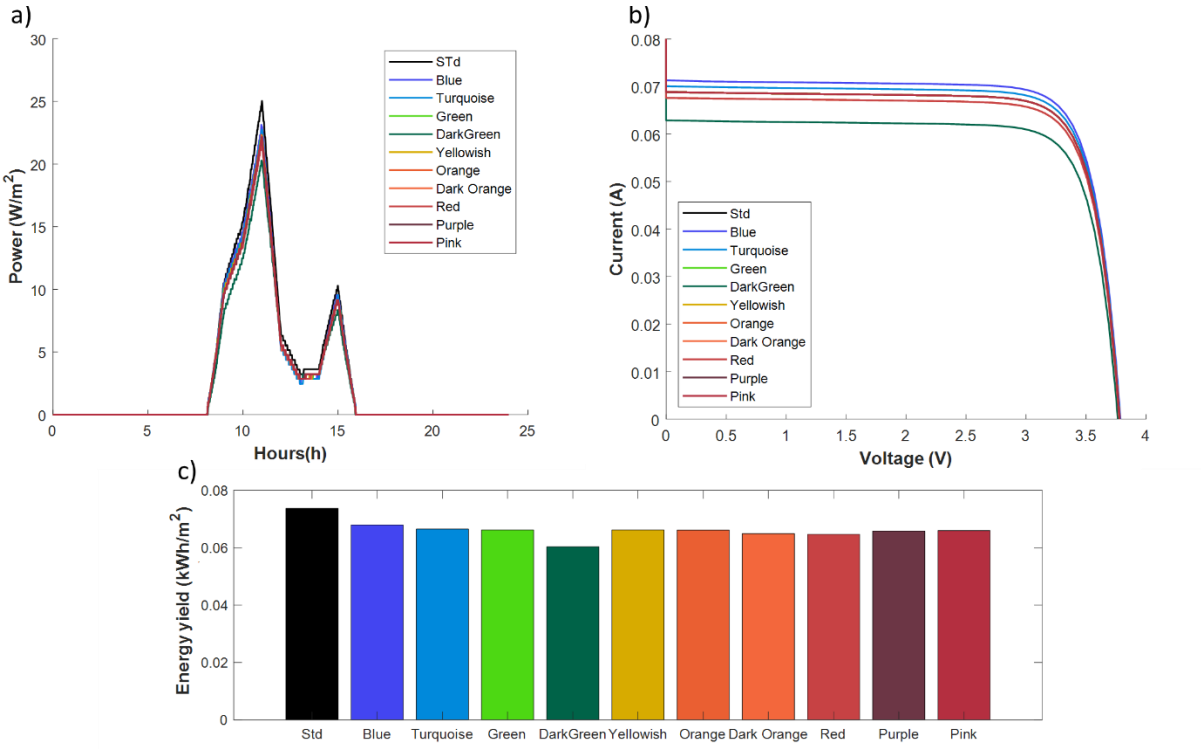

Figure A 66 Figure a) Power distribution for the standard module and the 10 main colors attached on a façade with an air gap on the 19th of January in Delft, Figure b) Efficiency distribution, Figure c) Energy yield difference for each color from the total energy yield of the standard module

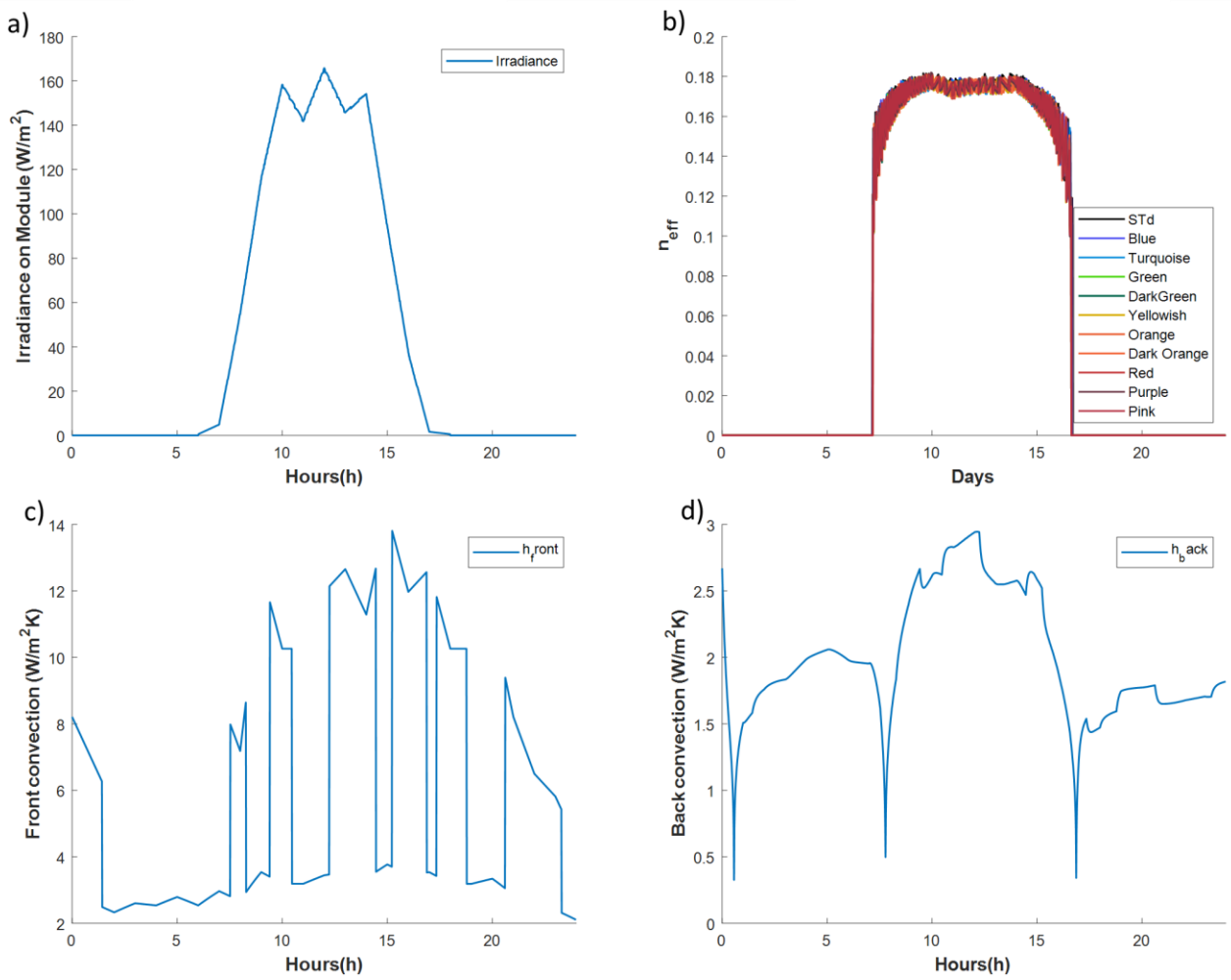

Figure A 67 Figure a) Total incident irradiance for the modules attached on a façade with an air gap on the 1st of January in Dubai, Figure b) Efficiency distribution for the modules attached on a façade on the 1st of January in Dubai, Figure c) Total convection on the front, Figure b) Total convection on the back side of the module attached on a façade with an air gap on the 1st of January in Dubai

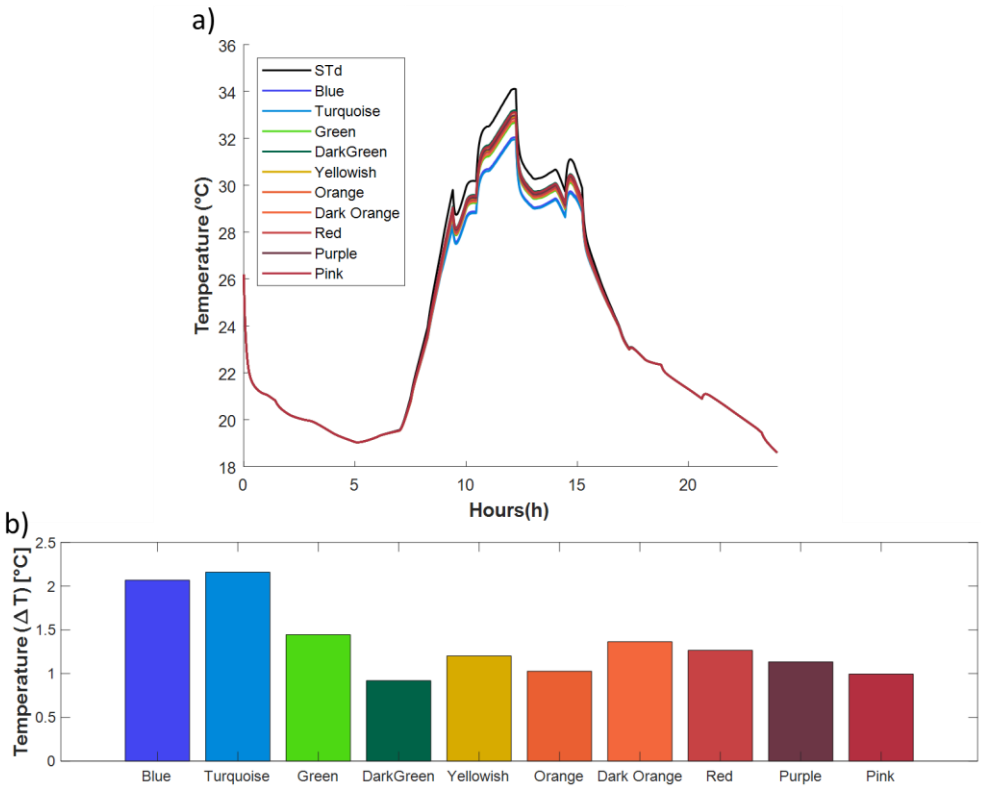

Figure A 68 Figure a) Temperature distribution for the standard module and the 10 main colors attached on a façade with an air gap on the 1st of January in Dubai, Figure b) Temperature difference for each color from the maximum temperature of the standard module

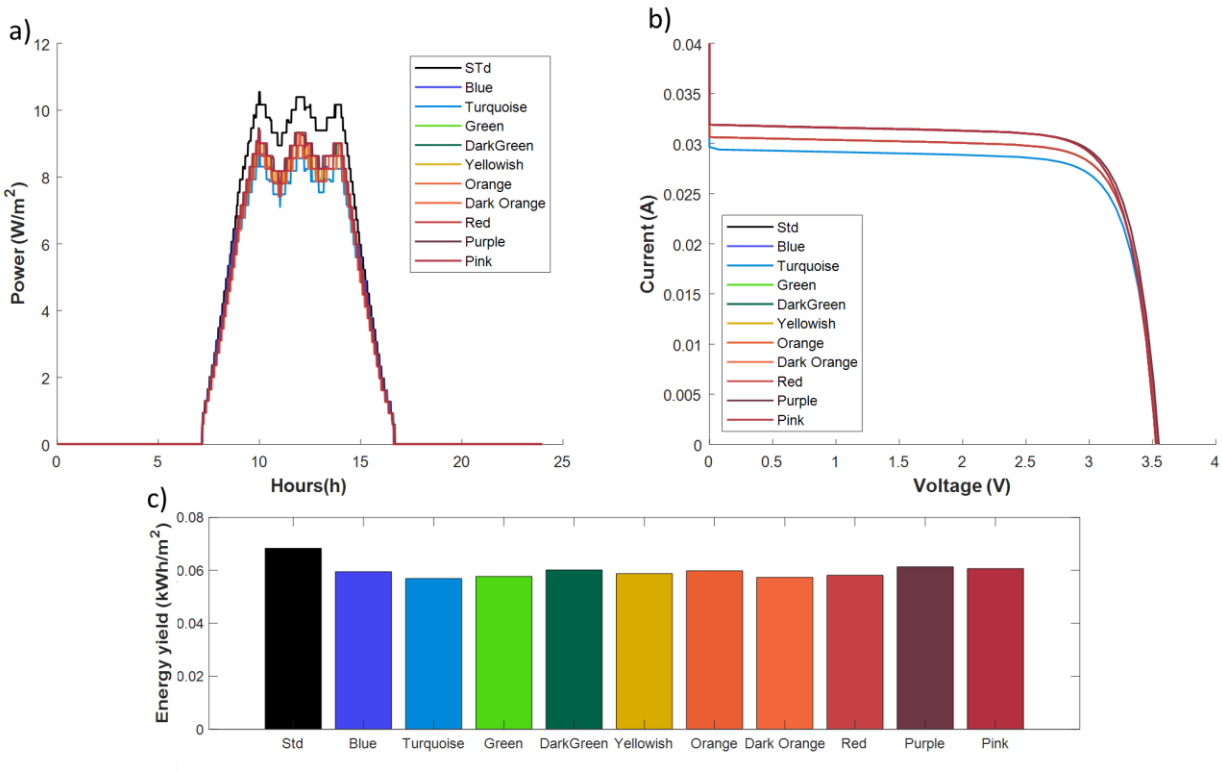

Figure A 69 Figure a) Power distribution for the standard module and the 10 main colors attached on a façade with an air gap on the 1st of January in Dubai, Figure b) Efficiency distribution, Figure c) Energy yield difference for each color from the total energy yield of the standard module

Bibliography

[1] I. Zanetti, P. Bonomo, and F. Frontini, “Building Integrated Photovoltaics : Product overview for solar building skins Status Report,” 2017.

[2] C. Catita, P. Redweik, M. C. Brito, S. Freitas, and S. Guimar, “The importance of facades for the solar PV potential of a Mediterranean city using LiDAR data,” vol. 111, 2017, doi: 10.1016/j.renene.2017.03.085.

[3] “eurostat Statistics Explained,” [Online]. Available: https://ec.europa.eu/eurostat/statistics-explained/index.php?title=File:Final_energy_consumption,_EU-28,_2015_(%25_of_total,_based_on_tonnes_of_oil_equivalent)_YB17.png.

[4] F. Frontini, A. Scognamiglio, G. Graditi, and C. S. Polo, “From BIPV to building component,” no. November 2015, 2013.

[5] WernerWeiß., “Solar Combisystems for a Sustainable Energy Future,” *Of, Newsl. Int. T H E Agency, Energy Heating, Sol.*, no. 35, pp. 1–8, 2000.

[6] T. James and A. Goodrich, “Building Integrated Photovoltaics : A Concise Description of the Current State of the Art and Possible Research Pathways,” pp. 1–30, 2016, doi: 10.3390/en9010021.

[7] J. C. O. Lizcano, “Optic Filters for Built-Integrated Photovoltaic (BIPV) applications,” 2014.

[8] S. Villa, “Colored PV modules 0.15em based on Interference Filters,” 2018.

[9] E. S. Marstein, J. H. Ã. Selj, T. T. Mongstad, and R. Sønden, “Reduction of optical losses in colored solar cells with multilayer antireflection coatings,” *Sol. Energy Mater. Sol. Cells*, vol. 95, pp. 2576–2582, 2011, doi: 10.1016/j.solmat.2011.03.005.

[10] H.Anglus Macleod, *Thin film optical Filter*. 2010.

[11] M. Li, L. Zeng, Y. Chen, L. Zhuang, X. Wang, and H. Shen, “Realization of colored multicrystalline silicon solar cells with SiO2/SiNx:H double layer antireflection coatings,” *Int. J. Photoenergy*, vol. 2013, 2013, doi: 10.1155/2013/352473.

[12] G. Peharz, B. Grosschädl, C. Prietl, W. Waldhauser, and F. P. Wenzl, “Tuning the colors of c-Si solar cells by exploiting plasmonic effects,” *Next Gener. Technol. Sol. Energy Convers. VII*, vol. 9937, no. September 2016, p. 99370P, 2016, doi: 10.1117/12.2237754.

[13] “Kameleon Solar.” https://kameleonsolar.com/about-colorblast/%0D.

[14] B. Bläsi *et al.*, “Morpho Butterfly Inspired Coloured BIPV Modules,” *33rd EUPVSEC*, no. September, pp. 2–6, 2017, [Online]. Available: https://www.ise.fraunhofer.de/content/dam/ise/de/documents/publications/conference-paper/33-eupvsec-2017/Blaesi_6BV370.pdf.

[15] K. Chung *et al.*, “Flexible, angle-independent, structural color reflectors inspired by morpho butterfly wings,” *Adv. Mater.*, vol. 24, no. 18, pp. 2375–2379, 2012, doi: 10.1002/adma.201200521.

[16] M. Tripathy, P. K. Sadhu, and S. K. Panda, “A critical review on building integrated photovoltaic

products and their applications," *Renew. Sustain. Energy Rev.*, vol. 61, pp. 451–465, 2016, doi: 10.1016/j.rser.2016.04.008.

[17] A. K. Shukla, K. Sudhakar, and P. Baredar, "Recent advancement in BIPV product technologies: A review," *Energy Build.*, vol. 140, pp. 188–195, 2017, doi: 10.1016/j.enbuild.2017.02.015.

[18] P. Heinstein, C. Ballif, and L. E. Perret-Aebi, "Building integrated photovoltaics (BIPV): Review, potentials, barriers and myths," *Green*, vol. 3, no. 2, pp. 125–156, 2013, doi: 10.1515/green-2013-0020.

[19] N. Jolissaint, R. Hanbali, J. C. Hadorn, and A. Schüler, "Colored solar façades for buildings," *Energy Procedia*, vol. 122, pp. 175–180, 2017, doi: 10.1016/j.egypro.2017.07.340.

[20] "Kromatix™ by SwissINSO," [Online]. Available: https://www.swissinso.com/.

[21] Xingshu Sun ; Timothy J. Silverman ; Zhiguang Zhou ; Mohammad Ryyan Khan ;, "Optics-Based Approach to Thermal Management of Photovoltaics: Selective-Spectral and Radiative Cooling," *IEEE*.

[22] M.P. Vaughan, *Optics*. 2014.

[23] Georgia State University "Hyperphysics" [Online], "dispersion @ hyperphysics.phy-astr.gsu.edu." .

[24] Georgia State University "Hyperphysics" [Online], "Fermat @ hyperphysics.phy-astr.gsu.edu." .

[25] C. M. Griot, *Fundamental Optics - Technical Guide*. 2009.

[26] W. H. Southwell, "Omnidirectional mirror design with quarter-wave dielectric stacks," *Appl. Opt.*, 1999.

[27] E. Biyik *et al.*, "A key review of building integrated photovoltaic (BIPV) systems," *Eng. Sci. Technol. an Int. J.*, vol. 20, no. 3, pp. 833–858, 2017, doi: 10.1016/j.jestch.2017.01.009.

[28] M. D'Orazio, C. Di Perna, and E. Di Giuseppe, "Experimental operating cell temperature assessment of BIPV with different installation configurations on roofs under Mediterranean climate," *Renew. Energy*, vol. 68, pp. 378–396, 2014, doi: 10.1016/j.renene.2014.02.009.

[29] F. P. INCROPERA, D. P. DEWITT, T. L. BERGMAN, and A. S. LAVINE, *Fundamentals of Heat and Mass Trasnfer*, Sixth Edit., vol. 112. 2015.

[30] "SMARTS weather data." https://www.nrel.gov/grid/solar-resource/smarts.html.

[31] A. Smets, K. Jager, O. Isabella, R. Van Swaaij, and M. Zeman, *Solar Energy The Physics and Engineering of Photovoltaic Conversion Technologies and Systems*. UIT Cambridge, 2015.

[32] F. Kasten and A. T. Young, "Revised optical air mass tables and approximation formula," vol. 28, no. 22, pp. 4735–4738, 2000.

[33] P. D. da Silva, "Infrared optical filters for passive cooling of photovolaic modules," 2017.

[34] M. Z. R. Santbergen, T. Meguro, T. Suezaki, G. Koizumi, K. Yamamoto, "GenPro4 optical model for solar cell simulation and its application to multijunction solar cells," *IEEE J. Photovoltaics 7*, pp. 919–926, 2017.

[35] P. Varshni, “Temperature dependence of the energy gap in semiconductors,” pp. 2–7, 1967.

[36] O. Dupré, R. Vaillon, and M. A. Green, “A full thermal model for photovoltaic devices A full thermal model for photovoltaic devices,” no. October 2017, 2016, doi: 10.1016/j.solener.2016.10.033.

[37] T. Neises, “Development and Validation of a Model to Predict the Temperature of a Photovoltaic Cell,” 2011.

[38] G. Nellis and S. Klein, *Heat Transfer*. Cambridge, 2009.

[39] E. Kaplani and S. Kaplanis, “Thermal modelling and experimental assessment of the dependence of PV module temperature on wind velocity and direction, module orientation and inclination,” *Sol. Energy*, vol. 107, pp. 443–460, 2014, doi: 10.1016/j.solener.2014.05.037.

[40] S. Armstrong and W. G. Hurley, “A thermal model for photovoltaic panels under varying atmospheric conditions,” *Appl. Therm. Eng.*, vol. 30, no. 11–12, pp. 1488–1495, 2010, doi: 10.1016/j.applthermaleng.2010.03.012.

[41] R. A. Agathokleous and S. A. Kalogirou, “Double skin facades (DSF) and building integrated photovoltaics (BIPV): A review of con fi gurations and heat transfer characteristics,” *Renew. Energy*, vol. 89, pp. 743–756, 2016, doi: 10.1016/j.renene.2015.12.043.

[42] J. A. Palyvos, “A survey of wind convection coefficient correlations for building envelope energy systems ’ modeling,” vol. 28, pp. 801–808, 2008, doi: 10.1016/j.applthermaleng.2007.12.005.

[43] P. Hoang, V. Bourdin, Q. Liu, G. Caruso, and V. Archambault, “Solar Energy Materials & Solar Cells Coupling optical and thermal models to accurately predict PV panel electricity production,” *Sol. Energy Mater. Sol. Cells*, vol. 125, pp. 325–338, 2014, doi: 10.1016/j.solmat.2013.11.032.

[44] I. Haedrich, D. C. Jordan, and M. Ernst, “Solar Energy Materials and Solar Cells Methodology to predict annual yield losses and gains caused by solar module design and materials under field exposure,” *Sol. Energy Mater. Sol. Cells*, vol. 202, no. July, p. 110069, 2019, doi: 10.1016/j.solmat.2019.110069.

[45] T. Yang and A. K. Athienitis, “ScienceDirect A study of design options for a building integrated photovoltaic / thermal (BIPV / T) system with glazed air collector and multiple inlets,” *Sol. Energy*, vol. 104, pp. 82–92, 2014, doi: 10.1016/j.solener.2014.01.049.

[46] University College of London., “Color vision research and laboratory,” 2006. http://www.cvrl.org/.

[47] “Solargis Prospect.” https://apps.solargis.com/prospect/map?s=25.202456,55.355988&c=25.08933,54.871216,10.

[48] “The Engineering Toolbox.” https://www.engineeringtoolbox.com/.

[49] 2001 Davies et al. JSE, vol. 123 No. 2, “Preiction of Builing Integrated Photovoltaic Cell Temperatures.”